UNIVERSITÀ DEGLI STUDI DI PALERMO

Ph.D. in Civil, Environmental and Materials Engineering
Department of Engineering

STRAIN LOCALIZATION AND FRACTURE IN ISOTROPIC DAMAGING MATERIALS: A NOVEL AUGMENTED-FINITE ELEMENT STRATEGY

La Dottoressa
Marianna Puccia

Il Coordinatore
Prof. Antonina Pirrotta

Il Tutor
Prof. Giuseppe Giambanco

CICLO XXIV
Anno 2022

Marianna Puccia
Palermo, Settembre 2022
e-mail:marianna.puccia@unipa.it
e-mail:mariannapuccia@libero.it

Thesis of the Ph.D. course in *Civil, Environmental and Materials Engineering (Ingegneria Civile, Ambientale e dei Materiali)*
Dipartimento di Ingegneria
Università degli Studi di Palermo
Viale delle Scienze, Ed.8 - 90128 Palermo, ITALY

Written in LaTeX
Examples and figures made with *MATLAB*© and *Adobe Illustrator*©

A mamma, papà e Vincenzo

Contents

List of Figures

List of Tables

Notations

In this Section the adopted mathematical notation is presented. In general, first-order tensors (vectors) are indicated with lower-case bold latin letters, second-order tensors with lower-case bold italic greek or latin letters and fourth-order tensors with bold capital latin letters. Voigt and matrix notations are used throughout the thesis.

General quantities

Scalar	α
First-order tensor	$\mathbf{a}$, a_i
Second-order tensor	$\boldsymbol{\sigma}$, σ_{ij}
Fourth-order tensor	$\mathbf{E}$, E_{ijkl}

Useful operators

Kronecker delta	$\boldsymbol{\delta}$, $\delta_{ij} = \begin{cases} 1 & \text{if} \quad i = j \\ 0 & \text{if} \quad i \neq j \end{cases}$
Permutation or Levi-Civita symbol	$\boldsymbol{\epsilon}$, $\epsilon_{ijk} = \begin{cases} 1 & \text{if } i,j,k \text{ in CW order} \\ -1 & \text{if } i,j,k \text{ in CCW order} \\ 0 & \text{other cases} \end{cases}$ being (C)CW=(Counter)ClockWise
Second-order unit tensor	$\boldsymbol{I}, I_{ij} = \delta_{ij}$
Fourth-order unit tensor	$\mathbf{I} = \boldsymbol{I} \otimes \boldsymbol{I} = \boldsymbol{\delta} \otimes \boldsymbol{\delta}, I_{ijkl} = \delta_{ik}\delta_{jl}$

Symmetrized fourth-order unit tensor	$\mathbf{I}^s = \boldsymbol{\delta}\overline{\otimes}\boldsymbol{\delta}, I^s_{ijkl} = \frac{1}{2}(\delta_{ik}\delta_{jl} + \delta_{il}\delta_{jk})$
Anti-symmetrized fourth-order unit tensor	$\mathbf{I}^a, I^a_{ijkl} = \frac{1}{2}(\delta_{ik}\delta_{jl} - \delta_{il}\delta_{jk})$

Mathematical notations

For all	$\forall$
Contained in	$\in$
Set of all real numbers	$\mathbb{R}$
Absolute value of a real number	$\|\alpha\|$
Norm of a vector	$\|\mathbf{a}\|$
Determinant of a second-order tensor	$\|\boldsymbol{A}\|$
Transpose of a second-order tensor	$\boldsymbol{A}^T$
Inverse of a second-order tensor	$\boldsymbol{A}^{-1}$
Dot or scalar product of two first-order tensors	$\mathbf{a} \cdot \mathbf{b} = a_i b_i$
Cross product of two first-order tensors	$[\mathbf{a} \times \mathbf{b}]_k = \epsilon_{ijk} a_i b_j$
Tensor product of two first-order tensors	$[\mathbf{a} \otimes \mathbf{b}]_{ij} = a_i b_j$
Contraction of two second order tensors	$\boldsymbol{A} : \boldsymbol{B} = A_{ij} B_{ij}$
Gradient operator	$\nabla(*)$
Divergence operator	div $(*)$
Trace of a second-order tensor	$\mathrm{tr}(\boldsymbol{A}) = A_{ii}$

Chapter 1

Introduction

This Chapter will introduce the fundamental problem underlying the entire thesis. The so-called strain localization in quasi-brittle solids will be investigated in the framework of Isotropic Damage Models. This physical phenomenon will be here presented by analyzing the main theoretical aspects developed over the years, as well as the numerical procedures and the computational approaches implemented to include the arising of weak and strong discontinuities and to predict its possible evolution in the framework of the Finite Element Method (FEM).

1.1 Strain localization in solids

It is already known that when a material is subjected to a high level of load, the strain tends to be concentrated in a quite narrow strip zone, where it increases until the material results in failure. Generally, structural collapse phenomena are often preceded or triggered by the loss of bearing capacity of one or more parts of the structure. The localization phenomenon develops in a small volume compared to the whole structure, where the dissipative process takes place. The formation of plastic hinges in metal frames, or fractures in masonry panels are typical examples. More specifically, we are concerned with the local aspect of such phenomenon, which can be understood from different points of view. In this thesis we will deal specifically with the *strain localization*, associated with the occurrence of displacement or strain gradients in small areas of the structure.

From a general point of view, a material could follow a linear-elastic response until a certain loading value, followed by the occurrence of micro-cracks

or internal voids. Strain localization consists in the onset of these micro-cracks or micro-defects, whose coalescence and interaction finally result in a physical crack. Although the strain localization phenomena appear at the macroscopic scale, as physical fractures, the prediction of this phenomenon at the microscopic level could provide useful indicators to prevent structural failure.

Strain localization involves different kinds of materials, such as concrete, rock, soils but also metals or fibre-reinforced composites, under various loading conditions such as uniaxial and multiaxial, monotonic and cyclic loading. Each material, however, responds differently based on its different constitutive and mechanical nature. Commonly, materials are divided into two major categories: *ductile materials*, such as steel, aluminium or plastics and *brittle materials*, such as glass, brick, diamond or some polymers [9].

The substantial differences between these two categories can be highlighted by studying the relative stress-strain curves, reported in Figure 1.1. The ductility or brittleness of a material depends substantially on whether or not it can develop plastic deformations during a loading process, which leads to a concentration of permanent and irreversible strains. Ductile materials, moreover, degrade gradually, undergoing the so-called yielding phase before failing, thus providing advance notice for the collapse; brittle materials, on the other hand, are subjected to sudden fracture since the post-elastic phase is practically nonexistent. As a result, the energy stored by ductile materials before failure is greater than that associated with brittle ones. Another substantial difference is related to a non-symmetric response of the material to tensile or compressive loads, as brittle materials have higher compressive strength than tensile one. Furthermore, ductility or brittleness is highly temperature dependent; consequently, a brittle material can behave like a ductile one at an elevated temperature.

However, not all materials can be easily placed in one of these two categories; such materials are therefore called *quasi-brittle materials*, on which my thesis will mainly focus. Quasi-brittle materials exhibit a post-elastic response characterized by the so-called stress softening, during which an increase in strain corresponds to a decrease in stress. Concrete, rocks or ceramics are typical examples of this class of materials.

As said before, the phenomenon of strain localization appears differently in relation to the constitutive nature of the material. The first analyses of this phenomenon were conducted to interpret experimental results on tensile tests on metal specimens. As discovered by LÜDERS in 1860 [72], steels experiencing tensile stresses present the so-called Lüders bands or stretcher-strain marks,

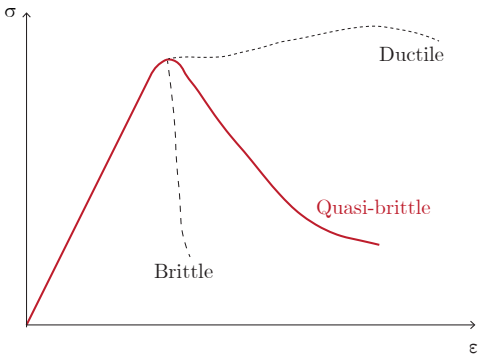

Figure 1.1: Stress-strain curves associated to ductile, brittle or quasi-brittle materials.

caused by localized plastic deformation as a result of a not uniform yielding. The Lüders band usually starts at one end of the specimen and proceeds toward the other one, with a typical inclination of $50° - 55°$ from the specimen axis. The emergence of such bands can be associated with the constitutive analysis of the deformation process in *ductile materials*, which includes several interacting mechanisms, summarized as follows: plastic deformation, damage diffusion, damage concentration (void coalescence) and consequent strain localization, and finally, crack formation and propagation [128]. During the post-elastic range, the spread of damage results in a plastic deformation component with consequent degradation of stiffness. After reaching the yield stress, the subsequent softening range goes along with a strain localization in a specific zone, causing the sliding of crystalline planes, which involves what for this reason is called "shear band" [76] (Figure 1.2-a). The degradation process associated to strain localization is modeled as lumped into a sufficiently thin cohesive band, which allows for a gradual transition between the onset of localization and the formation of a macro-crack (Figure 1.2-b).

Similar phenomena could be recorded in *granular materials*, such as rock, clay or sand. These materials are extremely heterogeneous as well as the strain distribution, which could involves shear bands [109]. As known in Geotechnics, it is possible to introduce a friction angle, which is a shear strength parameter of soils linked to the interaction forces developed between different grains and their reciprocal position and dimension. By considering this friction angle, it is possible to identify the plane along which the sliding will take place, after reaching a limit value of the tangential stress (Figure 1.3-a). Another parameter

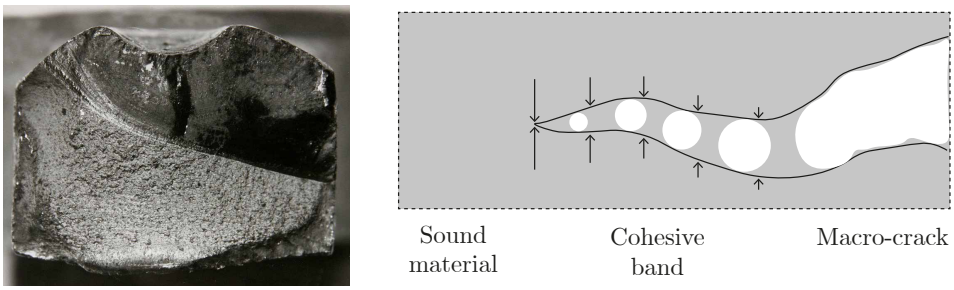

Figure 1.2: Strain localization in ductile materials: (a) shear band in metals; (b) representation of the cohesive zone concept.

that could have an effect is the dilatancy, which is a mechanical phenomenon for which the particles, under the action of external loads, increase their volume by reorganizing their internal distribution.

Differently, micro-mechanical fatigue analysis on *polymer matrix composites* has shown the possibility to record two different and often conflicting deformation mechanisms that develop simultaneously: crazing, which usually produces brittle cracks, and shear flow, which is usually associated with ductile failure. The existence of both deformation modes is linked to the long-chain macromolecular structure and the ductile-brittle transition behaviour, typical of polymers. Under certain loading condition, crack tip propagates in a certain direction (crazing), but secondary deformation mode leads to symmetric shear bands (shear flow), with a certain inclination, called *"epsilon modes"*, since their similarity to the Greek letter considering a cross-section [119] (Figure 1.3-b).

As regards *quasi-brittle materials*, cracks in concrete, for example, form by progressive microcracking within a certain non-negligible Fracture Process Zone (FPZ) at a preexisting notch/crack, in which the material progressively softens. In this type of materials, as said before, the stress-strain relation exhibits strain-softening behaviour after the elasticity limit. Experimental analysis has also shown that the crack width depends on the maximum aggregate size in the concrete [6] (Figure 1.4-a) or, generally, on the geometric nature of the material components.

In fact, it is necessary to emphasize that the phenomenon of strain localization, in addition to being related to the different constitutive models described

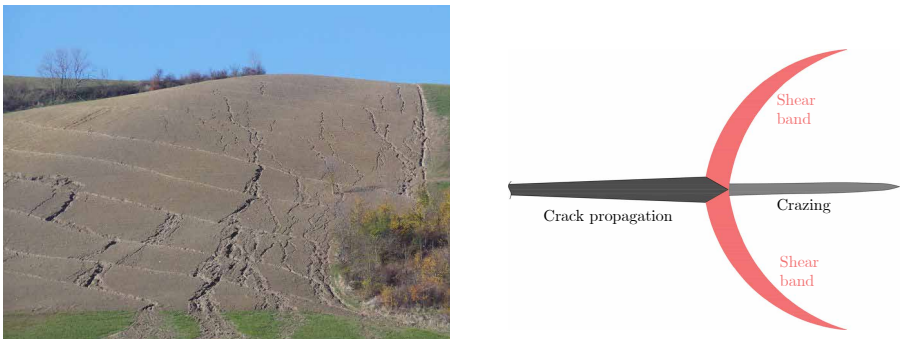

(a) (b)

Figure 1.3: Strain localization in materials with quasi-brittle behaviour: (a) soil sliding surfaces; (b) polymers representation of the so-called "epsilon-mode".

above, also depends on the geometric arrangement of its constituents. In structural engineering, it is common to work with *heterogeneous materials*, such as masonry, which are generally consisting of units of more resistant material connected by cohesive or adhesive joints of less resistant material. All the problems related to the modeling of the aforementioned materials are of great scientific interest, with the related inelastic phenomena that generally take place in their physical interfaces, which are the contact surfaces between two different materials (Figure 1.4-b).

Therefore, it can be concluded that research on the physical phenomenon of strain localization is open and constantly growing, in view of a possible prediction of the structural collapse. The phenomenon depends on the constitutive properties of the material, as well as on the geometric arrangement of the constituents and on global characteristics of the structural components.

1.2 Theoretical aspects of strain localization

In the previous Section, the phenomenon of strain localization was illustrated from a purely physical point of view, intended it as the preliminary phase of fracture inception. However, this phenomenon has a deep local nature, studied from a constitutive point of view since the early years of the last century. As it will be better explained later, the concentration of strains in a strip zone may result in the emergence of the so-called strong or weak discontinuities,

(a) **(b)**

Figure 1.4: Strain localization in quasi-brittle or heterogeneous materials: (a) shear bands in a concrete beam; (b) masonry crack between mortar interfaces.

depending on whether a jump in displacements or strains arises, respectively; consequently, the linear elastic problem may be ill-posed. The formation of a weak discontinuity, in fact, involves constitutive instability, so that the initial homogeneous strain field is no longer unique and stable, setting a *bifurcation point*, which consists of the possibility on the occurrence of more than one strain rate pattern related to the associated stress rate. For this reason, a definition of the term *stability* is therefore necessary: a system is stable if a small perturbation in the initial conditions causes a small change in the solution (as stated by `LYAPUNOV` in 1892 [73]). The term perturbation, therefore, alludes to the need to include considerations from the dynamic point of view as well.

The simplest and oldest criterion about the stability of structures is linked to an *energetic approach* [66]: the `LAGRANGE-DIRICHLET` theorem (1788) states that a conservative system is stable if its potential energy is positive definite, i.e. it has a strict minimum. Similarly, an equilibrium state is stable if the second variation of the potential energy Π is positive for any small variations $\delta\mathbf{u}$ of the generalized displacements from the equilibrium state

$$\partial^2\Pi > 0 \quad \forall\delta\mathbf{u} \neq 0. \tag{1.1}$$

The stability problem can be reduced to an investigation on the shape of the potential energy surface as a function of the generalized displacements of the structure. Alternative to this definition, the *loss of uniqueness*, i.e. the loss of material stability occurs when the second variation of the potential energy

vanishes:

$$\partial^2 \Pi = \frac{1}{2} \dot{\boldsymbol{\sigma}} \dot{\boldsymbol{\varepsilon}} = 0 \tag{1.2}$$

where $\dot{\boldsymbol{\sigma}}, \dot{\boldsymbol{\varepsilon}}$ are the stress and the strain rates, respectively. Let us analyze the following five local conditions regarding the stability of a material [13]:

C1 Positive-definiteness of the constitutive operator;

C2 Non-singularity of the constitutive operator;

C3 Strong-ellipticity;

C4 Ellipticity;

C5 Flutter.

First mathematical studies related to bifurcations have been pointed out by HADAMARD (1903) [47], regarding the positiveness of the eigenvalues of the elastic fourth-order tensor $\boldsymbol{E}$ (**C1**). Similarly, condition **C2** is associated to the condition of non-vanishing of these eigenvalues. The lack of positive definiteness of the aforementioned tensor, in fact, makes the wave propagation speed imaginary, as explained later. Same considerations can be extended considering the tangent elastic operator $\boldsymbol{E}_t$ of inelastic materials, as stated by HILL (1958) [50] or THOMAS (1961) [122]. Similarly, a constitutive approach was already highlighted by the first formulations of RUDNICKI and RICE (1975) [103]: the strain localization can be understood as an instability in the macroscopic constitutive description of inelastic deformation of the material which can be encountered when

$$det(\boldsymbol{E}_t) = 0. \tag{1.3}$$

The crucial consequence of the loss of positive-definiteness of the material tangent operator is the loss of ellipticity of the equilibrium rate equations. In fact, the boundary value problem is well-posed when three conditions are verified: ellipticity, the not-emergence of stationary surface waves (Rayleigh waves, along stress-free boundaries) and the not-emergence of stationary interfacial waves (Stonely waves) [88].

At this point, it is useful to underline that strain localization can be analyzed from a *dynamic* or *static* point of view. Regarding the first one, localization corresponds to an acceleration wave with a vanishing speed, as pursued by the

already mentioned Hadamard; in the second case, localization can be understood as the result of the interaction of internal mechanisms of coalescence of micro-defects, sliding, and decohesion that can evolve into a macro-mechanism of fracture.

Starting from these considerations, different approaches have been developed in order to identify at the local level the areas in which the material strongly exhibits localization characteristics [32]. One of these criteria could be summarized as the *velocity variation criterion*, adopted by ORTIZ and QUIGLEY (1991) [91]: in a dynamic context, strain localization is viewed as a stationary discontinuity, that corresponds to an acceleration wave whose wave speed tends to zero, as it represents a kind of internal obstacle to the propagation of the wave itself. The variation of the velocity field, therefore, can be regarded as an indicator of localization in the element.

The *acoustic tensor criterion* (among others, see BORRÉ and MAYER (1989) [17] or RIZZI et al. (1995) [102]) uses the determinant of this tensor as a localization indicator: localization is coincident with the condition of singularity of the acoustic tensor $\boldsymbol{L}$, which is obtained by contracting the tangent material stiffness with the normal vector to the eventual localized band. As explained in next sub-Section 2.2.1, the onset of localization and the associated *discontinuous and localized failure* can be recorded when

$$det(\boldsymbol{L}) = 0, \tag{1.4}$$

that is a condition formulated according to the development by OTTOSEN and RUNESSON (1991) [92] and then also solved by BIGONI and HUECKEL (1991) [14, 15] using Lagrange's multipliers. Analysis of the eigenvalues of the above tensor turns out to be of focal importance for the instability conditions presented above: **C3** corresponds to the positiveness of these eigenvalues, **C4** corresponds to the non-vanishing of the same eigenvalues and, finally, **C5** occurs when these eigenvalues become complex conjugate. The physical meaning of the acoustic tensor will be deeply discussed in several sections of this thesis.

From a computational point of view, as stated by DE BORST [29, 30], if the constitutive tangent operator $\boldsymbol{E}_t$ locally loses its positive-definiteness, the element tangent stiffness tensor $\boldsymbol{K}_t$ may lose its positive-definiteness as well. In fact, given a vector λ, the positive-definiteness of the constitutive tangent operator reads as

$$\lambda^T \cdot \boldsymbol{E}_t \cdot \lambda > 0 \qquad \forall \lambda. \tag{1.5}$$

The element tangent stiffness tensor is defined as follows

$$\boldsymbol{K}_t = \int_V \boldsymbol{B}^T \boldsymbol{E}_t \, \boldsymbol{B} \mathrm{d}V, \tag{1.6}$$

where $\boldsymbol{B}$ is the compatibility matrix. Its positive-definiteness reads as

$$\lambda^T \cdot \int_V \boldsymbol{B}^T \boldsymbol{E}_t \, \boldsymbol{B} \mathrm{d}V \cdot \lambda > 0 \qquad \forall \lambda. \tag{1.7}$$

Since λ is independent of the volume, it follows

$$\int_V \mu^T \boldsymbol{E}_t \, \mu \mathrm{d}V > 0 \qquad \forall \mu, \tag{1.8}$$

being $\mu = \boldsymbol{B}\lambda$. Condition (1.8), using a Gauss integration, reads as

$$\sum_{i=1}^{2} \sum_{j=1}^{2} w_i \, w_j \, |\boldsymbol{J}_i| \boxed{\mu_i^T \boldsymbol{E}_{t,i} \, \mu_i} t > 0 \qquad \forall \mu, \tag{1.9}$$

being w the integration weights, $\boldsymbol{J}$ the Jacobian matrix and t the element thickness. Therefore, if the constitutive operator is positive definite in each integration point (the expression in the box), the tangent stiffness matrix is positive definite as well.

Supposing that the loss of uniqueness condition is verified, which means different equilibrium states exist for the same load level. A non-trivial solution exists if and only if at least one eigenvalue of $\boldsymbol{K}_t$ vanishes or equivalently if

$$det(\boldsymbol{K}_t) = 0. \tag{1.10}$$

A point where the tangent stiffness matrix has a zero eigenvalue cannot be isolated exactly in a numerical process; for this reason, it is assumed that a bifurcation point is encountered when the lowest eigenvalue of the tangent stiffness matrix becomes slightly negative.

A more complicated condition occurs when the tangent stiffness matrix is non-symmetric. The singularity of this matrix implies bifurcation and stability is decided by the symmetric part of the stiffness matrix $\hat{\boldsymbol{K}}_{\boldsymbol{t}}$, whose lowest eigenvalue is known to be smaller or equal to the lowest eigenvalue of the non-symmetric matrix $\bar{\boldsymbol{K}}_t$ [21]. Then it is possible to conclude that localization condition can be associated with $det(\hat{\boldsymbol{K}}_t) = 0$. The positiveness of all the eigenvalues of matrix $\hat{\boldsymbol{K}}_t$ is a necessary and sufficient condition of stability for a structure with a non-symmetric tangent stiffness matrix. It is proved

by the *Bromwich Theorem*: every eigenvalue λ of a non-symmetric matrix $\boldsymbol{K}_t = \hat{\boldsymbol{K}}_{\boldsymbol{t}} + \bar{\boldsymbol{K}}_{\boldsymbol{t}}$ satisfies the following inequalities (called *Bromwich bounds*)

$$\hat{\lambda}_1 \leq Re(\lambda) \leq \hat{\lambda}_n \qquad \bar{\lambda}_1 \leq Im(\lambda) \leq \bar{\lambda}_n \tag{1.11}$$

where $\hat{\lambda}_1$ and $\hat{\lambda}_n$ are the smallest and largest eigenvalues of the symmetric matrix, and $\bar{\lambda}_1$ and $\bar{\lambda}_n$ are the smallest and largest eigenvalues of the anti-symmetric matrix.
Thus the real part of any eigenvalue of $\boldsymbol{K}_t$ lies within the spectrum of $\hat{\boldsymbol{K}}_t$.

It is possible to summarize that

1. If the tangent stiffness operator $\boldsymbol{K}_t$ does not depend on the direction of the vector of generalized displacement increments, a structure is stable if and only if all the eigenvalues of the symmetric part $\hat{\boldsymbol{K}}_t$ of this matrix are positive, and critical if and only if at least one of these eigenvalues vanishes. The vanishing of at least one eigenvalue of a non-symmetric $\boldsymbol{K}_t$ could imply either a limit point or bifurcation point, but not a critical state of stability.

2. If $\boldsymbol{K}_t$ depends on the direction of the generalized displacement increment vector, the vanishing of at least one eigenvalue of $\boldsymbol{K}_t$ implies either a limit point (with or without bifurcation) or a bifurcation occurring at increasing load.

3. If $\boldsymbol{K}_t$ varies discontinuously along the loading path, the first bifurcation occurs when the smallest eigenvalue of $\boldsymbol{K}_t$ becomes zero or negative.

1.3 Numerical analysis of strain localization

An instability problem cannot be easily solved analytically and numerical methods have to be introduced for its solution. The evolution of the localization band can be described using different modelling approaches, usually distinguished as follows: *continuous* methods, *discrete* methods or hybrid *continuous/discontinuous* methods.

The *continuous modelling approach* is based on the assumption that the domain is a continuous body and constitutive models such as plasticity or damage are adopted, making use of internal variables to capture the evolution of the micro-structural changes. Advanced formulations, such as *non-local* [97] and *gradient models* [2], where the response of a material point is related with

the neighbouring points, belong to this approach. In this case, for example, a strain discontinuity is regularized or smeared on the material volume enriching the physical content of the local material models with one or more intrinsic length parameters. As a result, the constitutive equations are capable to better describe the real material behaviour. More recently, the phase-field theory has been applied to the strain localization problem [40, 81] introducing the phase variable to describe the smooth transition from the sound material to the localized one. In this sense the phase-field models belong to the class of regularized continuum models: in fact a sharp crack surface embedded into the solid is substituted by a regularized crack surface, functional of the crack phase field variable.

The *discrete modelling approach* is instead based on the assumption that the material is seen as an assembly of different blocks, particles or elementary quantities, commonly used to model granular or discontinuous materials.

More complex, but often more efficient, are the *continuous/discontinuous models*, within which the computational implementation developed in this thesis also falls. While continuous modelling approaches consider damage and inelastic strains as distributed into the whole structure (*Smeared Crack Models* (SCM) or *Smeared Zone Models* (SZM) [18, 58]), hybrid models are based on the assumption that damage can be represented by a physical macro-fracture lumping all non-linearities into a discrete line or surface. We can generally refer this category to the so-called *Cohesive Zone Models* (CZM). It is therefore necessary to insert a mechanical device that simulates discontinuities and possesses its own constitutive law, different from that of the surrounding material. In this regard we can generally distinguish between *strong* or *weak discontinuities*.

Generally, a *strong discontinuity* is physically represented by a line or surface where the displacement field is discontinuous [90, 104, 111]. A *weak discontinuity*, instead, is depicted as a volume zone confined by two surfaces, where the strain field suffers discontinuity. In particular, the strain state in the narrow zone can be decomposed in the *in plane* components and in the *out of plane* components, being the former regular and the latter discontinuous. This weak discontinuity can be captured by an apposite reduction of the strain field [11, 112].
Under the hypothesis that the band thickness is small if compared to the typical dimension of the structure, the strain state can be approximately considered constant through the thickness and can be evaluated making use of the displacements of the surfaces delimiting the localization area. Adopting the Zero Thickness Interface (ZTI) model the in plane strain components are neglected

and the out of plane components are evaluated on the basis of the displacements jump between the two physical interfaces.

From the computational point of view, research efforts have been mostly concentrated on the simulation of the localization phenomenon in the framework of FEM. Generally, we can distinguish between studies where the discontinuity is *inter-element* located and studies where it is *intra-element* located.

In the first case, the ZTIs are pre-defined between opposite sides of adjacent elements and crack formation, branching and coalescing are guided by the interface constitutive law [20, 129]. In the second case, different strategies have been used to extend the capabilities of the classical finite elements to model intra-element displacement or strain jumps.

The Generalized-Finite Element Method (G-FEM) [39] and the Extended-Finite Element Method (X-FEM) [82] are examples of such numerical strategies. In both cases the approximation of the field variable is enriched making use of the Partition of Unity Method (PUM) which firstly appeared in the work of BABUŠKA et al. [4]. The most significant advantage of these methods is modelling discontinuities and their development without requiring the definition of a new mesh since they only increase the number of Degrees of Freedom (Dofs) in the elements intersected by the crack. However, the numerical integration of elements crossed by a discontinuity requires a special treatment, which is different in presence of different interpolation basis (triangles, quadrilateral, etc.) for 2D or 3D cases [22]. Therefore, despite the additional Dofs cause a small increase in the overall computational cost, the implementation itself is time-consuming.

The Phantom Node Method (PNM) has been derived from the work of HANSBO and HANSBO [48] and can be considered as a variant of the X-FEM [59, 99, 113] since it reinterprets the approximation of the X-FEM displacement field by the superposition of the displacement fields of two overlapped finite elements. The advantage of PNM compared to X-FEM is that no discontinuous interpolation functions are required since each overlapping element furnishes the displacement field on one side of the crack.

A tracking algorithm based on the Virtual Element Method (VEM) has been recently proposed [3]. This method is based on the introduction of a cohesive interface between polygons characterized by any number of edges. The ease of implementation, the no need of a parent element, and the good performances even in presence of distorted elements or not-conforming meshes are the main advantages of the method. The need of inserting new nodes or moving some of the existing ones, and difficulties in handling with crack branching are the

main drawbacks.

The Augmented Finite Element Method (A-FEM) [38, 69, 71, 74] operates at the element level and does not require the enrichment of the shape functions to approximate the displacement field. In a different manner with respect to the PNM, A-FEM simulates weak and strong discontinuities splitting the element in two mathematically separable standard elements which are adjacent to the discontinuity surface. Additional Dofs are firstly introduced to decompose the cracked element and then condensed at the element equilibrium level. Hence, they are not present at the global level.
Some of the benefits of A-FEM are:

- elements are split into standard finite elements, fully compatible with standard finite elements packages;
- possibility to consider different material properties for the sub-elements;
- no need of a level-set information or to necessarily know if a sub-element is below or above the discontinuity;
- reduced computational cost;
- straightforward implementation to 3D cases.

In this work attention is focused on the simulation of weak discontinuities, modelling the localization zone by the InterPHase model (IPH) introduced by GIAMBANCO and MRÓZ [41] and implemented in the finite element framework by Giambanco et al. [43]. The principal difference of our approach with the classical A-FEM and X-FEM regards the possibility to follow the material failure from the strain localization in a thin layer band to the crack opening by using the interphase concept in place of the quite common ZTI model. The IPH model can be considered the enrichment of the ZTI since, keeping as kinematic variables the displacements of the weak discontinuity surfaces, it allows to model the contact and the internal strains of the thin material layer and to extend the calculation of the stresses also to the internal components. As a consequence, the thin layer response is more realistic and some phenomena as the squeezing effect can be captured [43]. The most important point is that, differently than ZTI models, IPH does not require a specific tractions-displacement jump constitutive law and the constitutive laws adopted for the IPH can correspond to those of the bulk material.

Starting from the A-FEM formulation, the implemented computational approach aims the simulation of a finite element with an embedded weak discontinuity, modelled as an IPH element.

1.4 Motivations and outlines

The problem of modeling discontinuities that arise when materials are outside their elastic range is common in many engineering fields. In the framework of FE models, considerable research progress has been made in modeling strain localization and proposing computational approaches. Recently, several studies have been carried out to simulate the mechanical response of different materials with efficient and reliable models.

This thesis aims to propose a computational tool able to take into account and model strain localization in structures made up of quasi-brittle materials, studied in the framework of isotropic damage mechanics. The proposed tool should follow the entire process starting from strain localization to fracture propagation. Particular attention will be paid to the numerical loss of accuracy, generally encountered with the discretization of the geometrical domain. In this regard, a specific crack tracking algorithm has been developed in order to correctly follow the crack propagation. The problem related to the modeling of fractures and discontinuities in a material is developed both from the theoretical and from the numerical point of view, throughout eight chapters.

`Chapter 2` thoroughly investigates the physical meaning of the strain localization, presenting it as a consequence of a constitutive instability. A dynamic analysis approach is also pursued, mainly associated with the definition of the so-called acoustic tensor, whose spectral analysis constitutes one of the major criteria for identifying the onset of localization. An additional instability phenomenon called flutter is also presented, linked to a complex form of the acoustic tensor eigenvalues.

An overview on several computational strategies for modeling strain localization is presented in `Chapter 3`. In the framework of Continuous/Discontinuous models, attention is particularly paid to the A-FEM, strategy from which the computational tool implemented in this thesis takes its inspiration.

`Chapter 4` presents different constitutive models for damage mechanics, focusing the attention on the Isotropic Damage Models (IDM) with Strain-Based Loading Functions as formulated by Jirásek [58] and Mazars [79]. The numerical implementation of this formulation is presented, as well as the analysis on strain localization and flutter instability within it. Based on a specific analyt-

ical study, it is proved that flutter instability cannot occur for the given class of damage models. In addition, different localization criteria are compared, highlighting their peculiarities and shortcomings and the consequent need to find an alternative and more complete localization criterion.

The proposed computational methodology to model the finite element with embedded interphase is described in detail in `Chapter 5`. The intra-element weak discontinuity is modeled by referring to the IPH, which can be considered as an evolution of the ZTI. The fundamental relations are numerically treated for a quadrilateral linear 2D element, split into two sub-domains and an interposed IPH element.

Once that the procedure for modeling a finite element with embedded interphase has been defined, the attention is focused on the strategy for simulating fracture propagation at the structure level. Computational aspects regarding the crack tracking algorithm are described in `Chapter 6`. The algorithm allows to evaluate the crack propagation by grouping localized elements into clusters, in turn further divided into substructures.

The in-house code has been written in the Matlab language and used to run simulations on 2D specimens subjected to mode-I and mixed-mode stress states. The numerical examples in `Chapter 7` show the advantages and the accuracy of the proposed strategy, together with the convergence behaviour of the model. It is proved that the mechanical responses in terms of load-displacement curves and crack patterns are not dependent on the mesh-size or mesh-bias. Meaningful results are obtained even for multiple and simultaneous cracks.

A final discussion and future developments are presented in `Chapter 8`.

Chapter 2

Strain localization

This Chapter is devoted to the analysis of strain localization phenomenon. The theoretical aspects presented in Section 1.2 are here studied in detail. From a constitutive point of view, strain localization will be investigated both from a static and dynamic point of view. By referring to the traditional kinematic description for the discontinuities modeling, the differences between strong, weak discontinuities or regularized localization zones will be presented, as well as the related constitutive models. The dynamic aspects related to the strain localization are investigated, starting from the mathematical formulation of the continuous and discontinuous bifurcation problem. It leads to the definition of the acoustic tensor, whose physical meaning will be presented. As known, the spectral analysis of the aforementioned tensor turns out very significant for the analysis of the local conditions for the material stability.

2.1 Strain localization from a constitutive point of view

The focus is mainly on quasi-brittle materials, which localize in a process zone that usually behaves differently with respect to the surrounding bulk material when subjected to mechanical inelastic processes. Propagation and coalescence of initial micro-defects lead to the formation of a displacement discontinuity or a stress-free crack. However, outside this zone, the material unloads elastically. The onset of strain localization leads to strain or displacement discontinuities and, therefore, the standard kinematics of a continuous medium are no longer valid.

Generally, two types of failure can be distinguished: one is associated with a *distributed* or *diffuse failure* and the other with a *localized* or *discontinuous failure*. For the latter, different approaches have been proposed, which mainly differ in the kinematic and in the associated constitutive models, used to mechanically describe the area surrounding the localized band.

2.1.1 Kinematic description

The kinematic description of discontinuities is here addressed according to JIRÁSEK classification [54, 55] and, subsequently, analyzing the corresponding constitutive models. Following this systematic differentiation, three different models of discontinuities can be distinguished, that are schematized in Figure 2.1:

- *Displacement* or *Strong discontinuity*
  The first model corresponds to the physical case of opening cracks or slips along a line. It is characterized by a first-kind discontinuity jump in the displacement field $\mathbf{u}(\mathbf{x})$ across the crack surface. From the compatibility equation, the strain field $\varepsilon(\mathbf{x})$ represents the displacement gradient, which is a sort of measure of how rapid the displacement changes through the material. The jump discontinuity in $\mathbf{u}(\mathbf{x})$ corresponds to a singular part in $\varepsilon(\mathbf{x})$ that has the character of a multiple of the Dirac delta distribution (Figure 2.1-a);

- *Strain* or *Weak discontinuity*
  This model corresponds to the physical concentration of inelastic phenomena in a plastic zone with a finite thickness that usually depends on the microstructure and that is of the same scale of the characteristic material length. The band is separated from the bulk material through two weak discontinuity surfaces. Contrary to the previous case, this model is characterized by a continuous displacement field with two corner points which involve a jump discontinuity for some strain components. Since $\mathbf{u}(\mathbf{x})$ remains continuous, only the out-of-plane strain components could record the discontinuity (Figure 2.1-b);

- *Regularized localization zones* models
  The last model is associated with a continuously differentiable displacement field, so also the associated strain field remains continuous. While the previous model is related to a constant defects concentration in a finite thickness zone, in this case, a higher strain concentration is recorded

in the centre of the band with a gradual transition to lower strains in the surrounding material (Figure 2.1-c).

2.1.2 Constitutive models

Each kinematic case analyzed in sub-Section 2.1.1 can be modelled by referring to different constitutive models.

First of all, it is useful to give an overview on the aforementioned SCM, adopted for the numerical simulation of cracks in the late 1960 (`RASHID`, 1968) [100]. The basic idea is that plastic deformations remain distributed over a certain material volume, so as to ensure that the transition from the elastic to the plastic regime occurs smoothly. In this case, the overall nonlinear behaviour of the weakened material is modelled through a tensorial softening stress-strain law associated to the whole material. Generally, when principal stresses reach a limit value, the crack is inserted and the isotropic stress-strain previous relation is substituted by an orthotropic elasticity-type law associated to the (n, t) reference system, being n and t the axes of orthotropy, normal and tangential to the crack, respectively. Let us consider the stress components $\sigma_{sm} = \begin{bmatrix}\sigma_n & \sigma_t & \sigma_{nt}\end{bmatrix}$ and the associated strain components $\varepsilon_{sm} = \begin{bmatrix}\varepsilon_n & \varepsilon_t & \varepsilon_{nt}\end{bmatrix}$.

The orthotropic relation in plane stress reads as

$$\sigma_{sm} = \boldsymbol{E}_{sm}\,\varepsilon_{sm} \tag{2.1}$$

$$\text{where} \quad \boldsymbol{E}_{sm} = \begin{bmatrix} \mu E & 0 & 0 \\ 0 & E & 0 \\ 0 & 0 & \beta G \end{bmatrix}$$

The normal crack opening relation is linked to the elastic stiffness through a μ coefficient which gradually decreases from one to zero to simulate the progressive decrease of the transmitted normal stresses at the fracture. Shear tractions are instead proportional to the sliding crack opening with a proportionality factor $0 < \beta \leq 1$ called retention factor.

In this class of models we distinguish between fixed or rotating crack models. In *fixed crack models*, the crack direction is evaluated at the moment of crack nucleation and is maintained fixed throughout the analysis, even if principal axes could rotate during the loading process. However, for any value of $\beta \neq 0$, stresses and strains principal axes rotate, often losing their coaxiality: this means that a portion of the elastic shear stiffness is retained, which causes stress locking. To overcome problems related to stress locking and mesh-dependency,

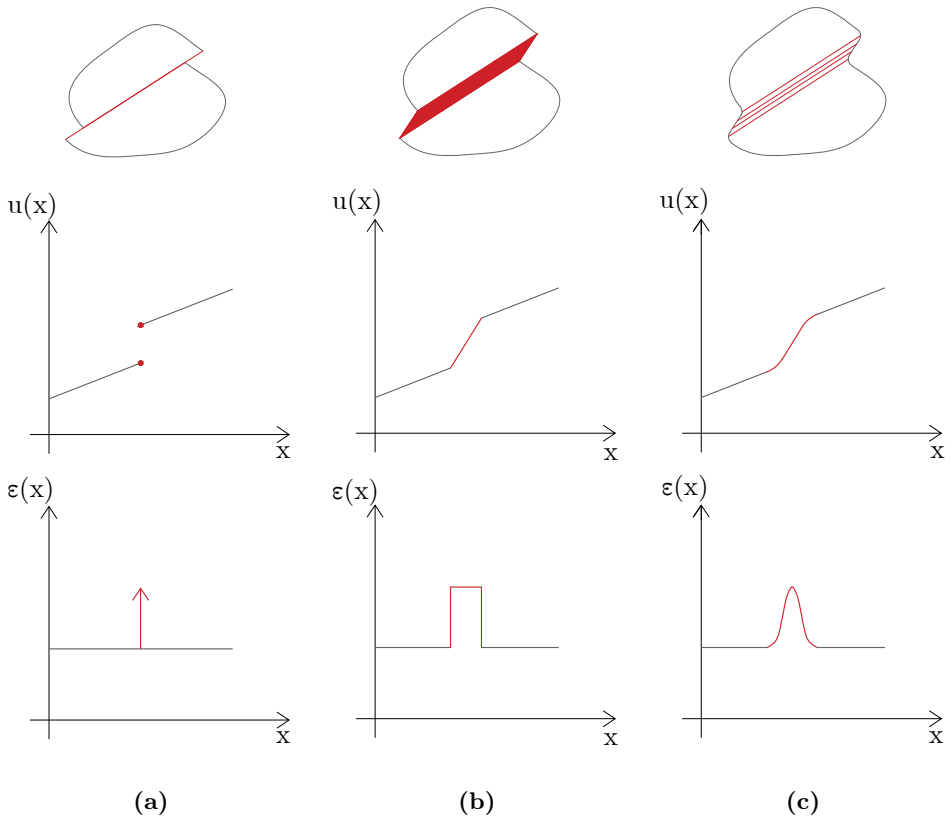

Figure 2.1: Kinematic representation of a discontinuity: (a) Displacement or strong discontinuity; (b) Strain or weak discontinuity; (c) Regularized localization zones.

the *rotating crack model* (RCM) is been introduced, which continuously adjusts the orientation of the crack, which is maintained perpendicular to the principal stress direction. It has been proved that even in this case, coaxiality between stresses and strains could be lost [53, 95]. Stress locking is one of the most relevant problems of SCM, which means a spurious stress transfer that is linked to the poor kinematic description of the displacement field near the macroscopic crack. `JIRÁSEK` and `ZIMMERMANN` [62] improved the RCM by combining it with a damage-type model (*Rotating crack model with transition to scalar damage RC-SD*), for the lack of stress locking in the isotropic damage models. Moreover, the *embedded discontinuity model* overcomes this problem by enriching standard

finite element interpolations by strain or displacement discontinuities [53, 63].

Even if the smeared crack model can be more easily implemented in a standard non-linear FE code, the observed mesh-size and mesh-bias dependence as well the stress locking analyzed have led to the implementation of continuous/discontinuous models, which are certainly more complex and computationally expensive but capable of overcoming these problems. The continuous/discontinuous approaches are based on the implementation of a strong or weak discontinuity: the first one is described as a zero-thickness interface characterized by a cohesive traction-separation law, formulated in terms of tractions versus displacement jumps; the second one is represented as a finite width band associated to a regularized cohesive law formulated in terms of tractions versus inelastic deformations [24].

In the `strong discontinuity` case, the displacement field is discontinuous across the surface of the crack. This type of discontinuity is a topic generally analyzed in Fracture Mechanics.

The simplest model is the so-called *stress intensity factor approach*: the fracture is a stress-free crack, with a stress singularity at the crack tip (Figure 2.2-a). According to the following relation

$$\sigma = \frac{K}{\sqrt{2\pi r}}, \tag{2.2}$$

where r is the distance from the crack tip and K the stress intensity factor, it can be concluded that if $r \to 0 \Rightarrow \sigma \to \infty$. This approach is typical of Linear Elastic Fracture Mechanics (LEFM), which could be applied if the crack width is negligible with respect to the crack length.

A second model is the *energy balance approach*: by taking into account `GRIFFITH`'s theory (1921) [45], from the theorem of minimum energy it can be concluded that the equilibrium state of an elastic body is that for which the system potential energy reaches a minimum. So, a crack could appear if the passage from the unbroken body to the cracked one involves a decrease in the potential energy. The crack formation implies an increase of the work done by the inter-elementary cohesive forces. When a crack propagates, a part of the stored energy is then released. A crack could propagate if the released energy is equal to or greater than the stored one, called potential surface energy, which corresponds to the energy for the formation of a unit area of a crack.

The stress singularity of the crack tip was removed in the *Cohesive Crack Models* or CZMs. Firstly `BARENBLATT` (1959) [5] and then `DUGDALE` (1960) [36], assumed a plastic zone at the crack tip where inelastic strain could be modelled

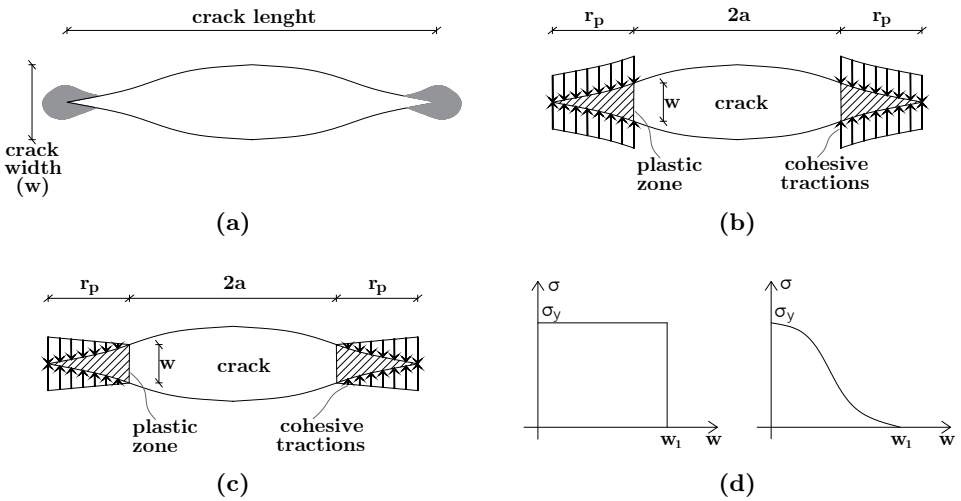

Figure 2.2: Differences between strong discontinuity models: (a) LEFM model; (b) Barenblatt's model; (c) Hillerborg's model; (d) Barenblatt's (left) and Hillerborg's (right) cohesive forces.

as cohesive forces acting on the surrounding. The opposite sides of the crack are smoothly joined at the crack tip, in order to obtain a finite value of stress also at this particular point. It is assumed that the crack opens when the stress reaches a yield value σ_y (Figure 2.2-b). Referring to the hypothesis that the plastic zone is smaller than the whole crack ($r_p \ll a$), it follows that

$$r_p = \frac{\pi}{8}\frac{K^2}{\sigma_y}, \qquad w = \begin{cases} \frac{K^2}{\sigma_y E} & \text{plane stress} \\ \frac{K^2}{2\sigma_y E} & \text{plane strain} \end{cases}, \tag{2.3}$$

where w is the opening of the crack. In Barenblatt's model, stress becomes suddenly zero when $w = w_1$, since for $w < w_1$ crack is not completely open so some remaining stresses transmitted have to be taken into account. Differently, in `HILLERBORG`'s model (1976) [51] stress decreases with increasing crack width (Figure 2.2-c). Differences between these two models are highlighted in Figure 2.2-d.

The presence of a discontinuity in the form of a displacement jump requires an additional constitutive description, in addition to the stress-strain law that describes the bulk material, which remains continuous. The so-called *traction-separation law* represents the constitutive equations of the crack and links the

surface forces to the displacement jump [[**u**]], known as the separation vector. This law is formulated by considering two different directions: the normal one (Mode-I), in which the crack opening is related to the normal traction and the tangential one (Mode-II), in which the relative sliding of the crack faces is related to the shear traction. As reported in literature [59, 124, 126], CZM depends on the maximum strength, on the fracture energy, which corresponds to the area under the traction-separation law, and on the shape of the traction-separation curve itself.

Models with localization bands with `weak discontinuities` can be regarded as an alternative to strong discontinuity models. Instead of considering a stress-free crack, in which tractions transmitted go to zero after crack nucleation, the crack initiation process is considered as the effect of a gradual loss of cohesion, more realistically. Weak discontinuity models represent the loss of continuity of the strain state and, also in this case, a specific constitutive model, expressed in terms of stress and strain within the band, is necessary. The opening of the crack can be viewed as the limit condition reached by the weak discontinuity models.

Lastly, `models with a continuous strain field` are implemented by applying *enriched or generalized continuum formulations*. Certain theories, indeed, depend on the particular scale of magnitude: below a certain limit, the idealization of considering material as a continuum cannot be done and it would be necessary to move to a discrete model. Alternatively, it is possible to introduce a *strongly or weakly non-local formulation*, that overcomes the hypothesis that the material can be analyzed as a set of infinitesimal volumes, described independently of each other. In particular, an integral-type nonlocal material model is a model in which the constitutive law at a point of a continuum depends on weighted averages of a state variable over a certain neighbourhood of that point [7, 56]. A gradient-type nonlocal model, instead, enriches the local constitutive laws with the first or higher gradients of some state variables or thermodynamic forces. Finally a *gradient model* refers to higher-order gradients in the constitutive variables, which are considered as a measure of the heterogeneity of the strain field.

2.2 Strain localization from a dynamic point of view

We have already mentioned that, based on the theoretical formulation regarding the stability of elastic materials as pursued by `Hadamard` (1903) and later extended by `Hill` (1958) and `Thomas` (1961) for inelastic materials, the localization process is analyzed as a constitutive instability that can be predicted by monitoring the pre-fail response of the material. This process corresponds, in fact, to a material instability which can be predicted by individuating the critical conditions for which the constitutive equations (in the pre-localized phase) may allow a bifurcation point.

We are looking for the mathematical conditions for which the loss of uniqueness of the solutions of a given boundary problem is recorded, which corresponds to a material instability in the `Liapunov` sense. In the following Section, strain localization is analyzed as the appearance of a discontinuity in strain rates, which leads to a bifurcation of the velocity field [57, 117]. In this sense, the dynamic aspect of such a physical phenomenon will be emphasized: as already demonstrated with the `Hadamard's stability criterion`, in fact, a material is stable if all the waves propagate with a real velocity. Consequently, strain localization is dynamically seen as the occurrence of a wave with a null velocity in the direction normal to the localized band.

2.2.1 Continuous and Discontinuous bifurcation

Let us consider an orthonormal reference system $(0, \mathbf{x_1}, \mathbf{x_2}, \mathbf{x_3})$ and a solid body Ω constituted by a strain-softening material (Figure 2.3-a). Along the boundary of the structure two parts can be identified, Γ_u and Γ_t, where respectively the kinematic and loading conditions are applied. The aim is to obtain a condition in which strain increments can localize in one or more narrow bands separated from the body by weak discontinuity surfaces, with a continuous displacement field but with discontinuity in some strain rate components. The volume is divided by a localization band Ω_b, with a finite width w_b and a unit normal vector $\mathbf{n}$ into two sub-domains, Ω^+, that contains the normal vector and Ω^-, the other one. By considering the plane tangent to the discontinuity surface, the stress rate tensor $\dot{\boldsymbol{\sigma}}$ can be decomposed in its in-plane components ($\dot{\boldsymbol{\sigma}}_{tt}$, $\dot{\boldsymbol{\sigma}}_{ss}$, $\dot{\boldsymbol{\sigma}}_{ts}$) and out-of-plane components ($\dot{\boldsymbol{\sigma}}_{nn}$, $\dot{\boldsymbol{\sigma}}_{nt}$, $\dot{\boldsymbol{\sigma}}_{ns}$), as explained in Figure 2.3-b.

The first fundamental hypothesis is obtained from the mechanical equilibrium across the shear band boundary, which leads to the *traction continuity*

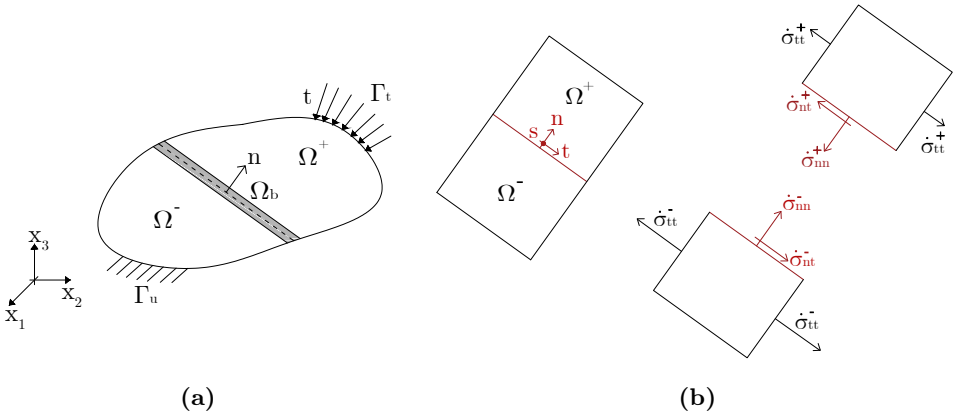

Figure 2.3: Geometry and boundary conditions of a volume crossed by a crack: (a) Strain localization in a strain softening material distinguishing a localization band that divides the volume into Ω^- and Ω^+; (b) Two sub-domains that the crack individuates, with a discontinuity in the in-plane stress rate discontinuity.

condition, which corresponds to the continuity between the out-of-plane stress rates. This condition can be written as

$$\mathbf{n} \cdot \dot{\boldsymbol{\sigma}}^+ = \mathbf{n} \cdot \dot{\boldsymbol{\sigma}}^-. \tag{2.4}$$

The second hypothesis is obtained from the *kinematic compatibility condition*, which expresses that the velocity field is to be continuous, which corresponds to the continuity between in-plane strain rates. So jumps could appear only in the in-plane stress rates or out-of-plane strain rates.

In order to derive this second set of equations, the compatibility conditions have to be written by considering the (n, t, s) reference system, in which the displacement rate derivative is continuous along (s, t) and presents a first-order jump tensor $\mathbf{g}$ along the normal direction n. As said in [103], since the velocity field remains continuous, derivatives of velocity in t and s, directions parallel to the band, remain uniform:

$$\frac{\partial \dot{\mathbf{u}}^+}{\partial t} = \frac{\partial \dot{\mathbf{u}}^-}{\partial t} \tag{2.5}$$

$$\frac{\partial \dot{\mathbf{u}}^+}{\partial s} = \frac{\partial \dot{\mathbf{u}}^-}{\partial s} \tag{2.6}$$

$$\frac{\partial \dot{\mathbf{u}}^+}{\partial n} = \frac{\partial \dot{\mathbf{u}}^-}{\partial n} + \boldsymbol{g}. \tag{2.7}$$

The spatial gradient of the displacement rate is a second-order tensor obtained from the gradient of each displacement rate component with respect to the global reference system. The following transformation rules have to be applied

$$\frac{\partial \dot{\mathbf{u}}^{+(-)}}{\partial \mathbf{x}} = \frac{\partial \dot{\mathbf{u}}^{+(-)}}{\partial t} \otimes \frac{\partial t}{\partial \mathbf{x}} + \frac{\partial \dot{\mathbf{u}}^{+(-)}}{\partial s} \otimes \frac{\partial s}{\partial \mathbf{x}} + \frac{\partial \dot{\mathbf{u}}^{+(-)}}{\partial n} \otimes \frac{\partial n}{\partial \mathbf{x}} \tag{2.8}$$

and considering equations (2.5)-(2.7) it can be summarized that

$$\frac{\partial \dot{\mathbf{u}}^{+}}{\partial \mathbf{x}} = \frac{\partial \dot{\mathbf{u}}^{-}}{\partial \mathbf{x}} + \mathbf{g} \otimes \mathbf{n}. \tag{2.9}$$

So $\mathbf{g}$ can be seen as a jump vector, with components g_1, g_2 and g_3. It can be written as $\mathbf{g} = \dot{g}\mathbf{m}$, where $\dot{g} = \|g\|$ is the magnitude of the jump vector and $\mathbf{m}$ is a first-order tensor called *polarization vector*. By substituting this relation in (2.9) and considering that the strain field is the symmetric part of the displacement gradient, it reads

$$\begin{aligned} \dot{\boldsymbol{\varepsilon}}^{+} &= \Big(\frac{\partial \dot{\mathbf{u}}^{+}}{\partial \mathbf{x}}\Big)_{sym} = \Big(\frac{\partial \dot{\mathbf{u}}^{-}}{\partial \mathbf{x}} + \dot{g}\mathbf{m} \otimes \mathbf{n}\Big)_{sym} = \dot{\boldsymbol{\varepsilon}}^{-} + \dot{g}(\mathbf{m} \otimes \mathbf{n})_{sym} \\ &= \dot{\boldsymbol{\varepsilon}}^{-} + \frac{1}{2}(\mathbf{m} \otimes \mathbf{n} + \mathbf{n} \otimes \mathbf{m})\dot{g}. \end{aligned} \tag{2.10}$$

The constitutive relation can be written in terms of rates components as $\dot{\boldsymbol{\sigma}} = \boldsymbol{E}_t : \dot{\boldsymbol{\varepsilon}}$, where $\boldsymbol{E}_t$ is the tangent stiffness tensor; by generalizing our case, it is considered that the two sub-domains have different behaviours after strain localization and, consequently, different strain-stress relationships:

$$\dot{\boldsymbol{\sigma}}^{+} = \mathbf{E}_t^{+} : \dot{\boldsymbol{\varepsilon}}^{+}, \qquad \dot{\boldsymbol{\sigma}}^{-} = \mathbf{E}_t^{-} : \dot{\boldsymbol{\varepsilon}}^{-}. \tag{2.11}$$

By substituting equation (2.10) in the traction continuity condition (2.4) and considering the previous constitutive equations (2.11) it follows

$$\mathbf{n} \cdot \Big[\mathbf{E}_t^{+} : \Big(\dot{\boldsymbol{\varepsilon}}^{-} + \dot{g}(\mathbf{m} \otimes \mathbf{n})_{sym}\Big)\Big] = \mathbf{n} \cdot \mathbf{E}_t^{-} : \dot{\boldsymbol{\varepsilon}}^{-} \tag{2.12}$$

$$\mathbf{n} \cdot \mathbf{E}_t^{+} : \dot{\boldsymbol{\varepsilon}}^{-} + \mathbf{n} \cdot \mathbf{E}_t^{+} : (\mathbf{m} \otimes \mathbf{n})_{sym}\dot{g} = \mathbf{n} \cdot \mathbf{E}_t^{-} : \dot{\boldsymbol{\varepsilon}}^{-}. \tag{2.13}$$

Considering the minor symmetry of the stiffness tensor, for which $\mathbf{n} \cdot \mathbf{E}_t^{+} : (\mathbf{m} \otimes \mathbf{n})_{sym} = (\mathbf{n} \cdot \mathbf{E}_t^{+} \cdot \mathbf{n}) \cdot \mathbf{m}$ the previous relation becomes

$$(\mathbf{n} \cdot \mathbf{E}_t^{+} \cdot \mathbf{n}) \cdot \mathbf{m}\dot{g} = \mathbf{n} \cdot (\mathbf{E}_t^{-} - \mathbf{E}_t^{+}) : \dot{\boldsymbol{\varepsilon}}^{-}. \tag{2.14}$$

This equation, related to an incipient discontinuity, could be simplified by considering the same stiffness tensor for both Ω^- and Ω^+, so by writing $\mathbf{E}_t^+ = \mathbf{E}_t^- = \mathbf{E}_t$. In this case, the right-hand term vanishes and, considering a non-zero jump vector, the relation becomes

$$(\mathbf{n} \cdot \mathbf{E}_t \cdot \mathbf{n}) \cdot \mathbf{m} = \mathbf{0}. \tag{2.15}$$

The localization or *acoustic tensor* is defined as follows

$$\boldsymbol{L} = \mathbf{n} \cdot \mathbf{E}_t \cdot \mathbf{n}. \tag{2.16}$$

In linear algebra, the *Rouchè-Capelli theorem* states that a system of linear equations $\boldsymbol{A}\mathbf{x} = \mathbf{b}$ with n variables has a non-trivial solution if and only if the rank of its coefficient matrix $\boldsymbol{A}$ is equal to the rank of its augmented matrix $\boldsymbol{A}|\boldsymbol{b}$. Considering that the linear system in (2.15) is homogeneous, it is clear that $rk(\boldsymbol{A}|\boldsymbol{b}) < n$. In order to obtain a unique solution, even $rk(\boldsymbol{A})$ has to be less than n or, in other terms, the coefficient matrix has to be singular. The *continuous bifurcation* condition in (2.15) leads to the following *localization condition*

$$det(\boldsymbol{L}) = 0. \tag{2.17}$$

Let us focus on the definition of the acoustic tensor, whose physical meaning will be investigated in the next sub-Section 2.2.2. It depends on the tangent stiffness tensor, which is linked to the current state of the material and on the unknown direction $\mathbf{n}$. The localization analysis implies the spectral analysis of the acoustic tensor in order to search for a direction $\mathbf{n}$ for which it becomes singular. If this vector exists, a band has to be inserted and a strain discontinuity considered.

Lastly, the polarization vector $\mathbf{m}$ is an indicator of the failure mode. If $\mathbf{m} \shortparallel \mathbf{n}$ a splitting failure is obtained, so a crack opens under the so-called Mode I; if $\mathbf{m} \perp \mathbf{n}$ a shear slip occurs, denoted as Mode II. If none of these conditions is verified, a crack opens under a mixed-mode.

2.2.2 The meaning of the acoustic tensor

As said before, the localization tensor is more properly known as the acoustic tensor. This name is linked to the original dynamic meaning of this tensor, which is related to the propagation of harmonic waves in an elastic medium [1, 46, 101].

The wave propagation is the result of a local excitation which creates a disturbance that could be transmitted in the considered volume. This perturbation couldn't be detected instantaneously at each point, since a deformable material is considered, that could try to oppose the propagation of the wave. The disturbance is transmitted as a chain process from one point to the next one. In an elastic, homogeneous and isotropic material, the velocity can be expressed as $v = \sqrt{\frac{E}{\rho}}$; so two parameters play a fundamental role in the resistance to the propagation of the wave. The first one is the *material stiffness*: only considering an infinitely rigid material the perturbation would have been recorded in all points in the same way since its propagation speed would have been infinite ($E \to \infty \Rightarrow c \to \infty$). The other one is the *material inertia* or its density ρ, since a poorly dense material record as well a high speed propagation ($\rho \to 0 \Rightarrow c \to \infty$).

The wave is the result of energy transmission between near molecules. The waves can be classified into *stationary waves* (standing waves), which do not transmit energy from one point to another one, and *progressive waves* (travelling waves), which transmit energy without transferring matter. Principal differences are that in stationary waves all points between two successive nodes are in the same *phase*, while in progressive waves two neighbouring points are not in the same phase. The other one is that in progressive waves each point achieves the same amplitude, while not for the stationary waves. In travelling waves the successive particle of the medium performs a motion similar to that of its predecessor along the direction of the propagation of the wave, but later. They travel from a point indefinitely, never returning to their origin, until the carried energy becomes zero. Classically, progressive waves are divided into *longitudinal waves* (P-waves, primary waves), where particles oscillate in parallel to the wave propagation's direction, and *transverse waves* (S-waves, secondary waves) where particles oscillate perpendicularly to the wave propagation's direction (Figure 2.4).

Let us consider a homogeneous body with a density ρ. A progressive wave can be represented by the following displacement field $\mathbf{u}(\mathbf{x}, t)$, with $\mathbf{x}$ defining the position of a material point and t the instant of time

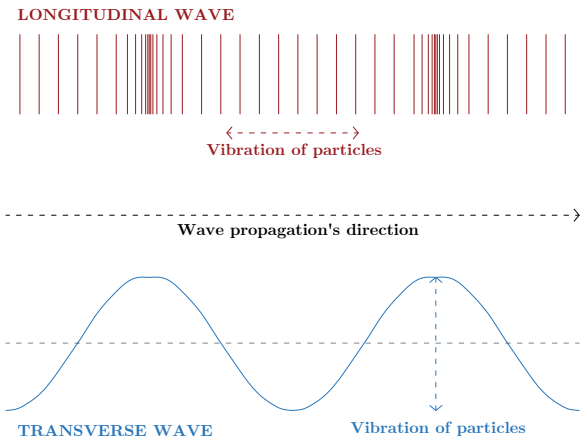

Figure 2.4: Representation of a longitudinal and a transverse wave.

$$\mathbf{u}(\mathbf{x}, t) = \mathbf{m}\phi(\mathbf{x} \cdot \mathbf{n} - ct) = \mathbf{m}\phi(s) \tag{2.18}$$

where

- $\phi(s)$ is the wave function of class $\mathbf{C}^2$ on $(-\infty, +\infty)$ with $\phi'' = \frac{\partial^2 \phi(s)}{\partial s^2} \neq 0$ since the displacement field must be twice differentiable and admit second derivative, i.e. acceleration, continuous as well;
- s is the wave phase;
- c is the wave speed;
- $\mathbf{m}$ is the polarization vector, or *direction of motion* of the material point and $\mathbf{n}$ is the *direction of propagation*.

The progressive wave is longitudinal if $\mathbf{m}$ and $\mathbf{n}$ are linearly dependent, transverse if they are perpendicular and elastic if it satisfies the Navier's equation of motion. It can be written as follows

$$\nabla \cdot (\boldsymbol{E} : \nabla \mathbf{u}) = \rho \ddot{\mathbf{u}}, \tag{2.19}$$

by considering the fourth-order elasticity tensor $\boldsymbol{E}$ and no volume forces. The gradient of the displacement field $\nabla \mathbf{u}$ can be written in a coordinate system (x_1, x_2, x_3) by referring to (2.18) as follows

$$\nabla \mathbf{u} = \begin{bmatrix} \frac{\partial u_1}{\partial x_1} & \frac{\partial u_1}{\partial x_2} & \frac{\partial u_1}{\partial x_3} \\ \frac{\partial u_2}{\partial x_1} & \frac{\partial u_2}{\partial x_2} & \frac{\partial u_2}{\partial x_3} \\ \frac{\partial u_3}{\partial x_1} & \frac{\partial u_3}{\partial x_2} & \frac{\partial u_3}{\partial x_3} \end{bmatrix} = \phi'(\mathbf{s}) \mathbf{m} \otimes \mathbf{n}. \tag{2.20}$$

In the hypothesis of small displacements, the strain tensor corresponds to the symmetric part of the gradient displacement tensor

$$\boldsymbol{\varepsilon} = (\nabla \mathbf{u})_{sym} = \phi'(\mathbf{s}) \frac{1}{2} (\mathbf{m} \otimes \mathbf{n} + \mathbf{n} \otimes \mathbf{m}). \tag{2.21}$$

The stress field from the Hooke constitutive law becomes

$$\boldsymbol{\sigma} = \mathbf{E} : \boldsymbol{\varepsilon} = \phi'(\mathbf{s}) \frac{1}{2} \mathbf{E} : (\mathbf{m} \otimes \mathbf{n} + \mathbf{n} \otimes \mathbf{m}). \tag{2.22}$$

Since the stiffness tensor $\mathbf{E}$ exhibits major symmetry ($E_{ijkl} = E_{klij}$) and minor symmetry ($E_{ijkl} = E_{jikl} = E_{ijlk}$), the previous relation becomes

$$\boldsymbol{\sigma} = \mathbf{E} : \boldsymbol{\varepsilon} = \phi'(\mathbf{s}) \frac{1}{2} \mathbf{E} : (2\mathbf{m} \otimes \mathbf{n}) = \phi'(\mathbf{s}) \boldsymbol{E} : \mathbf{m} \otimes \mathbf{n}. \tag{2.23}$$

In order to impose equation (2.19) and remembering definition (2.16) associated to the elastic constitutive operator, the divergence of the stress tensor is calculated

$$\nabla \cdot \boldsymbol{\sigma} = \phi''(\mathbf{s}) (\mathbf{n} \cdot \boldsymbol{E} \cdot \mathbf{n}) \cdot \mathbf{m} = \phi''(\mathbf{s}) \boldsymbol{L} \cdot \mathbf{m}. \tag{2.24}$$

The second-hand term in (2.19) is obtained by differentiating twice (2.18) with respect to time

$$\rho \ddot{\mathbf{u}} = \rho c^2 \phi''(\mathbf{s}) \mathbf{m}. \tag{2.25}$$

By imposing equivalence between (2.24) and (2.25), the *Fresnel-Hadamard propagation condition for progressive waves* is derived

$$\boldsymbol{L} \cdot \mathbf{m} = \rho c^2 \mathbf{m} \rightarrow (\boldsymbol{L} - \rho c^2 \boldsymbol{I}) \cdot \mathbf{m} = \mathbf{0}. \tag{2.26}$$

This condition corresponds to an eigenvalues and eigenvectors problem for the acoustic tensor $\boldsymbol{L}$: its eigenvalues $a_i = \rho c_i^2$ give the possible wave propagation speeds and the associated eigenvectors $\mathbf{m}_i$ identify the polarization directions.

2.2.3 Flutter instability analysis

As already mentioned in Section 1.2, material stability can be investigated by analyzing the non-negativity of the eigenvalues of both the constitutive operator $[det(\boldsymbol{E}_t) = 0]$ and the acoustic tensor $[det(\boldsymbol{L}) = 0]$. Generally, the strong ellipticity condition is linked to the definition and resolution of an eigenvalues and eigenvectors problem, so it is useful to summarize the main concepts.

Let us consider a $(n \times n)$ matrix $\mathbf{A} \in \Re^{n \times n}$; a scalar value λ for which exists an $(n \times 1)$ vector $\mathbf{x} \neq \mathbf{0}$ such the following equation is valid

$$\boldsymbol{A} \cdot \mathbf{x} = \lambda \cdot \mathbf{x} \tag{2.27}$$

is called *eigenvalue* of $\mathbf{A}$ and $\mathbf{x}$ is the *eigenvector* corresponding to λ. The set of eigenvalues of $\mathbf{A}$ constitutes the *spectrum* of $\mathbf{A}$ and the maximum module of the eigenvalues is said *spectral radius of* $\mathbf{A}$. The eigenvalue problem can be rewritten as:

$$(\boldsymbol{A} - \lambda \boldsymbol{I}) \cdot \mathbf{x} = 0. \tag{2.28}$$

As also said in 2.2.1, this equation admits non-trivial solutions if and only if

$$det(\boldsymbol{A} - \lambda \boldsymbol{I}) = 0. \tag{2.29}$$

By developing the determinant of the following matrix:

$$\boldsymbol{A} - \lambda \boldsymbol{I} = \begin{bmatrix} a_{11} - \lambda & a_{12} & \dots & a_{1n} \\ a_{21} & a_{22} - \lambda & \dots & a_{2n} \\ \vdots & \vdots & \ddots & \vdots \\ a_{n1} & a_{n2} & \dots & a_{nn} \end{bmatrix} \tag{2.30}$$

a n-th order *characteristic polynomial* $p(\lambda)$ is obtained and $p(\lambda) = 0$ is called the *characteristic equation of* $\mathbf{A}$, whose n roots are the eigenvalues of $\mathbf{A}$. The coefficients of λ^n and λ^{n-1} are respectively $(-1)^n$ and $(-1)^n(a_{11} + a_{22} + \dots + a_{nn})$. The last coefficient is obtained considering $p(0) = det(\mathbf{A})$. So it can be written as follows:

$$p(\lambda) = det(\boldsymbol{A} - \lambda \boldsymbol{I}) = (-1)^n \lambda^n + (-1)^{n-1} tr\boldsymbol{A} \lambda^{n-1} + \dots + det(\boldsymbol{A}) \tag{2.31}$$

where $tr\mathbf{A}$ is the trace of the matrix.

For the fundamental theorem of algebra, the characteristic equation has n roots in the complex field, taking into account their multiplicity. So an $(n \times n)$ array has n eigenvalues in the complex field. Eigenvectors are therefore the non-zero solutions of the linear homogeneous system in (2.28).

By comparing (2.15) with (2.28) the strain localization can be regarded as an eigenvalues and eigenvectors problem with $\lambda = 0$.

Because of the assumption of major symmetry on the stiffness tensor $\mathbf{E}$, the acoustic tensor is symmetric with real eigenvalues; initially $\boldsymbol{L}$ is positive definite. During a loading process, the evolution of state variables results in modifications to the stiffness tensor and the acoustic tensor, with the result that the lowest eigenvalue of $\boldsymbol{L}$ decreases. When this eigenvalue obtains a value of zero, material stability is lost or, alternatively, one can say that ellipticity of the spatial differential operator is lost: that condition corresponds to a stationary wave.

When the acoustic tensor is non-symmetric there is, in principle, the possibility of a particular type of instability. This is the so-called *flutter instability* [13, 16] and corresponds to the occurrence of two complex conjugate eigenvalues of the acoustic tensor. If one of the eigenvalues a_i of the localization tensor becomes negative, the wave speed formally evaluated as $c_i = \sqrt{\frac{a_i}{\rho}}$ becomes imaginary. So the onset of flutter can be defined by finding the numerical conditions which involve a complex form for the eigenvalues of the acoustic tensor.

2.2.3.1 Application on linear isotropic elasticity models

Flutter and strain localization are particular instabilities that don't appear frequently but only after the satisfaction of several conditions. By considering the expression of the acoustic tensor in (2.16), it is evident that it depends on the tangent stiffness operator, so on the particular constitutive nonlinear law adopted. However, it is useful to derive the expression of the acoustic tensor in the case of linear isotropic elasticity.

The generalized Hooke's law links the second-order strain and stress tensors through the fourth-order stiffness tensor $\mathbf{E}$. Since it exhibits both major symmetry and minor symmetry, it depends on 21 independent parameters; the constitutive law is defined as

$$\boldsymbol{\sigma} = \mathbf{E} : \boldsymbol{\varepsilon}. \tag{2.32}$$

By considering the hypothesis of isotropy, a general isotropic tensor $\mathbf{T}$ has

components that don't change by coordinate transformation and can be written as the result of each possible combination of the second-order unit tensor [118]

$$\mathbf{T} = \alpha\boldsymbol{\delta} \otimes \boldsymbol{\delta} + \beta\mathbf{I}^s + \gamma\mathbf{I}^a \tag{2.33}$$

being α, β, γ constant values and $\boldsymbol{\delta}$, $\mathbf{I}^s$ and $\mathbf{I}^a$ the second-order unit tensor, the symmetrized and anti-symmetrized fourth-order unit tensors, respectively. Since the stiffness operator exhibits major symmetry, it can be concluded that $\gamma = 0$ and that the linear elastic and isotropic stiffness tensor depends on only two elastic parameters, called *Lamè constants* λ and μ, such that

$$\mathbf{E}^e = \lambda\boldsymbol{\delta} \otimes \boldsymbol{\delta} + 2\mu\mathbf{I}^s. \tag{2.34}$$

Lamè coefficients are related to other pairs of material parameters associated with linear elastic isotropic material, known as Young's modulus E and Poisson's ratio ν, or bulk modulus K and shear modulus G:

$$\lambda = \frac{E\nu}{(1+\nu)(1-2\nu)} = K - \frac{2}{3}G \tag{2.35}$$

$$\mu = \frac{E}{2(1+\nu)} = G. \tag{2.36}$$

By considering equation (2.16) and (2.34), the elastic isotropic acoustic tensor can be derived as follows

$$\begin{aligned} \boldsymbol{L}^e &= \mathbf{n} \cdot (\lambda\boldsymbol{\delta} \otimes \boldsymbol{\delta} + 2\mu\mathbf{I}^s) \cdot \mathbf{n} \\ &= (\lambda + \mu)\mathbf{n} \otimes \mathbf{n} + \mu\boldsymbol{\delta}. \end{aligned} \tag{2.37}$$

Considering the propagation condition in (2.26) it is obtained that

$$(\lambda + \mu)(\mathbf{n} \otimes \mathbf{n}) \cdot \mathbf{m} + \mu\boldsymbol{\delta} \cdot \mathbf{m} - \rho c^2\mathbf{m} = \mathbf{0}. \tag{2.38}$$

Since $(\mathbf{n} \otimes \mathbf{n}) \cdot \mathbf{m} = (\mathbf{n} \cdot \mathbf{m})\mathbf{n}$ the previous relation becomes

$$(\mu - \rho c^2)\mathbf{m} + (\lambda + \mu)(\mathbf{n} \cdot \mathbf{m})\mathbf{n} = 0. \tag{2.39}$$

Since $\mathbf{n}$ and $\mathbf{m}$ are unit vectors, equation (2.39) can be satisfied only by considering $\mathbf{m} \shortparallel \mathbf{n}$, that corresponds to a P-wave, or $\mathbf{m} \perp \mathbf{n}$, that corresponds to a S-wave. In the first case equation (2.39) becomes

$$(\mu - \rho c_P^2)\mathbf{n} + (\lambda + \mu)\mathbf{n} = 0 \tag{2.40}$$

for which one eigenvalue $\rho c_P^2 = \lambda + 2\mu$ is obtained. In the second case equation (2.39) can be rewritten as

$$(\mu - \rho c_S^2)\mathbf{m} = 0 \tag{2.41}$$

for which a double eigenvalue $\rho c_S^2 = \mu$ is obtained. So it can be concluded that, as said before, for the linear elastic isotropic case the eigenvalues of the acoustic tensor are real and independent of the propagation direction $\mathbf{n}$.

For stiffness tensors satisfying major symmetry, the localization tensor is also symmetric and its eigenvalues are real, so flutter instability can only occur by one eigenvalue passing from positive to negative, which results into the wave speed passing from positive real to purely imaginary. Finally, if the elastic stiffness is replaced by the tangent stiffness of inelastic material and, consequently, the localization tensor is possibly not symmetric, a pair of complex conjugate eigenvalues could occur.

For that reason, it will be useful to analyze (as we will do later in the Section 4.4) this type of instability with the introduction of an isotropic damage model, at which the constitutive operator may lose its symmetry resulting in the possibility of the appearance of the flutter.

Chapter 3

Computational strategies to model strain localization

It was quickly pointed out in Section 1.1 how the phenomenon of strain localization appears with different characteristics depending on the type of material involved. Since the governing equations of the localization problem are difficult to solve by an analytical approach, numerical and computational methods were developed over the past 50 years. The goal is simulating the mechanical behaviour of the materials through mathematical/numerical models that most closely approximate their peculiarities. Not all materials, however, can be described by means of the same approaches. Moreover, the aforementioned mathematical models often rely on abstractions or simplifications to try to simulate reality without excessive computational effort. Many models, for example, are based on treating materials as if they were continuous, thus bypassing their actual microscopic nature. This simplification can only be made, however, if the scale of internal discontinuities is much smaller than the reference scale of the problem. If this condition is not met, such as in the case of masonry or rock masses, new models must be introduced that adequately simulate such internal heterogeneities or discontinuities.

In this Chapter, after an initial introduction on continuum and discrete models, the focus will be on the newly developed hybrid approaches which, starting from a continuum, introduce discontinuities by means of appropriate mechanical devices that simulate the cohesive forces. The basics of X-FEM, G-FEM, extended VEM and the A-FEM will be here recalled. Particular attention will be paid to the A-FEM, by which part of the algorithm implemented in this thesis is inspired, as analyzed later in Chapters 5 and 6.

3.1 Continuum models

The continuum models are based on the fundamental idea that the physical domain is considered as a single continuous body, whose changes at the micro-structural level are encountered by referring to continuum formulations based on theories of plasticity or damage mechanics. As already pointed out, such abstraction can be carried out without the consequent ill-posedness of the mathematical problem only when the internal non-homogeneity present in the materials is negligible with respect to the scale of the model. In this case, in fact, plastic deformations are encountered by referring to enriched constitutive models, based on internal variables which describe the micro-structural behaviour.

Quasi-brittle or heterogeneous materials, such as masonry or rock, require a realistic description of the strain-softening behaviour, which is the macroscopic result of distributed micro-cracking or void growth. However, the description of softening at a continuum level in the framework of classical plasticity or continuum damage theory leads to unsatisfactory results because the phenomenon of strain localization cannot be captured objectively. In these cases, the inelastic effects are distributed and smeared all over the material; therefore, numerical analysis have shown a strong dependence on mesh-size or mesh-bias, since strain localization occurs in an infinitely narrow band, which is physically meaningless since it does not allow for any dissipation in the process zone [70, 94].

The physical range of validity of continuum methods can be extended by adopting a generalized continuum approach in which the mathematical formulation is enhanced with additional terms. This latter technique, known as *regularization technique*, includes two main categories, namely the *nonlocal approach*, firstly formulated by BAŽANT and PIJAUDIER-CABOT in 1988 [8] or the *gradient approach*, formulated by MÜHLHAUS and ALFANTIS in 1991 [86].

An ideal continuum is seen as an assemblage of infinitesimal volumes of material, individually described by their own constitutive law. On the other hand, nonlocal models of the integral-type are based on the assumption that the stress field recorded in a point of a continuum body is dependant on the mechanical behaviour of the neighbouring points. As a consequence, the constitutive law in a specified point is calculated as weighted averages of the state variables in the area surrounding the material point. Similarly, a gradient-type nonlocal model includes the influence of the neighbouring material by enriching the local constitutive law with first or higher gradients of some state variables. Nonlocal formulations for quasi-brittle materials are strictly related to the definition of a *characteristic length*, presented as a material intrinsic property associated to

the maximum opening of a FPZ at the tip of a macroscopic crack. Finally, the necessity to introduce a nonlocal formulation is also linked to the so-called *size-effect* for which the structural strength, defined as the value of a certain nominal stress at the ultimate load, shows a dependence on the structural element size. The introduction of a nonlocal dissipation prevents the material to localize into a vanishing volume.

As mentioned above, the mathematical difficulties associated to the continuum approach can also be solved by adopting higher-order deformation gradients in the constitutive relations, for which additional (non-standard) boundary conditions are needed for the solution of equilibrium states.

3.2 Discrete models

In some cases, however, the representation of materials as continuous systems cannot be adopted, generally when the material has a length scale that is comparable with the structural scale. Materials such as rock or masonry belong to this class.

In the early '90s new modelling techniques were proposed with the aim to model the material as a set of separate blocks and discrete particles, commonly referred to as the *Discrete Element Method* (DEM), firstly formulated by `CUNDALL` and `HARD` in 1992 [28]. This method essentially divides the reference domain into solid material blocks and contact devices between the individual discrete elements that constitute the system. The overall response is based on the constitutive relationships associated with each of these components.

As regards the formulation of contacts or interfaces laws, two different strategies are identified: the *soft contact strategy*, which is based on the use of springs of finite stiffness to represent the joint, thus enabling the interpenetration between different bodies of the system. On the other hand, the *hard contact strategy*, which is based on the assumption that no interpenetration of the bodies occurs, although shear movement and opening can occur.

The representation of the solid material is also linked to two main groups: the material can be assumed as *rigid* or *deformable*. In the first case, the material deformability can be neglected and the inelastic phenomena are concentrated in the joints. In the latter, the deformability has a role that is comparable to the joints one.

Based on the adopted solving algorithm, DEM implementations can be grouped into implicit or explicit methods, in which the time interval of each step is or is not changed to reach convergence, respectively. In this regard,

we can mention the *Distinct Element Method*, based on solving the equations of motion by using an explicit-type scheme, leaving decoupled the differential equations; rigid or deformable discrete bodies with soft contacts are considered. An alternative method is the *Discontinuous Deformation Analysis* (DDA) method, formulated by `SHI` and `GOODMAN` in 1985 [108]. The DDA uses a system of algebraic equations obtained by minimizing the potential energy and solving that system using an explicit integration. Shi's original code uses a penalty-constraint approach to solve the contact, and is therefore based on the inclusion of springs with a very high stiffness (penalty springs) to prevent interpenetration. The solution is achieved through an iterative process.

DDA and DEM were initially designed for the analysis of the behaviour of fractured rock masses, so for application in the geotechnical field. In particular, DDA is basically an analysis method for discontinuous medium that allows the simulation of slips along the discontinuities between blocks, the opening of fractures, large rotations and the complete detachment between elements, which would be difficult to achieve using, for example, the classic FEM.

3.3 Continuous/Discontinuous models

In the framework of classical numerical methods, such as FEM, in the last decades the *Continuous/Discontinuoous approach* has been proposed in order to describe the gradual transition from the continuous material to the fractured one. Fractures can be analyzed as material discontinuities which can appear during the loading process.

The possibility to include strong or weak discontinuities in a continuum volume, as already mentioned in sub-Section 2.1.2, can be operated by principally referring to CZMs or ZTI models. Cohesive forces are introduced to model the dissipation process which develops in correspondence of the crack. Different constitutive laws may be associated with such mechanical devices simulating the evolution of fractures: the shape of these laws determines the actual link between the exchanged tractions $\mathbf{t}$ and the displacements jump $[[\mathbf{u}]]$ that such a discontinuity entails. Generally, two components are identified: the normal traction, linked to the crack opening, and the shear traction, linked to the relative sliding between the two surfaces. These types of models enhance the kinematic description of a continuum by introducing a displacement discontinuity. The cohesive constitutive relation can be presented with different shapes, classically divided into three groups: multi-linear, polynomial or exponential (see Figure 3.1). Despite differences regarding the reference functions, these

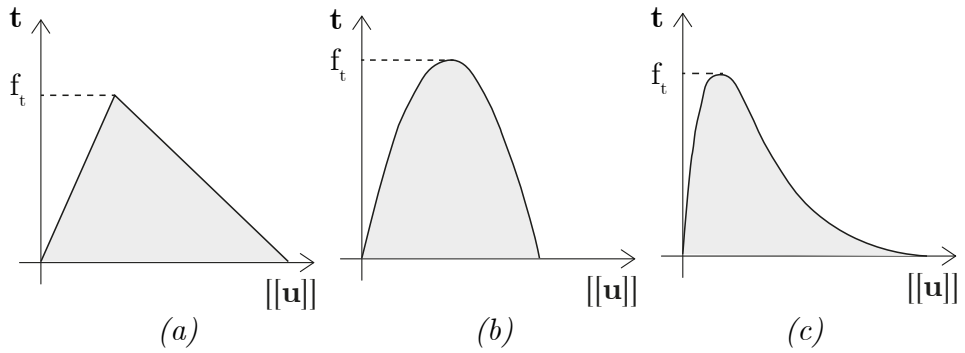

Figure 3.1: Different Traction-separation laws: (a) Multi-linear; (b) Polynomial; (c) Exponential.

curves are all constructed in a similar manner: tractions increase, reach a limit value and then tend to zero as separation between the weak discontinuity surfaces increases. Such constitutive law is in agreement with the real evolution of the rupture process, which is a consequence of the mutual interaction and coalescence between micro-fractures.

The previous relationship is controlled by two key material parameters: the *tensile-strength* f_t and the *fracture energy* G_f dissipated in developing a unit area of a crack, which is evaluated as the area subtended by the $\boldsymbol{t} - [[\boldsymbol{u}]]$ curve. First numerical methods were developed to include these discontinuities in the framework of FEM as inter-element bands. Discontinuities on the finite element edges were included by an adaptive remeshing, that was computationally expensive and difficult to implement. The strong mesh-dependency of finite element models with inter-element bands was overcome by enhancing the basic formulation to include intra-element displacement or strain jumps. In this regard, following sub-Sections will present an overview on some computational strategies to model strain localization: X-FEM, G-FEM, A-FEM and extended VEM.

3.3.1 Extended-Finite Element Method

General cohesive zone models require the potential crack path to be known *a priori*, which represents a limitation for the simulation of evolving arbitrary cracks. The Extended-Finite Element Method (X-FEM), firstly formulated by `BELYTSCHKO` et al. in 1999 [82, 83], overcomes the need for remeshing to capture the discontinuity evolution. The technique is based on a local enrichment

procedure of the cracked elements related to the Partition of Unity Method (PUM), formulated by BABUŠKA et al. in 1996 [80].

The PUM has some particular features:

- the a priori knowledge about the local behaviour of finite elements;
- it is a "meshless" method, that could be referred to as any general finite element shape.

Generally, a *partition of unity* on a space X is a collection G_i of continuous real functions on X such that

$$\sum_i G_i(x) = 1 \quad \forall x \in X. \tag{3.1}$$

The key idea is the local enrichment of cracked elements through the so-called *enrichment functions*, which are obtained from the analytical solution of the problem with some simplifying considerations.

In order to model the presence of the discontinuity, the displacement field $\mathbf{u}(\mathbf{x})$ is enriched by two additional terms:

$$\mathbf{u}(\mathbf{x}) = \underbrace{\sum_{i\in I} N_i(\mathbf{x})\mathbf{d}_i}_{\text{regular interpolation}} + \underbrace{\sum_{j\in J} N_j(\mathbf{x})H(\mathbf{x})\mathbf{b}_j + \sum_{k\in K} N_k(\mathbf{x})\left(\sum_{l=1}^{4} \mathbf{c}_k^l F_l(\mathbf{x})\right)}_{\text{enrichment}} \tag{3.2}$$

where $N(\mathbf{x})$ are the standard finite element shape functions. The first term is associated with the set I of regular nodes of the entire mesh, so $\mathbf{d}_i$ are the regular nodal displacements and $N_i(\mathbf{x})$ the related shape functions. The gray filled elements depicted in Figure 3.2 represent the set I, and the associated regular nodes are the gray filled circles as well.

The first additional term involves the *Jump function*, defined as follows:

$$H(\mathbf{x}) = \begin{cases} -1 & \text{if} \quad x > 0 \\ 1 & \text{if} \quad x < 0 \end{cases} \tag{3.3}$$

where $\mathbf{x}$ is the distance from the crack, whose sign is determined by the position of a node on one side or the other one respect to the crack surface. This enrichment regards the set J, which includes all nodes whose support is bisected by the crack. These elements are the green ones in Figure 3.2 and the associated

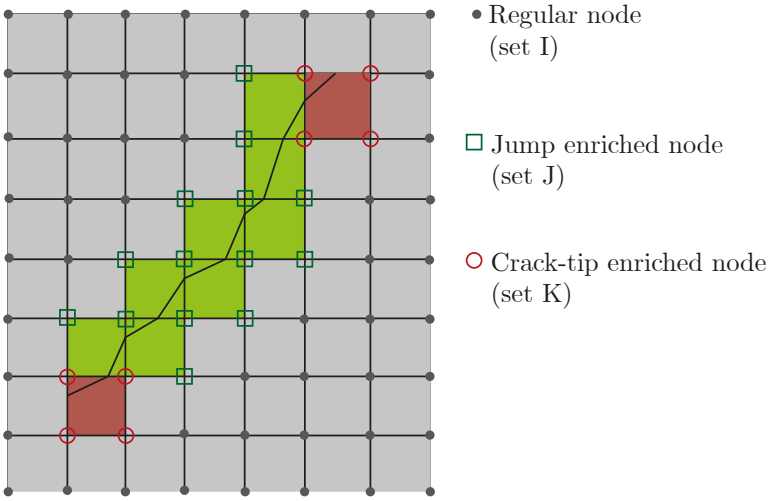

Figure 3.2: The X-FEM modeling of a cracked body with the Jump and the crack tip enrichment functions on a quadrilateral mesh.

Jump enriched nodes are the square green ones, whose displacement vectors are indicated as $\mathbf{b}_j$.

The second additional term regards the set K of nodes whose support contains the cohesive crack tips, depicted as red elements and associated circle red nodes in Figure 3.2. The nodal displacement vectors of the crack-tip enriched nodes are denotes as $\mathbf{c}_k$. This term involves the *branch function* $F_l(\mathbf{x})$, which models the displacement field around the tip of the discontinuity, defined as follows

$$\{F_l(r,\theta)\} = \left\{\sqrt{r}\sin\frac{\theta}{2}, \sqrt{r}\cos\frac{\theta}{2}, \sqrt{r}\sin\frac{\theta}{2}\sin\theta, \sqrt{r}\cos\frac{\theta}{2}\sin\theta\right\} \tag{3.4}$$

where (r,θ) are the local polar coordinate system with the origin in the crack tip and $\theta = 0$ tangent to the crack in the tip itself.

From equation (3.2), the displacement field can be seen as the sum of a regular part, that is related to the continuous part of the displacement, and a local enrichment contribution. It maintains the local property since the global enrichment functions $H(\mathbf{x})$ are multiplied by the nodal shape functions $N_j(\mathbf{x})$: the local term $N_j(\mathbf{x})H(\mathbf{x})$ ensures that the stiffness matrix will be sparse.

Unlike other models, in which a crack could be only an inter-elements one, which causes a continuous re-meshing to follow its evolution, in the X-FEM the

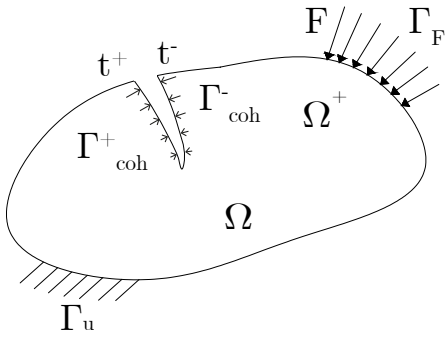

Figure 3.3: Boundary conditions on a volume Ω crossed by a cohesive crack.

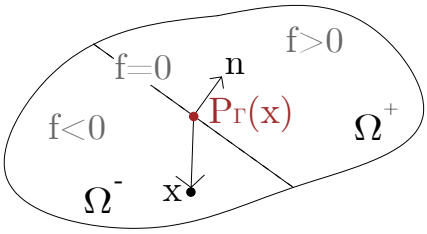

Figure 3.4: Level set function definition.

elements can be arbitrarily crossed by the fracture. Let us refer to a domain Ω as presented in Figure 3.3, which contains a FPZ denoted as Γ_{coh}. Boundary conditions are imposed on Γ_u and Γ_F as imposed displacements $\bar{\mathbf{u}}$ and prescribed tractions $\mathbf{F}$, respectively. Defined a cohesive constitutive law, which links the tractions on the two sides $\mathbf{t}$ with the crack opening $[[\mathbf{u}]] = \mathbf{u}^+ - \mathbf{u}^-$, the weak form of the equilibrium equations reads as

$$\int_{\Omega \setminus \Gamma_{coh}} \boldsymbol{\sigma} : \boldsymbol{\varepsilon} \, \mathrm{d}\Omega + \int_{\Gamma_{coh}} \mathbf{t} \cdot [[\mathbf{u}]] \, \mathrm{d}\Gamma_{coh} = \int_{\Gamma_F} \mathbf{F} \cdot \mathbf{u} \, \mathrm{d}\Gamma_F. \tag{3.5}$$

The X-FEM is usually coupled with the *Level Set Method* (LSM) [114] in order to model evolving cracks. The level set technique applied in fracture mechanics consists in associating a crack Γ to a set of points at which a certain function f_Γ vanishes: the crack is also called the zero level set and corresponds to

$$\Gamma = \{\mathbf{x} | f_\Gamma(\mathbf{x}) = 0\} \tag{3.6}$$

being $\mathbf{x}$ the position vector of a material point with respect the discontinuity origin P_Γ. Crack growth is obtained by updating the level set function and by considering the normal vector to Γ defined as

$$\mathbf{n}(\mathbf{x}) = \frac{\nabla f_\Gamma(\mathbf{x})}{\|\nabla f_\Gamma(\mathbf{x})\|}. \tag{3.7}$$

$\mathbf{n}$ could permit to identify negative and positive sub-domains in which the element is divided by the crack. Let us consider Figure 3.4 and the associated following level set function:

$$f_\Gamma(x) = \|\mathbf{x}\| sign[\mathbf{x} \cdot \mathbf{n}(\mathbf{x})]. \tag{3.8}$$

The domain is positive if $f_\Gamma > 0$ or negative if $f_\Gamma < 0$.

The enrichment functions used by the X-FEM can be easily explained by considering a one dimensional example, in which the discontinuity point Γ_d divides the element into Ω^- where $0 < x < a$ and Ω^+ where $a < x < L$ (top-side of Figure 3.5). The enrichment functions are expressed as $H(x-a)$, being H the Heaviside step function. Since N_1 and N_4 are not interested by the discontinuity, only N_2 and N_3 will be enriched. So the new shape function set consists of N_1, N_4, $N_2^- = N_2(1-H)$, $N_2^+ = N_2 H$, $N_3^- = N_3(1-H)$, $N_3^+ = N_3 H$, associated with the corresponding DoFs d_1, d_4, d_2^-, d_2^+, d_3^- and d_3^+. The two domains are two overlapping meshes, where b_2 and b_3 correspond to the displacement differences between the left and the right sides (bottom side of Figure 3.5).

For 1-D case, equation (3.2) can be re-written as follows:

$$\begin{aligned} u(x) &= \sum_{i=1}^{4} N_i(x) d_i + \sum_{j=2}^{3} N_j(x) H(x-a) b_j = \\ &= \sum_{i=1}^{4} N_i(x) d_i + \sum_{j=2}^{3} N_j(x)[1 - H(x-a)] d_j^- + \sum_{j=2}^{3} N_j(x) H(x-a) d_j^+. \end{aligned} \tag{3.9}$$

3.3.2 Generalized-Finite Element Method

Almost simultaneously with the X-FEM, also the Generalized-Finite Element Method (G-FEM) was presented by `STROUBOULIS` in 2000 [115]. This method was used to extend the capabilities of FE codes to include discontinuities through a nodal enrichment technique. The most important feature is that the local enrichment of approximation is done through the so-called *handbook functions*, which are solutions to local boundary-value problems reflecting the local geometry of the problem domain.

We refer to a volume domain Ω, crossed by a discontinuity Γ_d, which identifies two sub-domains Ω^+ (where the normal $\mathbf{n}$ to the crack enters) and Ω^-, as in Figure 3.6. $\mathbf{F}$ are applied on Γ_F and $\bar{\mathbf{u}}$ on Γ_u. As done in the previous sub-Section, the displacement field $\mathbf{u}(\mathbf{x})$ is the sum of a regular displacement field $\hat{\mathbf{u}}(\mathbf{x})$ and an enhanced part $\tilde{\mathbf{u}}(\mathbf{x})$:

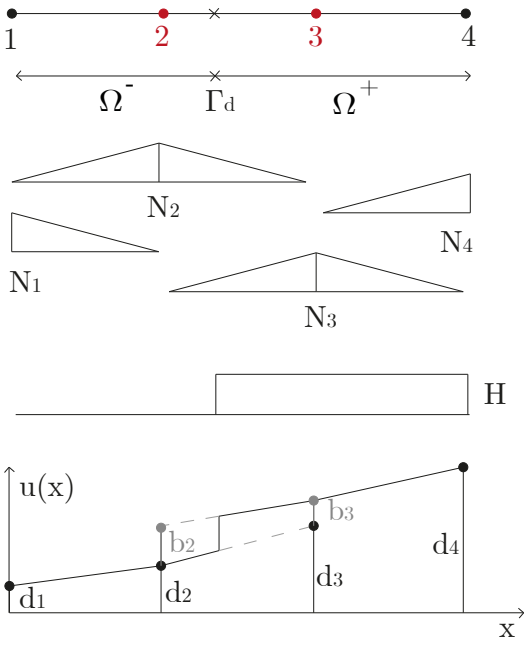

Figure 3.5: Discontinuous displacement approximation in 1-D example in X-FEM.

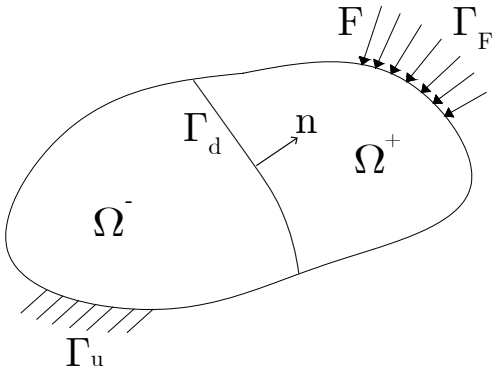

Figure 3.6: Boundary conditions on a volume Ω crossed by a discontinuity Γ_d.

$$\mathbf{u}(\mathbf{x}) = \hat{\mathbf{u}}(\mathbf{x}) + H_{\Gamma_d}\tilde{\mathbf{u}}(\mathbf{x}) \tag{3.10}$$

where H_{Γ_d} is the Heaviside function used to transmit the discontinuity, defined as follows

$$H_{\Gamma_d} = \begin{cases} 1 & \text{if} \quad x \in \Omega^+ \\ 0 & \text{otherwise} \end{cases} \tag{3.11}$$

Considering the small displacements hypothesis, the strain field can be written as

$$\boldsymbol{\varepsilon} = \nabla^s \mathbf{u}(\mathbf{x}) = \underbrace{\nabla^s \hat{\mathbf{u}} + H_{\Gamma_d}(\nabla^s \tilde{\mathbf{u}})}_{bounded} + \underbrace{\delta_{\Gamma_d}([[\mathbf{u}]] \otimes \mathbf{n})}_{unbounded} \tag{3.12}$$

where $(\cdot)^S$ is the symmetric part, $\otimes$ the tensor product and δ_{Γ_d} is the Dirac delta. The strain field is continuous except on Γ_d, where the unbounded term is taken into account. The displacements jump is evaluated as the enhanced displacement field on the discontinuity

$$[[\mathbf{u}]] = \tilde{\mathbf{u}}(\mathbf{x})|_{\Gamma_d}. \tag{3.13}$$

The weak form of equilibrium equations reads as

$$\int_{\Omega^{+/-}} (\nabla^s \delta\mathbf{u}) : \boldsymbol{\sigma} \mathrm{d}\Omega + \int_{\Gamma_d} \delta[[\mathbf{u}]] \cdot \mathbf{t} \mathrm{d}\Gamma = \int_{\Omega^{+/-}} \delta\mathbf{u} \cdot \mathbf{b} \mathrm{d}\Omega + \int_{\Gamma_F} \delta\mathbf{u} \cdot \mathbf{F} \mathrm{d}\Gamma \tag{3.14}$$

where $\delta\cdot$ is the admissible displacement variation, $\mathbf{t}$ the traction on the discontinuity and $\mathbf{b}$ the volume forces. The FE approximation reads as

$$\mathbf{u}^e = \boldsymbol{N}_e(\mathbf{x})(\hat{\mathbf{a}}^e + H_{\Gamma_d}\tilde{\mathbf{a}}^e) \qquad \text{on} \quad \Omega^{+/-} \tag{3.15}$$

$$[[\mathbf{u}]]^e = \boldsymbol{N}_e(\mathbf{x})\tilde{\mathbf{a}}^e \qquad \text{on} \quad \Gamma_d \tag{3.16}$$

where $\hat{\mathbf{a}}^e$ and $\tilde{\mathbf{a}}^e$ are the nodal Dofs associated with $\hat{\mathbf{u}}^e$ and $\tilde{\mathbf{u}}^e$, respectively and $\boldsymbol{N}_e$ contains the element shape functions.

Differently from other models where the jump displacement field is approximated by some one-dimensional shape functions defined along the crack, in the G-FEM it is obtained by using element shape functions themselves [35].

In this model, the DoFs associated with the parent element crossed by a discontinuity are doubled, and the enrichment is provided by a second layer of DoFs, that overlaps the given element. The nodal displacements $\mathbf{a}^e$ of the second layer could be seen as the sum of a regular part and an enhanced one:

$$\mathbf{a}^e = \hat{\mathbf{a}}^e + \tilde{\mathbf{a}}^e. \tag{3.17}$$

The discretized form of equations (3.14) reads as

$$\begin{bmatrix} \boldsymbol{K}_{\hat{a}\hat{a}} & \boldsymbol{K}_{\hat{a}\tilde{a}} \\ \\ \boldsymbol{K}_{\tilde{a}\hat{a}} & \boldsymbol{K}_{\tilde{a}\tilde{a}} + \boldsymbol{K}_d^e \end{bmatrix} \begin{bmatrix} \hat{\mathbf{a}}^e \\ \\ \tilde{\mathbf{a}}^e \end{bmatrix} = \begin{bmatrix} \hat{\mathbf{F}}^e \\ \\ \tilde{\mathbf{F}}^e \end{bmatrix} \tag{3.18}$$

where

$$\boldsymbol{K}_{\hat{a}\hat{a}} = \int_{\Omega^{+/-}} \boldsymbol{B}^T \boldsymbol{E} \boldsymbol{B} \mathrm{d}\Omega \qquad \boldsymbol{K}_{\hat{a}\tilde{a}} = \int_{\Omega^{+}} \boldsymbol{B}^T \boldsymbol{E} \boldsymbol{B} \mathrm{d}\Omega \tag{3.19}$$

$$\boldsymbol{K}_{\tilde{a}\hat{a}} = \boldsymbol{K}_{\tilde{a}\tilde{a}} = \boldsymbol{K}_{\hat{a}\tilde{a}}^T \qquad \boldsymbol{K}_d^e = \int_{\Gamma_d} \boldsymbol{N}_e^T \boldsymbol{E}_d \boldsymbol{N}_e \mathrm{d}\Gamma \tag{3.20}$$

$$\hat{\mathbf{F}}^e = \int_{\Omega} \boldsymbol{N}_e^T \mathbf{b} \mathrm{d}\Omega + \int_{\Gamma_F} \boldsymbol{N}_e^T \mathbf{F} \mathrm{d}\Gamma \tag{3.21}$$

$$\tilde{\mathbf{F}}^e = \int_{\Omega^{+}} \boldsymbol{N}_e^T \mathbf{b} \mathrm{d}\Omega + \int_{\Gamma_F^{+}} \boldsymbol{N}_e^T \mathbf{F} \mathrm{d}\Gamma. \tag{3.22}$$

In the previous equations system, $\boldsymbol{B}$ is the compatibility matrix, $\boldsymbol{E}$ is the constitutive matrix and $\boldsymbol{E}_d$ is the discontinuity constitutive matrix.

As done by Jirásek [59], let us consider the kinematic representation, from different points of view, of an element crossed by a vertical discontinuity subjected firstly to a relative displacement of the two domains and then to a compression of the right-hand part only. Figure 3.7-a represents the physical situation; Figure 3.7-b represents an element with a smeared discontinuity, for which normal and shear strains are necessarily transmitted between the two domains; Figure 3.7-c represents the same element crossed by an embedded discontinuity, where tractions are still transmitted so the left-hand domain has to be affected by the presence of the other one; finally, Figure 3.7-d simulates the X-FEM/G-FEM model, that could represent the two domains as two independent bodies. The enrichment is provided by a second layer of DoFs which overlaps the element (solid and dashed lines), with regular nodes (solid black circles) and enriched ones (empty red circles), which represents the natural extension of the displacement beyond the crack.

3.3.3 Augmented-Finite Element Method

Recently, researchers have proposed a FEM method to model the propagation of single and multiple fractures known as the *Augmented Finite Element Method* (A-FEM). This method lays its foundations in the works of `LING`, `YANG` and `COX` [69] then continued by `LIU` [71], `MOHAMMADIZADEH` and `SU` [84].

The A-FEM can take into account strong discontinuity (as a crack) or weak discontinuity (as a material interface) in a physical element.

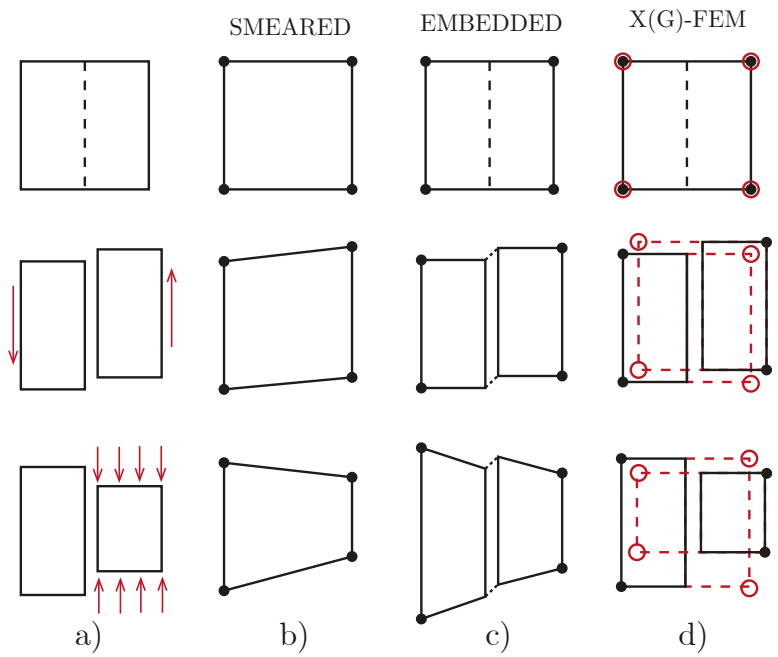

Figure 3.7: Different approaches to crack simulation: a) Physical body crossed by a crack; b) Element with smeared crack; c) Element with embedded discontinuity; d) X-FEM/G-FEM simulation with two overlapping elements.

The model takes into account multiple intra-element discontinuities with arbitrary paths and allows a numerical efficiency greater than other models. The main characteristic is that this method uses standard finite element shape functions, so it essentially maintains the advantage of element locality and the compatibility with existing standard FEM programs. Main advantages of this method can be summarized as follows:

- it allows intra-element discontinuities and not only inter-element ones;
- cracks are inserted during the analysis according to specific insertion criteria, without a priori imposition of the crack path;
- multiple cracks can be inserted by recursively augmenting elements;
- easy implementation of CZM to treat the discontinuity behaviour.

Additional nodes are inserted to describe the fracture but, through the

condensation process, the final equilibrium equations do not depend on the internal nodes.

This strategy is computationally efficient and leads to a significant improvement in numerical accuracy, efficiency and stability in problems related to the analysis of arbitrary cracks within materials.

The ability of the A-FEM to reproduce the formation of cohesive internal fractures in both homogeneous and heterogeneous solids is linked to the assumption that a cracked element is the assembly of two separated mathematical domains possessing standard finite element structure. The formulation allows the use of standard finite element shape functions for each domain.

As later analyzed in Section 5.2.1, the problem is solved by replacing the original element with at least 3 new elements: the two sub-domains and the localization band, through which they interact, with its defined constitutive behaviour.

By imposing the continuity of tractions along the fracture surfaces and starting from the equilibrium equations of each sub-domain, it is possible to calculate the displacements of the internal nodes as a function of the external ones: the condensed final equilibrium system does not depend on the internal Dofs, condition that releases the formulation from the prior knowledge of the fracture path.

3.3.4 Extended Virtual Element Method

The Virtual Element Method (VEM) is a generalization of the classic Finite Element Method (FEM), recently proposed by BEIRÃO DA VEIGA et al. in 2013 [3, 10, 19]. Its principal feature is related to its greater adaptability and flexibility since it is capable of modeling polygonal meshes, characterized by any number of edges without constraints. This permits VEM to be more efficient with respect to the classical FEM in mesh generation, also starting from irregular or distorted geometries. By coupling it with, for example, a classic ZTI element, it is possible to follow crack nucleation and evolution also by considering the decomposition of the computational domains into polygons with complex geometry.

The displacement field is obtained as an interpolation of values calculated on the element edges, without considering any approximation in the domain itself.

The first step to implement a virtual element Ω_e is establishing the number m of its straight edges defining the polygon. The displacement field $\mathbf{u}^h$ is fully

implicit in the interior of the element, being h the mesh refinement size. On the boundary $\partial\Omega_e$, instead, an explicit representation of the displacement field denoted with $\tilde{\mathbf{u}}^h$ is introduced, by evaluating them from the nodal values as follows

$$\tilde{\mathbf{u}}^h = \tilde{\boldsymbol{N}}_b \tilde{\mathbf{U}} \tag{3.23}$$

where $\tilde{\boldsymbol{N}}_b$ is the matrix of polynomial m-degree functions defined on the boundary $\partial\Omega_e$, $\tilde{\mathbf{U}}$ collects displacements of the DoFs associated with nodes lying on the edges of $\partial\Omega_e$. A different accuracy can be obtained by using different degrees k of the approximating functions evaluated on the boundary.

The equilibrium equation can be written as follows

$$\underbrace{\int_{\Omega_e} (\delta\mathbf{u}^h)^T \mathbf{b} \mathrm{d}\Omega + \int_{\partial\Omega_e} (\delta\mathbf{u}^h)^T \bar{\mathbf{t}} \mathrm{d}s}_{\delta L^e} = \underbrace{\int_{\Omega_e} [\delta\boldsymbol{\varepsilon}(\mathbf{u}^h)]^T \boldsymbol{E}\boldsymbol{\varepsilon}(\mathbf{u}^h)}_{\delta L^i} \tag{3.24}$$

where $\mathbf{b}$ are the volume forces, $\bar{\mathbf{t}}$ are the inter-element tractions, s is the coordinate on the edge and $\boldsymbol{E}$ is the element constitutive matrix.

An important consequence is that, since the displacement field $\mathbf{u}^h$ is not explicit within the element, the strain cannot be computed as the symmetric part of the gradient, so a projection operator Π is introduced to define the strain consistent field $\boldsymbol{\varepsilon}^c$ and, consequently, the stress one. It can be written as

$$\boldsymbol{\varepsilon}^c = \Pi(\mathbf{u}^h). \tag{3.25}$$

The fundamental hypothesis for this projection operator is that, since a linear approximation is assumed for displacement on the boundary ($k = 1$), the strain field in the element is constant. In addition, this condition has to be satisfied

$$(\boldsymbol{\varepsilon}^P)^T \int_{\Omega_e} \Pi(\mathbf{u}^h) = (\boldsymbol{\varepsilon}^P)^T \int_{\Omega_e} \boldsymbol{\varepsilon}(\mathbf{u}^h) \mathrm{d}\Omega \qquad \forall \boldsymbol{\varepsilon}^P \tag{3.26}$$

being $\boldsymbol{\varepsilon}^P$ a vector of constant components within the element. Π is defined as follows

$$\Pi(\mathbf{u}^h) = \boldsymbol{\Pi}^c \tilde{\mathbf{U}} \tag{3.27}$$

where $\boldsymbol{\Pi}^c$ is a matrix explicitly computable as follows

$$\mathbf{\Pi}^c = \frac{1}{A_e} \int_{\partial\Omega_e} \boldsymbol{N}_e^T \tilde{\boldsymbol{N}}_b \mathrm{d}s \tag{3.28}$$

by introducing (3.27) in the left-hand term of (3.26) and by integrating by parts the right-hand side. $\boldsymbol{N}_e$ contains the components of the normal to the edge and A_e is the area of the element.

Considering equations (3.25)-(3.27) it follows that

$$\boldsymbol{\varepsilon}^c = \mathbf{\Pi}^c \tilde{\mathbf{U}}. \tag{3.29}$$

There will therefore exist a displacement field $\mathbf{u}^c$ that is consistent with the strain field $\boldsymbol{\varepsilon}^c$, i.e. satisfying the following relationship:

$$\boldsymbol{\varepsilon}^c = \boldsymbol{B}\mathbf{u}^c \tag{3.30}$$

being $\boldsymbol{B}$ the compatibility operator. A linear-type expression for $\mathbf{u}^c$ can be defined as follows

$$\mathbf{u}^c = \boldsymbol{P}(\mathbf{x})\mathbf{d} \tag{3.31}$$

where $\mathbf{d} = \begin{bmatrix} u_1^0 & u_2^0 & \varepsilon_{11}^c & \varepsilon_{22}^c & \gamma_{12}^c & w_{12} \end{bmatrix}^T$ and $\boldsymbol{P}(\mathbf{x})$ is a polynomial matrix. u stands for the initial displacement, ε for the normal strain, γ for the shear strain and w for the rigid rotation.

Assembling the matrices $\boldsymbol{P}(\mathbf{x}^{(i)})$ into $\boldsymbol{D}$ and collecting the displacements at each node $\mathbf{u}^{c(i)}$ into a vector $\tilde{\mathbf{U}}^c = \begin{bmatrix} \mathbf{u}^{c(1)} & \dots & \mathbf{u}^{c(m)} \end{bmatrix}^T$, we can write

$$\tilde{\mathbf{U}}^c = \boldsymbol{D}\mathbf{d}. \tag{3.32}$$

The vector $\tilde{\mathbf{U}}^c$ can be evaluated by minimizing the difference between $\tilde{\mathbf{U}}$ and $\tilde{\mathbf{U}}^c$. However, $\tilde{\mathbf{U}}^c$ is not still equal to $\tilde{\mathbf{U}}$, which results in an energy discrepancy that therefore needs to be filled. Therefore, a stabilization part must be added to the consistent part of the energy associated with the projection operator, in order to recover the lost energy.

The internal work expression in the right-hand side of equation (3.24) by referring to the consistent strain component as expressed in (3.29) becomes

$$\delta L^i = \int_{\Omega_e} \delta\tilde{\mathbf{U}}^T \mathbf{\Pi}^{c^T} \boldsymbol{E} \mathbf{\Pi}^c \tilde{\mathbf{U}} \mathrm{d}\Omega + \delta\Phi^s \tag{3.33}$$

where $\delta\Phi^s$ represents the stabilizing term. It can be written as

$$\delta\Phi^s = \delta\tilde{\mathbf{U}}^T (\boldsymbol{I} - \mathbf{\Pi}^s)^T \bar{K} (\boldsymbol{I} - \mathbf{\Pi}^s) \tilde{\mathbf{U}} \tag{3.34}$$

where

$$\boldsymbol{\Pi}^s = \boldsymbol{D}(\boldsymbol{D}^T\boldsymbol{D})^{-1}\boldsymbol{D}^T. \tag{3.35}$$

The two consistent and stabilized stiffness matrices are derived

$$\boldsymbol{K}^c = \boldsymbol{\Pi}^{c^T}\boldsymbol{E}\boldsymbol{\Pi}^c A_e \tag{3.36}$$

$$\boldsymbol{K}^s = (\boldsymbol{I} - \boldsymbol{\Pi}^s)^T\bar{K}(\boldsymbol{I} - \boldsymbol{\Pi}^s) \qquad \text{where} \qquad \bar{K} = \frac{tr(\boldsymbol{K}^c)}{2}A_e. \tag{3.37}$$

Finally, as regards the left-hand side in (3.24), $\bar{\mathbf{t}}$ are neglected ant the other external term is evaluated as

$$\int_{\Omega_e}(\partial\mathbf{u}^h)^T\mathbf{b}\mathrm{d}\Omega = \partial(\bar{\mathbf{u}}^h)^T\bar{\mathbf{b}} \tag{3.38}$$

$$\text{where} \quad \bar{\mathbf{u}}^h = \frac{1}{m}\sum_{i=1}^{m}\tilde{\mathbf{u}}^{(i)} = \boldsymbol{M}\tilde{\mathbf{U}} \tag{3.39}$$

$$\bar{\mathbf{b}} = \frac{1}{A_e}\int_{\Omega_e}\mathbf{b}\mathrm{d}\Omega \tag{3.40}$$

being $\tilde{\mathbf{u}}^{(i)}$ the displacement vector of the $i-th$ node and $\boldsymbol{M}$ a $(2\times 2m)$ matrix defined as

$$\boldsymbol{M} = \frac{1}{m}\begin{bmatrix}1 & 0 & 1 & 0 & \dots\\ 0 & 1 & 0 & 1 & \dots\end{bmatrix} \qquad \text{from which} \qquad \boldsymbol{F} = \boldsymbol{M}^T\bar{\mathbf{b}}. \tag{3.41}$$

Given its easy formulation, VEM can also be used to include intra-element discontinuities by appropriately adding Dofs at the fracture tips itself. The extended VEM usually couples a standard VEM method with classical ZTI elements to simulate crack opening processes in domains with complex geometries.

Chapter 4

Strain localization in Isotropic Damage Models

In previous Chapters, it has been clarified that the phenomenon of strain localization depends on the type of material involved and on the choices made at the computational and constitutive level. The computational procedure proposed in this thesis in Chapters 5 and 6 refers to an Isotropic Damage Model (IDM), although any constitutive model that could describe a strain-softening behaviour could be implemented. For this reason, an overview on damage constitutive models is firstly presented, paying particular attention to the formulation proposed by JIRÁSEK in 2011 [58] and MAZARS in 1986 [79]. This model will be adopted and implemented to describe the mechanical behaviour of the material. Another point that will be investigated in this Chapter regards the different criteria to identify strain localization and its geometrical features, in the framework of IDM. Flutter instability will be also investigated.

4.1 Constitutive models for damage mechanics

Continuous Damage Mechanics (CDM) and Fracture Mechanics (FM) are theories that reproduce the progressive degradation processes developing due to mechanical, thermal or chemical agents.

Both fracture mechanics and damage mechanics aim to estimate the effect of damage processes, which consist in the formation, propagation, and coalescence of micro defects, on the macroscopic response of the material.

While FM analyzes the effects of cracks, considered as known discontinuities

in the material, thus removing the hypothesis of continuity of the medium, the CDM, starting from the hypothesis of continuity, studies the effects of damaging processes at a macroscopic continuum level, by defining a set of damage variables.

Although the degradation processes are the consequence of a single and general microscopic mechanism related to the breaking of atomic and molecular bonds, at the macroscopic level the damage can appear in different ways depending on the nature of the material, type of load and temperature.

The term *damage* was firstly introduced by KACHANOV in 1958 [64] to model creep rupture in ductile materials. Damage was considered as the result of internal micro-changes in material properties which induce a progressive material deterioration and stiffness degradation. Previous formulations in the framework of CDM were proposed by LEMAITRE and CHABOCHE in 1978 [68, 75]; similarly, MAZARS proposed a damage model specially designed for concrete in 1986 [79].

Generally, a damage mechanism for which the degradation is equally recorded in every direction is classically referred to an IDM, characterized by a single scalar parameter. Our analysis will be related to this kind of models. In addition, more complex theories represent the anisotropic character of damage through a vector, a second-order tensor or, generally, a fourth-order tensor damage variable. Such variables have to be used when damage evolves with no fixed direction and the complexity of the related theories is the greater the higher the order of the tensors chosen, corresponding to different damage mechanisms.

As also suggested by the name, the CDM refers to a damaged material modelled as a continuum medium. On the physical level, the internal mechanisms of damage can evolve differently and, therefore, different are the variables used to describe them from the mathematical point of view. It is clear that the first step in developing a damage theory involves the definition of the damage variable.

Our analysis will be related to an IDM with a variable intended as a measure of the irreversible defects in the material.

Let us consider a volume element, in which S represents the normal cross-section. As the applied load increases, cracks and voids start to develop in this section as the consequence of the loading process. The effective area $\bar{S}$ is defined as the unbroken resistant area; the damaged area S_d is defined as the total area of the defects, equal to the difference $S_d = S - \bar{S}$ (Figure 4.1). Let us define the *nominal stress* σ as the force per unit area S and the *effective stress* $\bar{\sigma}$ as the force per unit effective area.

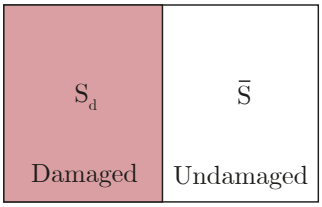

Figure 4.1: Representation of a damaged cross-section.

Since $\sigma S = \bar{\sigma}\bar{S}$ it is derived that

$$\sigma = \frac{\bar{S}}{S}\bar{\sigma} \tag{4.1}$$

where $\bar{S}/S$ represents the integrity parameter. The *damage parameter* D can be derived as follows

$$D = 1 - \frac{\bar{S}}{S} = \frac{S_d}{S}. \tag{4.2}$$

In Figure 4.2 three different loading conditions for the same volume element have been analyzed: step A refers to an elastic condition, step B to the arising of damage (small D value), step C corresponds to a very damaged volume (high D value). In the same Figure, from left to right, the evolution of the effective stress $\bar{\sigma}$, nominal stress σ and damage parameter D, for these three different conditions are reported, respectively. Step A corresponds to a condition for which $\sigma = \bar{\sigma}$, as the damage has not yet developed ($D = 0$). After damage activation, the nominal stress decreases as the damage increases and vanishes when $D = 1$.

As evident in Figure 4.2, the effective stress has always a linear trend, since it is governed by the Hooke's law

$$\bar{\sigma} = E\varepsilon. \tag{4.3}$$

By substituting equations (4.2)-(4.3) into (4.1) it follows that

$$\sigma = (1 - D)E\varepsilon. \tag{4.4}$$

In a multi-dimensional case, considering stresses and strains as tensors, it follows that

$$\bar{\boldsymbol{\sigma}} = \boldsymbol{E} : \boldsymbol{\varepsilon}; \qquad \boldsymbol{\sigma} = (1 - D)\boldsymbol{E} : \boldsymbol{\varepsilon}. \tag{4.5}$$

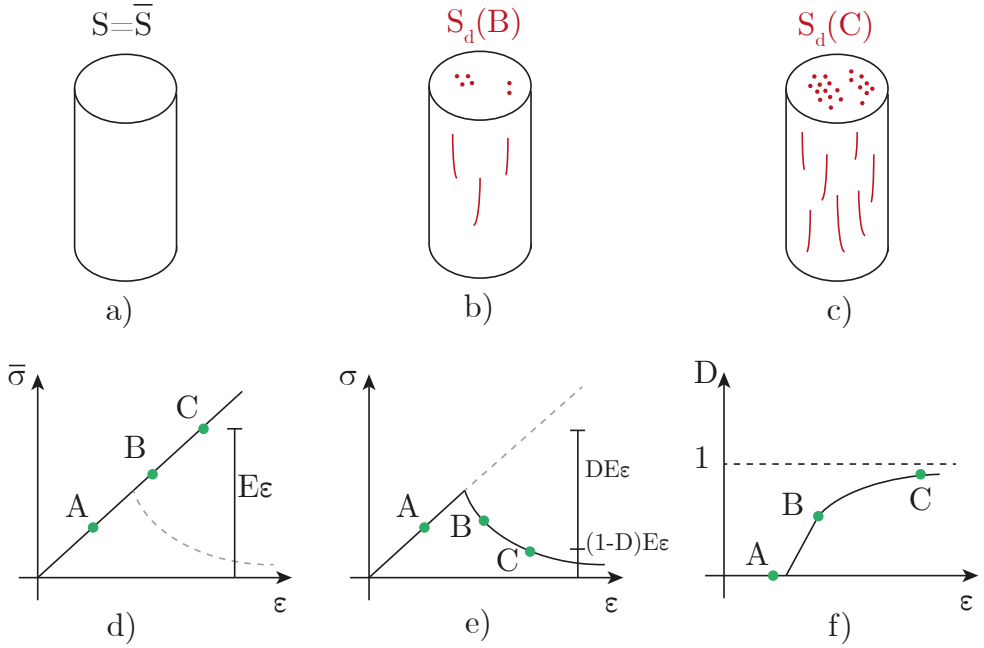

Figure 4.2: Mechanical effects of damage evolution on a volume element at the three configurations: a) A- undamaged; b) B- early damage; c) C- significant damage. Trends of effective stress (d), nominal stress (e) and damage parameter (f).

Previous equations suggest that when damage increases material Young's modulus is reduced by a factor $(1-D)$. Damage parameter could be dependent on the intensity of kinematic or mechanical variables as well as other measurable quantities. Different models are adopted in literature to describe the evolution of damage variable. Next sub-Sections 4.1.1 and 4.1.2 will explain the stress- or strain-based and thermodynamic approaches, respectively. The Jirásek-Mazars damage model formulation adopted in this thesis is reported in sub-Section 4.1.3.

4.1.1 Stress- or strain-based formulations

As stated by SIMO and JU in 1987 [110], CDM is based on theories related to the thermodynamics of irreversible processes and the associated internal state variables. These theories can be developed in two alternative frameworks: the *strain-space* damage models, based on the effective stress definition, and the *stress-space* damage models, based instead on the effective strain definition.

The effective stress concept is associated with the hypothesis of *strain equivalence* (Figure 4.3) which reads:

"the strain associated with a damaged state under the applied stress is equivalent to the strain associated with its undamaged state under the effective stress."

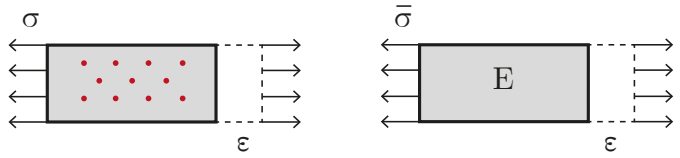

Figure 4.3: Illustration of the hypothesis of strain equivalence.

This can be proven by considering that

$$\bar{\sigma} = \frac{\sigma}{1-D} \tag{4.6}$$

$$\bar{\sigma} = E\varepsilon \tag{4.7}$$

from which it follows that

$$\sigma = (1-D)E\varepsilon \tag{4.8}$$

so the previous statement is confirmed.

Similarly, the effective strain concept is associated with the hypothesis of *stress equivalence* (Figure 4.4) which reads:

"the stress associated with a damaged state under the applied strain is equivalent to the stress associated with its undamaged state under the effective strain."

As done before, considering that

$$\bar{\varepsilon} = (1-D)\varepsilon \tag{4.9}$$

$$\sigma = E\bar{\varepsilon} \tag{4.10}$$

it follows

$$\sigma = (1-D)E\varepsilon \tag{4.11}$$

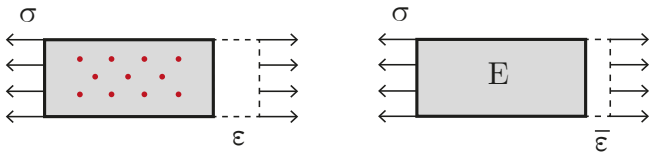

Figure 4.4: Illustration of the hypothesis of stress equivalence.

and the previous statement is confirmed.

As regards the strain-based damage formulation, the fundamental idea is the hypothesis that damage in the material is directly linked to the history of total strains. For this reason the concept of *equivalent strain* $\tilde{\varepsilon}$ is introduced. In general, it can be a function of the undamaged energy norm of the strain tensor in a strain-based formulation:

$$\tilde{\varepsilon} = \sqrt{2\Psi(\boldsymbol{\varepsilon})}, \tag{4.12}$$

as well as the *equivalent stress* $\tilde{\sigma}$ is a function of the undamaged complementary energy norm of the stress tensor:

$$\tilde{\sigma} = \sqrt{2\Phi(\boldsymbol{\sigma})}, \tag{4.13}$$

in a stress-based formulation, which is dual to the strain-based one.

4.1.2 Strain-based thermodynamic formulation

First damage formulations were proposed in the framework of CDM and a thermodynamic approach. A detailed description of these models was firstly developed by `LEMAITRE` in 1985 and then by `CHABOCHE` in 1988 [25, 26, 67]. The thermodynamic formulation is associated with internal variables and is based on the existence of two potentials:

- a *thermodynamic potential*, from which constitutive laws are derived;
- a *dissipation potential*, from which flow rules are derived.

The thermodynamic potential can be decomposed in a part associated with state variables, such as temperature T, strain $\boldsymbol{\varepsilon}$, or stress $\boldsymbol{\sigma}$, and a part associated with internal variables, governing the damage onset and growth.

Referring to a strain-based formulation and in the case of constant and uniform temperature, the Helmholtz free energy Ψ is assumed as thermodynamic potential, and its definition reads as

$$\Psi = \Psi_e(\boldsymbol{\varepsilon}, D) + \Psi_i(\xi), \tag{4.14}$$

being ξ the internal damage variable. As proposed by Chaboche in 1977, the damaged elastic behaviour can be described by referring to the effective stress concept. Ψ_e must be quadratic in $\boldsymbol{\varepsilon}$ and linear in $(1 - D)$. Considering the fourth-order elasticity tensor $\boldsymbol{E}$, it reads

$$\Psi_e = \frac{1}{2}(1 - D)\boldsymbol{\varepsilon} : \boldsymbol{E} : \boldsymbol{\varepsilon}. \tag{4.15}$$

As regards the dissipation potential, by combining the first and the second principles of thermodynamics, the following Clausius-Duhem inequality is imposed, which ensures the mechanical dissipation rate to be positive:

$$\dot{D}_{diss} = \boldsymbol{\sigma} : \dot{\boldsymbol{\varepsilon}} - \dot{\Psi} \geq 0 \tag{4.16}$$

where $\dot{D}_{diss}$ is the scalar intrinsic dissipation rate and $\dot{*}$ represents the time derivative. By substituting equation (4.14) in (4.16), it is obtained

$$\dot{D}_{diss} = \boldsymbol{\sigma} : \dot{\boldsymbol{\varepsilon}} - \frac{\partial \Psi_e}{\partial \boldsymbol{\varepsilon}} : \dot{\boldsymbol{\varepsilon}} - \frac{\partial \Psi_e}{\partial D}\dot{D} - \frac{\partial \Psi_i}{\partial \xi}\dot{\xi} \geq 0. \tag{4.17}$$

Since inequality (4.17) has to be hold for every incremental deformation process, including the purely elastic one, it follows that

$$\boldsymbol{\sigma} = \frac{\partial \Psi_e}{\partial \boldsymbol{\varepsilon}} = (1 - D)\boldsymbol{E} : \boldsymbol{\varepsilon}. \tag{4.18}$$

Since the Helmholtz free energy is a potential, other mechanical variables can be obtained by deriving equation (4.14) with respect to the associated kinematic variables. Defining:

$$\varsigma = -\frac{\partial \Psi_e}{\partial D} \qquad \text{and} \qquad \chi = \frac{\partial \Psi_i}{\partial \xi} \tag{4.19}$$

and remembering (4.18), the (4.17) now reads

$$\dot{D}_{diss} = \varsigma \dot{D} - \chi \dot{\xi} \geq 0. \tag{4.20}$$

ς and χ are the thermodynamic forces associated with the internal variables D and ξ, respectively. The onset and growth of damage is an evolutionary mechanical process, so the dissipation has a nonnegative maximum according to the theorem of maximum dissipation. Flow rules of the constitutive variables can be obtained looking for the maximum of the intrinsic dissipation $\dot{D}_{diss}$ subjected to the constraint $\phi_d(\varsigma, \chi) \leq 0$, with ϕ_d an activation function defining damage activation. Explaining the Lagrangian method, a Lagrangian function L is defined as follows

$$L = \dot{D}_{diss} - \dot{\lambda}\phi_d(\varsigma, \chi) = \varsigma\dot{D} - \chi\dot{\xi} - \dot{\lambda}_i\phi_d \tag{4.21}$$

where $\dot{\lambda}$ is the Lagrangian multiplier. The variables $\dot{\lambda}$ and ϕ_d have to satisfy the following Kuhn-Tucker relationships

$$\dot{\lambda} \geq 0, \quad \dot{\lambda}\,\phi_d = 0, \quad \phi_d \leq 0. \tag{4.22}$$

Flow rules are finally derived imposing the stationarity of the Lagrangian function with respect to each mechanical variable and under previous conditions. It is obtained that

$$\frac{\partial L}{\partial \varsigma} = \dot{D} - \dot{\lambda}\frac{\partial \phi_d}{\partial \varsigma} = 0 \qquad \Rightarrow \qquad \dot{D} = \dot{\lambda}\frac{\partial \phi_d}{\partial \varsigma} \tag{4.23}$$

$$\frac{\partial L}{\partial \chi} = -\dot{\xi} - \dot{\lambda}\frac{\partial \phi_d}{\partial \chi} = 0 \qquad \Rightarrow \qquad \dot{\xi} = -\dot{\lambda}\frac{\partial \phi_d}{\partial \chi} \tag{4.24}$$

$$\frac{\partial L}{\partial \dot{\lambda}} = \phi_d \leq 0, \tag{4.25}$$

which must be contemporary verified.

4.1.3 The Jirásek-Mazars formulation

This thesis will deal with the IDM with strain-based loading function as formulated by JIRÁSEK in [58] and MAZARS in [79]. We will refer to this formulation as J-MF. In the J-MF the damage parameter D is a function of the total strain. It can be calculated starting from the largest equivalent strain value even reached during the loading path, being the *equivalent strain* a scalar measure of the strain level. An internal kinematic variable κ is opportunely introduced as a memory variable to record the maximum principal strain level reached over a period t, as follows

$$\kappa = \max \tilde{\varepsilon}(t). \tag{4.26}$$

Hence, the damage evolution dependency can be written as

$$D = g(\kappa). \tag{4.27}$$

The explicit expression of damage variable is given by

$$D = g(\kappa) = \begin{cases} 0 & \text{if } \kappa \leq \varepsilon_0 \\ 1 - \frac{\varepsilon_0}{\kappa} \exp(-\frac{\kappa - \varepsilon_0}{\varepsilon_f - \varepsilon_0}) & \text{if } \kappa > \varepsilon_0 \end{cases} \tag{4.28}$$

being ε_0 the elastic limit strain and ε_f the post-peak limit strain.

The elastic domain and the loading-unloading conditions are defined by the following damage activation function and related Kuhn-Tucker conditions:

$$f(\tilde{\varepsilon}, \kappa) = \tilde{\varepsilon} - \kappa, \tag{4.29}$$

$$f(\tilde{\varepsilon}, \kappa) \leq 0, \quad \dot{\kappa} \geq 0, \quad \dot{\kappa}\, f(\tilde{\varepsilon}, \kappa) = 0. \tag{4.30}$$

From the first condition κ is always bigger or equal to $\tilde{\varepsilon}$; the second condition establishes that κ can't decrease and the third one that κ can increase only if a damage mechanism is activated.

The specific expression chosen to evaluate the equivalent strain determines the shape of the elastic domain. Let us summarize the most widely used definitions of the equivalent strain.

- `Scaled energy norm`

  The simplest definition of the equivalent strain is related to the Euclidean norm of the strain tensor $\boldsymbol{\varepsilon}$

  $$\tilde{\varepsilon} = \|\boldsymbol{\varepsilon}\| = \sqrt{\boldsymbol{\varepsilon} : \boldsymbol{\varepsilon}} \tag{4.31}$$

  or as the scaled energy norm

  $$\tilde{\varepsilon} = \sqrt{\frac{\boldsymbol{\varepsilon} : \boldsymbol{E} : \boldsymbol{\varepsilon}}{E}} \tag{4.32}$$

  where $\boldsymbol{E}$ is the 4-th order elastic constitutive operator and E the Young's modulus.

- `Rankine definition`

  If we refer to the Rankine criterion of maximum principal stress, the equivalent strain can be defined as

$$\tilde{\varepsilon} = \frac{1}{E} \underset{i=1,2,3}{max} \langle \boldsymbol{E} : \varepsilon \rangle_i = \frac{1}{E} \underset{i=1,2,3}{max} \langle \bar{\sigma}_i \rangle = \frac{\bar{\sigma}_1}{E} \tag{4.33}$$

  where $\langle \bar{\sigma}_i \rangle$ are the positive parts of the principal values of the effective stresses.

- `Modified Von Mises definition`

  `DE VREE`, `BREKELMANS`, and `VAN GILS` introduced in 1995 [31] the so-called modified Von Mises expression

$$\tilde{\varepsilon} = \frac{(K-1)I_{1\varepsilon}}{2K(1-2\nu)} + \frac{1}{2K}\sqrt{\frac{(1-K)^2}{(1-2\nu)^2} I_{1\varepsilon}^2 + \frac{12KJ_{2\varepsilon}}{(1+\nu)^2}} \tag{4.34}$$

  where $I_{1\varepsilon}$ is the first strain invariant of $\boldsymbol{\varepsilon}$ and $J_{2\varepsilon}$ the second deviatoric strain invariant of $\boldsymbol{\varepsilon}_{dev}$, defined respectively as follows

$$I_{1\varepsilon} = \boldsymbol{\varepsilon} : \boldsymbol{I} = tr(\boldsymbol{\varepsilon}), \qquad J_{2\varepsilon} = \frac{1}{2}\boldsymbol{\varepsilon}_{dev} : \boldsymbol{\varepsilon}_{dev} \tag{4.35}$$

$$\text{with} \quad \boldsymbol{\varepsilon}_{dev} = \boldsymbol{\varepsilon} - \frac{1}{3}\boldsymbol{I}. \tag{4.36}$$

  $\boldsymbol{I}$ is the identity matrix while K is a material parameter dependent on the ratio between the uniaxial compressive strength f_c and uniaxial tensile strength f_t.

- `Mazars definition`

  Typically, quasi-brittle materials have a different behaviour in tension and compression. Micro-cracks mostly grow when the material is stretched and it is natural to pay more attention to traction in the definition of the equivalent strain. Accordingly, the so-called *Mazars* definition of the equivalent strain is:

$$\tilde{\varepsilon} = \sqrt{\sum_{I=1}^{3} \langle \varepsilon_I \rangle^2} \tag{4.37}$$

where ε_I (I=1,2,3) are the principal strains and the McAuley brackets $\langle\cdot\rangle$ denote the positive part.

Starting from this definition, in 1986 `MAZARS` [79] proposed a damage model for concrete whose damage variable D was obtained as a combination of two variables, D_t and D_c, associated to tensile and compression, respectively. The general formula reads as

$$D = \alpha_t D_t + \alpha_c D_c \tag{4.38}$$

where the coefficients α_t and α_c were defined as

$$\alpha_t = \sum_{i=1}^{3} \frac{\varepsilon_{ti}\langle\varepsilon_I\rangle}{\tilde{\varepsilon}^2}, \qquad \alpha_c = 1 - \sum_{i=1}^{3} \frac{\varepsilon_{ti}\langle\varepsilon_I\rangle}{\tilde{\varepsilon}^2} \tag{4.39}$$

being ε_{ti} $(i = 1, 2, 3)$ the principal strains due to positive stresses. In this formulation two separate damage evolution laws were defined for D_t and D_c:

$$D_t = g_t(\kappa) = \begin{cases} 0 & \text{if } \kappa \leq \varepsilon_0 \\ 1 - (1 - A_t)\frac{\varepsilon_0}{\kappa} - A_t \exp[-B_t(\kappa - \varepsilon_0)] & \text{if } \kappa > \varepsilon_0 \end{cases} \tag{4.40}$$

$$D_c = g_c(\kappa) = \begin{cases} 0 & \text{if } \kappa \leq \varepsilon_0 \\ 1 - (1 - A_c)\frac{\varepsilon_0}{\kappa} - A_c \exp[-B_c(\kappa - \varepsilon_0)] & \text{if } \kappa > \varepsilon_0 \end{cases} \tag{4.41}$$

where A_c, A_t, B_c and B_t are material parameters related to the shape of the uniaxial stress-strain diagrams.

A recent formulation [58] is instead based on a unified formula combining the previous "purely tensile" and "purely compressive" stress cases, as in relation (4.28).

4.2 Numerical implementation of the J-MF in the framework of IDM

This thesis mainly focus on the analysis of quasi-brittle materials. In this Section the formulation regarding the adopted constitutive model, where inelastic phenomena are linked to damage evolution in the framework of IDM, is furnished. In order to introduce the aforementioned constitutive model in a nonlinear code based on an iterative Newton-Raphson procedure (see Appendix C), the tangent stiffness matrix at the Gauss point and at the element level is derived. The first two sub-Sections are devoted to the evaluation of the stiffness matrix. In a third sub-Section a numerical investigation on the mesh dependency of the IDM will be pursued.

4.2.1 Constitutive model tangent operator

Let us recall the stress-strain law (4.5) written in Voigt notation:

$$\boldsymbol{\sigma} = (1 - D)\boldsymbol{E}\boldsymbol{\varepsilon}, \tag{4.42}$$

with $\boldsymbol{\varepsilon}$ the strain vector and $\boldsymbol{\sigma}$ the stress one. We can define the elastic tangent operator $\boldsymbol{E}_t$ as the derivative of the stress field with respect to the strain one:

$$\boldsymbol{E_t} = \frac{\partial \boldsymbol{\sigma}}{\partial \boldsymbol{\varepsilon}} = (1 - D)\boldsymbol{E} - \boldsymbol{E}\boldsymbol{\varepsilon}\frac{\partial D}{\partial \boldsymbol{\varepsilon}}. \tag{4.43}$$

Recalling the dependence of damage on the equivalent strain, the derivative of the damage variable can be further rewritten as

$$\frac{\partial D}{\partial \boldsymbol{\varepsilon}} = \frac{\partial D}{\partial \kappa}\frac{\partial \kappa}{\partial \tilde{\varepsilon}}\frac{\partial \tilde{\varepsilon}}{\partial \boldsymbol{\varepsilon}}. \tag{4.44}$$

With reference to the damage variable expression (4.28), the first term is equal to

$$\frac{\partial D}{\partial \kappa} = -\frac{\exp\left(\frac{\kappa-\varepsilon_0}{\varepsilon_0-\varepsilon_f}\right)\varepsilon_0(\kappa - \varepsilon_0 + \varepsilon_f)}{\kappa^2(\varepsilon_0 - \varepsilon_f)}. \tag{4.45}$$

The second term can be evaluated from the following simple observations

$$\frac{\partial \kappa}{\partial \tilde{\varepsilon}} = \begin{cases} 0 & \text{if } \tilde{\varepsilon} < \kappa \text{ (damage not activated)} \\ 1 & \text{if } \tilde{\varepsilon} = \kappa \text{ (damage activated).} \end{cases} \tag{4.46}$$

Last term of (4.44) is evaluated by considering the Mazars' formulation of the equivalent strain as presented in (4.37). Explicitly, the equivalent strain $\tilde{\varepsilon}$ can be furnished in terms of the principal strains ε_1, ε_2, ε_3

$$\tilde{\varepsilon} = \sqrt{\langle\varepsilon_1\rangle^2 + \langle\varepsilon_2\rangle^2 + \langle\varepsilon_3\rangle^2}. \tag{4.47}$$

From (4.47), the third term can be derived according to a plane stress or a plane strain case that are separately investigated in the following.

- **Plane stress case** - $\sigma_z = 0$

  In plane stress condition, general Hooke's law leads to an expression of ε_z dependent on ε_x and ε_y as follows

  $$\varepsilon_z = \frac{-\nu}{1-\nu}(\varepsilon_x + \varepsilon_y). \tag{4.48}$$

  The strain tensor becomes

  $$\boldsymbol{\varepsilon} = \begin{bmatrix} \varepsilon_x & \frac{\gamma_{xy}}{2} & 0 \\ \frac{\gamma_{xy}}{2} & \varepsilon_y & 0 \\ 0 & 0 & \frac{-\nu}{1-\nu}(\varepsilon_x + \varepsilon_y) \end{bmatrix}. \tag{4.49}$$

  With reference to Figure 4.5, the related principal strains can be expressed as follows

  $$\varepsilon_1 = \hat{\varepsilon} + R_\varepsilon \tag{4.50}$$
  $$\varepsilon_2 = \hat{\varepsilon} - R_\varepsilon \tag{4.51}$$
  $$\varepsilon_3 = \frac{-\nu}{1-\nu} 2\hat{\varepsilon} \tag{4.52}$$

  where the following positions were made:

  $$\hat{\varepsilon} = \frac{\varepsilon_x + \varepsilon_y}{2} \qquad \text{and} \qquad R_\varepsilon = \sqrt{\left(\frac{\varepsilon_x - \varepsilon_y}{2}\right)^2 + \frac{\gamma_{xy}^2}{4}}. \tag{4.53}$$

  $\hat{\varepsilon}$ and R_ε in (4.53) fix the centre and the radius of the Mohr's circle of Figure 4.5. By substituting (4.50)-(4.51)-(4.52) in (4.47), the expression of the equivalent strain becomes:

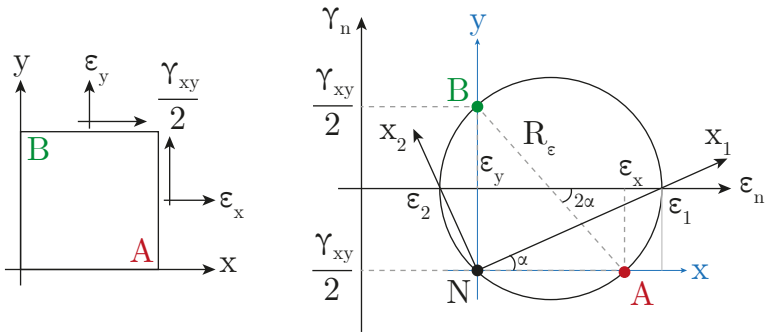

Figure 4.5: Strain components representation on the physical plane $x-y$ and the Mohr plane $\varepsilon_n - \gamma_n$; α represents the first principal strain direction with respect to the horizontal one.

$$\tilde{\varepsilon} = \sqrt{\langle \hat{\varepsilon} + R_\varepsilon \rangle^2 + \langle \hat{\varepsilon} - R_\varepsilon \rangle^2 + \left\langle \frac{-\nu}{1-\nu} 2\hat{\varepsilon} \right\rangle^2}, \tag{4.54}$$

whose derivative with respect to ε_x is:

$$\begin{aligned} \frac{\partial \tilde{\varepsilon}}{\partial \varepsilon_x} = \frac{1}{\tilde{\varepsilon}} \Bigg\{ \langle \hat{\varepsilon} + R_\varepsilon \rangle \left(\frac{1}{2} + \frac{\frac{\varepsilon_x - \varepsilon_y}{2}}{2R_\varepsilon} \right) + \langle \hat{\varepsilon} - R_\varepsilon \rangle \left(\frac{1}{2} - \frac{\frac{\varepsilon_x - \varepsilon_y}{2}}{2R_\varepsilon} \right) + \\ + \left\langle \frac{-\nu}{1-\nu} 2\hat{\varepsilon} \right\rangle \left(\frac{-\nu}{1-\nu} \right) \Bigg\}. \end{aligned} \tag{4.55}$$

In Figure 4.5, A and B represent two physical planes and α is the inclination of the first principal direction with respect to the $x-y$ reference system. From trigonometric considerations it can be deduced that

$$\tan\alpha = \frac{\frac{\gamma_{xy}}{2}}{\varepsilon_1 - \varepsilon_y} \qquad \tan 2\alpha = \frac{\frac{\gamma_{xy}}{2}}{\frac{\varepsilon_x - \varepsilon_y}{2}}. \tag{4.56}$$

Eliminating the terms $\gamma_{xy}/2$ from both equations it is obtained

$$\frac{\frac{\varepsilon_x - \varepsilon_y}{2}}{R_\varepsilon} = \frac{\tan\alpha}{\tan 2\alpha - \tan\alpha}. \tag{4.57}$$

By considering the trigonometric formulas of duplication

$$\tan 2\alpha = \frac{2\tan\alpha}{1-\tan^2\alpha} \tag{4.58}$$

it is possible to derive that

$$\frac{\tan\alpha}{\tan 2\alpha - \tan\alpha} = \frac{1-\tan^2\alpha}{1+\tan^2\alpha} = \cos 2\alpha. \tag{4.59}$$

Substituting opportunely in (4.55) it follows that

$$\frac{\partial\tilde{\varepsilon}}{\partial\varepsilon_x} = \frac{1}{2\tilde{\varepsilon}}\left\{\big(\langle\varepsilon_1\rangle + \langle\varepsilon_2\rangle\big) + \cos 2\alpha\big(\langle\varepsilon_1\rangle - \langle\varepsilon_2\rangle\big) - \frac{2\nu}{1-\nu}\langle\varepsilon_3\rangle\right\}. \tag{4.60}$$

With analogous considerations the following relation holds:

$$\frac{\frac{\gamma_{xy}}{2}}{R_\varepsilon} = \sin 2\alpha \tag{4.61}$$

and therefore it can be derived that

$$\frac{\partial\tilde{\varepsilon}}{\partial\varepsilon_y} = \frac{1}{2\tilde{\varepsilon}}\left\{\big(\langle\varepsilon_1\rangle + \langle\varepsilon_2\rangle\big) + \cos 2\alpha\big(\langle\varepsilon_2\rangle - \langle\varepsilon_1\rangle\big) - \frac{2\nu}{1-\nu}\langle\varepsilon_3\rangle\right\} \tag{4.62}$$

$$\frac{\partial\tilde{\varepsilon}}{\partial\gamma_{xy}} = \frac{\sin 2\alpha}{2\tilde{\varepsilon}}\big(\langle\varepsilon_1\rangle - \langle\varepsilon_2\rangle\big). \tag{4.63}$$

- **Plane strain case** - $\varepsilon_z = 0$

  In plain strain condition the ε_z term in the strain tensor in (4.49) is null and principal strains ε_1 and ε_2 are equal to expressions (4.50) and (4.51) while $\varepsilon_3 = 0$. The equivalent strain assumes now the following form

$$\tilde{\varepsilon} = \sqrt{\langle\hat{\varepsilon} + R_\varepsilon\rangle^2 + \langle\hat{\varepsilon} - R_\varepsilon\rangle^2}. \tag{4.64}$$

  Taking into account the same trigonometric equivalences as in the plane stress case it can be derived that

$$\frac{\partial\tilde{\varepsilon}}{\partial\varepsilon_x} = \frac{1}{2\tilde{\varepsilon}}\left\{\big(\langle\varepsilon_1\rangle + \langle\varepsilon_2\rangle\big) + \cos 2\alpha\big(\langle\varepsilon_1\rangle - \langle\varepsilon_2\rangle\big)\right\} \tag{4.65}$$

$$\frac{\partial\tilde{\varepsilon}}{\partial\varepsilon_y} = \frac{1}{2\tilde{\varepsilon}}\left\{\big(\langle\varepsilon_1\rangle + \langle\varepsilon_2\rangle\big) + \cos 2\alpha\big(\langle\varepsilon_2\rangle - \langle\varepsilon_1\rangle\big)\right\} \tag{4.66}$$

$$\frac{\partial\tilde{\varepsilon}}{\partial\gamma_{xy}} = \frac{\sin 2\alpha}{2\tilde{\varepsilon}}\big(\langle\varepsilon_1\rangle - \langle\varepsilon_2\rangle\big). \tag{4.67}$$

4.2.2 FE tangent stiffness matrix

The FE tangent stiffness tensor can be assumed as the local gradient of the force/displacement relationship.

Internal forces are equal to

$$\mathbf{f}_{int} = \int_V \boldsymbol{B}^T \boldsymbol{\sigma}\, dV, \tag{4.68}$$

where $\boldsymbol{B}$ is the second-order compatibility strain-displacement tensor and $\boldsymbol{\sigma}$ is the column matrix of stress components, written using Engineering notation. In a finite element approach, using the Gauss quadrature, the integral is replaced by a sum of contributions collected from a finite number of integration points n_{gp}:

$$\mathbf{f}_{int} = \sum_{i=1}^{n_{gp}} w_i \boldsymbol{B}_i^T \boldsymbol{\sigma}_i \tag{4.69}$$

where w_i are the weights associated to each point.

Introducing the compatibility equation in (4.42) it follows that

$$\boldsymbol{\sigma} = (1-D)\boldsymbol{E}(\boldsymbol{B}\mathbf{d}) \tag{4.70}$$

in which $\mathbf{d}$ is the vector of nodal displacements.

The sum in (4.69) can be rewritten as follows

$$\begin{aligned} \boldsymbol{f_{int}} &= \sum_{i=1}^{n_{gp}} w_i (1-D_i) \boldsymbol{B}_i^T \boldsymbol{E} \boldsymbol{B}_i \mathbf{d} \\ &= \sum_{i=1}^{n_{gp}} w_i (1-D_i) \boldsymbol{K}_i \mathbf{d} \end{aligned} \tag{4.71}$$

where $\boldsymbol{K}_i = \boldsymbol{B}_i^T \boldsymbol{E} \boldsymbol{B}_i$ is the *elastic stiffness matrix* evaluated at the generic integration point i.

The *tangent stiffness matrix* can be derived by differentiating the internal forces in (4.71) with respect to the nodal displacements:

$$\begin{aligned} \boldsymbol{K}_t &= \frac{\partial \boldsymbol{f_{int}}}{\partial \boldsymbol{d}} \\ &= \sum_{i=1}^{n_{gp}} w_i (1-D_i) \boldsymbol{K}_i - \sum_{i=1}^{n_{gp}} w_i \boldsymbol{K}_i \mathbf{d} \left(\frac{\partial D_i}{\partial \mathbf{d}} \right) \\ &= \boldsymbol{K}_u - \sum_{i=1}^{n_{gp}} w_i \boldsymbol{K}_i \mathbf{d} \left(\frac{\partial D_i}{\partial \boldsymbol{d}} \right) \end{aligned} \tag{4.72}$$

where the first term $\boldsymbol{K_u}$ represents the *secant stiffness tensor*, which is a symmetric matrix. Because of the presence of the second term, the tangent stiffness matrix can be symmetric only in particular cases [60].

The tangent stiffness matrix can be expressed in its integral form as follows:

$$\boldsymbol{K_t} = (1-D)\int_V \boldsymbol{B^T E B} dV - \int_V \boldsymbol{B^T E B d}\frac{\partial D}{\partial \mathbf{d}} dV \tag{4.73}$$

$$\text{being} \quad \frac{\partial D}{\partial \mathbf{d}} = \frac{\partial D}{\partial \boldsymbol{\varepsilon}}\frac{\partial \boldsymbol{\varepsilon}}{\partial \mathbf{d}} = \frac{\partial D}{\partial \boldsymbol{\varepsilon}}\frac{\partial (\boldsymbol{B}\mathbf{d})}{\partial \mathbf{d}} = \frac{\partial D}{\partial \boldsymbol{\varepsilon}}\boldsymbol{B} \tag{4.74}$$

By substituting (4.74) in (4.73) the final expression of the FE tangent stiffness matrix becomes

$$\boldsymbol{K_t} = \int_V \boldsymbol{B}^T \underbrace{[(1-D)\boldsymbol{E} - \boldsymbol{E\varepsilon}\frac{\partial D}{\partial \boldsymbol{\varepsilon}}]}_{\boldsymbol{E}_t} \boldsymbol{B} dV \tag{4.75}$$

where $\boldsymbol{E}_t$ is the elastic tangent tensor given in (4.43).

4.2.3 Mesh dependency of the IDM

Table 4.1: Adopted parameters for the analysis on a single edge notched (SEN) specimen under mixed mode.

$E\ [MPa]$	ν	ε_0	$\frac{\varepsilon_f}{\varepsilon_0}$
1000	0.2	$1.0E-3$	100

This sub-Section deals with the analysis of the adopted damage model formulation. The scope of this sub-Section is to investigate on continuum models where the inelastic effects are distributed and smeared all over the material. These approaches, as known, suffer from strong dependence on mesh-size.

In order to make this problem evident, a square specimen with dimensions $100 \times 100 \times 1\ mm$ and a non-symmetric notch was analyzed. Geometry and boundary conditions are reported in Figure 4.6, constitutive parameters in Table 4.1. The specimen is fixed on the bottom side while the top edge is subjected to uniform distribution of horizontal displacements and a linear distribution of vertical displacements, with a maximum on the left node and zero on the right node. The maximum final values of the horizontal and vertical displacements are set equal to $\bar{\delta}_x = 0.85\ mm$ and $\bar{\delta}_y = 1\ mm$, respectively.

To study the dependence of the model on mesh size and orientation, the example is performed using five different meshes, three of which are regular (RM) and two skewed (SM). The three regular meshes are shown in Figure 4.7 where, respecting a classical h-refinement rule, they are divided into 16×16, 32×32, and 64×64 quadrilateral linear elements. The two skewed meshes, on the other hand, are represented in Figure 4.8 using 16×16 (Figure 4.8-a) or 32×32 (Figure 4.8-b) quadrilateral linear elements respectively.

The reported data are those at the final step of the analysis for each one of the aforementioned meshes. For each mesh, two images are reported. In the first one (Figure 4.10), the contour plots of damage distribution are reported. In the second one (Figure 4.11), principal strain direction vectors scaled by damage value are shown, on a grid of 5×5 evaluation points for each element.

It is possible to see how damage evolves in certain areas of the specimen only. In particular, for all 5 meshes it evolves mainly in the central strip of the specimen, starting from the notch, and then deflects toward the lower right corner at the end of the analysis. In parallel, especially for coarser meshes, damage involves also a central area just below the notch, the lower left and upper right corners and a small area on the right edge of the specimen. However,

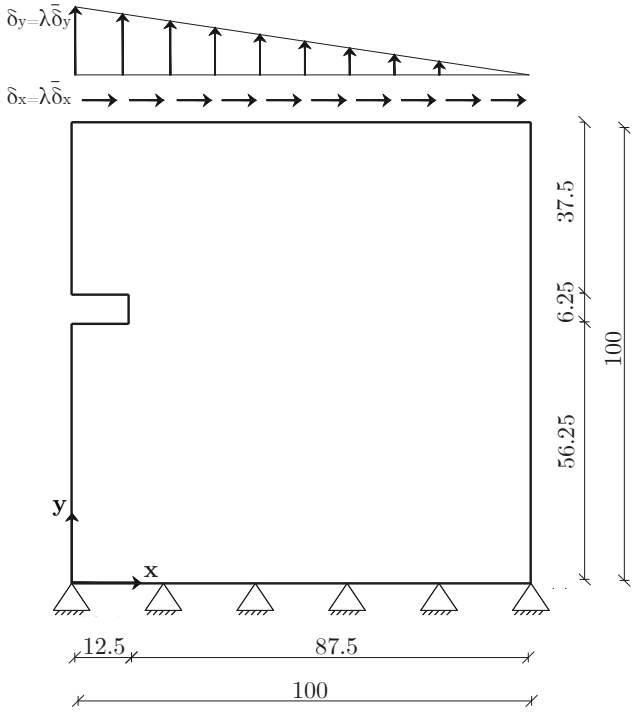

Figure 4.6: SEN specimen under mixed mode - Geometry and boundary conditions. Dimensions are given in mm.

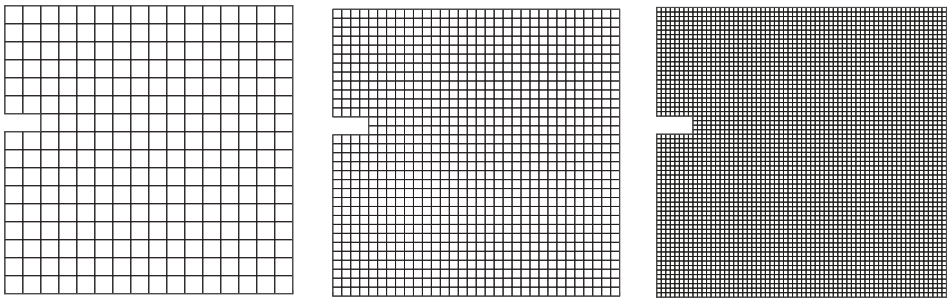

Figure 4.7: SEN specimen under mixed mode - Different employed RM: (a) 16×16, (b) 32×32, (c) 64×64.

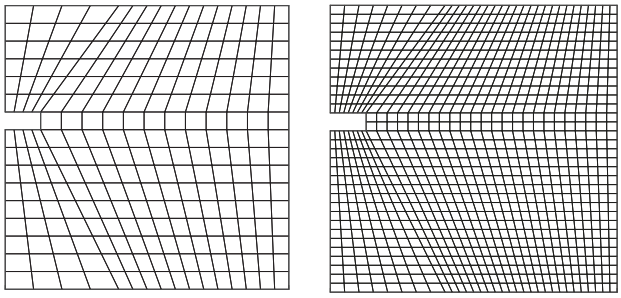

Figure 4.8: SEN specimen under mixed mode - Different employed SM: (a) 16×16, (b) 32×32.

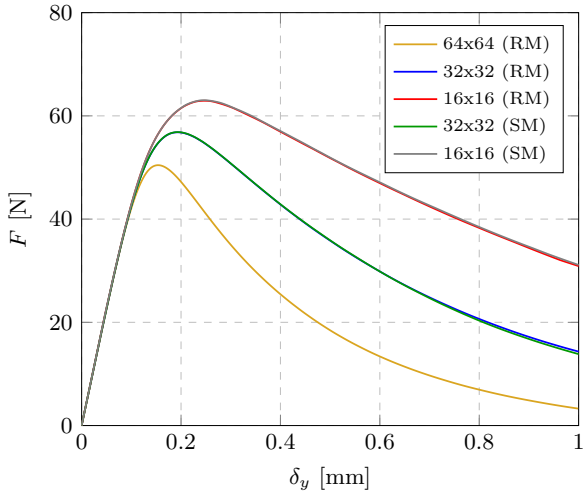

Figure 4.9: SEN specimen under mixed mode - Load-displacement curves.

these secondary areas tend to disappear as denser is the mesh, confirming, the dependence of these patterns on the mesh-size. Also, as evident from Figure 4.9, different load-displacement curves correspond to different meshes: in particular, the denser the mesh the lower the peak because the inelastic effects affect elements of progressively smaller size, resulting in a more localized damaged area.

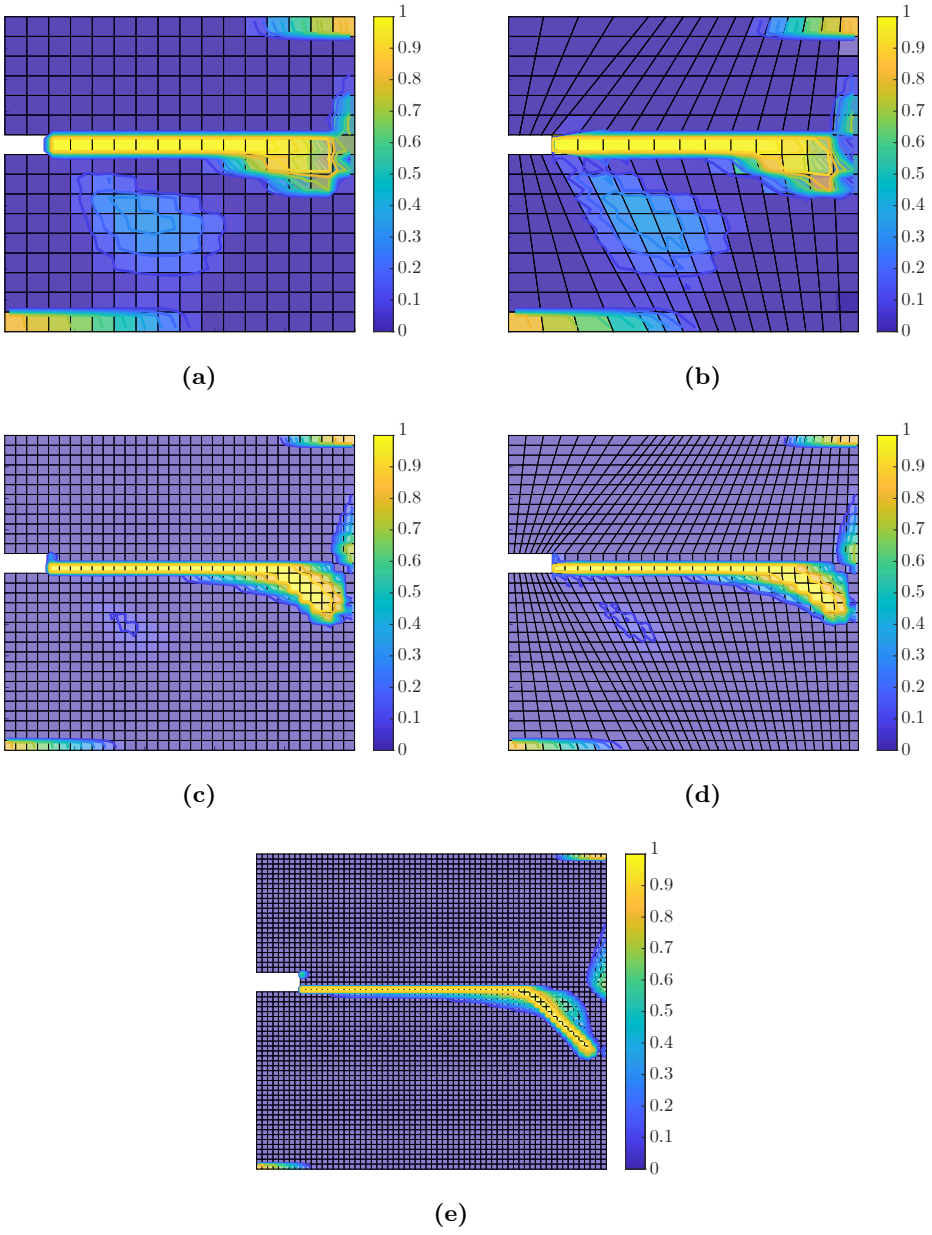

Figure 4.10: SEN specimen under mixed mode - Damage contour plots on a (a) 16×16 RM; (b) 16×16 SM; (c) 32×32 RM; (d) 32×32 SM; (e) 64×64 RM.

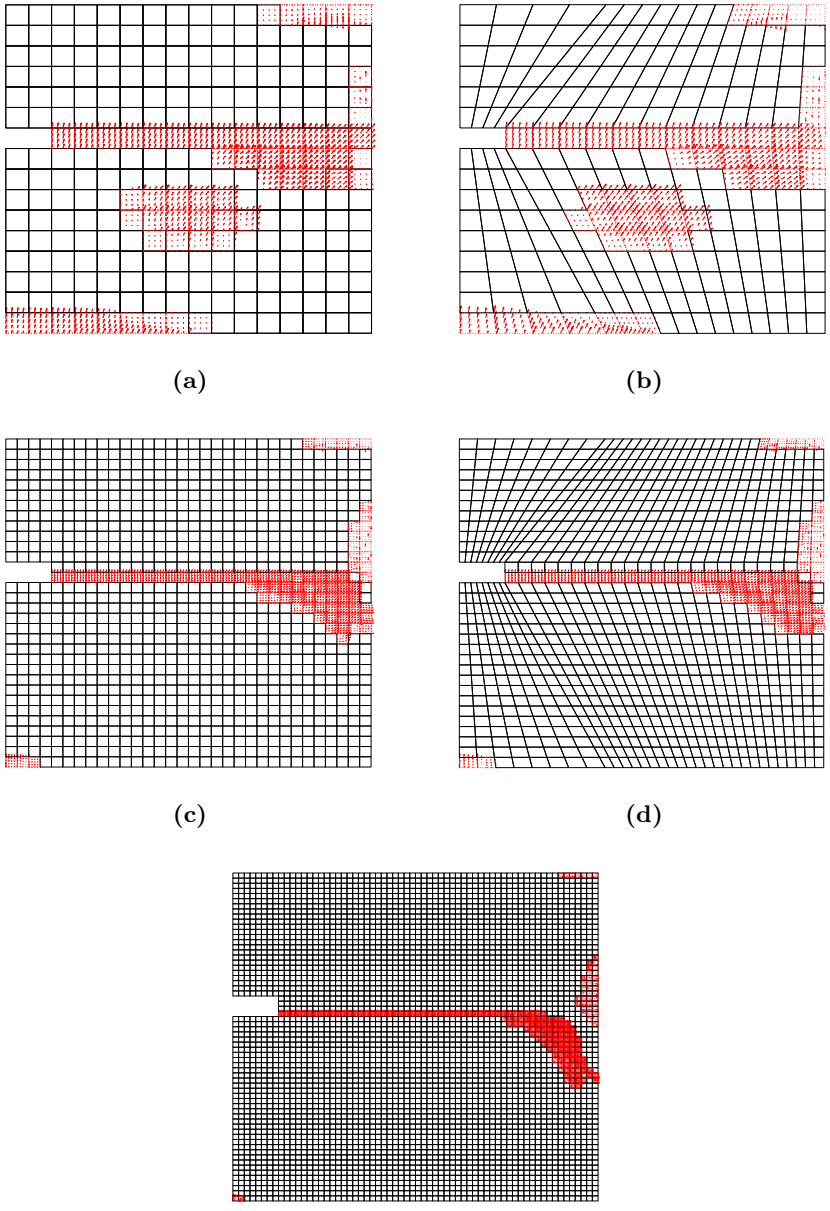

(a) **(b)**

(c) **(d)**

(e)

Figure 4.11: SEN specimen under mixed mode - Principal strain directions distribution on a (a) 16×16 RM; (b) 16×16 SM; (c) 32×32 RM; (d) 32×32 SM; (e) 64×64 RM.

4.3 Strain localization with J-MF

Strain localization has been presented in previous Sections from a general point of view as an instability problem linked to the constitutive nature of a material. This section is devoted to the analysis of this phenomenon with specific reference to the J-MF in the framework of IDM. Different strain localization criteria are reported. It will be shown how each criterion is able to correctly identify the localization instant but also how the acoustic tensor is not able to correctly identify the localization direction and needs to be substituted with a more suitable criterion.

4.3.1 Strain localization criteria

As already seen in Section 1.2, different local conditions regarding the uniqueness condition and the stability of a material can be identified. The most diffused of them are summarized in the expressions (1.3)-(1.4)-(1.10) and here explicitly recalled.

- `Singularity of the constitutive operator`

  As formulated by `HADAMARD`, `THOMAS` and `HILL` [47, 50, 122], the loss of the positive-definiteness of the constitutive tangent operator $\boldsymbol{E}_t$ leads to the existence of waves propagating in the material with imaginary speed, condition that is physically unreal. The condition whereby

  $$det(\boldsymbol{E}_t) = 0 \tag{4.76}$$

  can be therefore intended as the first local indicator of strain localization. Alternatively, by investigating on the sign of the eigenvalues of the constitutive operator, incipient localization can be identified. However, this criterion provides only the instant of formation of a potential band, but no indication is retrieved regarding its inclination. This criterion, therefore, should be coupled with a second criterion giving its correct position.

- `Spectral analysis of the acoustic tensor`

  The physical meaning of the acoustic tensor $\boldsymbol{L}$ has been already discussed in sub-Sections 2.2.1-2.2.2. The continuous/discontinuous bifurcation condition leads to a localization criterion that reads as

  $$det(\mathbf{n} \cdot \boldsymbol{E}_t \cdot \mathbf{n}) = det(\boldsymbol{L}) = 0. \tag{4.77}$$

Being $\boldsymbol{n} = [n_x \quad n_y]^T$ the unit vector normal to the localization band, the previous expression in plane stress reads as

$$\boldsymbol{L} = \begin{bmatrix} n_x & 0 & n_y \\ 0 & n_y & n_x \end{bmatrix} \begin{bmatrix} E_{11} & E_{12} & E_{13} \\ E_{21} & E_{22} & E_{23} \\ E_{31} & E_{32} & E_{33} \end{bmatrix} \begin{bmatrix} n_x & 0 \\ 0 & n_y \\ n_y & n_x \end{bmatrix} =$$

$$= \left[\begin{array}{c|c} E_{11}n_x^2 + (E_{13} + E_{31})n_x n_y + E_{33}n_y^2 & E_{12}n_x n_y + E_{13}n_x^2 + E_{32}n_y^2 + E_{33}n_x n_y \\ \hline E_{21}n_x n_y + E_{23}n_y^2 + E_{31}n_x^2 + E_{33}n_x n_y & E_{22}n_y^2 + E_{23}n_x n_y + E_{32}n_x n_y + E_{33}n_x^2 \end{array}\right] \tag{4.78}$$

Through the spectral analysis of the aforementioned tensor both the onset and position of a localization band are identified at that step when its minimum eigenvalue is null or negative. The direction of the localization band then corresponds to the eigenvector associated with the minimum eigenvalue.

Let us refer to the acoustic tensor expression in (4.78). The determinant can be written as a function of the components n_x and n_y:

$$det(\boldsymbol{L}) = C_1 n_x^4 + C_2 n_x^3 n_y + C_3 n_x^2 n_y^2 + C_4 n_x n_y^3 + C_5 n_y^4 \tag{4.79}$$

where

$$\begin{aligned} C_1 &= (E_{11}E_{33} - E_{13}E_{31}) \\ C_2 &= (E_{11}E_{23} + E_{11}E_{32} - E_{31}E_{12} - E_{13}E_{21}) \\ C_3 &= (E_{11}E_{22} + E_{13}E_{32} + E_{31}E_{23} - E_{12}E_{21} - E_{12}E_{33} - E_{21}E_{33}) \\ C_4 &= (E_{13}E_{22} + E_{31}E_{22} - E_{21}E_{32} - E_{23}E_{12}) \\ C_5 &= (E_{22}E_{33} - E_{23}E_{32}). \end{aligned} \tag{4.80}$$

Considering that $n_y = \sqrt{1 - n_x^2}$, the unknown variable n_x is calculated solving a single-variable bounded nonlinear minimization problem:

$$\text{Find } n_x \mid n_x = min\ det(\boldsymbol{L}) \text{ with } -1 \leq n_x \leq 1.$$

Using this formulation, however, as demonstrated in the next sub-Section 4.3.2, the acoustic tensor is unable to furnish reliable localization directions, so the spectral analysis of the acoustic tensor could be used only to individuate the onset of localization, again leaving the task of identifying the direction of localization to a second criterion.

- `Singularity of the FE tangent stiffness`

  As stated by `DE BORST` [29, 30], localization can be understood as the loss of positive-definiteness of the FE tangent stiffness matrix. This condition coincides to impose that

$$det(\boldsymbol{K}_t) = 0 \tag{4.81}$$

  where the tangent stiffness matrix $\boldsymbol{K}_t$ is that one introduced in (4.75) for a finite element. Also, this criterion furnishes only an indication regarding the incipient localization condition while no information is given about the band direction.

  As for the previous two criteria, the identification of the localization direction for the J-MF model must be entrusted to a second criterion.

4.3.2 Strain localization in pure modes

Table 4.2: Comparison between different localization criteria on a single element.

$E\ [MPa]$	ν	ε_0	$\frac{\varepsilon_f}{\varepsilon_0}$
100000	0.30	$9.0E-4$	10

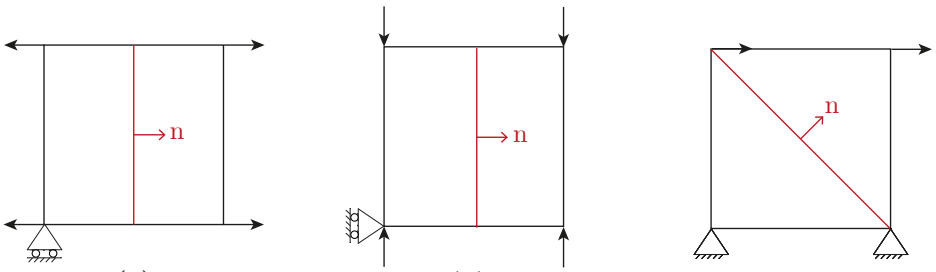

Figure 4.12: Comparison between different localization criteria on a single element subjected to (a) horizontal tensile load, (b) vertical compressive load and (c) shear load.

The localization criteria listed in the previous sub-Section will be here applied on a single element, subjected to a horizontal tensile load (Figure 4.12-a), a vertical compressive load (Figure 4.12-b) and a shear load (Figure 4.12-c).

In these pure modes cases, vertical Mode-I cracks are expected for (a) and (b) cases, while a Mode-II crack, with an inclination of 45°, is expected for case (c).

The analysis has been conducted considering a simple $10 \times 10 \times 1$ mm element, having the constitutive parameters reported in Table 4.2. The element has been subjected to an imposed displacement $\lambda\bar{u}$, being $\bar{u} = 0.001$ the maximum imposed value and λ its multiplier. A total of 50 load steps have been considered.

Figures 4.13-a, 4.14-a and 4.15-a compare the results of the three localization criteria, referred to one of the four integration points, for which the same values are recorded. The trend of the determinant of the constitutive operator $f(\boldsymbol{E}_t)$, of the minimum value of the determinant of the acoustic tensor $f(\boldsymbol{L})$ and of the minimum eigenvalue of the FE tangent stiffness matrix $f(\boldsymbol{K}_t)$ are reported with respect to the step number. The reported values are normalized to the correspondent elastic values (indicated by superscript 0) as follows:

$$f(\boldsymbol{E}_t) = \frac{det(\boldsymbol{E}_t)}{det(\boldsymbol{E}_t^0)}, \qquad f(\boldsymbol{L}) = \left(\frac{det(\boldsymbol{L})}{det(\boldsymbol{L}^0)}\right)_{min}, \qquad f(\boldsymbol{K}_t) = \frac{\lambda_{min}(\boldsymbol{K}_t)}{\lambda_{min}(\boldsymbol{K}_t^0)}. \tag{4.82}$$

In each case the initial values are positive but, at the localization step (LS), they assume a minimum value to subsequently proceed asymptotically until an almost null value.

Since the *acoustic tensor criterion* is the only one that could provide the localization direction, Figures 4.13-b, 4.14-b and 4.15-b report the values of $det(\boldsymbol{L})$ with respect to the orientation α_n of the unit vector $\mathbf{n}$ with respect to the horizontal axis. The curves are reported, for the localization step LS and for other 4 subsequent steps. In all 5 steps the trend is the same, but after localization it flattens towards the horizontal axis. For the case (a) the minimum value of the $det(\boldsymbol{L})$ is assumed for $\alpha_n \simeq 20°$ or 160°, although an angle of about 0° is expected. Similarly, for the case (b) the minimum value is assumed for $\alpha_n \simeq 49°$ or 131°, although an angle of about 0° is expected. For the case (c) the minimum value is obtained for $\alpha_n \simeq 80°$, although an angle of about 45° is expected. It can be concluded that localization directions returned by the acoustic tensor do not respect the expected directions, and therefore, as will be explained later in Section 6.3, a new localization criterion is necessary.

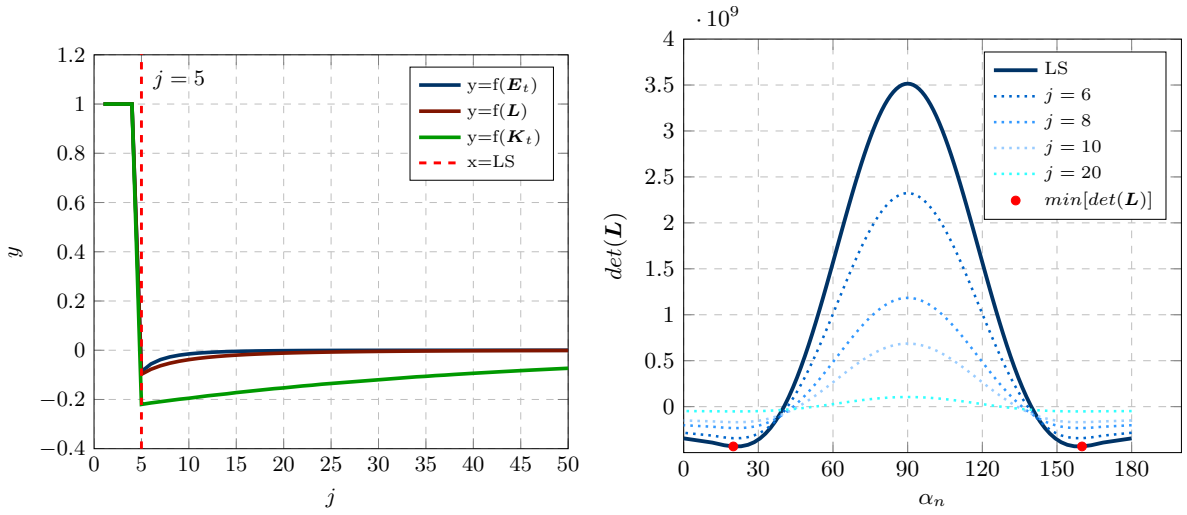

(a) **(b)**

Figure 4.13: Comparison between different localization criteria (a) and trend of the $det(\boldsymbol{L})$ with respect to the angle α_n between $\mathbf{n}$ and the x-axis (b) for case 4.12-a.

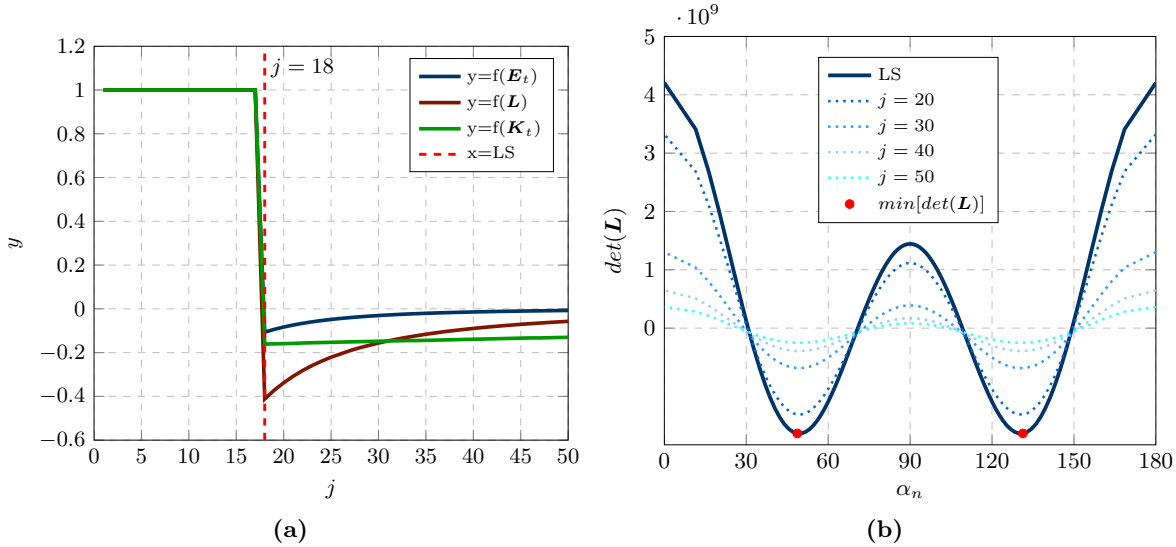

(a) **(b)**

Figure 4.14: Comparison between different localization criteria (a) and trend of the $det(\boldsymbol{L})$ with respect to the angle α_n between $\mathbf{n}$ and the x-axis (b) for case 4.12-b.

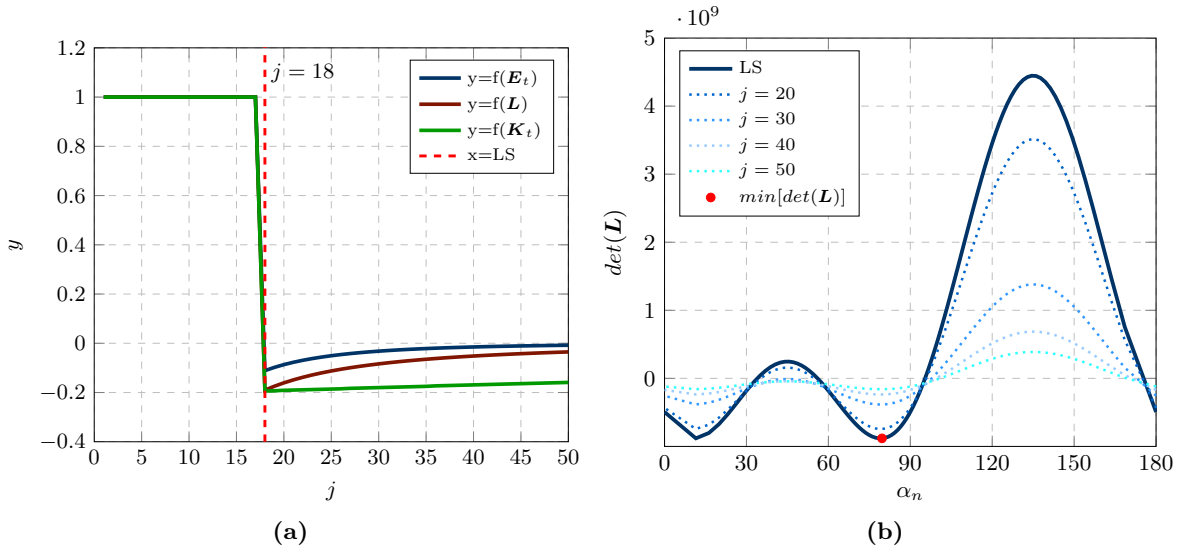

Figure 4.15: Comparison between different localization criteria (a) and trend of the $det(\boldsymbol{L})$ with respect to the angle α_n between $\mathbf{n}$ and the x-axis (b) for case 4.12-c.

4.4 Flutter instability with J-MF

Strong-ellipticity and ellipticity are necessary conditions for the material stability, linked to the positiveness and non-vanishing of the eigenvalues of the acoustic tensor, respectively. Conditions for the occurrence of the flutter instability will be here investigated, based on the spectral analysis of the acoustic tensor in the framework of the Jirásek-Mazars formulation.

4.4.1 Flutter instability in plane stress

As already explained, flutter instability corresponds to the occurrence of two complex conjugate eigenvalues of the acoustic tensor. Under plane stress condition, the acoustic tensor is a 2×2 second-order tensor. By representing the acoustic tensor in (4.78) by components L_{ij} respect to a certain coordinate system, it reads

$$\boldsymbol{L} = \begin{bmatrix} L_{11} & L_{12} \\ L_{21} & L_{22} \end{bmatrix} \tag{4.83}$$

whose associated characteristic equation assumes the form

$$\lambda^2 - (\operatorname{tr} \boldsymbol{L})\lambda + \det \boldsymbol{L} = 0 \tag{4.84}$$

with

$$\operatorname{tr} \boldsymbol{L} = L_{11} + L_{22}, \qquad \det \boldsymbol{L} = L_{11}L_{22} - L_{12}L_{21}. \tag{4.85}$$

Flutter condition then reads:

$$(\operatorname{tr} \boldsymbol{L})^2 - 4 \det \boldsymbol{L} < 0. \tag{4.86}$$

Equation (4.86) shows that the localization condition $\det \boldsymbol{L} \leq 0$ and the flutter condition can never be satisfied simultaneously for the same direction $\boldsymbol{n}$. Of course, for a given state of the material, the localization condition could be satisfied with some directions and the flutter condition with other ones.

By substituting (4.85) in (4.86) it is obtained

$$(L_{11} + L_{22})^2 - 4L_{11}L_{22} + 4L_{12}L_{21} < 0 \tag{4.87}$$

$$\Rightarrow (L_{11} - L_{22})^2 + 4L_{12}L_{21} < 0. \tag{4.88}$$

Equation (4.88) indicates that the flutter condition can be satisfied only if $L_{12}L_{21} < 0$, i.e. when the out-of-diagonal components of the acoustic tensor have opposite signs. This is a necessary condition, but not sufficient, to record flutter instability.

Let us consider the tangent stiffness constitutive operator for the M-JF in the framework of IDM, as in (4.43). It can be rewritten as

$$\boldsymbol{E}_t = (1 - D)\boldsymbol{E} - D_\kappa \bar{\boldsymbol{\sigma}} \otimes \boldsymbol{\eta} \tag{4.89}$$

where $D_\kappa = \frac{\partial D}{\partial \kappa} \frac{\partial \kappa}{\partial \tilde{\varepsilon}}$ is the derivative of damage with respect to the equivalent strain, $\bar{\boldsymbol{\sigma}} = \boldsymbol{E} : \boldsymbol{\varepsilon}$ is the effective stress and $\boldsymbol{\eta} = \partial \tilde{\varepsilon} / \partial \boldsymbol{\varepsilon}$. The corresponding acoustic tensor is then

$$\boldsymbol{L} = \boldsymbol{L}_u - \boldsymbol{L}_l = \boldsymbol{L}_u - D_\kappa \bar{\boldsymbol{\sigma}}_n \otimes \boldsymbol{\eta}_n \tag{4.90}$$

where

$$\boldsymbol{L}_u = (1 - D)\boldsymbol{n} \cdot \boldsymbol{E} \cdot \boldsymbol{n} \tag{4.91}$$

is the elastic acoustic tensor for unloading and

$$\bar{\boldsymbol{\sigma}}_n = \bar{\boldsymbol{\sigma}} \cdot \boldsymbol{n}, \qquad \boldsymbol{\eta}_n = \boldsymbol{\eta} \cdot \boldsymbol{n} \tag{4.92}$$

are first-order tensors. The out-of-diagonal components are therefore considered

$$L_{12} = L_{u12} - D_\kappa \bar{\sigma}_{n1} \eta_{n2} \tag{4.93}$$

$$L_{21} = L_{u21} - D_\kappa \bar{\sigma}_{n2} \eta_{n1} \tag{4.94}$$

in order to look for cases where relation (4.88) is satisfied. With E, ν being the elastic constants, D the damage variable and considering a $x-y$ plane, the elastic acoustic tensor for unloading in (4.91) becomes (considering $n_x = \cos\alpha$ and $n_y = \sin\alpha$)

$$\begin{aligned} \boldsymbol{L}_u &= (1-D)\frac{E}{1-\nu^2} \begin{bmatrix} n_x & 0 & n_y \\ 0 & n_y & n_x \end{bmatrix} \begin{bmatrix} 1 & \nu & 0 \\ \nu & 1 & 0 \\ 0 & 0 & \frac{1-\nu}{2} \end{bmatrix} \begin{bmatrix} n_x & 0 \\ 0 & n_y \\ n_y & n_x \end{bmatrix} \\ &= (1-D)\frac{E}{2(1-\nu^2)} \begin{bmatrix} 2\cos^2\alpha + (1-\nu)\sin^2\alpha & (1+\nu)\sin\alpha\cos\alpha \\ (1+\nu)\sin\alpha\cos\alpha & 2\sin^2\alpha + (1-\nu)\cos^2\alpha \end{bmatrix}. \end{aligned} \tag{4.95}$$

The out-of-diagonal equal terms are

$$L_{u12} = L_{u21} = \frac{(1-D)E}{4(1-\nu)} \sin 2\alpha. \tag{4.96}$$

Similarly, the "correction" term $\boldsymbol{L}_l$ can be written as

$$\boldsymbol{L}_l = D_\kappa \begin{bmatrix} \bar{\sigma}_{nx}\eta_{nx} & \bar{\sigma}_{nx}\eta_{ny} \\ \bar{\sigma}_{ny}\eta_{nx} & \bar{\sigma}_{ny}\eta_{ny} \end{bmatrix} \tag{4.97}$$

where

$$\bar{\sigma}_{nx} = n_x \bar{\sigma}_x + n_y \bar{\tau}_{xy} \tag{4.98}$$

$$\bar{\sigma}_{ny} = n_y \bar{\sigma}_y + n_x \bar{\tau}_{xy} \tag{4.99}$$

$$\eta_{nx} = n_x \eta_x + n_y \eta_{xy} \tag{4.100}$$

$$\eta_{ny} = n_y \eta_y + n_x \eta_{xy}. \tag{4.101}$$

Since the material is isotropic, the relations remain valid even choosing a different reference system. It is certainly more convenient to work with the system aligned with the principal axes of the strain tensor, which are at the same time the principal axes of effective stress and of tensor $\boldsymbol{\eta}$.

Therefore, it can be set $\bar{\sigma}_x = \bar{\sigma}_1$, $\bar{\sigma}_y = \bar{\sigma}_2$, $\bar{\tau}_{xy} = 0$, $\eta_x = \eta_1$, $\eta_y = \eta_2$ and $\eta_{xy} = 0$. In this case, the angle α denotes the angle between the major principal axis and the unit vector $\mathbf{n}$.

Let us remember the general Hooke's law in the principal reference system

$$\bar{\sigma}_1 = \frac{E}{1-\nu^2}(\varepsilon_1 + \nu\varepsilon_2) \tag{4.102}$$

$$\bar{\sigma}_2 = \frac{E}{1-\nu^2}(\varepsilon_2 + \nu\varepsilon_1). \tag{4.103}$$

The principal values of $\boldsymbol{\eta}$ depend on the strain state and on the selected expression for equivalent strain. The out-of-plane strain component is derived from the others as follows

$$\varepsilon_3 = -\frac{\nu}{E}(\bar{\sigma}_1 + \bar{\sigma}_2) = -\frac{\nu}{E}\frac{E(1+\nu)}{1-\nu^2}(\varepsilon_1 + \varepsilon_2) = -\frac{\nu}{1-\nu}(\varepsilon_1 + \varepsilon_2). \tag{4.104}$$

Remembering the Mazars formulation expressed in (4.47), the equivalent strain reads as

$$\tilde{\varepsilon} = \sqrt{\langle\varepsilon_1\rangle^2 + \langle\varepsilon_2\rangle^2 + \frac{\nu^2}{(1-\nu)^2}\langle -\varepsilon_1 - \varepsilon_2\rangle^2} \tag{4.105}$$

and its derivatives with respect to the strain components become

$$\eta_1 = \frac{\partial\tilde{\varepsilon}}{\partial\varepsilon_1} = \frac{1}{\tilde{\varepsilon}}\left(\langle\varepsilon_1\rangle - \frac{\nu^2}{(1-\nu)^2}\langle -\varepsilon_1 - \varepsilon_2\rangle\right) \tag{4.106}$$

$$\eta_2 = \frac{\partial\tilde{\varepsilon}}{\partial\varepsilon_2} = \frac{1}{\tilde{\varepsilon}}\left(\langle\varepsilon_2\rangle - \frac{\nu^2}{(1-\nu)^2}\langle -\varepsilon_1 - \varepsilon_2\rangle\right). \tag{4.107}$$

Let us introduce a new variable, called *stress angle* ζ, such that

$$\tan\zeta = \frac{\bar{\sigma}_2}{\bar{\sigma}_1} \Rightarrow \bar{\sigma}_1 = \bar{\sigma}\cos\zeta; \quad \bar{\sigma}_2 = \bar{\sigma}\sin\zeta \tag{4.108}$$

being $\bar{\sigma}$ the magnitude of the effective stress, equal to

$$\begin{aligned}\bar{\sigma} &= \sqrt{\bar{\sigma}_1^2 + \bar{\sigma}_2^2} = \frac{E}{1-\nu^2}\sqrt{(\varepsilon_1 + \nu\varepsilon_2)^2 + (\varepsilon_2 + \nu\varepsilon_1)^2} = \\ &= \frac{E}{1-\nu^2}\sqrt{(1+\nu^2)(\varepsilon_1^2 + \varepsilon_2^2) + 4\nu\varepsilon_1\varepsilon_2}.\end{aligned} \tag{4.109}$$

Previous expressions (4.98)-(4.101) can be simplified as

$$\bar{\sigma}_{nx} = \bar{\sigma}\cos\alpha\cos\zeta \tag{4.110}$$
$$\bar{\sigma}_{ny} = \bar{\sigma}\sin\alpha\sin\zeta \tag{4.111}$$
$$\eta_{nx} = \eta_1\cos\alpha \tag{4.112}$$
$$\eta_{ny} = \eta_2\sin\alpha \tag{4.113}$$

and (4.97) becomes

$$\boldsymbol{L}_l = D_\kappa\bar{\sigma}\begin{bmatrix} \eta_1\cos\zeta\cos^2\alpha & \eta_2\cos\zeta\cos\alpha\sin\alpha \\ \eta_1\sin\zeta\cos\alpha\sin\alpha & \eta_2\sin\zeta\sin^2\alpha \end{bmatrix}. \tag{4.114}$$

Introducing (4.95) and (4.114) in (4.90), the acoustic tensor terms become

$$\begin{aligned} L_{11} &= \frac{E_u}{2(1-\nu^2)}\left[2\cos^2\beta + (1-\nu)\sin^2\beta\right] - D_\kappa\bar{\sigma}\eta_1\cos\zeta\cos^2\beta = \\ &= \frac{E_u}{2(1-\nu^2)}\left[1-\nu+(1+\nu)(1-\psi\eta_1\cos\zeta)\cos^2\beta\right] \end{aligned} \tag{4.115}$$

$$\begin{aligned} L_{12} &= \frac{E_u}{2(1-\nu^2)}\left[(1+\nu)\cos\beta\sin\beta\right] - D_\kappa\bar{\sigma}\eta_2\cos\zeta\cos\beta\sin\beta = \\ &= \frac{E_u}{2(1-\nu^2)}(1+\nu)(1-\psi\eta_2\cos\zeta)\cos\beta\sin\beta \end{aligned} \tag{4.116}$$

$$\begin{aligned} L_{21} &= \frac{E_u}{2(1-\nu^2)}\left[(1+\nu)\cos\beta\sin\beta\right] - D_\kappa\bar{\sigma}\eta_1\sin\zeta\cos\beta\sin\beta = \\ &= \frac{E_u}{2(1-\nu^2)}(1+\nu)(1-\psi\eta_1\sin\zeta)\cos\beta\sin\beta \end{aligned} \tag{4.117}$$

$$\begin{aligned} L_{22} &= \frac{E_u}{2(1-\nu^2)}\left[2\sin^2\beta + (1-\nu)\cos^2\beta\right] - D_\kappa\bar{\sigma}\eta_2\sin\zeta\sin^2\beta = \\ &= \frac{E_u}{2(1-\nu^2)}\left[2-(1+\nu)\psi\eta_2\sin\zeta-(1+\nu)(1-\psi\eta_2\sin\zeta)\cos^2\beta\right] \end{aligned} \tag{4.118}$$

where $E_u = (1-D)E$ is the damaged elastic modulus and

$$\psi = \frac{2(1-\nu)D_\kappa\bar{\sigma}}{E_u} \tag{4.119}$$

a dimensionless parameter.

4.4.2 Flutter instability in pure modes

The simplifications done in the previous Section lead to write the flutter instability condition (4.88) as a second-order inequality that has to be solved with respect to the band normal inclination α

$$\Delta = f\left(\nu, E, \bar{\sigma}, \varepsilon_0, \varepsilon_f, \zeta, \alpha\right) < 0. \tag{4.120}$$

When analyzing potential flutter instability for a certain type of stress and for assigned constitutive parameters $E, \nu, \varepsilon_0, \varepsilon_f$, it is useful to fix the stress angle ζ and increase the magnitude of the effective stress, $\bar{\sigma}$, which plays the role of a load parameter.

Then, for each fixed ζ, the resulting expression for the discriminant can be minimized with respect to α in order to check whether the minimum can be negative. In this case, indeed, the discriminant depends only on this angle, since other parameters are fixed, so condition $\Delta = f\left(\alpha\right) < 0$ has to be checked.

Analysis are performed by considering the constitutive parameters reported in Table 4.3. Results will be reported for three particular stress conditions: $\zeta = 0°$ (uniaxial tension), $\zeta = -45°$ (shear) and $\zeta = -90°$ (uniaxial compression), in plane stress conditions.

Table 4.3: Constitutive parameters adopted for flutter instability analysis in pure modes and for different $\bar{\sigma}$ values.

$E\ [MPa]$	ν	ε_0	$\frac{\varepsilon_f}{\varepsilon_0}$
100	0.15	0.9	100

Since ζ is a fixed parameter, it is useful to rewrite the principal strain values for each given $\bar{\sigma}$, as follows:

$$\varepsilon_1 = \frac{1}{E}(\bar{\sigma}_1 - \nu\bar{\sigma}_2) = \frac{\bar{\sigma}}{E}(\cos\zeta - \nu\sin\zeta) \tag{4.121}$$

$$\varepsilon_2 = \frac{1}{E}(\bar{\sigma}_2 - \nu\bar{\sigma}_1) = \frac{\bar{\sigma}}{E}(\sin\zeta - \nu\cos\zeta) \tag{4.122}$$

$$\varepsilon_3 = \nu\frac{\bar{\sigma}}{E}(-\cos\zeta - \sin\zeta). \tag{4.123}$$

The equivalent strain can be calculated by relation (4.105) and its derivatives with (4.106)-(4.107). The acoustic tensor components are evaluated using (4.115)-(4.118) in order to plot $\Delta = (L_{11} - L_{22})^2 + 4L_{12}L_{21}$.

Figure 4.16 reports the discriminant value with respect to α for each different stress angle ζ and for different values of $\bar{\sigma} = a \cdot 400MPa$, being a a multiplier. As it is possible to notice, in none of these cases the discriminant becomes negative: therefore, for such parameters, it results impossible to have flutter instability.

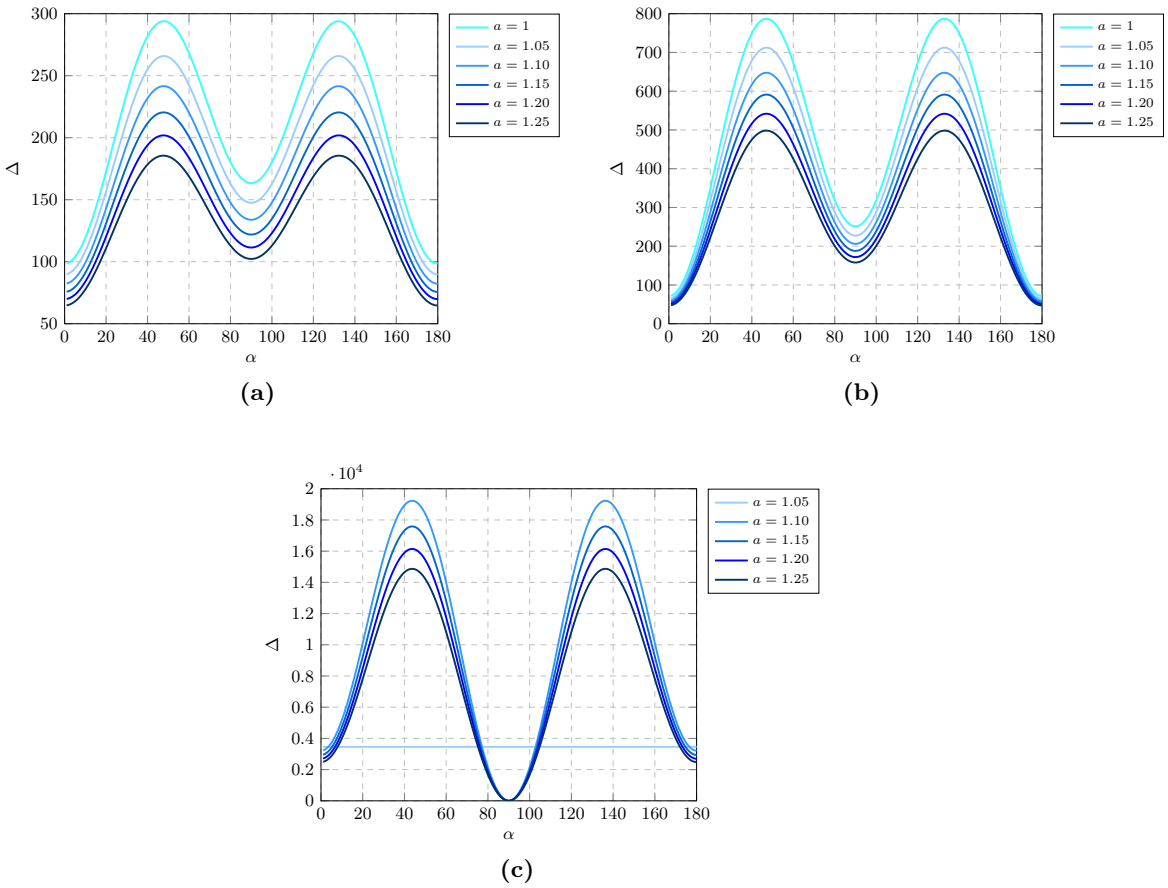

Figure 4.16: Discriminant of the acoustic tensor $\Delta = 0$ considering varying values of $\bar{\sigma} = a \cdot 400MPa$ for different cases: (a) $\zeta = 0°$, (b) $\zeta = -45°$, (c) $\zeta = -90°$.

The same analysis could be done by considering a different equivalent strain definition. The simplest one is the *Rankine-type* definition, which deals with the criterion of maximum principal stress, as expressed in (4.33). The derivative

of the equivalent strain with respect to strain components (considering that $\bar{\sigma}_3 = 0$ for the in-plane stress condition) can be calculated as

$$\frac{\partial \tilde{\varepsilon}}{\partial \varepsilon_i} = \sum_{j=1}^{2} \frac{\partial \tilde{\varepsilon}}{\partial \bar{\sigma}_j} \cdot \frac{\partial \bar{\sigma}_j}{\partial \varepsilon_i} \qquad \text{i=1,2,} \tag{4.124}$$

so, remembering expressions (4.102)-(4.103) for the effective stresses, it follows that:

$$\eta_1 = \frac{\partial \tilde{\varepsilon}}{\partial \varepsilon_1} = \frac{\partial \tilde{\varepsilon}}{\partial \bar{\sigma}_1} \cdot \frac{\partial \bar{\sigma}_1}{\partial \varepsilon_1} + \frac{\partial \tilde{\varepsilon}}{\partial \bar{\sigma}_2} \cdot \frac{\partial \bar{\sigma}_2}{\partial \varepsilon_1} = \frac{1}{E} \cdot \frac{E}{1-\nu^2} + 0 = \frac{1}{1-\nu^2} \tag{4.125}$$

$$\eta_2 = \frac{\partial \tilde{\varepsilon}}{\partial \varepsilon_2} = \frac{\partial \tilde{\varepsilon}}{\partial \bar{\sigma}_1} \cdot \frac{\partial \bar{\sigma}_1}{\partial \varepsilon_2} + \frac{\partial \tilde{\varepsilon}}{\partial \bar{\sigma}_2} \cdot \frac{\partial \bar{\sigma}_2}{\partial \varepsilon_2} = \frac{1}{E} \cdot \frac{E\nu}{1-\nu^2} + 0 = \frac{\nu}{1-\nu^2} \tag{4.126}$$

Table 4.4: Constitutive parameters adopted for flutter instability analysis in pure modes and for different ν values.

$E\ [MPa]$	$\bar{\sigma}\ [MPa]$	ε_0	$\frac{\varepsilon_f}{\varepsilon_0}$
100	500	0.9	100

The analysis are repeated considering the parameters reported in Table 4.4, fixing this time $\bar{\sigma}$ and plotting results for different values of the Poisson ratio $\nu = a \cdot 0.1$. For seek of comparison, the equivalent strain is evaluated considering Mazars Definition (blue plots on the left of Figures 4.17-4.18-4.19, indicated as MD) and Rankine Definition (red plots on the right of Figures 4.17-4.18-4.19, indicated as RD).

As can be observed, the introduction of a different formulation of the equivalent strain still does not make it possible to find an α range for which results $\Delta < 0$.

4.4.3 Dimensionless formulation

Being interested only in the sign of the discriminant, it is sufficient to evaluate the dimensionless discriminant by inserting the parameter given in (4.119) and evaluating $\tilde{\Delta}$ as follows

$$\tilde{\Delta} = \frac{4(1-\nu)^2}{E_u^2}\Delta = \frac{4(1-\nu)^2}{E_u^2}\left[(L_{22}-L_{11})^2 + 4L_{12}L_{21}\right] =$$

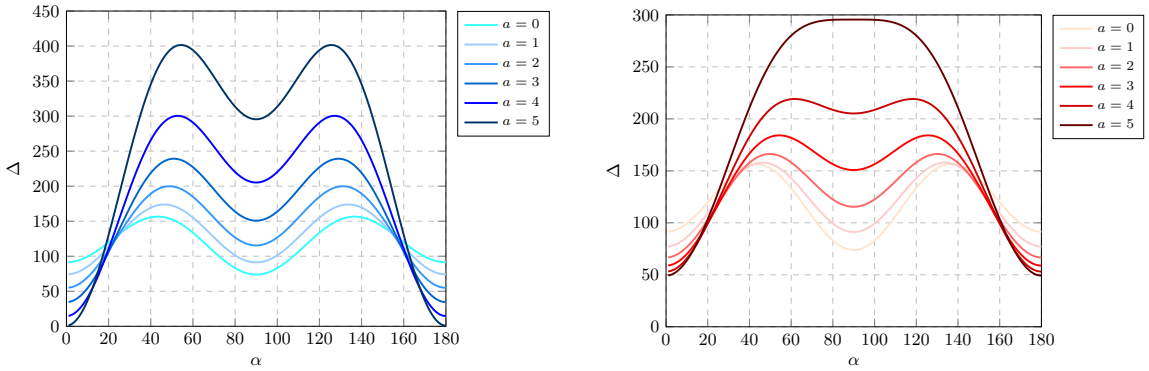

Figure 4.17: $\Delta = 0$ considering varying values of $\nu = a \cdot 0.1$ for $\zeta = 0°$: MD (left) and RD (right).

$$
\begin{aligned}
&= \frac{1}{(1+\nu)^2}\Big\{\big[(1+\nu)(1-\psi\eta_2\sin\zeta - 2\cos^2\beta + \psi\eta_2\sin\zeta\cos^2\beta + \psi\eta_1\cos\zeta\cos^2\beta)\big]^2 \\
&+ 4(1+\nu)^2(1-\psi\eta_2\cos\zeta)(1-\psi\eta_1\sin\zeta)\cos^2\beta\sin^2\beta\Big\} \\
&= \big[(1-\psi\eta_2\sin\zeta - (2-\psi\eta_2\sin\zeta - \psi\eta_1\cos\zeta)\cos^2\beta\big]^2 + \\
&\quad +4(1-\psi\eta_2\cos\zeta)(1-\psi\eta_1\sin\zeta)\cos^2\beta(1-\cos^2\beta). \qquad (4.127)
\end{aligned}
$$

This can be seen as a quadratic function of variable $N_1 \equiv \cos^2\beta$:

$$\tilde{\Delta} = AN_1^2 + BN_1 + C \qquad (4.128)$$

$$
\begin{aligned}
A &= (2-\psi\eta_2\sin\zeta - \psi\eta_1\cos\zeta)^2 - 4(1-\psi\eta_2\cos\zeta)(1-\psi\eta_1\sin\zeta) = \\
&= 4\psi(\eta_2-\eta_1)(\cos\zeta-\sin\zeta) + \psi^2(\eta_2\sin\zeta - \eta_1\cos\zeta)^2 \qquad (4.129)
\end{aligned}
$$

$$
\begin{aligned}
B &= -2(1-\psi\eta_2\sin\zeta)(2-\psi\eta_2\sin\zeta - \psi\eta_1\cos\zeta) + 4(1-\psi\eta_2\cos\zeta)(1-\psi\eta_1\sin\zeta) = \\
&= 2\psi(3\eta_2\sin\zeta - 2\eta_2\cos\zeta + \eta_1\cos\zeta - 2\eta_1\sin\zeta) + \\
&+ 2\psi^2\eta_2\sin\zeta(\eta_1\cos\zeta - \eta_2\sin\zeta) \qquad (4.130)
\end{aligned}
$$

$$C = (1-\psi\eta_2\sin\zeta)^2. \qquad (4.131)$$

Figures 4.20-4.21-4.22 show the profiles of $\tilde{\Delta}$ with respect to the inclination α of the band: also in this case, obviously, the dimensionless discriminant is non-negative for every inclination and for different values of the Poisson ratio, both using Rankine or Mazars models.

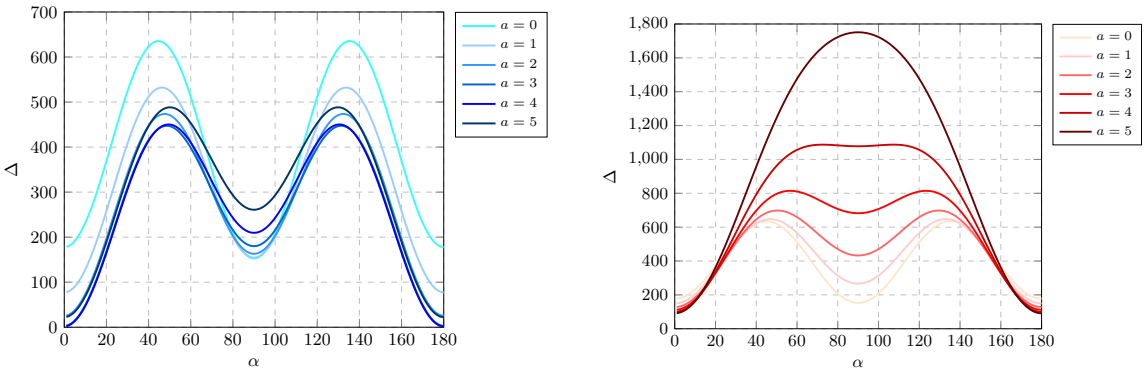

Figure 4.18: $\Delta = 0$ considering varying values of $\nu = a \cdot 0.1$ for $\zeta = -45°$: MD (left) and RD (right).

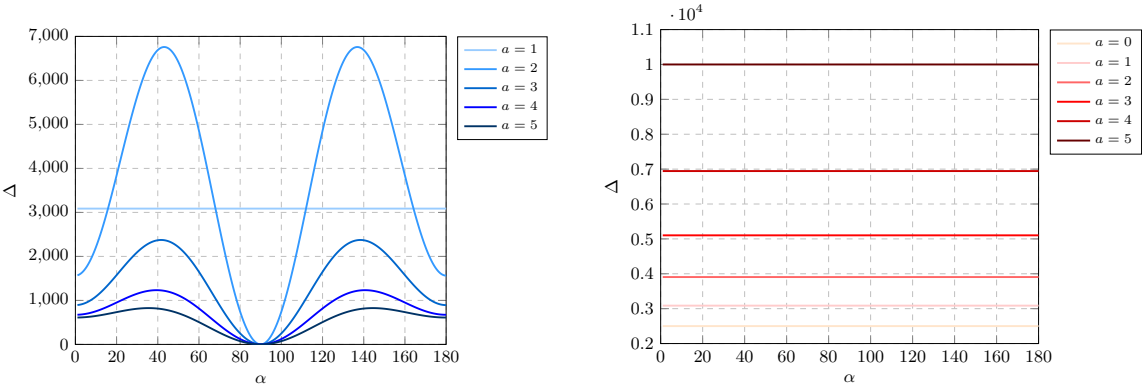

Figure 4.19: $\Delta = 0$ considering varying values of $\nu = a \cdot 0.1$ for $\zeta = -90°$: MD (left) and RD (right).

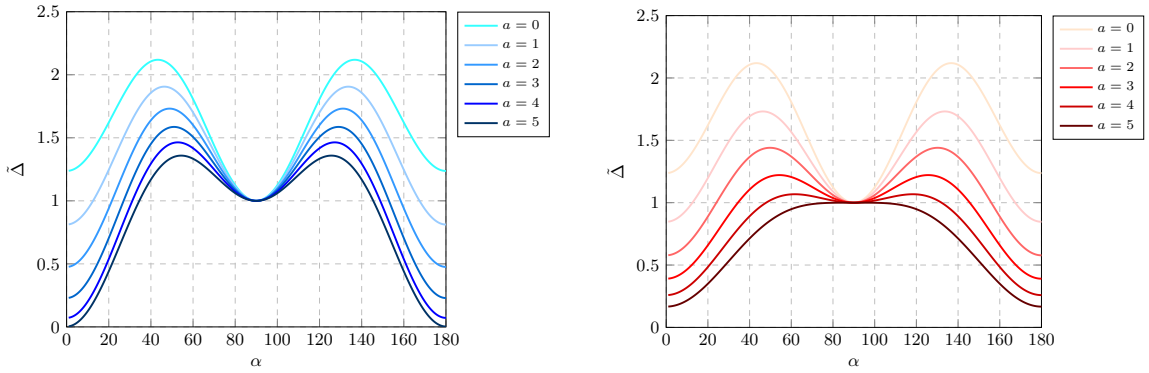

Figure 4.20: $\tilde{\Delta} = 0$ considering varying values of $\nu = a \cdot 0.1$ for $\zeta = 0°$: MD (left) and RD (right).

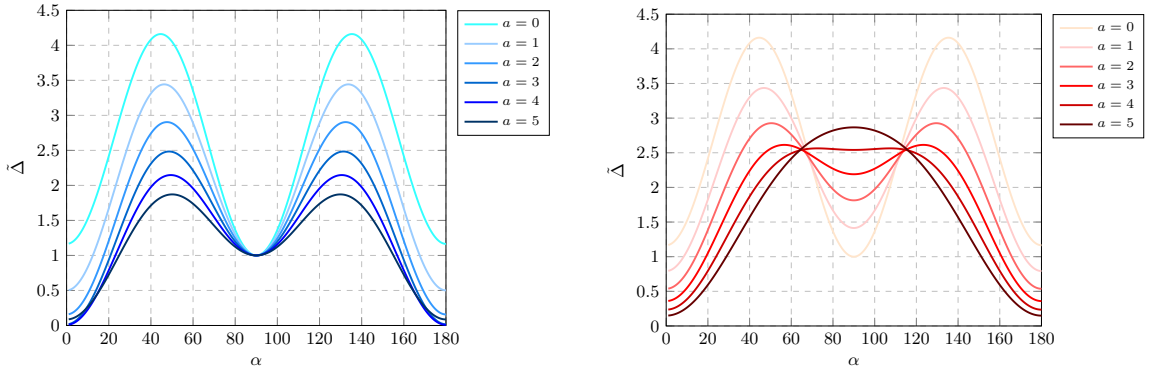

Figure 4.21: $\tilde{\Delta} = 0$ considering varying values of $\nu = a \cdot 0.1$ for $\zeta = -45°$: MD (left) and RD (right).

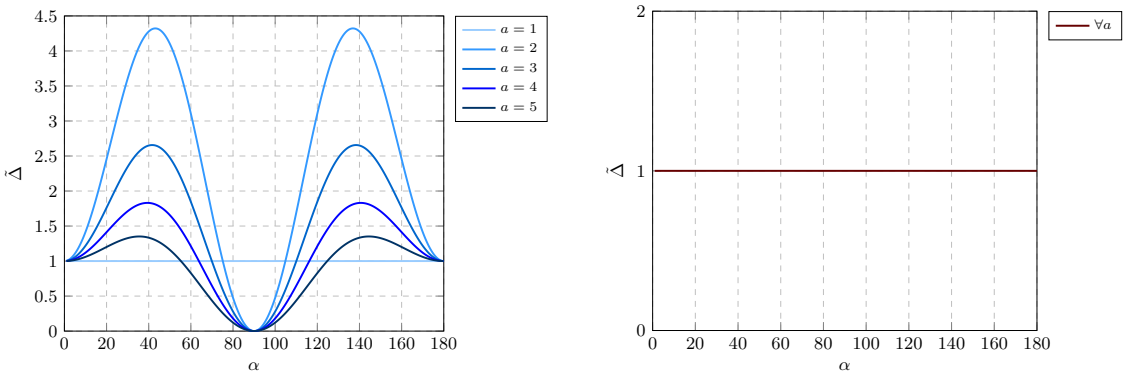

Figure 4.22: $\tilde{\Delta} = 0$ considering varying values of $\nu = a \cdot 0.1$ for $\zeta = -90°$: MD (left) and RD (right).

In order to satisfy flutter condition $\tilde{\Delta} < 0$ for some $0 < N_1 < 1$ value, the quadratic equation $\tilde{\Delta}(N_1) = 0$ must have at least one real root between 0 and 1. Its roots are real if the discriminant of this equation is positive, that is

$$
\begin{aligned}
M = B^2 - 4AC = \qquad & (4.132)\\
= \left[2\psi(3\eta_2 \sin\zeta - 2\eta_2 \cos\zeta + \eta_1 \cos\zeta - 2\eta_1 \sin\zeta) + 2\psi^2\eta_2 \sin\zeta(\eta_1 \cos\zeta - \eta_2 \sin\zeta)\right]^2 \\
- 4(1 - \psi\eta_2 \sin\zeta)^2 \left[4\psi(\eta_2 - \eta_1)(\cos\zeta - \sin\zeta) + \psi^2(\eta_2 \sin\zeta - \eta_1 \cos\zeta)^2\right] \\
= 4\psi^2 \left[\cos\zeta(\eta_1 - 2\eta_2 + \eta_1\eta_2\psi \sin\zeta) - \sin\zeta(2\eta_1 - 3\eta_2 + \eta_2^2\psi \sin\zeta)\right]^2 \\
- 4\psi(1 - \eta_2\psi \sin\zeta)^2 \left[-4(\eta_1 - \eta_2)(\cos\zeta - \sin\zeta) + \psi(\eta_1 \cos\zeta - \eta_2 \sin\zeta)^2\right] \geq 0.
\end{aligned}
$$

After some manipulation M can written as follows

$$M = 16(\eta_1 - \eta_2)\psi(1 - \eta_2\psi \cos\zeta)(\cos\zeta - \sin\zeta)(1 - \eta_1\psi \sin\zeta) \geq 0. \qquad (4.133)$$

With reference to parameters in Table 4.4, but with a $\bar{\sigma} = 100MPa$, Figures 4.23 report the variable M with respect to the stress angle ζ, considering different $\nu = a \cdot 0.1$ values, both for the Mazars model and for the Rankine one.

It is reasonable to assume that $\eta_1 \geq \eta_2$, since the major principal strain ε_1 should have a greater influence on the equivalent strain than ε_2. In our formulation, moreover, since $\bar{\sigma}_1 = \bar{\sigma}\cos\zeta$ and $\bar{\sigma}_2 = \bar{\sigma}\sin\zeta$ and considering that $\bar{\sigma}_1 > \bar{\sigma}_2$, it always results that $\cos\zeta \geq \sin\zeta$. So, considering that $\psi > 0$, the

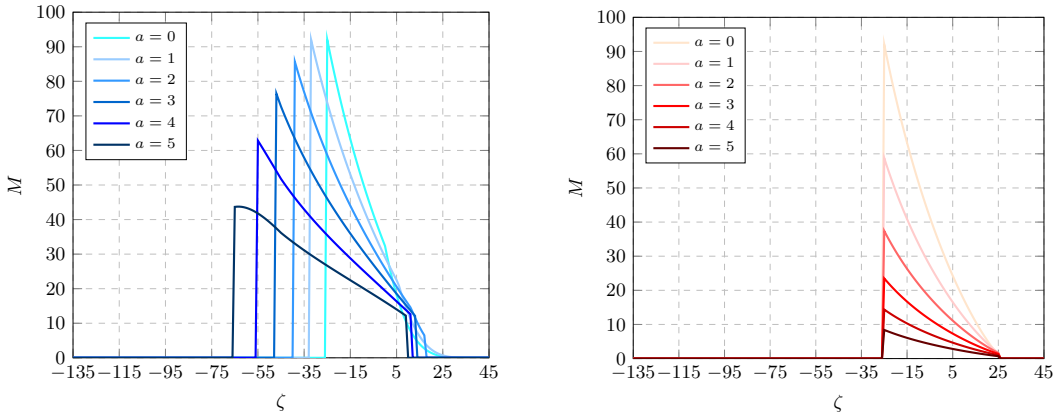

Figure 4.23: Representation of function $M = 0$ considering varying values of $\nu = a \cdot 0.1$ and different stress angles ζ: MD (left) and RD (right).

previous inequality (4.133) corresponds to the following two cases:

$$\begin{cases} 1 \geq \eta_2 \psi \cos\zeta \\ 1 \geq \eta_1 \psi \sin\zeta \end{cases} \quad \vee \begin{cases} 1 \leq \eta_2 \psi \cos\zeta \\ 1 \leq \eta_1 \psi \sin\zeta \end{cases} \tag{4.134}$$

The previous conditions guarantee that $\tilde{\Delta}$ becomes negative for some values of N_1, but not that these values are between 0 and 1. So, in addition to $M > 0$ the condition that at least one of the roots of the quadratic equation $\tilde{\Delta}(N_1) = 0$ is inside the interval $(0, 1)$ has to be set up.

This condition can be written as

$$0 < N_1^{\pm} = \frac{-B \pm \sqrt{M}}{2A} < 1. \tag{4.135}$$

It is known that $C \geq 0$, but A and B could have an arbitrary sign. So different cases have to be distinguished. For example the sign of A depends on the variable ψ: since $\eta_1 > \eta_2$ but $\cos\zeta > \sin\zeta$, A could be positive for large ψ and negative in other cases. Figures 4.24 and 4.25 report the trends of variables A, B and ψ with respect to the stress angle ζ, by considering different values for the Poisson's ratio $\nu = a \cdot 0.1$ and the Mazars definition for the equivalent strain. $\bar{\sigma} = 100MPa$ is set in Figure 4.24 and $\bar{\sigma} = 500MPa$ in Figure 4.25. Figures 4.26-4.27 report same trends, referring instead to the Rankine model. The constitutive parameters reported in Table 4.3 are used in both cases.

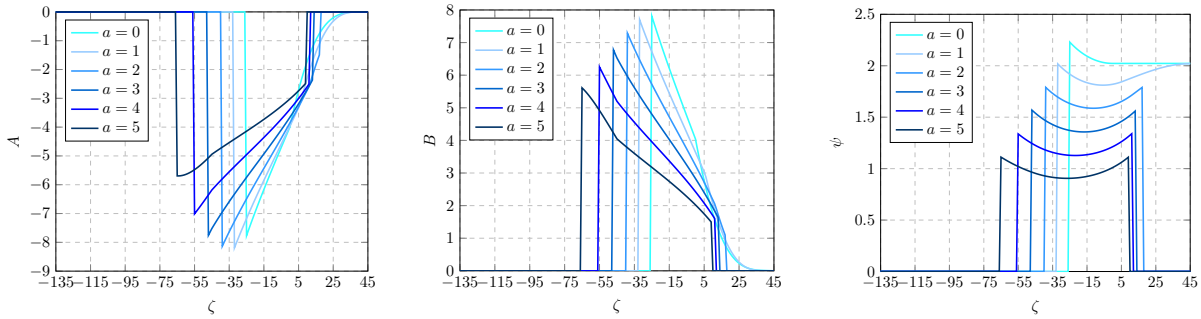

(a) (b) (c)

Figure 4.24: Analysis with $\bar{\sigma} = 100MPa$, $\nu = a \cdot 0.1$ and MD: (a) A, (b) B, (c) ψ.

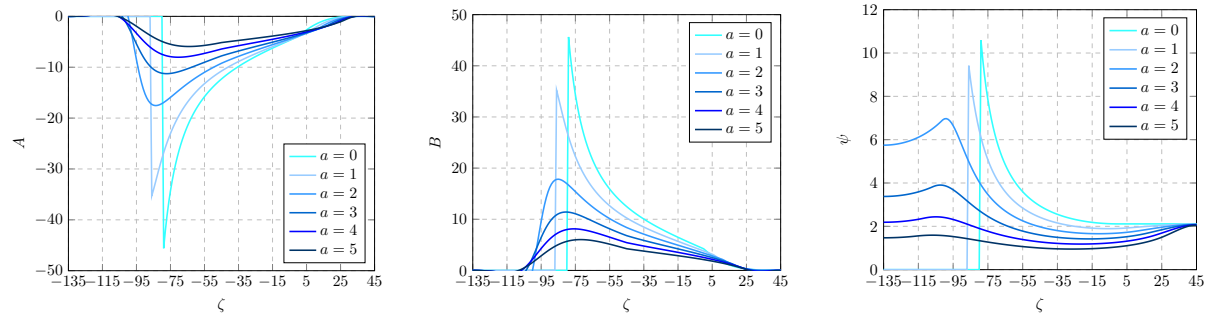

(a) (b) (c)

Figure 4.25: Analysis with $\bar{\sigma} = 500MPa$, $\nu = a \cdot 0.1$ and MD: (a) A, (b) B, (c) ψ.

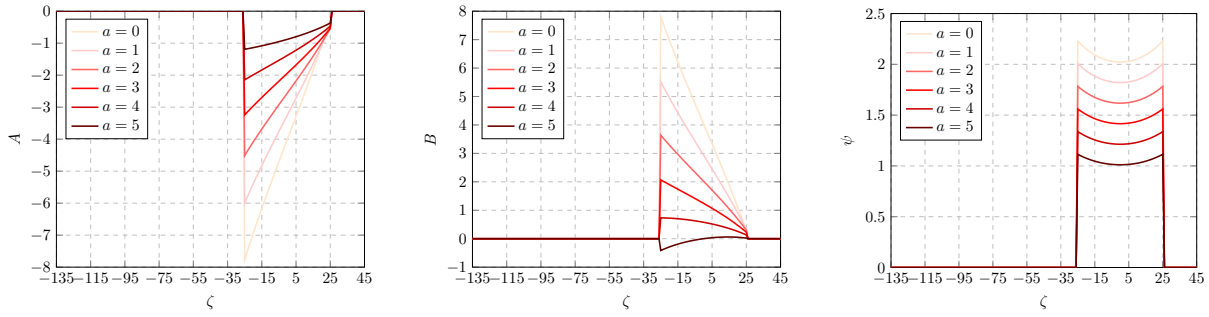

(a) (b) (c)

Figure 4.26: Analysis with $\bar{\sigma} = 100MPa$, $\nu = a \cdot 0.1$ and RD: (a) A, (b) B, (c) ψ.

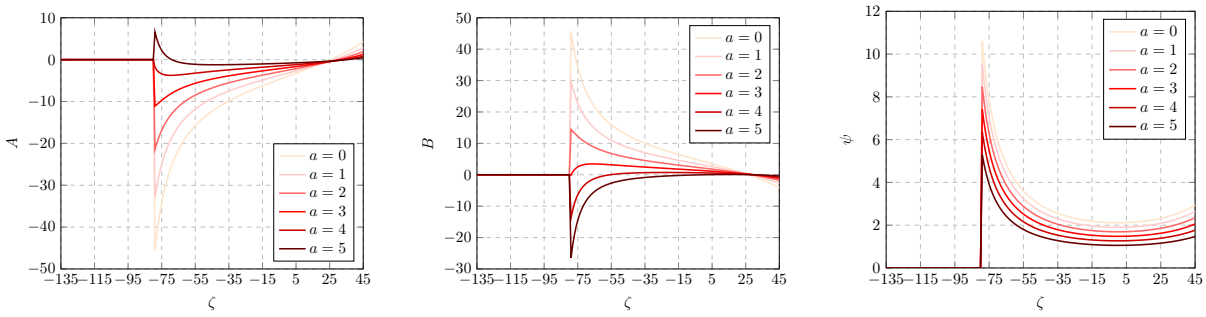

(a) **(b)** **(c)**

Figure 4.27: Analysis with $\bar{\sigma} = 500MPa$, $\nu = a \cdot 0.1$ and RD: (a) A, (b) B, (c) ψ.

4.4.3.1 Analysis of different terms of flutter existence inequality

Condition (4.135) can be rewritten as follows, assuming that $A > 0$:

$$B < \pm\sqrt{B^2 - 4AC} < 2A + B. \tag{4.136}$$

By considering terms under the square root, since $A > 0$ and $C \geq 0$, it follows that $\sqrt{B^2 - 4AC} \leq |B|$. Consequently, the *left inequality* can be satisfied only if $B < 0$, and in this case, it is satisfied for both signs. The *right inequality*, instead, depends on the sign of $2A + B$. If it is positive, the right inequality is automatically satisfied for the negative sign before the square root, while for the positive sign it is satisfied if

$$B^2 - 4AC < (2A + B)^2 \tag{4.137}$$

which leads to the condition $A + B + C > 0$, which is always satisfied for the case analyzed.

On the other hand, if the term $2A+B$ is negative, the right inequality could be satisfied only for the negative sign before the square root, but this would require $A + B + C < 0$, which is excluded. Concluding, for $M > 0$ and $A > 0$ flutter occurs if $B < 0$ and $2A + B > 0$.

Let us assume now that $A < 0$. Condition (4.135) becomes

$$2A + B < \pm\sqrt{B^2 - 4AC} < B. \tag{4.138}$$

In this case, considering the terms under the square root, it can be written that $\sqrt{B^2 - 4AC} > |B|$, and so the right inequality is satisfied only for the

negative sign before the square root. However, the left inequality, considering that it can be satisfied only for $2A + B < 0$, leads to $A(A + B + C) > 0$, which cannot be satisfied with $A < 0$ since $A + B + C > 0$. Concluding, when $M > 0$ and $A < 0$ flutter cannot occur.

Flutter existence conditions can be summarized as

$$\begin{cases} A > 0 \\ B < 0 \\ M = B^2 - 4AC > 0 \\ 2A + B > 0 \end{cases} \tag{4.139}$$

that can be satisfied simultaneously if

$$-2A < B < -2\sqrt{AC} \qquad \Rightarrow \qquad \underbrace{A}_{T_1} > \underbrace{-\frac{B}{2}}_{T_2} > \underbrace{\sqrt{AC}}_{T_3} \tag{4.140}$$

Considering terms in (4.129)-(4.130)-(4.131) and previous positions, relation (4.140) can be written as

$$\begin{aligned} T_1 &= \psi^2(\eta_2 \sin\zeta - \eta_1 \cos\zeta)^2 - 4\psi(\eta_1 - \eta_2)(\cos\zeta - \sin\zeta) > \\ T_2 &= -\psi(3\eta_2 \sin\zeta - 2\eta_2 \cos\zeta + \eta_1 \cos\zeta - 2\eta_1 \sin\zeta) - \psi^2 \eta_2 \sin\zeta(\eta_1 \cos\zeta - \eta_2 \sin\zeta) > \\ T_3 &= |1 - \psi\eta_2 \sin\zeta| \sqrt{\psi^2(\eta_2 \sin\zeta - \eta_1 \cos\zeta)^2 - 4\psi(\eta_1 - \eta_2)(\cos\zeta - \sin\zeta)}. \end{aligned} \tag{4.141}$$

Left inequality becomes

$$T_1 - T_2 = \psi^2 \eta_1 \cos\zeta(\eta_1 \cos\zeta - \eta_2 \sin\zeta) + \psi(2\eta_1 \sin\zeta - 3\eta_1 \cos\zeta + 2\eta_2 \cos\zeta - \eta_2 \sin\zeta) > 0. \tag{4.142}$$

Considering the cases in which $\eta_1 \cos\zeta > 0$ and $\eta_1 \cos\zeta > \eta_2 \sin\zeta$, the previous condition will always be satisfied for sufficiently large ψ.
This can be proven considering, for example, $\bar{\sigma} = 100MPa$ or $\bar{\sigma} = 500MPa$: only in the second case inequality (4.142) is positive for a small range, both considering the Mazars definition (Figure 4.28) or the Rankine one (Figure 4.29). The same can be done for the right inequality term $T_2 - T_3$, reported in Figure 4.30 for the MD and in Figure 4.31 for the RD.

A quick example can be reported considering the simplest case: the Rankine model applied with $\nu = 0$. Considering expressions (4.125)-(4.126), it follows that $\eta_1 = 1$ and $\eta_2 = 0$ so the terms in (4.129)-(4.130)-(4.131) become

$$A = 4\psi(\sin\zeta - \cos\zeta) + \psi^2 \cos^2\zeta; \quad B = 2\psi(\cos\zeta - 2\sin\zeta); \quad C = 1. \tag{4.143}$$

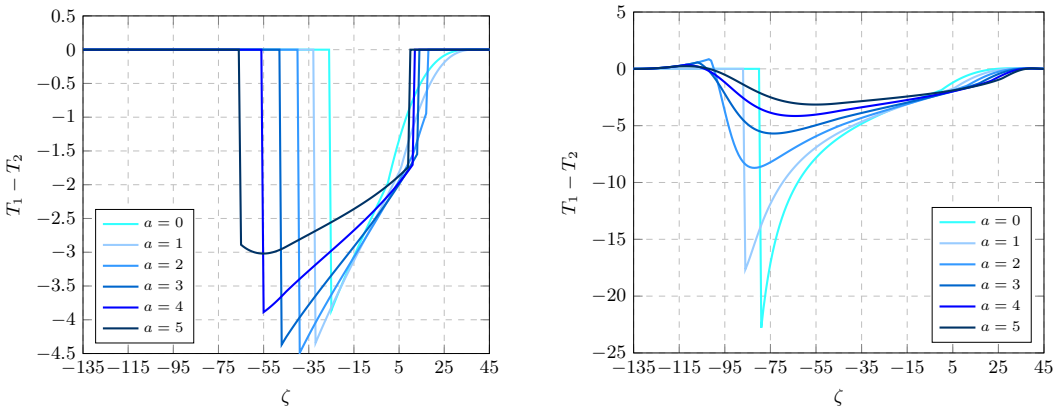

(a) **(b)**

Figure 4.28: Analysis on the sign of the first inequality $T_1 - T_2$ with $\nu = a \cdot 0.1$ and MD : (a) $\bar{\sigma} = 100MPa$, (b) $\bar{\sigma} = 500MPa$.

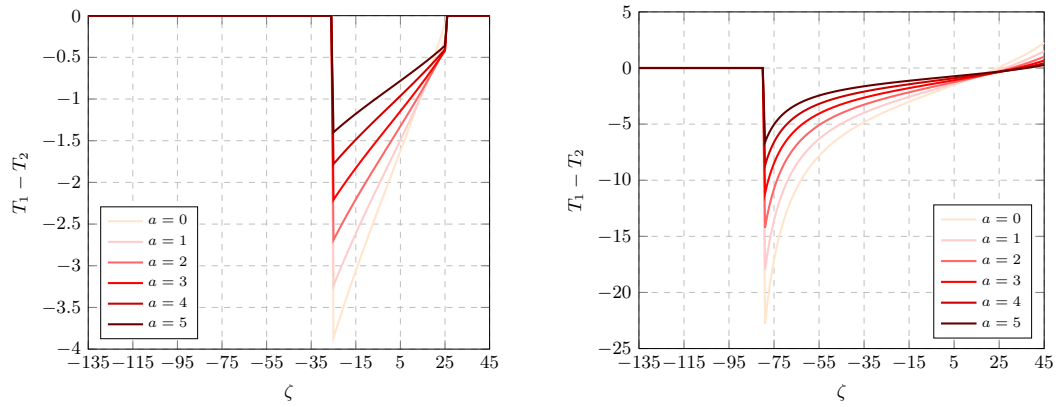

(a) **(b)**

Figure 4.29: Analysis on the sign of the first inequality $T_1 - T_2$ with $\nu = a \cdot 0.1$ and RD : (a) $\bar{\sigma} = 100MPa$, (b) $\bar{\sigma} = 500MPa$.

With these simplifications, the inequalities (4.140) can be written as

$$\begin{cases} \psi > \frac{3\cos\zeta - 2\sin\zeta}{\cos^2\zeta} \\ \psi(2\sin\zeta - \cos\zeta) > \sqrt{\psi^2\cos^2\zeta - 4\psi(\cos\zeta - \sin\zeta)}. \end{cases} \tag{4.144}$$

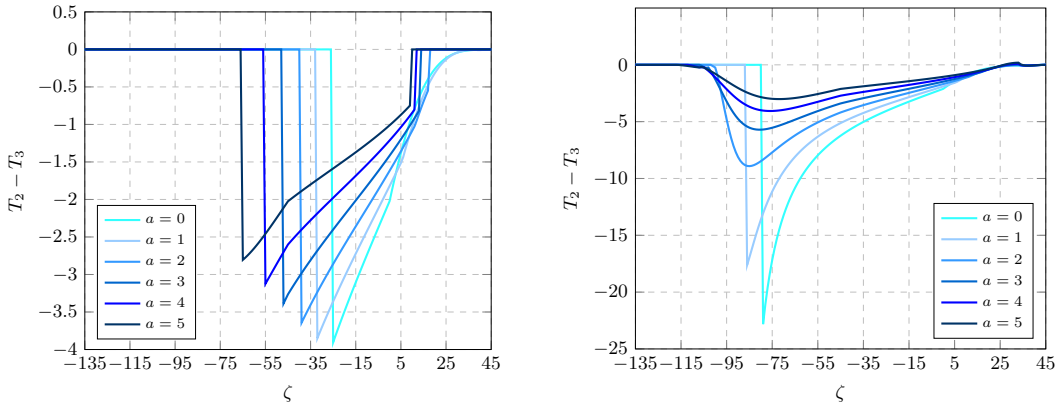

(a) **(b)**

Figure 4.30: Analysis on the sign of the second inequality $T_2 - T_3$ with $\nu = a \cdot 0.1$ and MD : (a) $\bar{\sigma} = 100MPa$, (b) $\bar{\sigma} = 500MPa$.

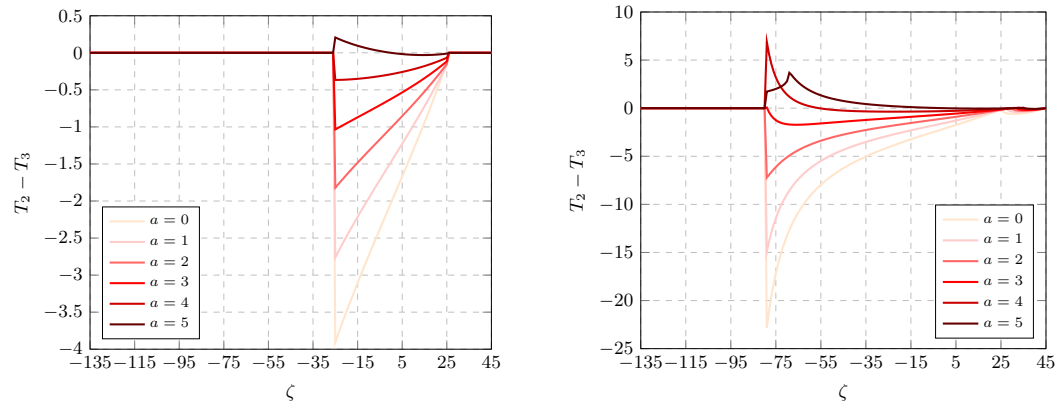

(a) **(b)**

Figure 4.31: Analysis on the sign of the second inequality $T_2 - T_3$ with $\nu = a \cdot 0.1$ and RD : (a) $\bar{\sigma} = 100MPa$, (b) $\bar{\sigma} = 500MPa$.

In order to simplify the second previous expression by eliminating the square root, a positive left-hand term has to be considered, which corresponds to impose $2\sin\zeta > \cos\zeta$. In this case, it is obtained that

$$\begin{cases} \psi > \frac{3\cos\zeta - 2\sin\zeta}{\cos^2\zeta} \\ 4(1-\psi\sin\zeta)(\cos\zeta - \sin\zeta) > 0 \\ 2\sin\zeta > \cos\zeta \end{cases} \tag{4.145}$$

which leads to

$$\begin{cases} \frac{3\cos\zeta - 2\sin\zeta}{\cos^2\zeta} < \psi < \frac{1}{\sin\zeta} \\ \zeta > \arctan\frac{1}{2}. \end{cases} \tag{4.146}$$

The angles range $\zeta > \arctan\frac{1}{2} \approx 26.57°$ represents a case close to the biaxial tension. Figure 4.32 reports the three different inequality terms of (4.146), both considering $\bar{\sigma} = 100MPa$ or $\bar{\sigma} = 500MPa$: the first term is smaller than the second one only for $\zeta < \arctan\frac{1}{2}$. So it can be concluded that flutter could not occur considering the Rankine model and $\nu = 0$.

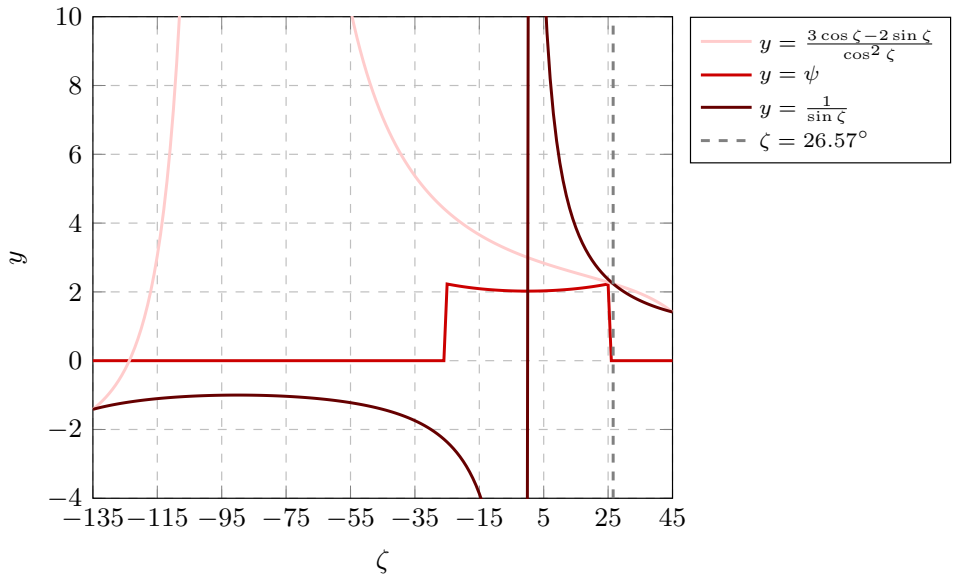

(a)

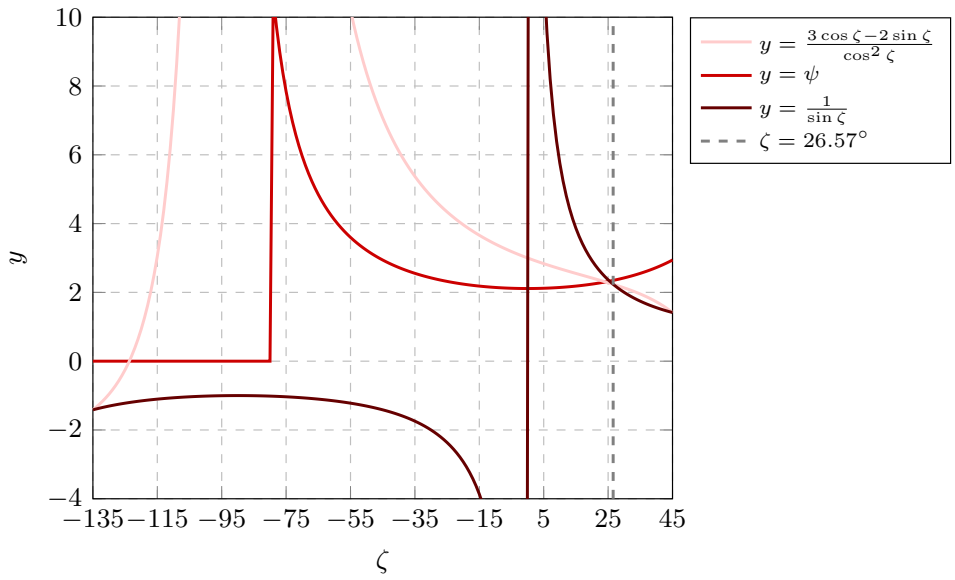

(b)

Figure 4.32: Representation of terms of inequality (4.146) with $\nu = 0$ and RD: (a) $\bar{\sigma} = 100MPa$, (b) $\bar{\sigma} = 500MPa$.

4.4.3.2 Application to the Rankine model with general Poisson ratio

Let us consider the equivalent strain expression in the Rankine model with a general value of Poisson ratio. So, considering expressions (4.125)-(4.126), inequality (4.142) reads

$$\frac{\psi}{1-\nu^2}\cos\zeta(\cos\zeta-\nu\sin\zeta)+(2-\nu)\sin\zeta-(3-2\nu)\cos\zeta>0 \tag{4.147}$$

from which

$$\frac{\psi}{1-\nu^2}>\frac{(3-2\nu)\cos\zeta-(2-\nu)\sin\zeta}{\cos\zeta(\cos\zeta-\nu\sin\zeta)} \tag{4.148}$$

while the second inequality $T_2-T_3>0$ can be written as

$$\begin{aligned}&\frac{\psi}{1-\nu^2}[(2-3\nu)\sin\zeta-(1-2\nu)\cos\zeta]-\left(\frac{\psi}{1-\nu^2}\right)^2\nu\sin\zeta(\cos\zeta-\nu\sin\zeta)>\\ >&\left|1-\frac{\psi}{1-\nu^2}\nu\sin\zeta\right|\sqrt{\left(\frac{\psi}{1-\nu^2}\right)^2(\nu\sin\zeta-\cos\zeta)^2-4\frac{\psi}{1-\nu^2}(1-\nu)(\cos\zeta-\sin\zeta)}.\end{aligned} \tag{4.149}$$

Defining the variable $\tilde{\psi}=\psi/(1-\nu^2)$, the previous conditions can be written as

$$\tilde{\psi}>\frac{(3-2\nu)\cos\zeta-(2-\nu)\sin\zeta}{\cos\zeta(\cos\zeta-\nu\sin\zeta)} \tag{4.150}$$

and

$$\begin{aligned}&\tilde{\psi}[(2-3\nu)\sin\zeta-(1-2\nu)\cos\zeta]-\tilde{\psi}^2\nu\sin\zeta(\cos\zeta-\nu\sin\zeta)>\\ >&\left|1-\tilde{\psi}\nu\sin\zeta\right|\sqrt{\tilde{\psi}^2(\nu\sin\zeta-\cos\zeta)^2-4\tilde{\psi}(1-\nu)(\cos\zeta-\sin\zeta)}.\end{aligned} \tag{4.151}$$

Since the second expression is too difficult to analyze, the conditions of the system (4.139) have to be considered. The second inequality can be rewritten considering $M>0$ and $B<0$. Since $\eta_1>\eta_2$ and $\cos\zeta>\sin\zeta$, and of course also $\psi>0$, these two conditions can be written as

$$\begin{cases}(1-\eta_2\psi\cos\zeta)(1-\eta_1\psi\sin\zeta)>0\\ 3\eta_2\sin\zeta-2\eta_2\cos\zeta+\eta_1\cos\zeta-2\eta_1\sin\zeta+\psi\eta_2\sin\zeta(\eta_1\cos\zeta-\eta_2\sin\zeta)<0\end{cases} \tag{4.152}$$

or considering the variable $\tilde{\psi}$ and expressions (4.125)-(4.126):

$$\begin{cases} (1-\nu\tilde{\psi}\cos\zeta)(1-\tilde{\psi}\sin\zeta) > 0 \\ 3\nu\sin\zeta - 2\nu\cos\zeta + \cos\zeta - 2\sin\zeta + \tilde{\psi}\nu\sin\zeta(\cos\zeta - \nu\sin\zeta) < 0. \end{cases} \tag{4.153}$$

Since $\cos\zeta - \nu\sin\zeta > 0$, depending on the sign of the stress angle ζ, the second inequality corresponds to two cases

$$\tilde{\psi} < \frac{(2-3\nu)\sin\zeta - (1-2\nu)\cos\zeta}{\nu\sin\zeta(\cos\zeta - \nu\sin\zeta)} \qquad \text{if } \zeta > 0 \tag{4.154}$$

$$\tilde{\psi} > \frac{(2-3\nu)\sin\zeta - (1-2\nu)\cos\zeta}{\nu\sin\zeta(\cos\zeta - \nu\sin\zeta)} \qquad \text{if } \zeta < 0. \tag{4.155}$$

In summary, to get flutter, it is looked for $\tilde{\psi}$ that satisfies simultaneously conditions (4.150), first one in (4.153) and (4.154) or (4.155). Two main cases arise:

$$\text{CASE 1}: \begin{cases} \tilde{\psi} > \dfrac{(3-2\nu)\cos\zeta - (2-\nu)\sin\zeta}{\cos\zeta(\cos\zeta - \nu\sin\zeta)} \\ (1-\nu\tilde{\psi}\cos\zeta)(1-\tilde{\psi}\sin\zeta) > 0 \\ \tilde{\psi} > \dfrac{(2-3\nu)\sin\zeta - (1-2\nu)\cos\zeta}{\nu\sin\zeta(\cos\zeta - \nu\sin\zeta)} \\ \zeta < 0 \end{cases} \tag{4.156}$$

$$\text{CASE 2}: \begin{cases} \tilde{\psi} > \dfrac{(3-2\nu)\cos\zeta - (2-\nu)\sin\zeta}{\cos\zeta(\cos\zeta - \nu\sin\zeta)} \\ (1-\nu\tilde{\psi}\cos\zeta)(1-\tilde{\psi}\sin\zeta) > 0 \\ \tilde{\psi} < \dfrac{(2-3\nu)\sin\zeta - (1-2\nu)\cos\zeta}{\nu\sin\zeta(\cos\zeta - \nu\sin\zeta)} \\ \zeta > 0. \end{cases} \tag{4.157}$$

CASE 1: $\zeta < 0$

Only the range $-90° < \zeta < 0°$ is considered since biaxial compression is excluded because a state in which damage propagates (for the Rankine criterion) cannot never be got. Under this condition it results that $\cos\zeta > 0$ and $\sin\zeta < 0$. The second inequality in (4.156) is rewritten as

$$\tilde{\psi}^2(\nu\sin\zeta\cos\zeta) + \tilde{\psi}(-\sin\zeta - \nu\cos\zeta) + 1 > 0 \tag{4.158}$$

which leads to the following simplified version of (4.156):

$$\text{CASE 1}: \begin{cases} \tilde{\psi} > f_1 = \dfrac{(3-2\nu)\cos\zeta - (2-\nu)\sin\zeta}{\cos\zeta(\cos\zeta - \nu\sin\zeta)} \\ \tilde{\psi} > f_2 = \dfrac{(2-3\nu)\sin\zeta - (1-2\nu)\cos\zeta}{\nu\sin\zeta(\cos\zeta - \nu\sin\zeta)} \\ \tilde{\psi} < f_3 = \dfrac{1}{\nu\cos\zeta}. \end{cases} \tag{4.159}$$

CASE 2: $\zeta > 0$

In this case, that represents a stress state close to biaxial tension, it results $\cos\zeta > 0$ and $\sin\zeta > 0$. It follows

$$\text{CASE 2.1}: \begin{cases} \dfrac{(3-2\nu)\cos\zeta - (2-\nu)\sin\zeta}{\cos\zeta(\cos\zeta - \nu\sin\zeta)} < \tilde{\psi} < \dfrac{(2-3\nu)\sin\zeta - (1-2\nu)\cos\zeta}{\nu\sin\zeta(\cos\zeta - \nu\sin\zeta)} \\ \tilde{\psi} < f_4 = \min\left(\dfrac{1}{\nu\cos\zeta}, \dfrac{1}{\sin\zeta}\right) \end{cases} \tag{4.160}$$

$$\text{CASE 2.2}: \begin{cases} \dfrac{(3-2\nu)\cos\zeta - (2-\nu)\sin\zeta}{\cos\zeta(\cos\zeta - \nu\sin\zeta)} < \tilde{\psi} < \dfrac{(2-3\nu)\sin\zeta - (1-2\nu)\cos\zeta}{\nu\sin\zeta(\cos\zeta - \nu\sin\zeta)} \\ \tilde{\psi} > f_5 = \max\left(\dfrac{1}{\nu\cos\zeta}, \dfrac{1}{\sin\zeta}\right). \end{cases} \tag{4.161}$$

Figure 4.33 represents inequalities terms of CASE 1 (4.159) considering two extreme cases with $\nu = 0.1$ and $\nu = 0.5$, respectively. Constitutive parameters are reported in Table 4.4. It is clear that $\tilde{\psi}$ is never above f_1 in both cases.

Similarly, Figure 4.34 represents inequalities terms of CASE 2.1 (4.160) as well as Figure 4.35 represents inequalities terms of CASE 2.2 (4.161), considering $\nu = 0.1$ and $\nu = 0.5$, respectively. They confirm that there is no range where all the conditions are contemporary respected.

These results confirm that there is no range of ζ for any nonzero value of Poisson ratio where the conditions on $\tilde{\psi}$ are respected. It is possible to mathematically confirm that the flutter instability cannot occur in all the analyzed cases. Finally, it can be concluded that no flutter instability can appear with the Rankine model for any $0 \leq \nu \leq 0.5$.

In conclusion, for the given class of damage models (isotropic damage with one scalar damage variable driven by equivalent strain), flutter cannot occur. The convexity of the elastic domain implies that $\eta_1 \geq \eta_2 \geq \eta_3$. In 2D, the

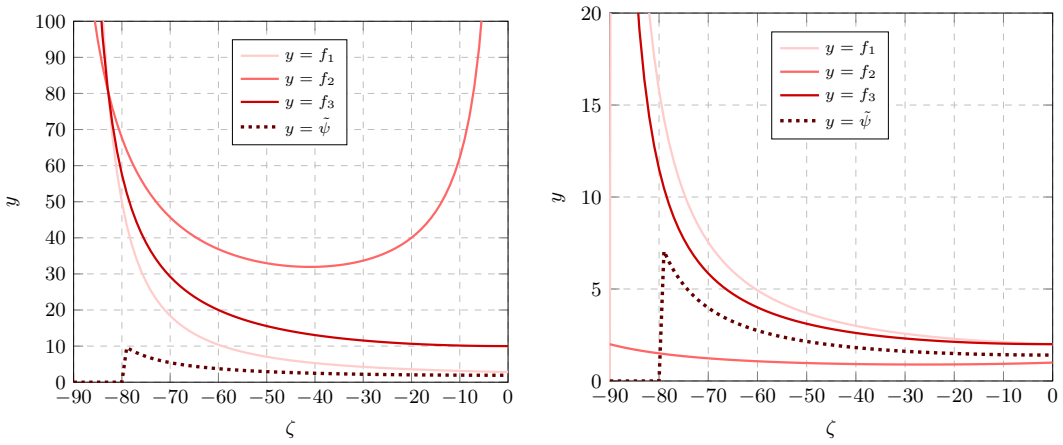

Figure 4.33: Terms of inequalities in CASE 1 (4.159): (a) $\nu = 0.1$, (b) $\nu = 0.5$.

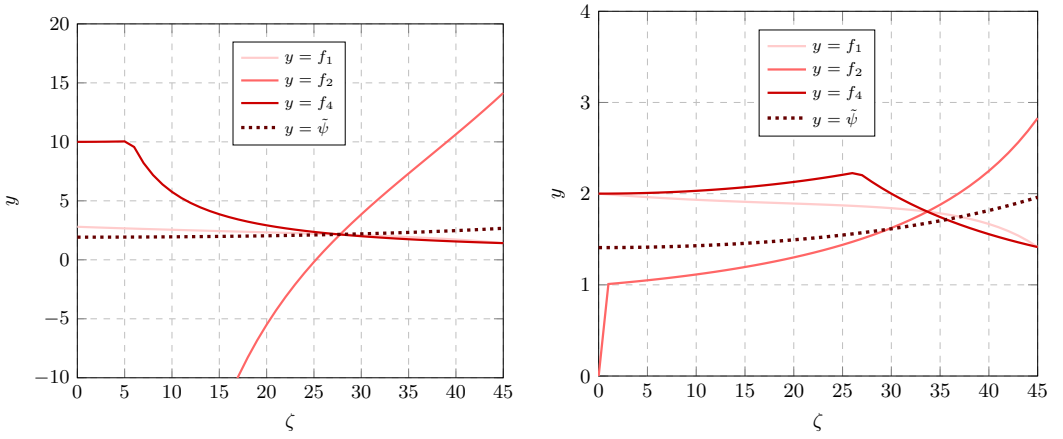

Figure 4.34: Terms of inequalities in CASE 2.1 (4.160): (a) $\nu = 0.1$, (b) $\nu = 0.5$.

analogous statement that $\eta_1 \geq \eta_2$ whenever $\bar{\sigma}_1 \geq \bar{\sigma}_2$ indeed follows from convexity based on the graphical representation in the principal strain plane, since the tensors $\boldsymbol{\sigma}$ and $\boldsymbol{\eta}$ have the same principal directions and the principal values are arranged in the same way. For isotropic models, condition $\bar{\sigma}_1 \geq \bar{\sigma}_2$

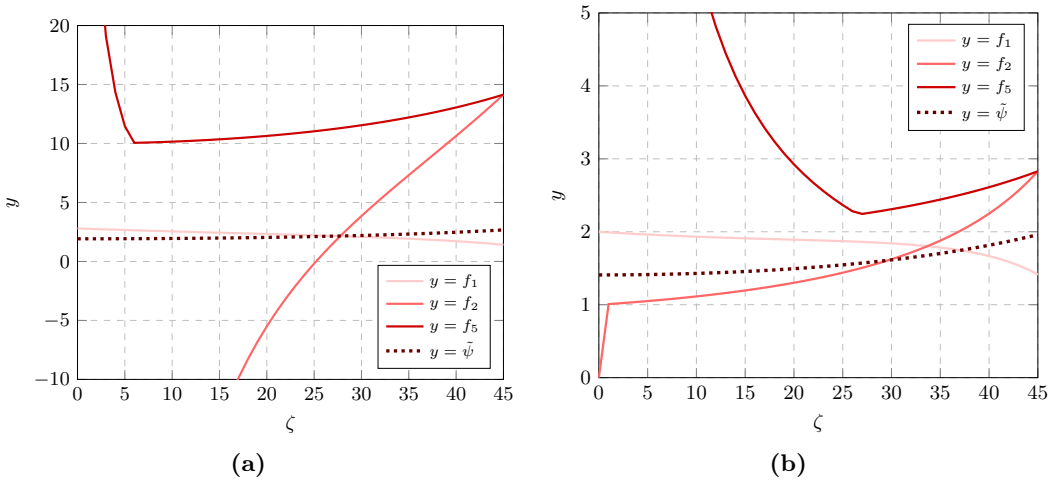

(a) **(b)**

Figure 4.35: Terms of inequalities in CASE 2.2 (4.161): (a) $\nu = 0.1$, (b) $\nu = 0.5$.

is equivalent to $\varepsilon_1 \geq \varepsilon_2$. If the elastic domain in the principal strain plane is convex, the normal to its boundary (i.e., the vector with components η_1 and η_2) is characterized by an angle (measured from the ε_1 axis) that must monotonically increase from $-135°$ to $45°$ by travelling along the boundary from the point corresponding to biaxial compression to the point corresponding to biaxial tension, and in this range it results that $\eta_1 \geq \eta_2$.

Probably, our initial assumption on which the formulation is based is incorrect: the only way to satisfy the flutter condition in 2D would be to use a model for which $\eta_2 > \eta_1$, i.e., the equivalent strain that drives damage would depend more strongly on the minor principal strain than on the major one.

In order to show possible flutter instabilities, it is convenient to look at an anisotropic model, such as Desmorat's model [34], with an initially elastic material with damage described by a tensor. Anisotropy can be either induced by damage or already present due to the material micro-structure. The analysis of flutter instability could be extended to more general cases contemplating anisotropic constitutive models.

Chapter 5

Finite element with embedded interphase

This Chapter is devoted to the implementation of a finite element with an embedded interphase element. The IPH will be here presented, by initially highlighting its improvements with respect to the ZTI model. Then the element with an embedded narrow band will be implemented in the framework of the A-FEM technique. Summarily, the proposed strategy can be briefly described for one localized element as follows: a general finite element that has reached its elastic limit is split into three elements, two sub-elements with an interposed IPH, whose behaviour is nonlinear and governed by the isotropic damage model presented in `Chapter 4`, and then re-assembled by condensing internal additional Dofs at the equilibrium level.

5.1 Modeling strategies of contact elements

Heterogeneous materials, such as masonry structures, concrete or composite materials, present a mechanical response strictly related to the static and kinematic phenomena occurring in each constituent and at their joints. Their mechanical behaviour is also strongly related to the effective position of heterogeneities within the overall structure. The most important inelastic mechanisms occur at the so-called *mesoscopic scale*, where each constituent is analysed separately. However, overall behaviour remains governed by the geometric and global morphological configuration, concerning the *macroscopic scale* [78].

In the mesoscopic approach, the discontinuity is analyzed as a potential

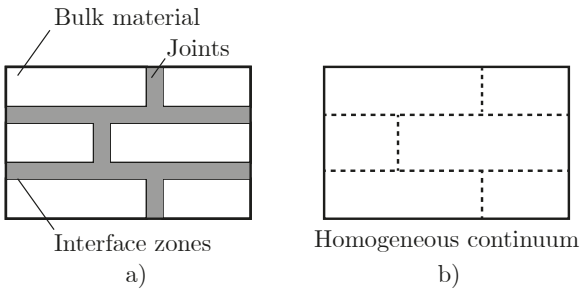

Figure 5.1: Differences between mesoscopic approach *a*) and macroscopic approach *b*).

fracture plane and this allows to study separately the combined action of the bulk material, the thin joint and the interface zones by which they transfer quantities to each other. Meso-modeling is preferable if the local behaviour of the structure has to be analyzed in detail, even if it is computationally more expensive than macro-modeling. In the macroscopic approach, instead, the material is idealized as a homogeneous continuum, without distinction between the different components: in this way, computational effort is significantly reduced with respect to the micro-modeling (Figure 5.1).

In the classic mesoscopic approach solid blocks are separately modelled as classic 2D or 3D continuum elements while the joints are simulated through mechanical devices (contact elements) able to reproduce the inelastic phenomena occurring in the weakest areas of the structure, such as opening-closing, sliding or dilatancy effects. *Contact elements* are classified in the following categories:

- *Link elements* between two opposite nodes;
- *Thin layer elements*, with small but finite thickness;
- *ZTI* or *Interphase* elements, in which the displacements discontinuities between the upper and the lower surfaces represent the main kinematic variables.

Next sub-Sections will deal with the analysis of the latter mentioned category.

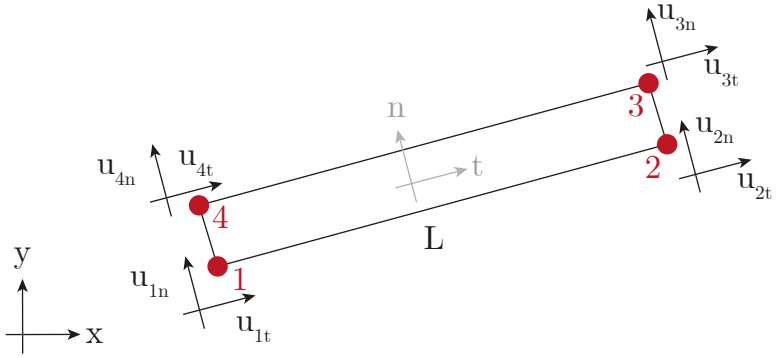

Figure 5.2: Goodman's interface element.

5.1.1 ZTI models

The first FEM application using ZTI elements appears in the last sixties and it is attributed to GOODMAN [44], who analysed the mechanical response of rock masses. The 4-node element initially presented two pairs of nodes placed at the same geometric location, from which the name of Zero-Thickness Interface (Figure 5.2). Introducing the matrix $\boldsymbol{N}$ containing the standard shape functions, the vector of relative displacements $\boldsymbol{\delta}$ is related to the vector of absolute nodal displacements $\mathbf{u}^e = \begin{bmatrix} u_{1t} & u_{1n} & u_{2t} & u_{2n} & u_{3t} & u_{3n} & u_{4t} & u_{4n} \end{bmatrix}^T$ as follows

$$\boldsymbol{\delta} = \begin{bmatrix} \delta_t \\ \delta_n \end{bmatrix} = \boldsymbol{N}\mathbf{u}^e \tag{5.1}$$

where δ_t and δ_n represent the tangential and normal relative displacements at the generic node of the ZTI and $\boldsymbol{N}$ is

$$\boldsymbol{N} = \begin{bmatrix} -N_1 & 0 & -N_2 & 0 & N_2 & 0 & N_1 & 0 \\ 0 & -N_1 & 0 & -N_2 & 0 & N_2 & 0 & N_1 \end{bmatrix}; \tag{5.2}$$

$$\text{with} \quad N_{1,2} = \frac{1}{2} \mp \frac{t}{L}. \tag{5.3}$$

The tangential and normal stresses, τ and σ_n respectively, are calculated from the relative displacements through the following constitutive relation

$$\begin{bmatrix} \tau \\ \sigma_n \end{bmatrix} = \begin{bmatrix} E_t & 0 \\ 0 & E_n \end{bmatrix} \boldsymbol{\delta} = \boldsymbol{E}\boldsymbol{N}\mathbf{u}^e \tag{5.4}$$

where E_t and E_n are the tangential and normal stiffness per unit length. By integrating this contribution along the t direction and considering the lenght L, the element stiffness matrix $\boldsymbol{K}^e$ is obtained

$$\boldsymbol{K}^e = \int_{-L/2}^{-L/2} \boldsymbol{N}^T \boldsymbol{E} \boldsymbol{N} dt = \int_{-1}^{1} \boldsymbol{N}^T \boldsymbol{E} \boldsymbol{N} |\boldsymbol{J}| d\xi \tag{5.5}$$

where $\boldsymbol{J}$ is the Jacobian transformation matrix. The stiffness matrix needs to be rotated from the local reference system (t, n) to the global one (x, y) using the rotation matrix $\boldsymbol{R}$

$$\boldsymbol{K} = \boldsymbol{R}^T \boldsymbol{K}^e \boldsymbol{R} \tag{5.6}$$

First numerical applications showed spurious oscillations of the stress field, in particular when the interface is stiffer than the remaining part of the body. The Goodman's model, although exhibiting robust response normal to the interface, has basic kinematic deficiencies attributed to the form of the element equations, which appear as tangential force oscillations. This deficiency was attributed to the uncoupled form of the element equations.

SCHELLEKENS et al. [107] related also this bad performance to the numerical integration schemes used to calculate the stiffness matrix in (5.6). The element performs badly with the Gauss quadrature integration scheme. The impact of Gauss, Newton-Cotes, Lobatto and lumped integration quadrature on the stress prediction in interfaces was investigated. The nodal or Lobatto quadrature has the advantage that the constraint matrix is decoupled and becomes diagonal, since the contributions from the different shape functions do not interact. They concluded, however, that inaccurate results occur when the Newton-Cotes and Lobatto integration schemes are used, due to an incorrect calculation of the contribution $det(\boldsymbol{J})$ in each integration point. In this case, in fact, the ZTI element degenerates in discrete springs located at the nodes of the element.

This model was improved by the ZTI element proposed by HERMANN [49]. According to this approach, the mechanical behaviour of the interface is modeled through two springs, one normal and one tangential at the interface, at each pair of coupling nodes. The insertion of these springs could solve some deficiencies of the Goodman's model: Hermann's approach in fact defines three distinct response regimes to simulate the non-slip, the slip, and the separation modes by changing the springs' stiffness.

The same bad performance was analysed by KALIAKIN and LI [65]: the behaviour of two in-series linear zero-thickness interface elements was studied and some fundamental behavioural deficiencies noted.

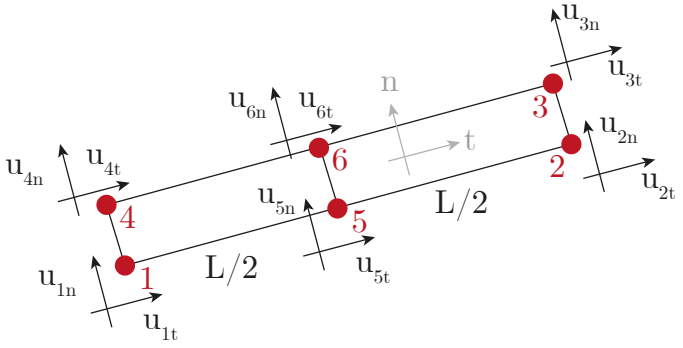

Figure 5.3: Kaliakin's interface model.

For this purpose, an improved six-node element was proposed, as the result of the assembly of two aligned 4-node interface elements (Figure 5.3). Nodes $1-4$, $2-3$ and $5-6$ are coincident since the element has no thickness. For each element the stiffness matrix is given by equation (5.5), then assembled into the global stiffness matrix. Finally by using the static condensation technique the DoFs associated with nodes 5 and 6 are condensed out, so the resulting equation assumes the classic form

$$\boldsymbol{K}^e \mathbf{u}^e = \mathbf{f}^e \tag{5.7}$$

with $\mathbf{f}^e = \begin{bmatrix} f_{1t} & f_{1n} & f_{2t} & f_{2n} & f_{3t} & f_{3n} & f_{4t} & f_{4n} \end{bmatrix}^T$.

Even if the structure of the stiffness matrices obtained with the Goodman's approach and the Kaliakin's one is similar, the numerical coefficients and more importantly the signs of certain off-diagonal terms differ. This leads to an improved ZTI element which eliminates the kinematic inconsistencies and spurious traction oscillations recorded in the previous models.

The model proposed by `GIAMBANCO` et al. [42] simulates the *third body* Ω^3 using an interface, with a uniform thickness h, in contact by two physical surfaces Σ^1 and Σ^2 with the two bodies Ω^1 and Ω^2. The static and kinematic quantities are referred to a Cartesian coordinate system (x_1, x_2, x_3), with x_1, x_2 lying in the middle plane of Ω^3 and x_3 coinciding with the normal direction to the interface (Figure 5.4).

Joints are modelled following these assumptions:

- Continuity of the tractions at the physical surfaces:

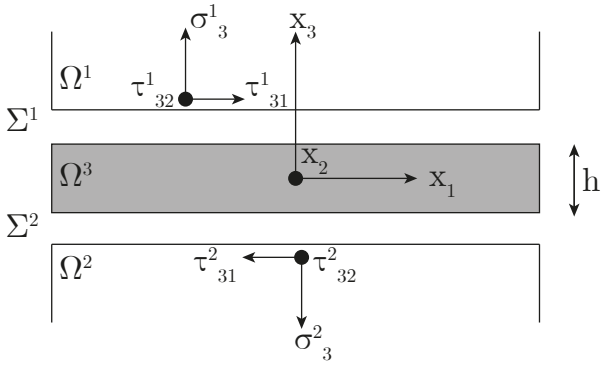

Figure 5.4: Interface layer Ω^3 of thickness h between bodies Ω^1 and Ω^2, connected by physical surfaces Σ^1 and Σ^2.

$$[\![\boldsymbol{\sigma}]\!] = 0 \tag{5.8}$$

where $[\![*]\!]$ represents the jump of the enclosed quantity.

- The strain components are uniform along the thickness and are calculated from the associated displacements discontinuities:

$$\boldsymbol{\varepsilon} = \frac{[\![\mathbf{u}]\!]}{h}. \tag{5.9}$$

The constitutive laws are expressed in terms of contact tractions and conjugate generalized joint strains: contact stresses and displacement discontinuities represent the primary static and kinematic variables. The constitutive laws at the integration points read:

$$\boldsymbol{\sigma} = \boldsymbol{E}\boldsymbol{\varepsilon} = \frac{1}{h}\boldsymbol{E}[\![\mathbf{u}]\!] = \boldsymbol{K}[\![\mathbf{u}]\!] \qquad \text{with} \qquad \boldsymbol{K} = \frac{1}{h}\begin{bmatrix} G_1 & 0 & 0 \\ 0 & G_2 & 0 \\ 0 & 0 & E \end{bmatrix} \tag{5.10}$$

where G_1, G_2, E are the tangential and normal elastic moduli.

Interface elements are characterized by an uncoupled form of the equilibrium equations, thanks to the diagonal form of the stiffness matrix. The usual assumption that the response is governed by contact stress components only may require an advancement when the effect of the internal stresses must be included to catch particular nonlinear behaviours. The advancement of ZTI elements is represented by IPH elements, as discussed in the next sub-Section.

5.1.2 The interphase model

The interphase model reproduces a thin material layer Ω_b with thickness w_b, which crosses a solid body Ω defined in the Euclidean space R^3, referred to the coordinate system $(\mathbf{e}_x, \mathbf{e}_y, \mathbf{e}_z)$ (Figure 5.5). It is separated from Ω^+ and Ω^- by two weak discontinuity surfaces Σ^+, Σ^- where the displacement field is continuous while the strain field is discontinuous. The body is subjected to the volume forces $\mathbf{f}$, while along the boundary two parts could be identified, Γ_u and Γ_t, where respectively the kinematic constraints $\mathbf{u} = \overline{\mathbf{u}}$ and tractions $\mathbf{t}$ are applied. It is assumed that the band thickness is small if compared with the characteristic dimensions of the body and is modelled using an IPH model. As typical in IPH or ZTI models, it is also assumed that the band can be considered locally planar, so that any mechanical quantity related to a band curvature is neglected.
In order to study the static and kinematic conditions of the interphase element a local Cartesian coordinate system (x_b, y_b, z_b) is considered, with x_b, y_b axes lying within the middle plane Σ_b of the joint and the z_b axis identified by the unit vector normal to the band and directed towards the body Ω^+. The thin layer is subjected to the external tractions $\mathbf{t}$ on the lateral surface Γ_b (Γ_b is synonymous with Γ_t, with different subscript only to indicate reference to the band) and to the contact traction $\mathbf{q}^+$ and $\mathbf{q}^-$ on the physical surfaces Σ^+ and Σ^-, respectively.

5.1.2.1 Geometry and Kinematics

The geometric and kinematic assumptions for the localization band are:

- the localization band is planar;
- the fibers along z_b are maintained rectilinear during the deformation process, so the displacement field $\mathbf{u}_b$ is derived from the displacements $\mathbf{u}_b^+$ and $\mathbf{u}_b^-$ of Σ^+ and Σ^-:

$$\mathbf{u}_b\left(x_b, y_b, z_b\right) = \left(\frac{1}{2} + \frac{z_b}{w_b}\right)\mathbf{u}_b^+\left(x_b, y_b\right) + \left(\frac{1}{2} - \frac{z_b}{w_b}\right)\mathbf{u}_b^-\left(x_b, y_b\right); \quad (5.11)$$

- the band thickness w_b is small with respect to the characteristic dimensions of the remaining part of the body;

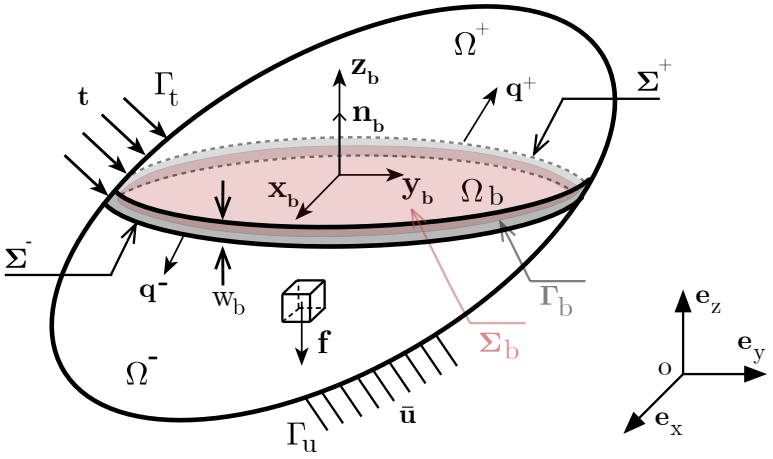

Figure 5.5: Schematic representation of a continuous body with a localization band Ω_b.

- the strain state is uniform in the band thickness and its value is obviously equal to the average value along the same direction.
  By considering the thin layer as collapsed in its middle plane Σ_b, the strain field could be calculated as follows:

$$\boldsymbol{\varepsilon}_b = \frac{1}{w_b} \int_{\frac{-w_b}{2}}^{\frac{w_b}{2}} \nabla^s \mathbf{u}_b \, \mathrm{d}z_b = \frac{1}{w_b} \left([\![\mathbf{u}_b]\!] \otimes \mathbf{n}_b \right)^s + \nabla^s \hat{\mathbf{u}}_b \tag{5.12}$$

where $(\cdot \otimes \cdot)^s$ is the symmetric part of the resulting tensor, $\mathbf{n}_b$ is the unit vector normal to the middle surface of the localization band, ∇^s is the symmetric part of the gradient operator and

$$[\![\mathbf{u}_b]\!] = \mathbf{u}_b^+ - \mathbf{u}_b^-, \qquad \hat{\mathbf{u}}_b = \left(\frac{\mathbf{u}_b^+ + \mathbf{u}_b^-}{2} \right). \tag{5.13}$$

Let us note that the joint curvatures generated by the displacement field (5.11) and the flexural effects are neglected.
Equation (5.12) can be given in its explicit form in terms of components as:

$$\varepsilon_{x_b} = \frac{1}{w_b} \int_{\frac{-w_b}{2}}^{\frac{w_b}{2}} \left(\frac{\partial u_{x_b}}{\partial x_b} \right) \partial z_b = \frac{1}{2} \left(\frac{\partial u_{x_b}^+}{\partial x_b} + \frac{\partial u_{x_b}^-}{\partial x_b} \right) \tag{5.14}$$

$$\varepsilon_{y_b} = \frac{1}{w_b}\int_{\frac{-w_b}{2}}^{\frac{w_b}{2}} \left(\frac{\partial u_{y_b}}{\partial y_b}\right) \partial z_b = \frac{1}{2}\Big(\frac{\partial u^+_{y_b}}{\partial y_b} + \frac{\partial u^-_{y_b}}{\partial y_b}\Big) \tag{5.15}$$

$$\varepsilon_{z_b} = \frac{1}{w_b}\int_{\frac{-w_b}{2}}^{\frac{w_b}{2}} \left(\frac{\partial u_{z_b}}{\partial z_b}\right) \partial z_b = \boxed{\frac{[\![u_{z_b}]\!]}{w_b}} \tag{5.16}$$

$$\varepsilon_{x_b y_b} = \frac{1}{w_b}\int_{\frac{-w_b}{2}}^{\frac{w_b}{2}} \left[\frac{1}{2}\left(\frac{\partial u_{x_b}}{\partial y_b} + \frac{\partial u_{y_b}}{\partial x_b}\right)\right] \partial z_b = \frac{1}{4}\left(\gamma^+_{x_b y_b} + \gamma^-_{x_b y_b}\right) \tag{5.17}$$

$$\varepsilon_{z_b x_b} = \frac{1}{w_b}\int_{\frac{-w_b}{2}}^{\frac{w_b}{2}} \left[\frac{1}{2}\left(\frac{\partial u_{x_b}}{\partial z_b} + \frac{\partial u_{z_b}}{\partial x_b}\right)\right] \partial z_b = \boxed{\frac{[\![u_{x_b}]\!]}{w_b}} + \frac{1}{2}\Big(\frac{\partial u^+_{z_b}}{\partial x_b} + \frac{\partial u^-_{z_b}}{\partial x_b}\Big) \tag{5.18}$$

$$\varepsilon_{z_b y_b} = \frac{1}{w_b}\int_{\frac{-w_b}{2}}^{\frac{w_b}{2}} \left[\frac{1}{2}\left(\frac{\partial u_{y_b}}{\partial z_b} + \frac{\partial u_{z_b}}{\partial y_b}\right)\right] \partial z_b = \boxed{\frac{[\![u_{y_b}]\!]}{w_b}} + \frac{1}{2}\Big(\frac{\partial u^+_{z_b}}{\partial y_b} + \frac{\partial u^-_{z_b}}{\partial y_b}\Big). \tag{5.19}$$

In equation (5.12) it is clear how the strain field can be decomposed into two parts: the first one is typical of an interface strain field and is related to contact strain components only (the boxed terms $\boxed{*}$ in the previous explicit relations). The second term takes into account additional contributions due to the appearance of internal strains.

5.1.2.2 Forces and equilibrium

The Principle of Virtual Displacements (PVD) asserts that the external work produced by the contact tractions and the external loads must be equivalent to the internal work developed in the localization band, thus

$$\int_{\Sigma^+} \delta\mathbf{u}_b^+ \cdot \mathbf{q}^+ \,\mathrm{d}\Sigma + \int_{\Sigma^-} \delta\mathbf{u}_b^- \cdot \mathbf{q}^- \,\mathrm{d}\Sigma + \int_{\Gamma_b} \delta\mathbf{u}_b \cdot \mathbf{t} \,\mathrm{d}\Gamma = \int_{\Omega_b} \delta\boldsymbol{\varepsilon}_b : \boldsymbol{\sigma}_b \,\mathrm{d}\Omega. \tag{5.20}$$

The virtual displacements, preceded by the symbol δ, are assigned while the virtual strains must satisfy the Eq. (5.12). Since the strain state is uniform along $\mathbf{n}_b$ in a consistent manner also the stress state can be considered uniform along the same direction. Therefore the internal work assumes the following expression:

$$\int_{\Omega_b} \delta\boldsymbol{\varepsilon}_b : \boldsymbol{\sigma}_b \,\mathrm{d}\Omega = \int_{\Sigma_b} [(\delta[\![\mathbf{u}_b]\!] \otimes \mathbf{n}_b)^s + w_b \nabla^s \delta\hat{\mathbf{u}}_b] : \boldsymbol{\sigma}_b \,\mathrm{d}\Sigma. \tag{5.21}$$

Integrating by parts the second term in the right-hand integral, we can write:

$$\int_{\Sigma_b} w_b \nabla^s \delta\hat{\mathbf{u}}_b : \boldsymbol{\sigma}_b \, \mathrm{d}\Sigma = \int_{C_b} w_b \delta\hat{\mathbf{u}}_b \cdot (\boldsymbol{\sigma}_b \cdot \mathbf{m}_b) \mathrm{d}C - \int_{\Sigma_b} w_b \, \delta\hat{\mathbf{u}}_b \cdot \mathrm{div}\boldsymbol{\sigma}_b \mathrm{d}\Sigma \quad (5.22)$$

where C_b is the contour of the localization band middle surface ($C_b = \Sigma_b \cap \Gamma_b$) and $\mathbf{m}_b$ is the vector normal to the contour line.
Substituting, expression (5.21) reads as

$$\int_{\Omega_b} \delta\boldsymbol{\varepsilon}_b : \boldsymbol{\sigma}_b \, \mathrm{d}\Omega = \int_{\Sigma_b} \left[(\delta[\![\mathbf{u}_b]\!] \otimes \mathbf{n}_b)^s : \boldsymbol{\sigma}_b - w_b \, \delta\hat{\mathbf{u}}_b \cdot \mathrm{div}\boldsymbol{\sigma}_b \right] \mathrm{d}\Sigma + w_b \int_{C_b} \delta\hat{\mathbf{u}}_b \cdot (\boldsymbol{\sigma}_b \cdot \mathbf{m}_b) \, \mathrm{d}C. \quad (5.23)$$

Substituting the integral (5.23) in the PVD, assuming that $\Sigma^+ \equiv \Sigma^- \equiv \Sigma_b$, using positions (5.13) and considering that the surface forces $\mathbf{t}$ on Γ_b are uniform along with the thickness of the thin layer, it follows

$$\int_{\Sigma_b} \delta\mathbf{u}_b^+ \cdot \left(\mathbf{q}^+ + \frac{w_b}{2} \mathrm{div}\boldsymbol{\sigma}_b - \boldsymbol{\sigma}_b \cdot \mathbf{n}_b \right) \mathrm{d}\Sigma + \int_{\Sigma_b} \delta\mathbf{u}_b^- \cdot \left(\mathbf{q}^- + \frac{w_b}{2} \mathrm{div}\boldsymbol{\sigma}_b + \boldsymbol{\sigma}_b \cdot \mathbf{n}_b \right) \mathrm{d}\Sigma + \int_{C_b} w_b \delta\hat{\mathbf{u}}_b \cdot (\mathbf{t} - \boldsymbol{\sigma}_b \cdot \mathbf{m}_b) \, \mathrm{d}C = 0, \quad (5.24)$$

where the following equivalences have been considered: $\mathrm{d}\Gamma_b = w_b \mathrm{d}C_b$; $\left(\delta\mathbf{u}_b^{(-,+)} \otimes \mathbf{n}_b \right)^s : \boldsymbol{\sigma}_b = \delta\mathbf{u}_b^{(-,+)} \cdot (\boldsymbol{\sigma}_b \cdot \mathbf{n}_b)$. As the equality (5.24) must be valid for any virtual displacements $\delta\mathbf{u}^+$ and $\delta\mathbf{u}^-$ and since Cauchy's Theorem permits to write $\mathbf{q}^+ = \boldsymbol{\sigma}^+ \cdot \mathbf{n}_b$ and $\mathbf{q}^- = -\boldsymbol{\sigma}^- \cdot \mathbf{n}_b$, the equilibrium equations for the *interphase element* can be obtained [41]-[43]:

$$w_b \, \mathrm{div}\boldsymbol{\sigma}_b + [\![\boldsymbol{\sigma}_b]\!] \cdot \mathbf{n}_b = \mathbf{0} \quad \text{on } \Sigma_b \quad (5.25)$$

$$(\boldsymbol{\sigma}_b - \hat{\boldsymbol{\sigma}}_b) \cdot \mathbf{n}_b = \mathbf{0} \quad \text{on } \Sigma_b \quad (5.26)$$

$$\boldsymbol{\sigma}_b \cdot \mathbf{m}_b = \mathbf{t} \quad \text{in } C_b \quad (5.27)$$

where

$$[\![\boldsymbol{\sigma}_b]\!] = \boldsymbol{\sigma}_b^+ - \boldsymbol{\sigma}_b^-, \qquad \hat{\boldsymbol{\sigma}}_b = \frac{\boldsymbol{\sigma}_b^+ + \boldsymbol{\sigma}_b^-}{2}. \quad (5.28)$$

Eqs. (5.25) and (5.26) can be regarded as internal and external equilibrium equations of the interphase element and (5.27) represents the equilibrium boundary conditions.

In the circumstance that the same constitutive behaviour of the bulk material is used for the IPH, w_b represents the only additional parameter to furnish in order to solve Equation (5.25). It is important to remark that w_b is a parameter that needs to be specified in any model where the band is assumed collapsed in its middle plane, as it happens for IPH or ZTI models.

5.1.3 Differences between the IPH and the ZTI

The IPH is an enhancement of the ZTI from different points of view:

- enrichment of the stress and strain fields: not only the contact components but also the internal ones. This makes the IPH closer to a solid element than the ZTI;
- absence of requirement of specific adhesive contact constitutive equations since the same constitutive relations of the bulk material can be considered;
- the adoption of the IPH and the consequent distinction between contact tractions and internal stresses allows to introduce different failure conditions for the physical interfaces and the bulk material;
- more realistic response and the possibility to capture some phenomena, such as the *squeezing effect*, that the ZTI model can't analyze.

Let us consider, as an illustrative example, the so-called sandwich model related to the uniaxial compression test on a masonry volume [43, 123]. Generally, when a stack consisting of alternating layers of stiffer and more flexible layers is subjected to uniaxial compression, elements will deform perpendicularly to the loading direction. By considering two bricks interfaced by a mortar joint, two different cases can be distinguished.

The first case is when mortar is stiffer than the brick ($E_m > E_b$): the mortar responds with a confinement action on the two blocks, and causes the arising of tangential stresses that imply a tensile normal action on the mortar and a compression one on the blocks (Figure 5.7-a). The second case is when blocks are stiffer than the mortar ($E_b > E_m$): the stiffer material prevents the softer one from expanding laterally, so the mortar is literally "squeezed" between the blocks and subjected to a compression normal stress. However, the tensile

action on the blocks may lead to failure consisting on a vertical crack (Figure 5.7-b).

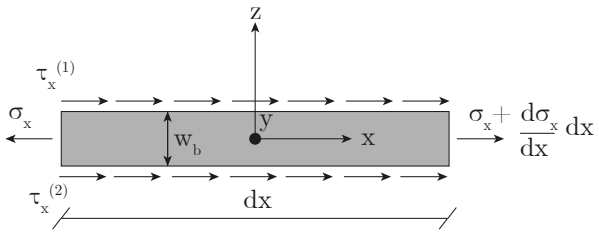

Figure 5.6: Uniaxial tension for the mortar joint.

Let us now consider an interface element, with width w_b, thickness t and referred to the (x, y, z) coordinate system, subjected to uniaxial tension along the axial direction x, by imposing $\sigma_z = 0$. Since in the ZTI model this stress component σ_x is not present (Figure 5.6) therefore, in order to respect the equilibrium, the jump in the tangential tractions $\mathbf{t}$ must be zero, as explained in the following passages:

$$\left(\sigma_x + \frac{d\sigma_x}{dx}dx\right) \cdot w_b \cdot t + (\tau_x^{(1)} + \tau_x^{(2)})dx \cdot t - \sigma_x \cdot w_b \cdot t = 0 \qquad (5.29)$$

$$\frac{d\sigma_x}{dx} \cdot w_b + (\tau_x^{(1)} + \tau_x^{(2)}) = 0 \qquad (5.30)$$

$$\frac{w_b}{2}\frac{d\sigma_x}{dx} + \hat{\tau}_x = 0 \qquad (5.31)$$

$$\sigma_{\mathbf{x}} = 0 \qquad \text{in ZTI} \qquad \rightarrow \qquad \hat{\tau}_x = 0 \qquad (5.32)$$

It can be concluded that the ZTI model can provide only the stress in the normal direction, so the enhancement of the IPH is necessary to include also internal stress and strain components.

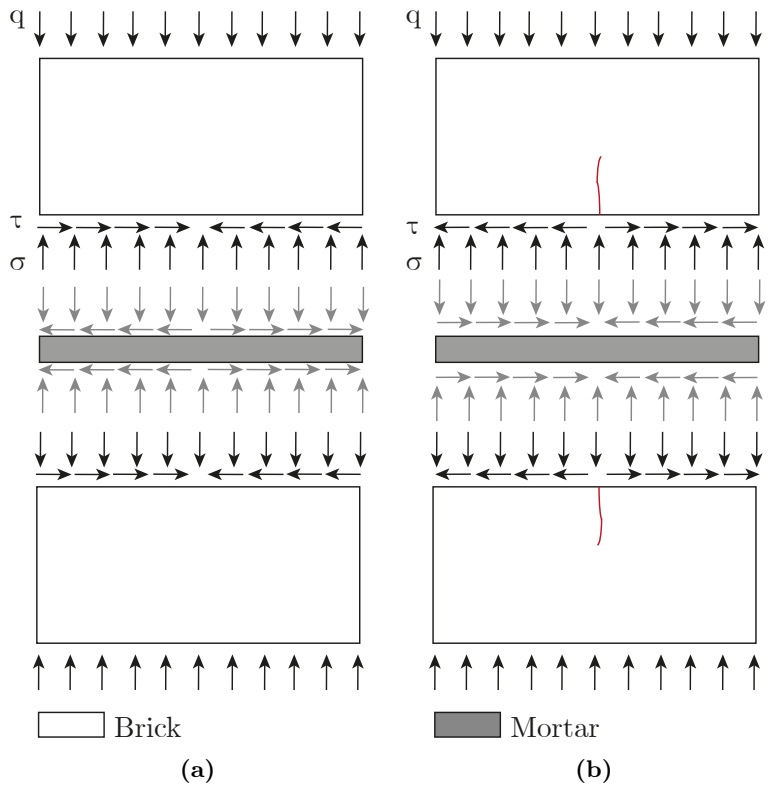

Figure 5.7: Uniaxial compression test on masonry volume: (a) mortar stiffer than the blocks ($E_m > E_b$); (b) blocks stiffer than the mortar ($E_b > E_m$).

5.2 Numerical procedure at the finite element level

In order to numerically simulate the collapse of structures where cracks propagate or strains concentrate, the IPH is implemented in the framework of A-FEM [69, 71, 84] strategy in presence of an IDM constitutive behaviour. The IPH element is used to substitute those narrow bands where strains concentrate. The fundamental relations are here furnished with reference to a quadrilateral 2D element and an efficient procedure that exploits the A-FEM idea is presented. The extension to mesh constituted by triangular 2D elements or generic 3D elements is straightforward since it involves the same fundamental relations. It is important to highlight that in the present formulation the crack can be only straight within each element. Variations of the crack direction and crack branching inside the element will be included in future developments.
Stress and strain states are written using Voigt's notation.

A single finite element is split in 3 parts (Figure 5.8): two sub-elements Ω^+ and Ω^- and an IPH Σ_b. In the following two sub-Sections the equilibrium equations for the sub-elements and the IPH are derived, respectively. In the third sub-Section the condensation procedure typical of A-FEM strategy is illustrated.

Let us consider a 4-node finite element crossed by a localization band which identifies the two parts Ω^+ and Ω^- (Figure 5.8-a). The quantities referred to the localization band will be identified with the subscript b.

In a 2D problem, the band is represented by the line Σ_b passing through the point (ρ_{b_x}, ρ_{b_z}) and identified with its unit vector $\mathbf{n}_b$, pointing to the subdomain Ω^+. According to the A-FEM procedure, four nodes (m, n, r, s) are added, providing the DoFs $\mathbf{U}_b$ of the interphase. $\mathbf{U}^+$ and $\mathbf{U}^-$, instead, collect the Dofs of Ω^+ and Ω^- sub-elements, respectively.

A single quadrilateral element could be divided into two quadrilateral subelements (Figure 5.8-a) or a triangular and a pentagonal sub-elements (Figure 5.9-a). Vectors are here explicitly furnished for the first case only, but fundamental equations have a general character and are valid for any sub-element shape.

5.2.1 Sub-element equilibrium equations

As regards the two sub-elements, the isoparametric formulation of a quadrilateral finite element is considered. The displacement field on each domain $\mathbf{u}^{(-,+)}$ and the associated strain field are obtained by mapping the nodal displacement

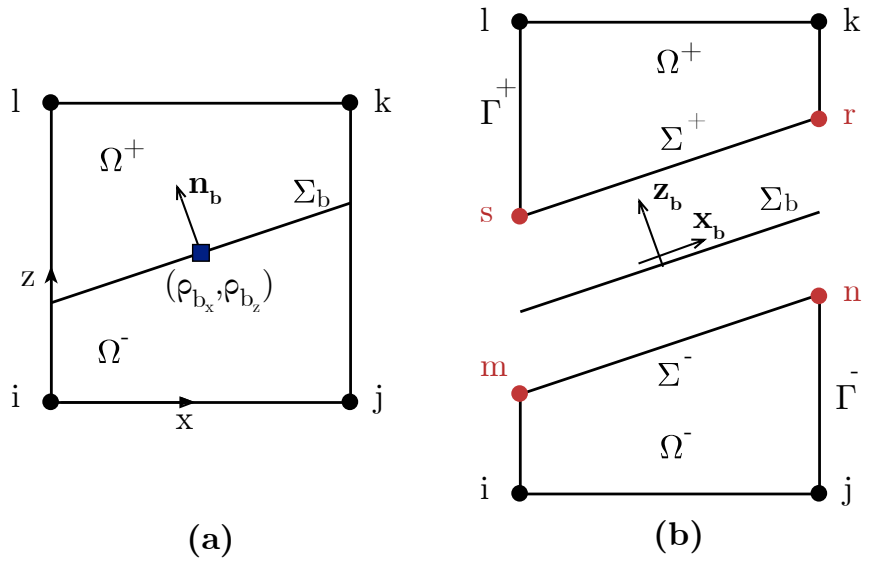

Figure 5.8: Four-node finite element crossed by the localization band (a) and its separation into two quadrangular sub-elements Ω^+ and Ω^- and the interphase element identified by its middle plane Σ_b (b).

vectors $\mathbf{U}^{(-,+)}$ as follows

$$\mathbf{u}^{(-,+)} = \mathbf{N}\,\mathbf{U}^{(-,+)}, \qquad \boldsymbol{\varepsilon}^{(-,+)} = \boldsymbol{C}\,\boldsymbol{N}\,\mathbf{U}^{(-,+)} = \boldsymbol{B}\,\mathbf{U}^{(-,+)} \tag{5.33}$$

where $\boldsymbol{N}$ is the shape functions matrix and $\boldsymbol{C}$ is the kinematic compatibility matrix for plane problems.

With reference to Figure 5.8-b, nodal displacement vectors for the two sub-elements are:

$$\mathbf{U}^- = \begin{bmatrix} \mathbf{U}_i \\ \mathbf{U}_j \\ \mathbf{U}_n \\ \mathbf{U}_m \end{bmatrix}, \quad \mathbf{U}^+ = \begin{bmatrix} \mathbf{U}_k \\ \mathbf{U}_l \\ \mathbf{U}_s \\ \mathbf{U}_r \end{bmatrix}. \tag{5.34}$$

The PVD written for Ω^+ and Ω^- reads

$$\delta\mathbf{U}^{(-,+)T}\left(\int_{\Omega^{(-,+)}} \mathbf{N}^T\mathbf{f}\,\mathrm{d}\Omega + \int_{\Gamma^{(-,+)}} \mathbf{N}^T\mathbf{t}^{(-,+)}\mathrm{d}\Gamma + \int_{\Sigma^{(-,+)}} \mathbf{N}^T\mathbf{q}^{(-,+)}\mathrm{d}\Sigma - \int_{\Omega^{(-,+)}} \mathbf{B}^T\boldsymbol{\sigma}^{(-,+)}\mathrm{d}\Omega\right) = 0. \tag{5.35}$$

Assuming an isotropic damaging behaviour of the elements material, solving the integrals by using the Gauss quadrature integration and considering that the equality (5.35) has to be true for any virtual nodal displacement vector, the equilibrium equations of the two sub-domains are obtained:

$$\mathbf{F}_e^{(-,+)} + \mathbf{F}_i^{(-,+)} = \mathbf{K}^{(-,+)}\mathbf{U}^{(-,+)}, \tag{5.36}$$

where

$$\mathbf{F}_e^{(-,+)} = \int_{\Omega^{(-,+)}} \mathbf{N}^T\mathbf{f}\,\mathrm{d}\Omega + \int_{\Gamma^{(-,+)}} \mathbf{N}^T\mathbf{t}^{(-,+)}\mathrm{d}\Gamma \tag{5.37}$$

$$\mathbf{F}_i^{(-,+)} = \int_{\Sigma^{(-,+)}} \mathbf{N}^T\mathbf{q}^{(-,+)}\mathrm{d}\Sigma \tag{5.38}$$

$$\mathbf{K}^{(-,+)} = \int_{\Omega^{(-,+)}} \mathbf{B}^T\mathbf{E}_t\,\mathbf{B}\,\mathrm{d}\Omega. \tag{5.39}$$

$\mathbf{F}_e$ represents the nodal force array originated by external forces and tractions. $\mathbf{F}_i$ contains the nodal internal forces originated by tractions due to the discontinuity. $\mathbf{K}$ is the element tangent stiffness matrix, dependent on the elastic tangent operator $\mathbf{E}_t$, defined as (4.43) in sub-Section 4.2.1.

As stated before, previous formulation refers to the case in which the band divides the element into two quadrilateral elements. However, it also holds a pentagonal and a triangular sub-elements form. The pentagonal sub-element is modeled as a composition of three triangles (Figure 5.9-b). In this case, and for the triangular sub-element as well, the shape functions are those for triangular elements only. The stiffness matrix and the force vector of the pentagon are obtained assembling the correspondent quantities of the three triangles, which are identified linking the internal nodes m and n with the external node j, as in Figure 5.9-b.

The subdivisions showed in Figures 5.8-5.9 hold for a 4-node quadrilateral element with bi-linear shape functions, that are the easiest numerical assumptions used as a first attempt in this work. In presence of higher-order shape functions, in quadrilateral elements with more than 4 nodes, Ω^+ and Ω^- would be both subdivided in triangles, while for the interphase element six nodes can be used, instead of four.

5.2.2 Interphase equilibrium equation

As regards the interphase element, a 2D element in the rotated (x_b, z_b) plane under the hypothesis of plane stress condition is considered (Figure 5.10-a). Let

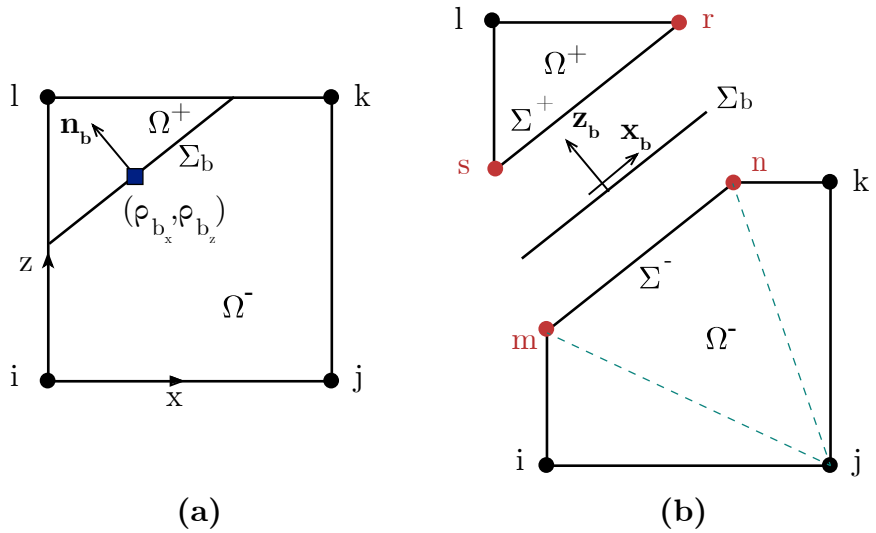

Figure 5.9: Four-node finite element crossed by the localization band (a) and its separation into a pentagonal and a triangular sub-elements, called Ω^- and Ω^+, and the interphase element identified by its middle plane Σ_b (b).

us refer to the displacement field relation (5.11), presented in sub-Section 5.1.2. The interphase element constitutive equation for the specific 2D case reads as follows:

$$\boldsymbol{\sigma}_b = \boldsymbol{E}_t \boldsymbol{\varepsilon}_b \qquad \text{where} \qquad \boldsymbol{\varepsilon}_b = \begin{bmatrix} \varepsilon_{x_b} \\ \varepsilon_{z_b} \\ \varepsilon_{x_b z_b} \end{bmatrix}, \quad \boldsymbol{\sigma}_b = \begin{bmatrix} \sigma_{x_b} \\ \sigma_{z_b} \\ \tau_{x_b z_b} \end{bmatrix}. \tag{5.40}$$

Remembering expressions (5.14-5.19) we can summarize

$$\varepsilon_{x_b} = \frac{\partial}{\partial x_b}\hat{u}_{x_b}, \quad \varepsilon_{z_b} = \frac{[\![u_{z_b}]\!]}{w_b}, \quad \varepsilon_{x_b z_b} = \frac{[\![u_{x_b}]\!]}{w_b} + \frac{\partial}{\partial x_b}\hat{u}_{z_b}. \tag{5.41}$$

An isotropic damage constitutive model is considered for the interphase element. $\boldsymbol{E}_t$ is the elastic tangent operator expressed in (4.43). Note that the same expression of the elastic tangent operator of the bulk material is adopted. As explained in paragraph 4.2.1, this matrix is evaluated with a linearization procedure.

The isoparametric formulation is based on a 4-node element in the reference system (ξ, η) of Figure 5.10-b. The interphase nodal displacements are calculated as follows

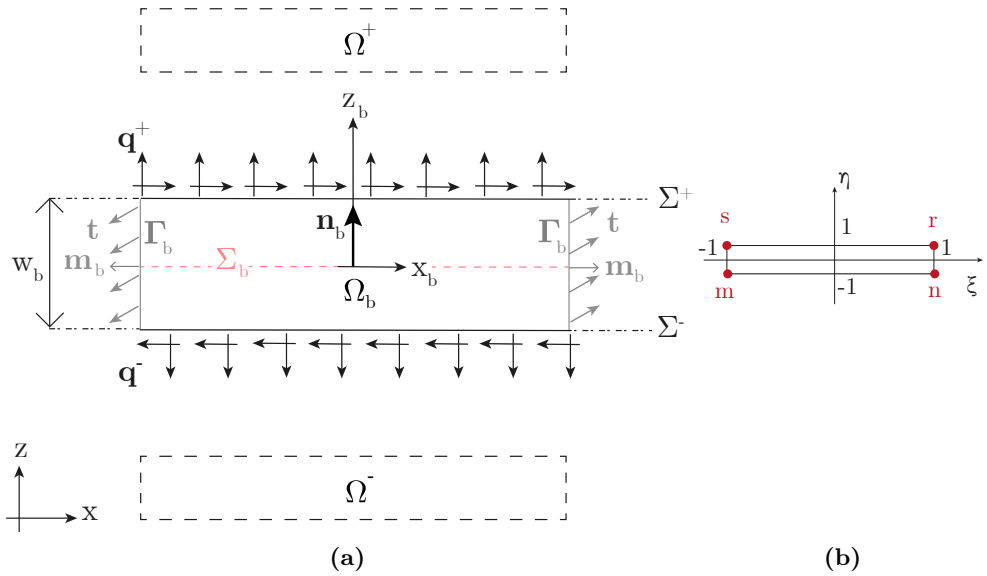

Figure 5.10: The schematic representation of the mechanical behaviour of the interphase element: (a) the interphase element referred to (x_b, z_b), rotated respect to the reference system (x, z); (b) The isoparametric interphase element.

$$\overline{\mathbf{U}}_b = \begin{bmatrix} \overline{\mathbf{U}}_b^- \\ \overline{\mathbf{U}}_b^+ \end{bmatrix} \qquad \text{where} \qquad \overline{\mathbf{U}}_b^- = \begin{bmatrix} \overline{\mathbf{U}}_m \\ \overline{\mathbf{U}}_n \end{bmatrix}; \qquad \overline{\mathbf{U}}_b^+ = \begin{bmatrix} \overline{\mathbf{U}}_r \\ \overline{\mathbf{U}}_s \end{bmatrix}. \tag{5.42}$$

The displacement fields of the lower and upper physical interfaces $\Sigma^{(-,+)}$ are derived using a linear interpolation of the nodal displacements

$$\overline{\mathbf{u}}_b^- = \mathbf{N}_b^- \overline{\mathbf{U}}_b^-, \qquad \overline{\mathbf{u}}_b^+ = \mathbf{N}_b^+ \overline{\mathbf{U}}_b^+. \tag{5.43}$$

The symbol $(\overline{*})$ means that the relative quantity is referred to the interphase coordinate system. Shape functions matrices are expressed as

$$\mathbf{N}_b^- = \begin{bmatrix} N_1 & 0 & N_2 & 0 \\ 0 & N_1 & 0 & N_2 \end{bmatrix} \qquad \mathbf{N}_b^+ = \begin{bmatrix} N_2 & 0 & N_1 & 0 \\ 0 & N_2 & 0 & N_1 \end{bmatrix} \tag{5.44}$$

where

$$N_1 = \frac{1}{2}(1-\xi), \qquad N_2 = \frac{1}{2}(1+\xi), \qquad \text{with} \quad \xi \in [-1, 1]. \tag{5.45}$$

By writing relations (5.41) in a compact form and using the symbol $(\overline{*})$, it follows

$$\boldsymbol{\varepsilon}_b = \frac{1}{w_b}\mathbf{C}_{b_1}\left(\bar{\mathbf{u}}_b^+ - \bar{\mathbf{u}}_b^-\right) + \frac{1}{2}\mathbf{C}_{b_2}\left(\bar{\mathbf{u}}_b^+ + \bar{\mathbf{u}}_b^-\right) \tag{5.46}$$

where

$$\mathbf{C}_{b_1} = \begin{bmatrix} 0 & 0 \\ 0 & 1 \\ 1 & 0 \end{bmatrix}; \quad \mathbf{C}_{b_2} = \begin{bmatrix} \frac{\partial}{\partial x_b} & 0 \\ 0 & 0 \\ 0 & \frac{\partial}{\partial x_b} \end{bmatrix}. \tag{5.47}$$

Introducing the displacement expressions (5.43) into (5.46) we obtain

$$\boldsymbol{\varepsilon}_b = \mathbf{B}_b^+ \overline{\mathbf{U}}_b^+ + \mathbf{B}_b^- \overline{\mathbf{U}}_b^- \tag{5.48}$$

with

$$\mathbf{B}_b^+ = \left(\frac{1}{w_b}\mathbf{C}_{b_1} + \frac{1}{2}\mathbf{C}_{b_2}\right)\mathbf{N}_b^+; \qquad \mathbf{B}_b^- = -\left(\frac{1}{w_b}\mathbf{C}_{b_1} - \frac{1}{2}\mathbf{C}_{b_2}\right)\mathbf{N}_b^-. \tag{5.49}$$

By re-writing the PVD problem for the interphase in equation (5.20), considering the kinematic equations (5.43) and (5.48) and neglecting the external traction applied on the lateral surface ($\mathbf{t} = \mathbf{0}$ in Γ_b), it follows:

$$\begin{aligned} &\delta\overline{\mathbf{U}}_b^{+T} \int_\Sigma \left(w_b\, \mathbf{B}_b^{+T}\mathbf{E}_t\, \mathbf{B}_b^+ \overline{\mathbf{U}}_b^+ + w_b\, \mathbf{B}_b^{+T}\mathbf{E}_t\, \mathbf{B}_b^- \overline{\mathbf{U}}_b^- - \mathbf{N}_b^{+T}\overline{\mathbf{q}}^+\right) \mathrm{d}\Sigma + \\ &\delta\overline{\mathbf{U}}_b^{-T} \int_\Sigma \left(w_b\, \mathbf{B}_b^{-T}\mathbf{E}_t\, \mathbf{B}_b^+ \overline{\mathbf{U}}_b^+ + w_b\, \mathbf{B}_b^{-T}\mathbf{E}_t\, \mathbf{B}_b^- \overline{\mathbf{U}}_b^- - \mathbf{N}_b^{-T}\overline{\mathbf{q}}^-\right) \mathrm{d}\Sigma = 0 \end{aligned} \tag{5.50}$$

which, being satisfied for any value of virtual displacements, gives

$$\overline{\mathbf{K}}_b^{++}\overline{\mathbf{U}}_b^+ + \overline{\mathbf{K}}_b^{+-}\overline{\mathbf{U}}_b^- = \overline{\mathbf{F}}_b^+ \tag{5.51}$$

$$\overline{\mathbf{K}}_b^{-+}\overline{\mathbf{U}}_b^+ + \overline{\mathbf{K}}_b^{--}\overline{\mathbf{U}}_b^- = \overline{\mathbf{F}}_b^- \tag{5.52}$$

where

$$\overline{\mathbf{K}}_b^{++} = \int_\Sigma w_b\, \mathbf{B}_b^{+T}\mathbf{E}_t\, \mathbf{B}_b^+ \mathrm{d}\Sigma \qquad \overline{\mathbf{K}}_b^{+-} = \int_\Sigma w_b\, \mathbf{B}_b^{+T}\mathbf{E}_t\, \mathbf{B}_b^- \mathrm{d}\Sigma \tag{5.53}$$

$$\overline{\mathbf{K}}_b^{-+} = \int_\Sigma w_b\, \mathbf{B}_b^{-T}\mathbf{E}_t\, \mathbf{B}_b^+ \mathrm{d}\Sigma \qquad \overline{\mathbf{K}}_b^{--} = \int_\Sigma w_b\, \mathbf{B}_b^{-T}\mathbf{E}_t\, \mathbf{B}_b^- \mathrm{d}\Sigma. \tag{5.54}$$

5.2.2.1 Numerical performance of the interphase element

As for interface elements, unfortunately even interphase elements showed some numerical problems associated with spurious oscillations in the stress profiles.

Table 5.1: Material parameters in the uniaxial compression test of masonry specimen: case a) $E_b = 10E_m$; b) $E_m = 30E_b$.

Case	E_b $[MPa]$	ν_b	E_m $[MPa]$	ν_m
a)	15000	0.30	1500	0.35
b)	500	0.30	15000	0.35

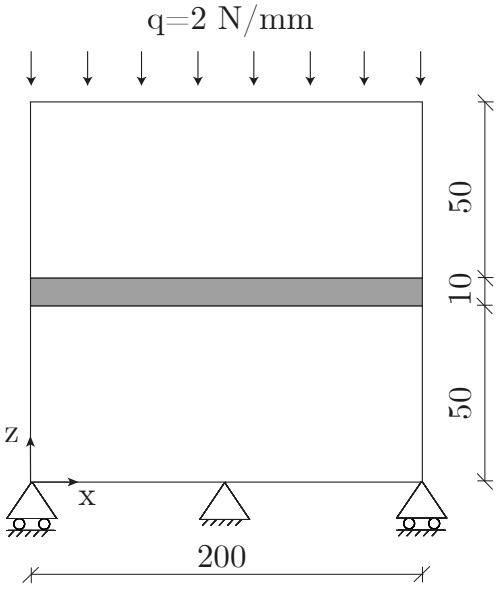

Figure 5.11: Geometry and boundary conditions of the uniaxial compression test of masonry specimen. Dimensions are given in mm.

They are related to the integration scheme chosen to derive the stiffness matrix. In order to analyze the numerical performance of the interphase element a patch test was run, regarding the linear elastic response of two masonry blocks joined by a mortar thin layer subjected to uniaxial compression, following what was done in [43]. The boundary and loading conditions are illustrated in Figure 5.11. The model thickness is equal to 10 mm and the stress state was considered as plane. Two cases were analyzed: the first one with a block stiffer than the mortar (constitutive parameters in Table 5.1-case a); the second one with the mortar stiffer than the block (constitutive parameters in Table 5.1-case b). The numerical convergence was tested by using a number of interphase elements

varying from 10 to 80 to model the mortar joint. The interphase stiffness matrix was integrated by using the conventional Gauss quadrature scheme.

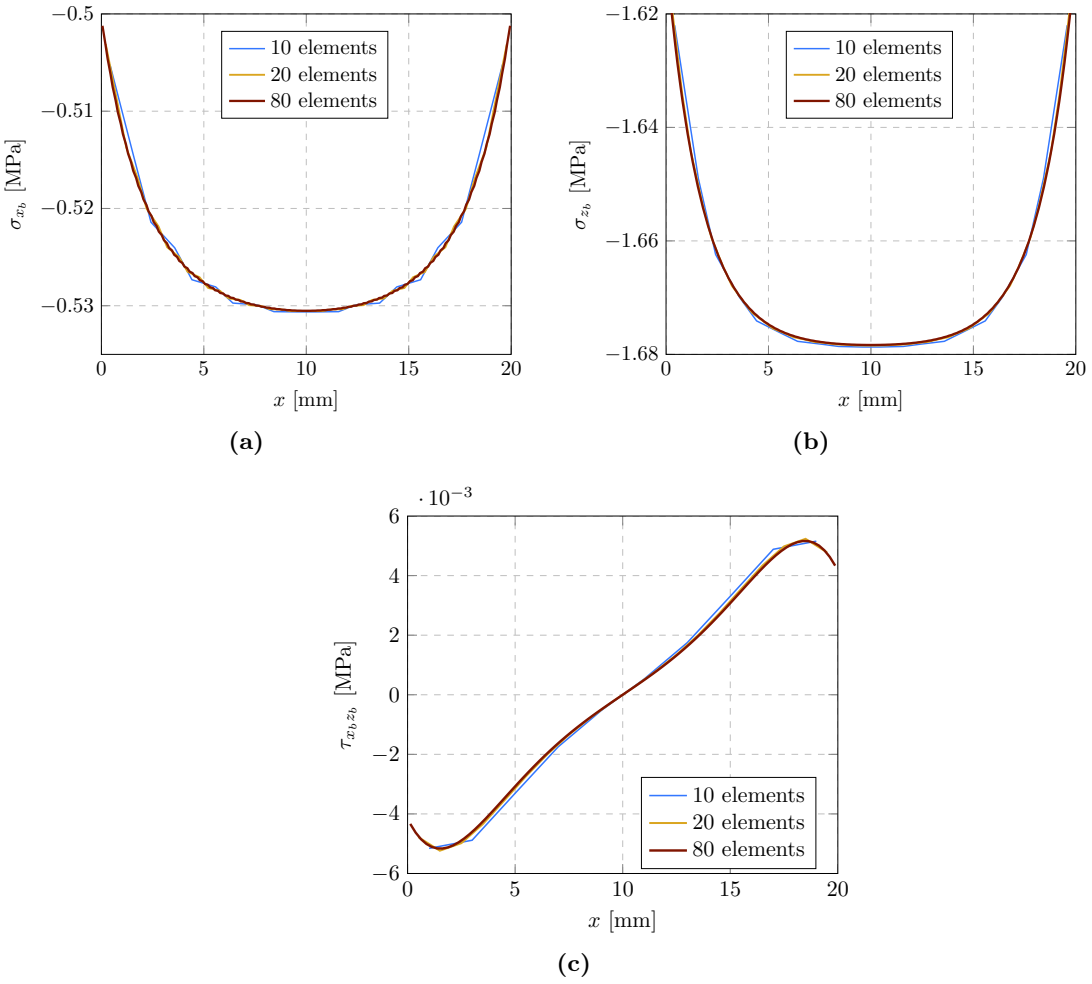

Figure 5.12: Case a): $E_b = 10E_m$ - standard Gauss quadrature. Internal stresses σ_{x_b} (a), σ_{z_b} (b) and contact tractions $\tau_{x_b z_b}$ (c) trends with respect to the x position in the IPH element.

Numerical results for the case a) are reported in Figure 5.12. It is clear how, respect to the ZTI elements, the normal internal stress σ_{x_b} and the tangential contact traction $\tau_{x_b z_b}$ appear. Profiles are also more defined as the number

of elements increases. Accordingly to what said before, the mortar joint is subjected to a compressive normal stress.

Numerical results for the case *b*) are reported in Figure 5.13- a, b and c. As expected, the mortar joint in this case is subjected to a tensile normal stress. Bad results are obtained for the tangential traction, which is affected by an unacceptable oscillation of the profile, not disappearing when the number of elements increases. Similar spurious oscillations of the stress field have been also recorded by different authors in the ZTI elements, when the layer is stiffer than the bulk material. This is the consequence of the so-called *shear locking*, consisting on an overestimation of the shear stiffness when the aspect ratio of the element tends to zero. This instability has been avoided by using the *Selective Reduced Integration* (SRI): this procedure essentially consists in using one Gauss point for the shear part of the energy and a full integration for the remaining normal part. Oscillations disappear, as visible in Figure 5.13-d.

5.2.3 Assembling procedure

In order to assemble sub-elements and interphase element we need to refer the kinematic and static quantities to the global reference system. Since the orientation of the band is individuated by the unit vector $\mathbf{n} = \begin{bmatrix} n_x & n_z \end{bmatrix}^T$, we can proceed with a reference system rotation in a classical way:

$$\overline{\mathbf{U}}_b^{(-,+)} = \mathbf{R}\mathbf{U}_b^{(-,+)} \qquad \overline{\mathbf{F}}_b^{(-,+)} = \mathbf{R}\mathbf{F}_b^{(-,+)} \tag{5.55}$$

where the rotation matrix $\boldsymbol{R}$ reads as

$$\boldsymbol{R} = \begin{bmatrix} n_z & -n_x & 0 & 0 \\ n_x & n_z & 0 & 0 \\ 0 & 0 & n_z & -n_x \\ 0 & 0 & n_x & n_z \end{bmatrix} \tag{5.56}$$

with $n_x = -\sin\alpha$ and $n_z = \cos\alpha$ (Figure 5.14). By replacing equation (5.55) in equations (5.51)-(5.52) the equilibrium equations of the interphase element written in the global reference system (x, z) are obtained. Nodal displacement vectors $\mathbf{U}^{(-,+)}$ are partitioned into external (e) and internal (i) components:

$$\mathbf{U}_e^- = \begin{bmatrix} \mathbf{U}_i \\ \mathbf{U}_j \end{bmatrix} \qquad \mathbf{U}_i^- = \begin{bmatrix} \mathbf{U}_n \\ \mathbf{U}_m \end{bmatrix} \tag{5.57}$$

$$\mathbf{U}_e^+ = \begin{bmatrix} \mathbf{U}_k \\ \mathbf{U}_l \end{bmatrix} \qquad \mathbf{U}_i^+ = \begin{bmatrix} \mathbf{U}_s \\ \mathbf{U}_r \end{bmatrix}, \tag{5.58}$$

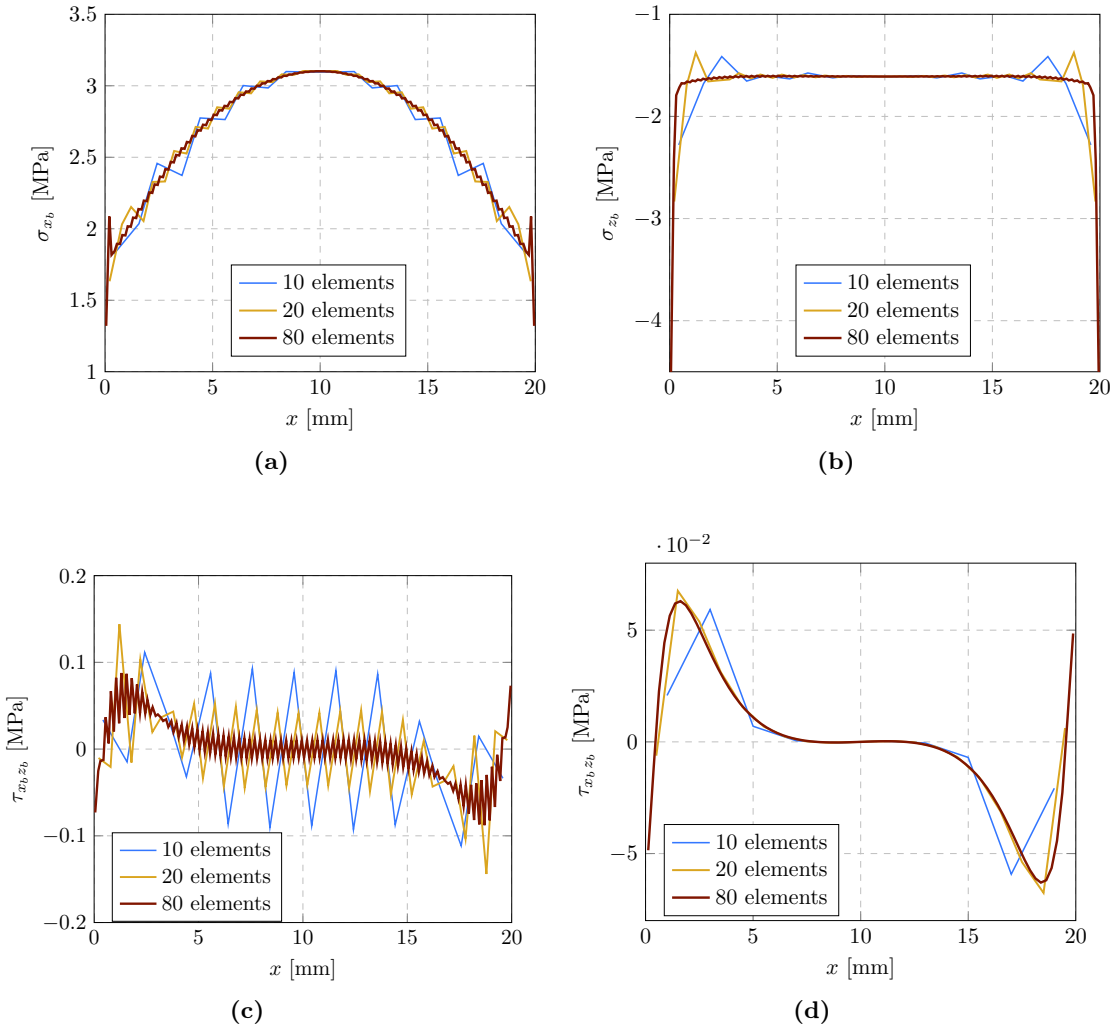

Figure 5.13: Case b): $E_m = 30E_b$ - standard Gauss quadrature (a-b-c) and SRI (d). Internal stresses σ_{x_b} (a), σ_{z_b} (b) and contact tractions $\tau_{x_b z_b}$ (c-d) trends with respect to the x position in the IPH element.

so equations (5.36) become

$$\begin{bmatrix} \mathbf{F}_{ee}^{(-,+)} \\ \mathbf{F}_{ei}^{(-,+)} \end{bmatrix} + \begin{bmatrix} \mathbf{0} \\ \mathbf{F}_{ii}^{(-,+)} \end{bmatrix} = \begin{bmatrix} \mathbf{K}_{ee}^{(-,+)} & \mathbf{K}_{ei}^{(-,+)} \\ \mathbf{K}_{ie}^{(-,+)} & \mathbf{K}_{ii}^{(-,+)} \end{bmatrix} \begin{bmatrix} \mathbf{U}_{e}^{(-,+)} \\ \mathbf{U}_{i}^{(-,+)} \end{bmatrix}. \tag{5.59}$$

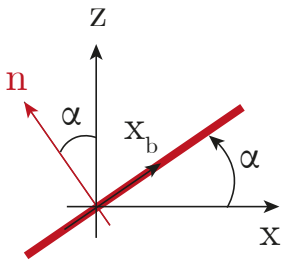

Figure 5.14: Interphase element rotation.

In order to follow the anti-clockwise order of nodes in Ω^+ and Ω^-, the displacements in Ω_b can be expressed as:

$$\mathbf{U}_b^+ = \mathbf{A}\mathbf{U}_i^+ \qquad \mathbf{U}_b^- = \mathbf{A}\mathbf{U}_i^- \tag{5.60}$$

being $\mathbf{A}$ an operator defined as

$$\mathbf{A} = \begin{bmatrix} \mathbf{0} & \mathbf{I} \\ \mathbf{I} & \mathbf{0} \end{bmatrix}, \tag{5.61}$$

with $\mathbf{0}$ and $\mathbf{I}$ being the 2×2 null and identity matrices, respectively.

Substituting equations (5.60) into (5.55), the interphase equilibrium equations (5.51)-(5.52) can be re-written by pre-multiplying each term by $\boldsymbol{S}^T$, being $\mathbf{S} = \mathbf{R}\mathbf{A}$. This operation leads to

$$\mathbf{K}_b^{++}\mathbf{U}_i^+ + \mathbf{K}_b^{+-}\mathbf{U}_i^- = \mathbf{F}_{ii}^+ \tag{5.62}$$
$$\mathbf{K}_b^{-+}\mathbf{U}_i^+ + \mathbf{K}_b^{--}\mathbf{U}_i^- = \mathbf{F}_{ii}^- \tag{5.63}$$

where the following positions have been done

$$\mathbf{K}_b^{\iota\kappa} = \mathbf{S}^T\overline{\mathbf{K}}_b^{\iota\kappa}\mathbf{S}, \quad \mathbf{F}_{ii}^{\iota} = \mathbf{S}^T\bar{\mathbf{F}}_b^{\iota}, \quad \text{with} \quad \iota,\kappa \in \{+,-\}. \tag{5.64}$$

Internal forces in (5.62)-(5.63) can be substituted into the equilibrium equations of the two sub-elements (5.59) to obtain the internal displacements

$$\mathbf{U}_i^+ = \mathbf{H}^+\left[\mathbf{F}_{ei}^+ - \mathbf{K}_{ie}^+\mathbf{U}_e^+ + \mathbf{M}^+\left(\mathbf{F}_{ei}^- - \mathbf{K}_{ie}^-\mathbf{U}_e^-\right)\right] \tag{5.65}$$
$$\mathbf{U}_i^- = \mathbf{H}^-\left[\mathbf{F}_{ei}^- - \mathbf{K}_{ie}^-\mathbf{U}_e^- + \mathbf{M}^-\left(\mathbf{F}_{ei}^+ - \mathbf{K}_{ie}^+\mathbf{U}_e^+\right)\right] \tag{5.66}$$

where

$$\mathbf{H}^+ = \left[\mathbf{K}_{ii}^+ - \mathbf{K}_b^{++} - \mathbf{K}_b^{+-}\left(\mathbf{K}_{ii}^- - \mathbf{K}_b^{--}\right)^{-1}\mathbf{K}_b^{-+}\right]^{-1} \tag{5.67}$$

$$\mathbf{H}^{-} = \left[\mathbf{K}_{ii}^{-} - \mathbf{K}_{b}^{--} - \mathbf{K}_{b}^{-+}\left(\mathbf{K}_{ii}^{+} - \mathbf{K}_{b}^{++}\right)^{-1}\mathbf{K}_{b}^{+-}\right]^{-1} \tag{5.68}$$

$$\mathbf{M}^{+} = \mathbf{K}_{b}^{+-}\left(\mathbf{K}_{ii}^{-} - \mathbf{K}_{b}^{--}\right)^{-1} \tag{5.69}$$

$$\mathbf{M}^{-} = \mathbf{K}_{b}^{-+}\left(\mathbf{K}_{ii}^{+} - \mathbf{K}_{b}^{++}\right)^{-1}. \tag{5.70}$$

Finally, after some mathematical manipulations, the equilibrium equations of the element with the embedded interphase are obtained:

$$\begin{bmatrix} \mathbf{F}_{ee}^{-} - \mathbf{K}_{ei}^{-}\mathbf{H}^{-}\left(\mathbf{F}_{ei}^{-} + \mathbf{M}^{-}\mathbf{F}_{ei}^{+}\right) \\ \\ \mathbf{F}_{ee}^{+} - \mathbf{K}_{ei}^{+}\mathbf{H}^{+}\left(\mathbf{F}_{ei}^{+} + \mathbf{M}^{+}\mathbf{F}_{ei}^{-}\right) \end{bmatrix} = \begin{bmatrix} \mathbf{K}_{ee}^{-} - \mathbf{K}_{ei}^{-}\mathbf{H}^{-}\mathbf{K}_{ie}^{-} & -\mathbf{K}_{ei}^{-}\mathbf{H}^{-}\mathbf{M}^{-}\mathbf{K}_{ie}^{+} \\ \\ -\mathbf{K}_{ei}^{+}\mathbf{H}^{+}\mathbf{M}^{+}\mathbf{K}_{ie}^{-} & \mathbf{K}_{ee}^{+} - \mathbf{K}_{ei}^{+}\mathbf{H}^{+}\mathbf{K}_{ie}^{+} \end{bmatrix} \begin{bmatrix} \mathbf{U}_{e}^{-} \\ \\ \mathbf{U}_{e}^{+} \end{bmatrix}. \tag{5.71}$$

The new equilibrium system does not depend on the internal nodes. The element stiffness matrix incorporates the presence of sub-elements and interphase as well as the effect of the damage in all of them.

The proposed formulation is based on the use of the same constitutive model for both the sub-elements and for the interphase element. With respect to other models, such as the ZTI one in which additional cohesive laws have to be introduced, in this case no additional material parameters are needed apart the band thickness.

Chapter 6

Implementation of a crack tracking algorithm

The previous Section is referred to the formulation of a finite element with an embedded interphase that is a-priori known. In the present section also the macro-scale or structural-scale problem is investigated. It requires the formulation of an algorithm capable to predict the formation and propagation of the band/fracture among the finite elements of the numerical model.
This issue has been treated in several papers, with the principal aim to make the fracture pattern independent of the finite elements density and orientation. In the case where the strain localization band is not known a priori, the principal issues regard:

- the identification of the numerical step at which a strain localization band can be introduced;
- the evaluation of strain localization band position and orientation;
- the intra-element propagation of bands or fractures;
- the identification of the crack pattern and the coexistence of multiple cracks.

The first two aspects are strongly related to the constitutive model adopted for the quasi-brittle material. The remaining ones deal with the finite element mesh processing, and require a specific crack tracking algorithm in order to define the evolution of the discontinuity surface during the loading process. The entire numerical procedure has been implemented in an entirely homemade

MatLab© code. Nonlinear equations are solved using the Newton-Raphson iterative procedure. The time integration scheme is based on a backward Euler method. For the sake of completeness, the code for the generic time step n is reported in Algorithm 1 on page 157 [98].

6.1 Overview on fracture initiation criteria

In the case where the strain localization band is not known a priori, a classic crack tracking algorithm predicts `when` to switch from a diffuse to a continuous/discontinuous model, `where` to locate the localization band and `how` to model it.

A tracking algorithm allows to identify the crack propagation direction and predict the crack path within a certain domain [105]. It is possible to qualitatively distinguish three different categories of tracking algorithm:

- local algorithms, in which the crack direction is computed locally, using values referred to a single element or a restricted area surrounding it;
- global algorithms, which compute simultaneously all the potential crack paths at each step of the analysis, by constructing a scalar function θ whose isolines represent the crack propagation directions within the whole structure;
- partial-domain algorithms, in which the solution of a boundary value problem at each step is done within a sub-domain rather than in the whole structure.

Some of the typical criteria used in literature to model and follow the propagation of one or more fractures will be presented below.

In `CERVERA` et al. [23], a Rankine criterion based on the value of the maximum principal stress is applied, in which it is assumed that the crack propagates in a plane orthogonal to the corresponding principal stress eigenvector. For this reason, principal stress directions are evaluated in the surrounding of the crack tip. A scalar field θ is defined, whose gradient is parallel to the normal vector $\mathbf{n}$, so that $\mathbf{n} = \frac{\nabla\theta}{|\nabla\theta|}$. An isoline, defined by $\theta = constant$, is orthogonal to $\mathbf{n}$; thus, the problem of evaluating the direction of crack propagation is equivalent to find the scalar field θ and determine the iso-level locus $\theta = \theta_0$, with a θ_0 threshold value (see Figure 6.1).

In `WANG` et al. [125] a damage variable D_Ω is introduced, as an average measure of the microcracks at each Gauss point. The values of D_Ω in the

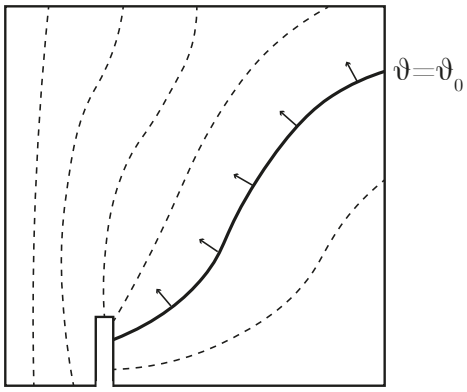

Figure 6.1: Tracking algorithm in [23]: isolines identification, normal to the crack direction.

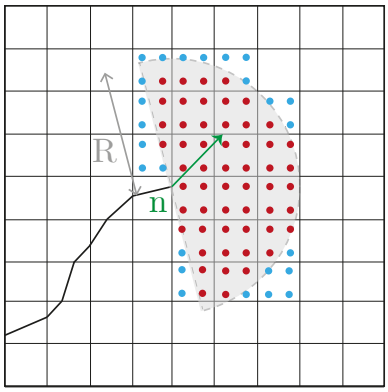

Figure 6.2: Tracking algorithm in [125]: **n** is the growth direction, obtained as a weighted average of the damage values D_Ω calculated in the red Gauss points.

Gauss points close to the crack tip are checked at the end of each loading step: if they exceed a damage threshold value D_{crit}, the existing crack is extended. The crack direction is chosen on the basis of a geometric approach, wherein the crack is located as the medial axis of the damage isoline. In order to take into account contributions related to different elements in the same region and not only to a local element, the growth direction **n** is calculated using a weighted average of bulk damage, calculated on points belonging to a half circle from the crack tip, since the crack is unlikely to snap back. The radius R is a geometric parameter defining where the bell-shaped weighting function is applied. Figure 6.2 explains this procedure (red points are used for the weighted average, blue ones are excluded).

In SALOUSTROS et al. [106], a new crack starts at an element according to a specified tensile damage criterion. Elements which satisfy the failure criterion are labeled as *crack root* elements. By defining a sub-domain radius r_{sub}, the crack root element is identified as the one having the highest value of the tensile equivalent stress and the crack origin is positioned in its centroid. This radius is a parameter of the model, dependent on the mesh dimension. The second phase corresponds to the identification of the so-called *next potential elements* of the

crack. Starting from the crack origin, two vectors $\mathbf{s}_1$ and $\mathbf{s}_2$ are identified, which are perpendicular to $\mathbf{n}$, associated with the maximum principal stress direction, and with opposite orientations. Both for $\mathbf{s}_1$ and $\mathbf{s}_2$, the potential elements are identified by considering the neighbouring elements that share the edge intercepted by the propagation vector, until the influence radius r_{sub} is reached (see Figure 6.3).

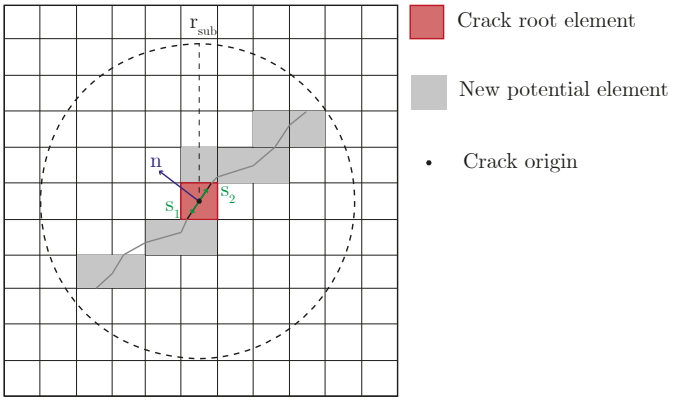

Figure 6.3: Tracking algorithm in [106]: $\mathbf{n}$ is the maximum principal stress direction, $\mathbf{s}_1$ and $\mathbf{s}_2$ are the two possible crack propagation directions.

Rather than using a local approach, based on the information recorded in the neighbouring of the crack tip, in `TAMAYO` et al. [120] a global geometrical approach is proposed. The crack is inserted in the medial axis of the damaged area individuated by the isoline $D = D_{crit}$, which represents the locus of the centres of the interior bitangent circles (Figure 6.4). At the end of each step, if one or more elements reach a damage value $D \geq D_{crit}$, their nodes are marked for the X-FEM enrichment (see section 3.3.1). The technique allows to capture complex crack patterns and the crack branching phenomenon.

6.2 Summary of the implemented algorithm

The entire nonlinear code, based on Algorithm 1 for the generic step and associated to the flowchart in Figure 6.6, can be summarized as follows:

- let us consider a structure where some cracks are present. The groups of elements crossed by a unique crack are referenced here as substructures.

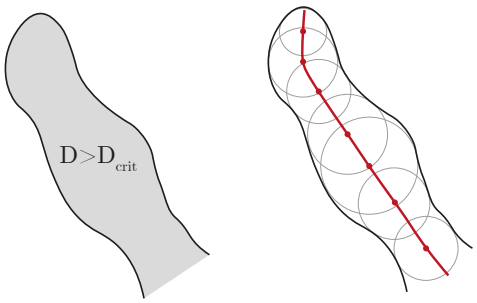

Figure 6.4: Tracking algorithm in [120]: medial axis of the isoline associated with $D = D_{crit}$.

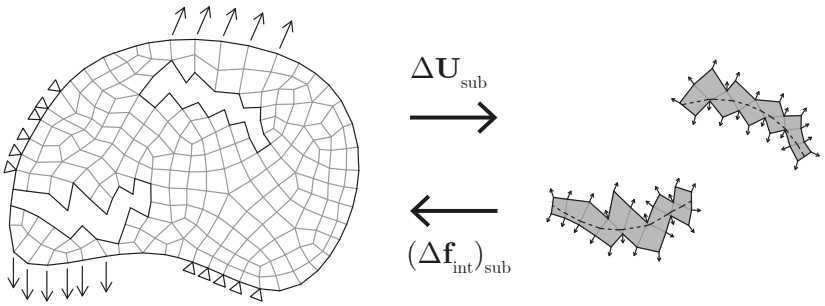

Figure 6.5: Representation of the implemented Algorithm.

At the beginning, the overall structure is analyzed as a composition of not yet localized elements and distinct substructures. Nodal displacements are evaluated at the end of an `ELASTIC PREDICTION` stage (lines 1-13 of Algorithm 1). Then, each substructure is solved individually, considering the displacements exchanged with the rest of the structure as boundary conditions ($\Delta\mathbf{U}_{sub}$); the resulting nodal forces ($\Delta\mathbf{f}_{int_{sub}}$) are then transferred as internal forces to the whole structure. Forces and stiffness matrices of the substructures and of the remaining elements are assembled and convergence checked. If no convergence is reached, a `NONLINEAR CORRECTION` stage (lines 14-18 of Algorithm 1) takes place, which is repeated until convergence, based on a Newton-Raphson iterative procedure (see Appendix C);

- at convergence of the nonlinear correction procedure, the `STRAIN LOCAL-`

IZATION procedure (lines 19-29 of Algorithm 1) is applied to identify new localized elements with associated band position and orientation;

- finally, the CRACK TRACKING ALGORITHM procedure is applied (lines 30-32 of Algorithm 1). New localized elements were either divided into existing substructures or form new ones and manipulated in order to form continuous cracks.

Figure 6.5 illustrates the core of the numerical strategy: substructures are individuated, separately solved (by imposing nodal displacements $\Delta\mathbf{U}_{sub}$) and then assembled with the remaining part of the structure (nodal forces are transferred to the rest of the structure as internal forces $\Delta\mathbf{f}_{int_{sub}}$).

6.3 Band formation, position and orientation

As said in Chapter 2, the strain localization corresponds to a constitutive bifurcation problem, for which the equilibrium equations show a loss of uniqueness. The bifurcation point could be obtained through the acoustic tensor, since the localization condition corresponds to the achievement of its singularity for a specific direction identifying the localization band.
Unfortunately, as shown in Section 4.3.2, the spectral analysis of the aforementioned tensor for the specific IDM does not give the expected localization directions, which are often not consistent with the kinematic conditions.

In the implemented code, fracture insertion occurs when three different constraints are simultaneously verified. For what regards the identification of the bifurcation point, the singularity of the tangent stiffness matrix is looked for or, analogously, the change in the sign from positive to negative of its lowest eigenvalue.

A transition criterion formulated in terms of principal stresses, strains or local damage values is commonly adopted in literature. In practice, when the maximum principal stress or strain or damage reaches an assigned threshold value, the condition of diffuse damage is switched to the condition of localized damage. The proposed formulation is even inspired by this approach, by using the damage variable as the second localization constraint.
Following the formulation reported in [27] and applied in [121, 125], if simultaneously the tangent stiffness matrix becomes singular and if the damage variable $\hat{D}$, averaged on the volume V_e of the element, exceeds a fixed critical damage of the material D_{crit}, a new interphase is inserted in the element and the

continuous-discontinuous transition is applied. This condition can be mathematically written as

$$\hat{D} = \frac{1}{V_e} \int_{\Omega_e} D \, \mathrm{d}\Omega \; > \; D_{crit}. \tag{6.1}$$

In order to give answer to other questions related with the position and inclination of the interphase band, the balance point of damage $\boldsymbol{\rho}_b$ is identified through a damage-weighted average of the coordinates of the integration points, as follows

$$\boldsymbol{\rho}_b = \frac{\sum_{i=1}^{ngp} D_i \, \boldsymbol{\rho}_i}{\sum_{i=1}^{ngp} D_i}, \tag{6.2}$$

where ngp is the number of the Gauss points and $\boldsymbol{\rho}_i$ and D_i are the coordinates vectors and the values of damage variable at the same points, respectively.

Localization direction $\mathbf{n}_b$ coincides with the eigenvector associated with the maximum eigenvalue of the so-called *fracture tensor*, defined as follows:

$$\boldsymbol{T}_b = \frac{\sum_{i=1}^{ngp} D_i \, \mathbf{n}_i \otimes \mathbf{n}_i}{\sum_{i=1}^{ngp} D_i}, \tag{6.3}$$

and built as the damage-weighted average of the tensorial products of the direction $\mathbf{n}_i$ of the maximum principal strain at each Gauss point. This localization criterion permits to overcome the mismatch between numerical and experimental data obtained by using the acoustic tensor criterion. This criterion, at the element level, takes into account the local information recorded on each integration point in a weighted form with respect to its damage level.

Once condition (6.1) and the singularity of the tangent stiffness matrix are verified, $(\boldsymbol{\rho}_b, \mathbf{n}_b)$ are calculated; finally, the third check is performed. This check verifies if the localization direction $\mathbf{n}_b$ is stabilized, comparing the slope evaluated at the actual step with that obtained at the previous one [62]. When the difference in the slopes is below a certain tolerance, even the third condition for localization is reached. Once localization is confirmed, the element is divided into the two sub-domains Ω^+ and Ω^- and the interphase element Ω_b is inserted between them, respecting the position of the balance point $\boldsymbol{\rho}_b$ and localization direction $\mathbf{n}_b$.

Depending on the topology of the two sub-elements, strain and damage values can be initialized at the Gauss points of Ω^+, Ω^-, and Ω_b, exploiting the same shape functions of the original element. In the sub-elements Ω^+ and Ω^- the damage is kept frozen and the response is linear and elastic, with the stiffness attained at the fragmentation instant. Damage, instead, is free to evolve in the interphase element Ω_b.

6.4 The crack tracking algorithm

In presence of new localized elements an efficient crack tracking algorithm is essential to correctly update the fracture path, which must be continuous and representative of the real fracture propagation.
At the end of the strain localization stage in Algorithm 1, some of the elements of the FE mesh could be localized. For these elements the three aforementioned localization checks are all verified and the band in each element is identified through its balance point and orientation.

The number of new localized elements in a load step is dependent on the load step size. As is common in nonlinear FE, in order to avoid inaccurate solutions in terms of crack-path and mechanical response, the load step should be in some way calibrated to the element size and should not be too large. It could happen to see clouds of localized elements, usually having sub-parallel localization bands, as the consequence of the diffuse damage formulation. In these cases not all the localized elements can be crossed by the crack and the clouds need to be in a certain sense 'cleaned'.

An efficient crack tracking algorithm is therefore necessary to correctly transform the bands inside localized elements into macroscopic continuous cracks. The proposed crack tracking algorithm operates in a three-stage process. This process is depicted in a simplified manner in Figure 6.7.

In the first stage all the new localized elements are partitioned into different clusters, as explained in sub-Section 6.4.1 (Figure 6.7-a).

In the second stage, clusters are subsequently converted into substructures (Figure 6.7-b). Only the localized elements ensuring the most correct continuous crack are retained, converting the remaining elements into not localized elements again. The selection is carried out on the basis of specific checks that will be introduced in the sub-Section 6.4.2.

The third stage, described in sub-Section 6.4.3, deals with crack propagation among elements and performs the alignment of bands in order to have continuous cracks (Figure 6.7-c).

The crack tracking algorithm has been numerically structured into three correspondent in-series modules, namely the `NO-BINARY-SEARCH MODULE` (Algorithm 1, line 30), the `UPDATE-SUBS MODULE` (Algorithm 1, line 31), and the `ALIGN MODULE` (Algorithm 1, line 32).

Algorithm 1 Code at step n

▷ Update BCs and/or ext. forces
▶ ELASTIC PREDICTION
$j \leftarrow 1$ ▷ Initialize iterations
$\mathbf{U}_n \leftarrow \mathbf{U}_{n-1}$ ▷ Initialize $\mathbf{U}_n$
$\mathbf{F}_n^{ext} \leftarrow \mathbf{F}_{n-1}^{ext} + \Delta\mathbf{F}_n^{ext}$ ▷ Update ext. forces
$\mathbf{K}_n^{(j)} \leftarrow \mathrm{A}_{e=1}^{e_{no-loc}}(\mathbf{K}_{n-1}^e) + \mathrm{A}_{s=1}^{subs}(\mathbf{K}_{n-1}^s)$ ▷ Assemble global stiffness matrix
$\mathbf{K}_n^{(j)}\,\Delta\mathbf{U}_n^{(j)} = \Delta\mathbf{F}_n^{ext}$ ▷ Solve equilibrium equations
$\mathbf{U}_n \leftarrow \mathbf{U}_n + \Delta\mathbf{U}_n^{(j)}$ ▷ Update mech. & kin. variables
for $s = 1 : subs$ **do** ▷ Loop over all substructures
  $\mathbf{U}_n^s \leftarrow S(\mathbf{U}_n)$ ▷ Extract displ. at subs. boundary nodes
  $\mathbf{F}_n^{int,\,s} \leftarrow$ CALL SOLVE-SUBS($\mathbf{U}_n^s$) ▷ Solve NL problem for subs. imposing $\mathbf{U}_n^s$
end for
$\mathbf{F}_n^{int} \leftarrow \mathrm{A}_{e=1}^{e_{no-loc}}(\mathbf{F}_n^{int,e}) + \mathrm{A}_{s=1}^{subs}(\mathbf{F}_n^{int,s})$ ▷ Assemble int force vector
if $\mathbf{Err}_n^{(j)} = \left|\mathbf{F}_n^{ext} - \mathbf{F}_n^{int}\right| \geq tol$ **then** ▷ check convergence
  ▶ NONLINEAR CORRECTION
  $j \leftarrow j + 1$
  $\mathbf{K}_n^{(j)} \leftarrow \mathrm{A}_{e=1}^{e_{no-loc}}(\mathbf{K}_n^e) + \mathrm{A}_{s=1}^{subs}(\mathbf{K}_n^s)$ ▷ Assemble global stiffness matrix
  $\mathbf{K}_n^{(j)}\,\Delta\mathbf{U}_n^{(j)} = \mathbf{Err}_n^{(j)}$ ▷ Solve equilibrium equations
  go to 7
end if
▶ STRAIN LOCALIZATION
for $e = 1 : e_{no-loc}$ **do** ▷ Loop over not localized elements
  $\lambda_{min}^e \leftarrow eig[\mathbf{K}^e]$ ▷ Find tangent stiffness eigenvalues
  $\hat{D}^e \leftarrow \frac{1}{V_e}\int_{\Omega_e} D\,\mathrm{d}\Omega$ ▷ Calculate volume average of damage
  if $(\lambda_{min}^e \leq 0)\ .and.\ (\hat{D}^e \geq D_{crit})$ **then** ▷ Check localization
    $\rho_b, \mathbf{T}_b \leftarrow$ Use Eqs.(6.2-6.3) ▷ Find balance point & fracture tensor
    $\mathbf{n}_b \leftarrow eig[\mathbf{T}_b]$ ▷ Evaluate band orientation
    if $\left|\mathbf{n}_b^n - \mathbf{n}_b^{n-1}\right| \leq tol$ **then** ▷ Check band stabilization
      $\mathbf{e}_{loc} \leftarrow [\mathbf{e}_{loc}\ e]$ ▷ Insert e among new localized elements
    end if
  end if
end for
▶ CRACK TRACKING ALGORITHM
clusters ← CALL NO-BINARY-SEARCH($\mathbf{e}_{loc}$) ▷ Partition of $\mathbf{e}_{loc}$ into clusters
subs ← CALL UPDATE-SUBS(clusters) ▷ Update existing subs or create new ones
CALL ALIGN(subs) ▷ Align bands in new localized elements

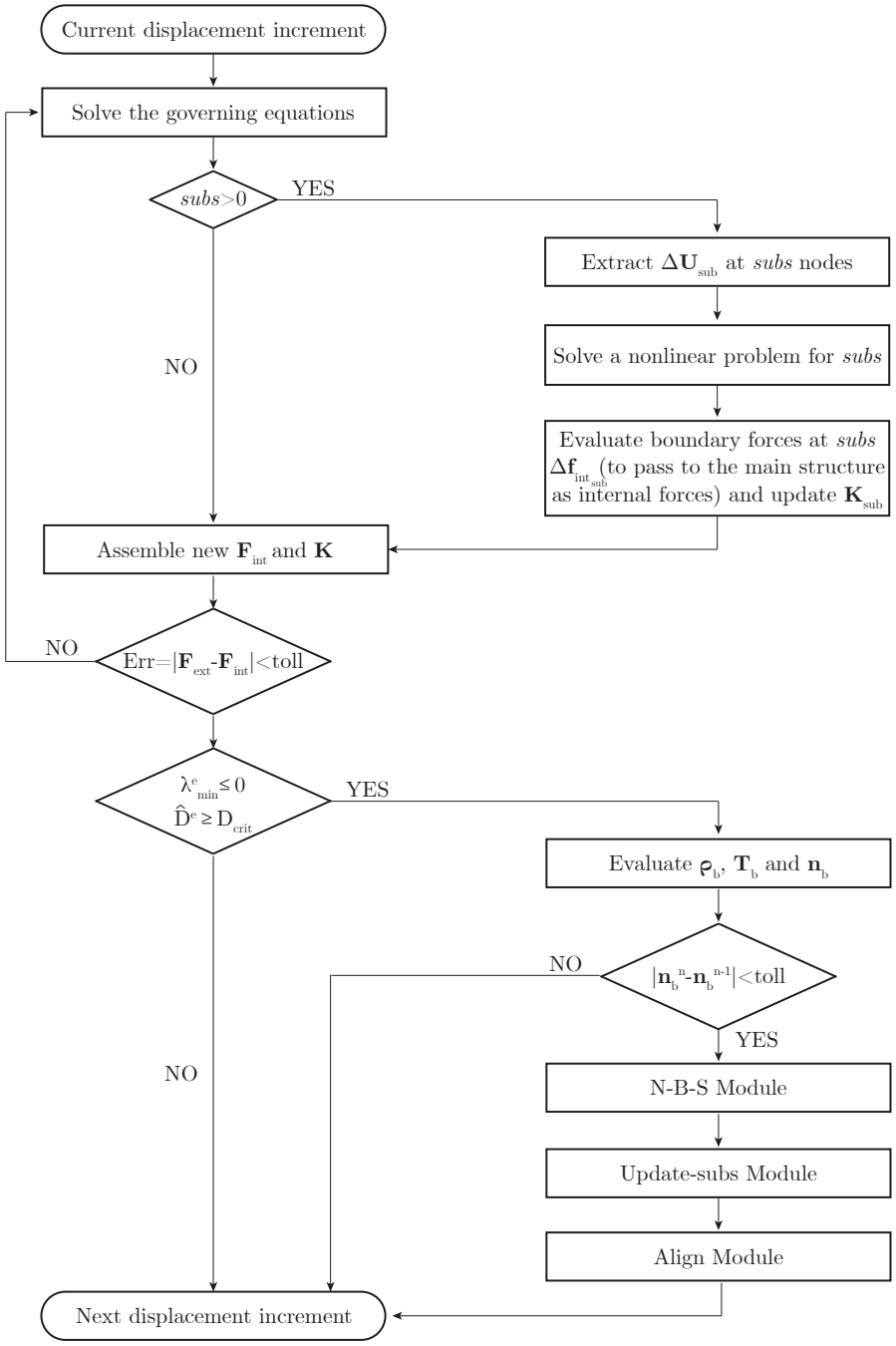

Figure 6.6: Flowchart representation of the implemented Algorithm 1.

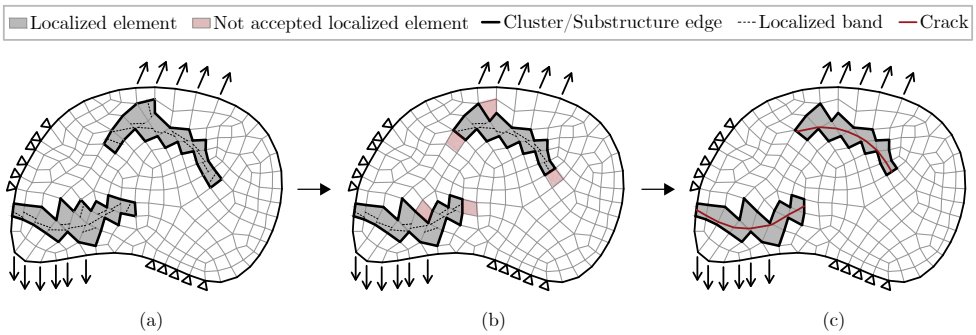

Figure 6.7: Three-stage process of the crack tracking algorithm. (a) Clusters identification. (b) Substructures identification. (c) Alignment of bands in substructures.

6.4.1 Clusters of localized elements

Clustering is an important data exploration technique that in recent years has been applied in different engineering fields. Data clustering consists in dividing a data set into several homogeneous clusters on the basis of fixed constraints. Each cluster contains points that share the same properties and characteristics [96].

Generally, it is possible to distinguish between *partitioning algorithms*, which have the limitation to specify a-priori the number of the clusters, and *hierarchical algorithms*, that is the technique applied in the implemented code to divide new localized elements. In particular, an agglomerative approach is applied, instead of a divisive one. Starting from clusters containing a single element, this technique operates a series of agglomerations in which these small clusters are merged to form larger clusters.

The procedure which collects new localized elements into homogeneous clusters follows the main features of the so-called *No Binary Search* (NBS) contact detection algorithm [87].
For each localized element, a circle of radius R is partially inscribed within the quadrilateral, with a diameter equal to the longest axis bisecting two pairs of opposite sides.
Given two localized elements, when $R_1 + R_2 \geq d$, where d represents the distance between the centres of the two circles, it can be concluded that the two elements are in contact (Figure 6.8-a). In other words, as in [87], all the circles in contact are those for which the distance between their closest point is less or equal to zero, which means that circles overlap or touch. A cluster is therefore

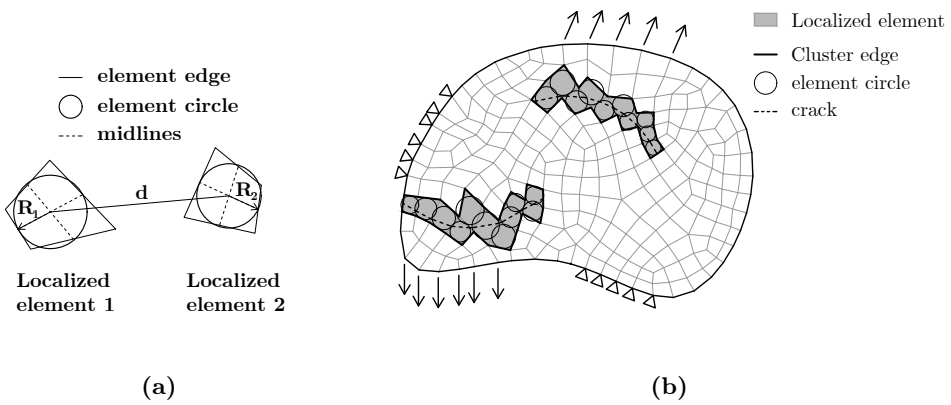

Figure 6.8: Clusters of localized elements. (a) Circles and schematic representation touching check of two elements; (b) global structure with clusters.

a set of elements two by two in contact (Figure 6.8-b).

6.4.2 Substructures of localized elements

The second module is related to the conversion of clusters into one or more substructures. Under specific circumstances, not all the elements of a cluster can be part of a substructure and they need to be opportunely shortlisted. It is therefore necessary, for each cluster, to guarantee the continuity of the crack and to identify all the substructures associated with it.
The selection is made on the basis of a total of four checks. Some of these are consolidated in the literature, some are specifically designed according to the adopted localization criteria. Two of these checks are always invoked, two are recalled anytime the new localized elements could extent an existing crack.
All the four checks are explained in Figure 6.9 and listed below:

- considering the position vector obtained by joining the crack tip with the centroid of the new localized element, its scalar product with the outgoing versor normal to the element edge containing the crack tip must be positive, in order to exclude reversal cracks (Figure 6.9-a):

$$\mathbf{v} \cdot \mathbf{n} > \mathbf{0};$$

- band orientations in two adjacent localized elements must not differ more than a prescribed limit value (Figure 6.9-b), in order to distinguish elements belonging to two different crack paths;
- the extremes of the bands in two adjacent localized elements should share the same edge to avoid locking issues (Figure 6.9-c);
- if almost parallel bands are localized in adjacent elements only one crack is inserted, associated with those elements for which the longest fracture path is obtained (as also represented in Figure 6.9-c) or, in the case of crack involving a single element, associated with the element recording the highest value of damage variable $\hat{D}$ (Figure 6.9-d). Other elements are not accepted and remain not localized.

At the end of the `Update-subs module`, clusters have now been decomposed into substructures, whose lists of associated elements are then returned to the main code. Each list is provided as a sequence of numbers corresponding to the localized elements of every single substructure. A single substructure has to be intended as associated to a unique crack. It is important to highlight that the code does not require 'a-priori' the initialization of a crack. Multiple and simultaneous fractures are also allowed.

6.4.3 Crack propagation criterion

The last part of the crack tracking algorithm (`Align module`) is devoted to the alignment of bands in elements constituting the substructure, in order to guarantee crack-path continuity. Three possibilities arise:

1. extension of existing cracks;
2. merging of existing cracks;
3. formation of a new crack.

Let us analyze the first case. A single crack always has two active tips used to eventually extend the fracture in one direction or the other one, by the attachment of one or more elements. Active tips are located in those elements where circles have a unique connection with another circle. The remaining circles of the chain have instead two connections. The elements in the list, therefore, starting from a crack tip, are ordered following the sequence of the connections to reach the opposite end of the band (Figure 6.10-a).

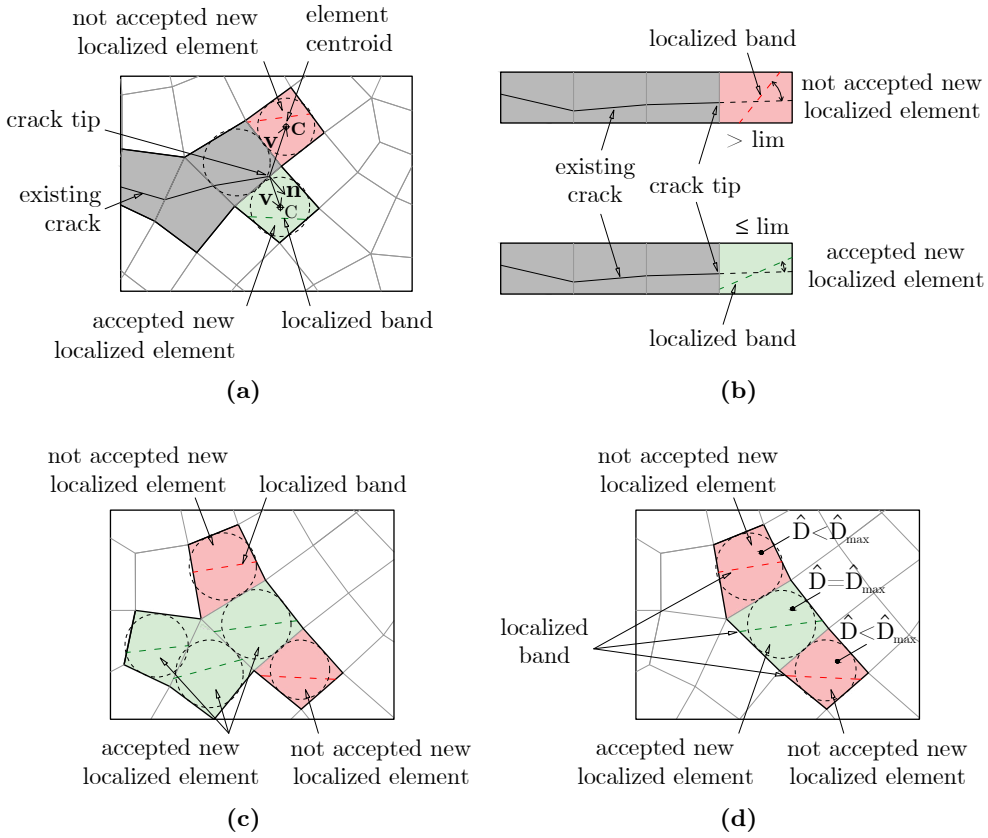

Figure 6.9: Substructures of localized elements: (a) element centroid position check; (b) band slope check; (c) sharing edges or new crack length check; (d) $\hat{D}$ check.

The code starts scanning the existing substructure lists at the previous step and checks if at the actual step new elements have been added. If yes, one or more already existing cracks have been extended. The need for continuity implies that the added band must pass through the crack tip. In this code then the requirement to pass through the balance point is removed while the localization direction is maintained (Figure 6.10-b). The band is translated in parallel by forcing the passage from the crack tip of the adjacent element. If more than one element is added, the procedure continues until the entire list is completed. For each new localized element added to an existing crack four nodes are internally introduced as vertexes of the interphase element. In order

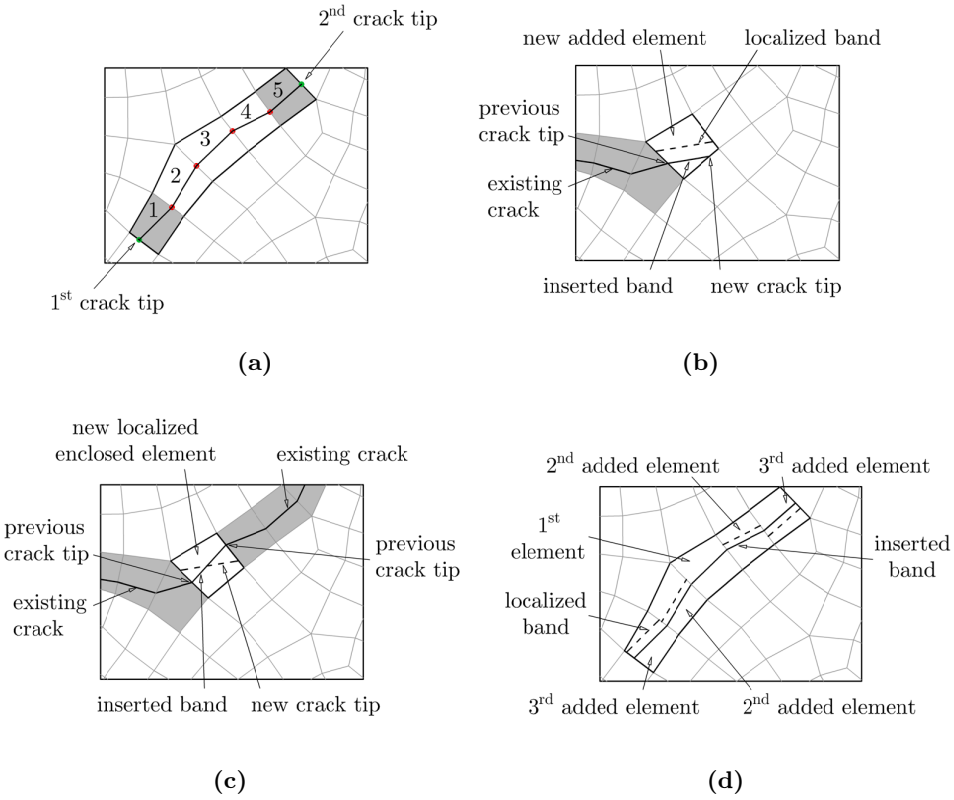

Figure 6.10: Crack propagation: (a) localized elements list; (b) addition of a new element to an existing crack; (c) addition of an enclosed element; (d) insertion of a new crack with more than one element.

to guarantee the deformation continuity among the element containing the new crack tip and the adjacent not localized element that share the same edge, the new internal nodes placed on the crack tip are overlapped and enforced to move together and to lie on the same edge. These constraints are removed once the crack tip moves ahead on a new element.

It could also occur that a new substructure comes from the fusion of two substructures. Initially, it may happen that old cracks are extended by following the order of elements collected in the list of each substructure. Going ahead, there could be an element that is in contact with two substructures. This is the case of an enclosed element, and both requirements of passing from the balance

point and the localization direction are abandoned in favour of the restriction that the band must pass through the two adjacent crack tips (Figure 6.10-c). Additionally, nodes constrained to coincide on the two old crack tips are released.

Finally, once the existing cracks have been scanned over, the remaining new substructures are inserted as new cracks starting from the central element towards the extremes. For the first element, the band is inserted as localized, since both constraints on the balance point and localization direction are maintained. For the subsequent elements, the balance point is substituted by the crack tip, while the band orientation remains unchanged and the band translated (Figure 6.10-d) as for the first case.

The key point of the implemented numerical procedure is to split at the generic time step the solution of the substructures from the solution of the remaining part of the finite element model. In this sense the procedure contemplates two nested nonlinear iterative procedures, one at the substructure level, where the nodal displacements are considered as boundary essential conditions, and the other at the whole model level. At the substructure level, the Newton-Raphson iterative procedure leads to the correspondent boundary nodal forces together with the updated substructure stiffness matrix. The stiffness matrix and the nodal forces contribute to in turn update the stiffness matrix and internal force vector of the whole structure.

Chapter 7

Numerical applications

The effectiveness of the proposed numerical method has been tested through different applications ranging in mode I and combined mode I-mode II loading stress states, reported in the following Sections. Several numerical applications will be presented to illustrate the flexibility and efficiency of the proposed approach and to assess its accuracy and robustness.
Each application is performed in plane stress and under displacement control.
Firstly, a parametric analysis is presented, in order to investigate on the influence of geometric and constitutive parameters.
In Example 2, a single edge notched specimen subjected to a mixed mode I-mode II stress state is tested. This example shows the capability of the crack tracking algorithm to follow the crack pattern in absence of mesh dependency. The same example is also run with three different load step sizes in order to analyze the influence of the load step size on the results and on the convergence of the iterative solution.
In Example 3, a classic three-point bending test is examined. Two simple meshes are used to discretize the fracture propagation zone to further strengthen the mesh independence and investigate on the interphase thickness parameter.
A mode I test on a double edge notched specimen is run in Example 4. The particularity of this example lies in the double crack propagation and in the comparison of the overall response with the similar test performed by Benvenuti et al. [12] who used the regularized X-FEM method.
In Example 5 the capability of the code to reproduce the experimental results for a double edge notched specimen undergoing a combination of mode I-mode II stress state is presented. The same example is exploited to show a comparison between the IPH and the ZTI model.

Example 6 reports the experimental results on an L-shaped concrete specimen, performed following constitutive parameters reported in [77].
Example 7 reproduces a predominantly mode II crack developed in a pull-out test for anchor bolts embedded in concrete, simulated in [116].

For each numerical application, a table including constitutive and geometrical parameters is reported: the Young's modulus E, the Poisson's ratio ν, the elastic limit strain ε_0, the $\frac{\varepsilon_f}{\varepsilon_0}$ ratio, the interphase thickness w_b and the critical damage value D_{crit}.

7.1 Example 1: mode-I and mode-II crack in a single element

Table 7.1: Example 1 - Material parameters.

$E\ [MPa]$	ν	ε_0	D_{crit}
338456	0.15	$2.66E-4$	0.5

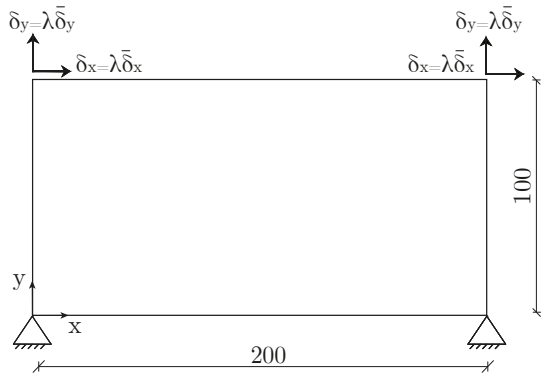

Figure 7.1: Example 1 - Geometry and boundary conditions. Dimensions are given in mm.

A first application, for parametric investigation, was carried out considering a single element of size 200×100 mm, unitary thickness and constitutive parameters given in Table 7.1. The value of critical damage is a not very influential parameter in this case since, being a single element, the damage increases almost abruptly, without affecting the actual instant of band insertion. The boundary conditions are schematically reproduced in Figure 7.1. The analyses were conducted by varying two parameters: the interphase thickness (w_b) and the ($\frac{\varepsilon_f}{\varepsilon_0}$) ratio.

Firstly, the specimen was subjected to a $\delta_x = 0$ and an incremental vertical displacement δ_y, in order to simulate a mode-I fracture. In Figure 7.2 different load-displacement curves are reported for varying interphase thicknesses with $\frac{\varepsilon_f}{\varepsilon_0} = 100$ (Figure 7.2-a) or for varying $\frac{\varepsilon_f}{\varepsilon_0}$ ratios keeping $w_b = 1\ mm$ (Figure 7.2-b).

Similarly, the second simulation considered a value of $\delta_y = 0$ and an incremental horizontal displacement δ_x, in order to simulate a mode-II fracture.

In Figure 7.3 different load-displacement curves are reported for varying interphase thicknesses with $\frac{\varepsilon_f}{\varepsilon_0} = 500$ (Figure 7.3-a) or for varying $\frac{\varepsilon_f}{\varepsilon_0}$ ratios keeping $w_b = 1\ mm$ (Figure 7.3-b).

Figure 7.4 reports the final deformed configuration for mode-I (a) and mode-II (b).

The curve falls the faster the smaller both the interphase thickness and the $\frac{\varepsilon_f}{\varepsilon_0}$ ratio. Remembering the expression of strain in the interphase element, in fact, as the thickness increases, the strain decreases and thus the lower the damage value will be, implying a higher stress and, consequently, a higher force in Figures 7.2-a and 7.3-a. For the same reason, since the damage variable has the value $\varepsilon_f - \varepsilon_o$ in the denominator, as the ratio $\frac{\varepsilon_f}{\varepsilon_0}$ increases the damage variable decreases and thus the force in the load-displacement curves in Figures 7.2-b and 7.3-b increases.

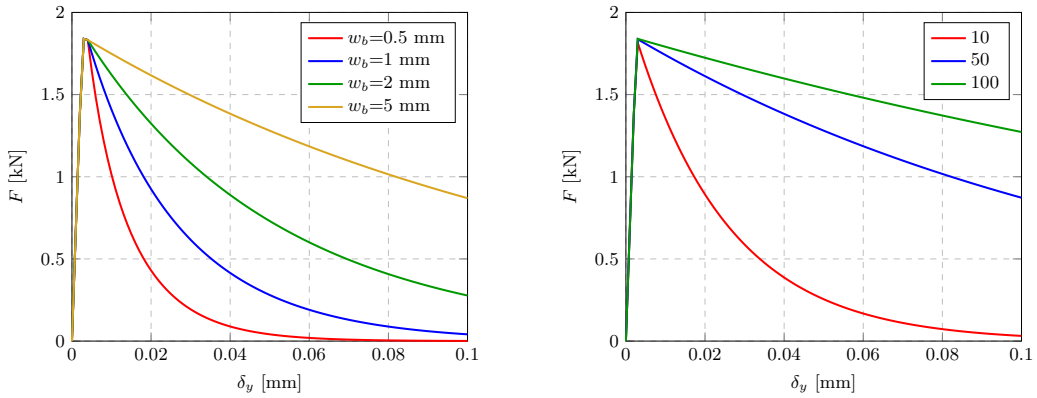

Figure 7.2: Example 1 - Load-displacement curves, related to the mode-I crack, for different interphase thicknesses w_b (a) and different $\frac{\varepsilon_f}{\varepsilon_0}$ ratios (b).

7.2 Example 2: single edge notched specimen under mixed mode

In sub-Section 4.2.3 the mesh-size dependency of the IDM has been tested by referring to a single edge notched square specimen under mixed mode. Boundary conditions are reported in Figure 4.6 on page 89 and the analyzed regular

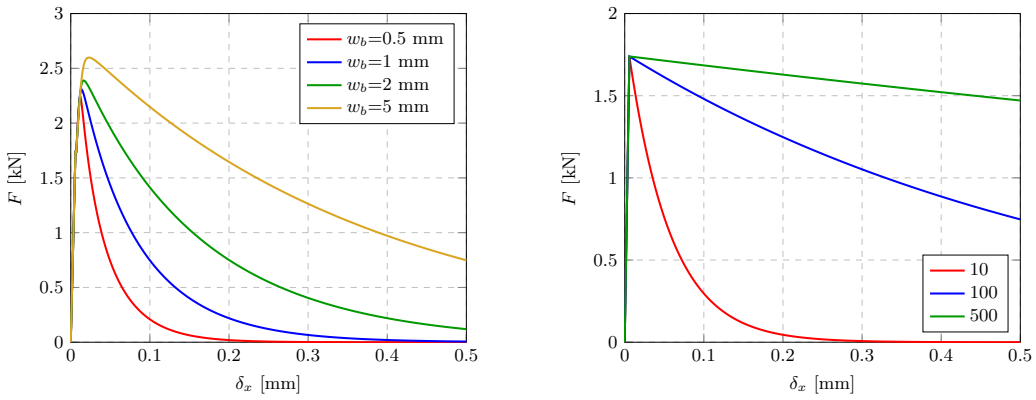

(a) **(b)**

Figure 7.3: Example 1 - Load-displacement curves, related to the mode-II crack, for different interphase thicknesses w_b (a) and different $\frac{\varepsilon_f}{\varepsilon_0}$ ratios (b).

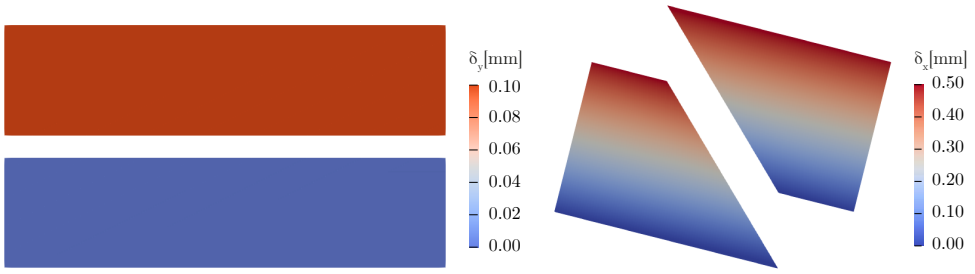

(a) **(b)**

Figure 7.4: Example 1 - Final deformed shapes for the (a) mode-I and (b) mode-II.

Table 7.2: Example 2 - Material parameters.

$E\ [MPa]$	ν	ε_0	$\frac{\varepsilon_f}{\varepsilon_0}$	$w_b\ [mm]$	D_{crit}
1000	0.2	$1.0E-3$	100	1	0.1

meshes (RM) and skewed meshes (SM) in Figures 4.7-4.8 on page 89, respectively. The same previous analyses were performed with the implemented code, in which the strain localization module is activated, allowing the previously tested diffuse damage condition to be switched to a localized fracture condition.

Tests on each one of the five meshes have been run by referring to constitutive parameters reported in Table 7.2.

For each test, a crack begins to propagate from the notch toward the right edge of the specimen, maintaining the same inclination for all tests. The final fracture patterns are shown in Figure 7.5-b. It can be seen that the fractures are very similar and almost overlapping, with a slight difference due to the mesh size.

No influence due to mesh orientation is observed. This is an important result since it is known from literature [105] how much the application of a bias factor to the mesh can affect the overall behaviour. As known, the so-called *directional mesh-bias dependency/sensitivity* is a common numerical difficulty reported in the simulation of propagating cracks in solids. Many simulations have reported how fractures tend to propagate following the orientation of the finite elements' edges: in this example, however, this problem has not been encountered.

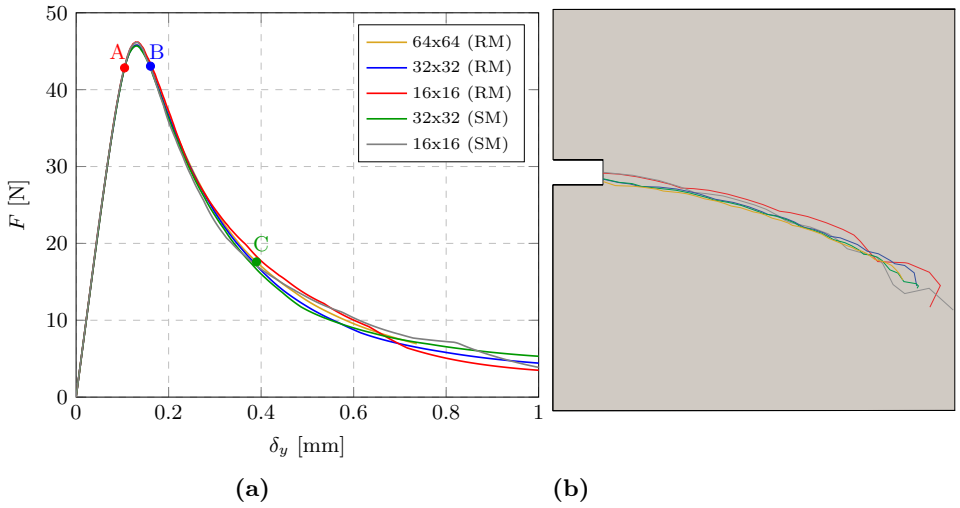

Figure 7.5: Example 2 - (a) Load-displacement curves; markers A, B, C indicate three states for which the deformed shapes are plotted in Figure 7.6. (b) Crack patterns: the fractures are mostly overlapping.

Load-displacement curves, in Figure 7.5-a, are in good agreement with each other, confirming the absence of mesh-dependence of the response. This result is in contrast with the different curves reported in Figure 4.9 on page 90, when

the same tests were run without activating the localization but allowing only the damage evolution: in this case, a strong mesh dependency was encountered.

The damage constitutive model returns a nonlinear behaviour with softening. After the initial elastic phase, the highest principal strains are concentrated near the notch, leading to strain localization and crack initiation. The nonlinear phase reaches its peak at around 45 N, beyond which crack evolves quicker dividing the specimen into a lower block, which remains mostly stationary throughout the test, and an upper one.

In Figure 7.6 the deformed shapes and the related crack patterns for the 64× 64 RM are reported at the three marked points of Figure 7.5-a, corresponding to a $\bar{\delta}_y$ multiplier λ equal to 0.105 (point A), 0.161 (point B), 0.390 (point C) respectively. Crack evolves from the lower part of the notch toward the opposite edge of the specimen following a curvilinear trajectory.

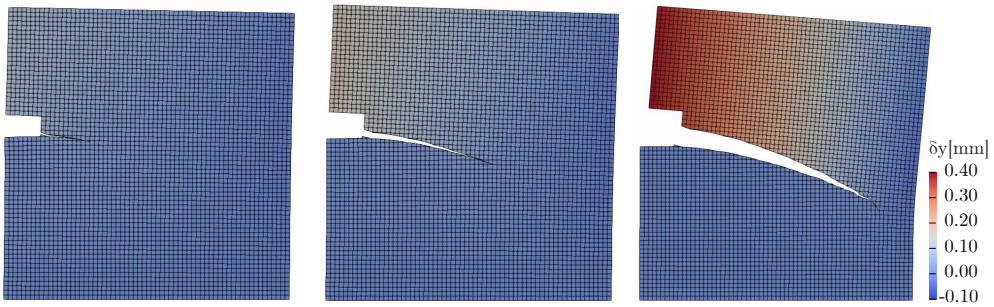

Figure 7.6: Example 2 - Deformed shapes at points (a) A, (b) B, and (c) C indicated in Figure 7.5-a.

The same test is run on the 32×32 SM in order to show the convergence behaviour of the numerical code. Three different load step sizes are considered, so that the influence of the load step size can be highlighted. In the first test the amplitude of the imposed vertical displacement in the step is equal to $\Delta\delta_y = 2 \cdot 10^{-4}\ mm$, for a total of 5000 steps. In the second and third tests the step size is 10 times and 15 times that one of the first test, respectively.
The results in terms of load-displacement curves are shown in Figure 7.7-a. As expected from the literature, a loading increment influences the peak force value for a fixed grid spacing. Besides, the crack patterns show differences in their final parts (Figure 7.7-b), bringing to different residual load values. The difference in the residual loads could be explained considering the different

amount of elements remaining between the crack and the right edge of the specimen, constituting a sort of rotational hinge with a different stiffness. The farther this hinge is from the right edge of the specimen the greater the upper part of the specimen that is resistant and, therefore, the higher the residual force in the associated curve.
Convergence data are reported in Tables 7.3-7.4 and 7.5 for the same multipliers λ (A, B, C) and for each load step size respectively. In each table the errors at the end of the global time steps are reported, together with the number of iterations used to reach convergence at the substructure level. The quadratic convergence is ensured and the number of iterations increases at the increasing of the load step size.

Table 7.3: Example 2 - Convergence data with $\Delta\delta_y = 2 \cdot 10^{-4}$ mm.

Global n_{it}	A (Step 525)		B (Step 805)		C (Step 1950)	
	Error	Total n. local iter.	Error	Total n. local iter.	Error	Total n. local iter.
1	1.11E-4	3	5.48E-5	3	3.61E-6	2
2	5.13E-10	3	3.49E-10	3	2.53E-13	2
3	1.05E-14	3	2.92E-14	3	-	-

Table 7.4: Example 2 - Convergence data with $10\Delta\delta_y$.

Global n_{it}	A (Step 52)		B (Step 80)		C (Step 195)	
	Error	Total n. local iter.	Error	Total n. local iter.	Error	Total n. local iter.
1	2.22E-2	4	8.12E-3	3	1.60E-3	3
2	2.05E-3	4	4.35E-6	3	1.36E-7	3
3	1.85E-8	4	9.76E-13	3	1.12E-13	3
4	9.12E-15	4	-	-	-	-

Table 7.5: Example 2 - Convergence data with $15\Delta\delta_y$.

Global n_{it}	A (Step 34) Error	A (Step 34) Total n. local iter.	B (Step 54) Error	B (Step 54) Total n. local iter.	C (Step 130) Error	C (Step 130) Total n. local iter.
1	3.11E-1	5	3.30E-1	4	9.89E-4	3
2	3.83E-2	4	1.38E-2	4	2.22E-8	3
3	1.59E-4	4	2.49E-3	4	1.15E-13	3
4	6.05E-9	4	4.20E-8	4	-	-
5	1.01E-14	4	1.91E-14	4	-	-

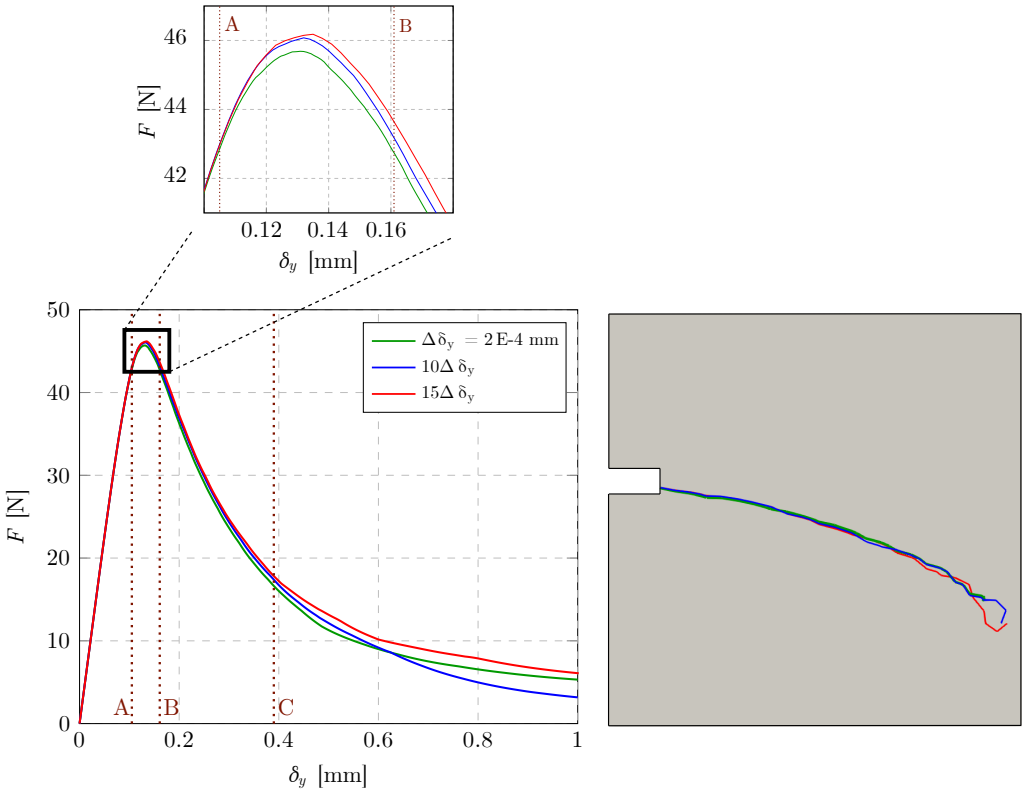

(a) **(b)**

Figure 7.7: Example 2 - Influence of the load step size: (a) Load-displacement curves; (b) crack patterns.

7.3 Example 3: three-point bending test

Table 7.6: Example 3 - Material parameters.

$E\ [MPa]$	ν	ε_0	$\frac{\varepsilon_f}{\varepsilon_0}$	D_{crit}
20000	0.2	$1.2E-4$	58	0.5

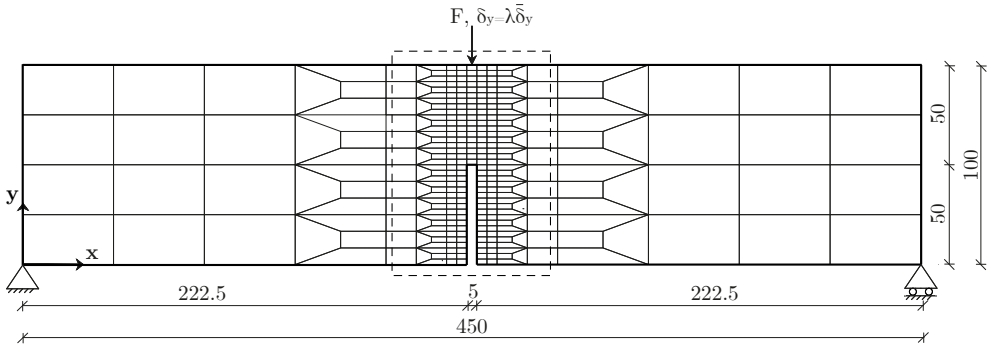

Figure 7.8: Example 3 - Geometry and boundary conditions. Dimensions are given in mm.

In this example, a classical three-point bending test is analyzed, for which the crack is expected to evolve in the pure mode-I. The specimen geometry and boundary conditions are given in Figure 7.8; thickness is unitary. Material parameters are given in Table 7.6. Since the evolution of the crack is rather simple in this application, the real purpose of the test is to investigate the effect of the interphase thickness parameter, ascertained that the fracture appears vertical. In addition, this test is used to compare the advantages of the implemented model with respect to the classic diffused crack model.

For this purpose, let us consider the two different meshes adopted for the strip above the notch, as shown in Figure 7.9. Specifically, the mesh in Figure 7.9-a (M1) has one vertical row of elements only, with a width equal to that of the notch (5 mm), while the mesh in Figure 7.9-b (M2) has three vertical rows of elements, each one having width equal to one-third that of the notch (5/3 mm). The mesh outside the localization zone is left unchanged. All the elements are quadrilateral and bilinear.

At the beginning, tests are performed on both meshes considering the dif-

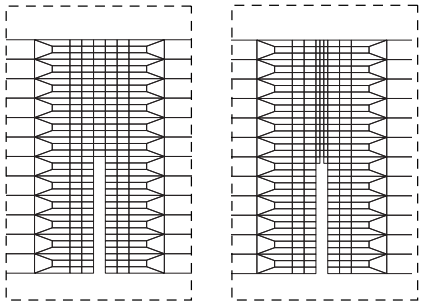

Figure 7.9: Example 3 - (a) Mesh 1 (M1); (b) Mesh 2 (M2).

fused approach, until the final displacement $\bar{\delta}_y = 0.5\ mm$. The resulting nonlinear behaviour is represented by the load-displacement curves plotted as dotted lines in Figure 7.10. Since damage localizes in elements of different width, and thus is more concentrated the thinner the elements, a lower load-displacement curve is obtained running the M2 mesh. Considering that same material parameters are used for both meshes, the different result depends on the different mesh size only.

Subsequently, the same test is run on M1 mesh using the proposed model, by considering an interphase thickness ranging from 0.5 mm to 5 mm. As highlighted in Figure 7.10, a greater thickness correlates with a higher load-displacement curve, as expected. Besides, when the interphase thickness equals the element width of M1 or M2 mesh, the load-displacement curve overlaps the corresponding dotted line, demonstrating that even in this case the results are not mesh-dependent.

Figure 7.11 shows a comparison between the diffused approach (on the left) and the proposed one (on the right) in terms of damage distribution and deformed shape at a multiplier $\lambda = 0.24$ of the final imposed displacement. Figure 7.11-a corresponds to points A of Figure 7.10, while Figure 7.11-b to points B. Considering that the proposed model freezes damage outside the interphase and that damage inside the interphase isn't visible in Figure 7.11, the damage maps after strain localization look less intense with respect to the diffused approach, where damage is distributed all over the elements.

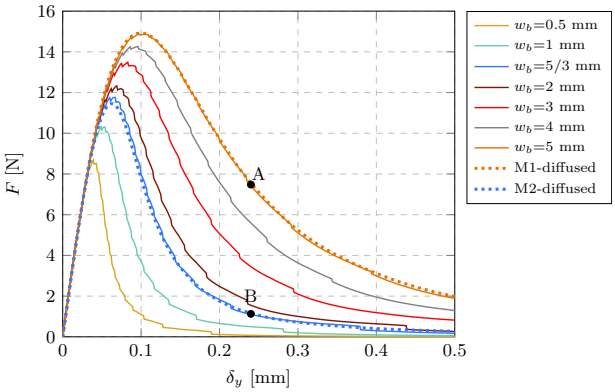

Figure 7.10: Example 3 - Load-displacement curves. Markers A and B indicate two states for which the deformed shapes are plotted in Figure 7.11.

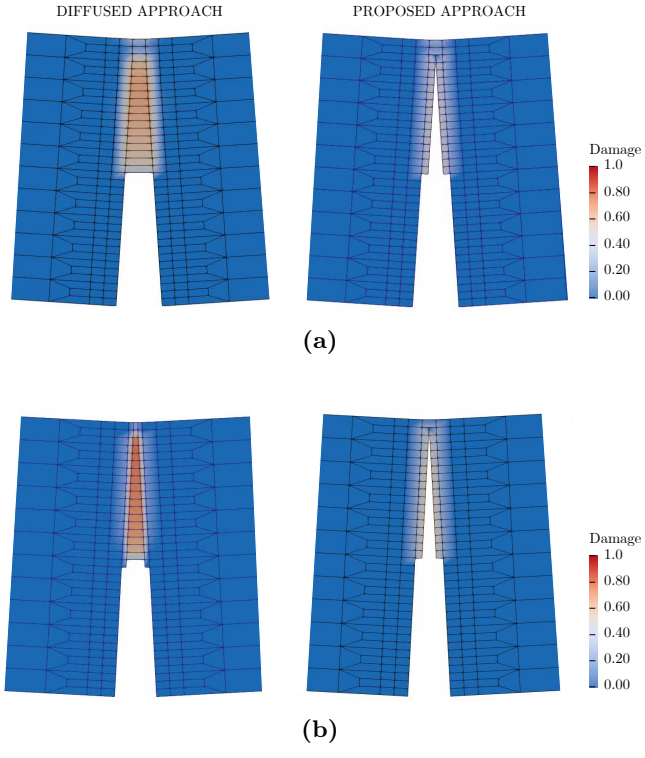

Figure 7.11: Example 3 - Damage maps and deformed shapes comparison between the proposed approach applied on M1 mesh (on the right) and the diffused approach (on the left) for (a) M1 and (b) M2 meshes.

7.4 Example 4: double edge notched specimen under tensile load

Table 7.7: Example 4 - Material parameters.

$E\ [MPa]$	ν	ε_0	$\frac{\varepsilon_f}{\varepsilon_0}$	$w_b\ [mm]$	D_{crit}
2000	0.2	$5E-4$	500	1	0.55

In this test on a double edge notched specimen, the fracture opens in mode I. The special feature of this test is related to the simultaneous propagation of two cracks which finally merge into one. Our results were also compared with others available in the literature and, in particular, with those obtained by Benvenuti et al. [12]. For this purpose, the same geometry and material parameters as in [12] are adopted. The geometry of the specimen, which has a thickness of 10 mm, is reported in Figure 7.12-a, where the coarser mesh, boundary and loading conditions are also visible. Figure 7.12-b shows instead a second adopted denser mesh, also used in this case to demonstrate that the code is not mesh-dependent. Material parameters are listed in Table 7.7. All elements are quadrilateral and linear. The specimen is constrained on the underside and loaded by imposing vertical incremental displacements $\lambda\bar{\delta}_y$ on the upper edge until the final value of $\bar{\delta}_y = 1\ mm$ is reached.

The load-displacement curves for the two meshes are reported in Figure 7.13, together with the numerical result of the regularized X-FEM model reported in [12]. Since the interphase thickness is fixed to 1 mm for both meshes and cracks proceed in a perfectly horizontal manner, both coarse and dense meshes return the same mesh independent response. This behaviour is also in very good agreement with reference [12].

Strain localization occurs when the load-displacement curve reaches its peak value. At this point, two cracks appear symmetrically at the two notches, propagate during the softening branch and meet halfway until they merge on the symmetry axis. Crack patterns are reported, for the denser mesh, on the deformed shapes of Figure 7.14, corresponding to a multiplier $\lambda = 0.104$ (Figure 7.14-a), $\lambda = 0.116$ (Figure 7.14-b), and $\lambda = 0.134$ (Figure 7.14-c), respectively.

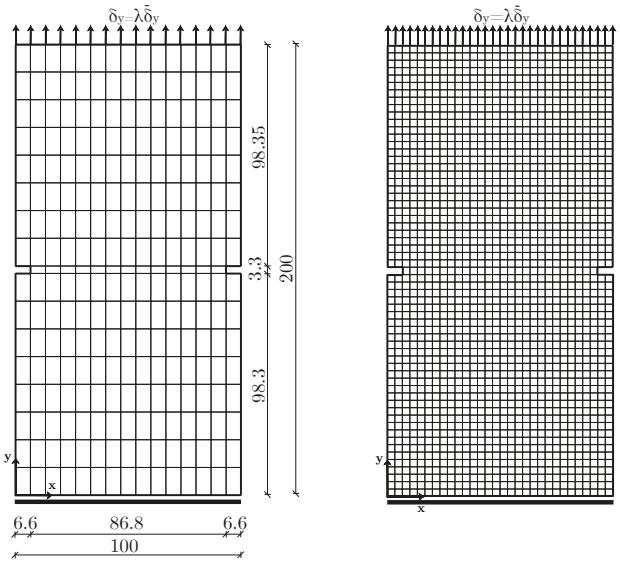

(a) **(b)**

Figure 7.12: Example 4. Meshes and boundary conditions, with dimensions given in *mm*. (a) Coarse mesh, (b) Dense mesh.

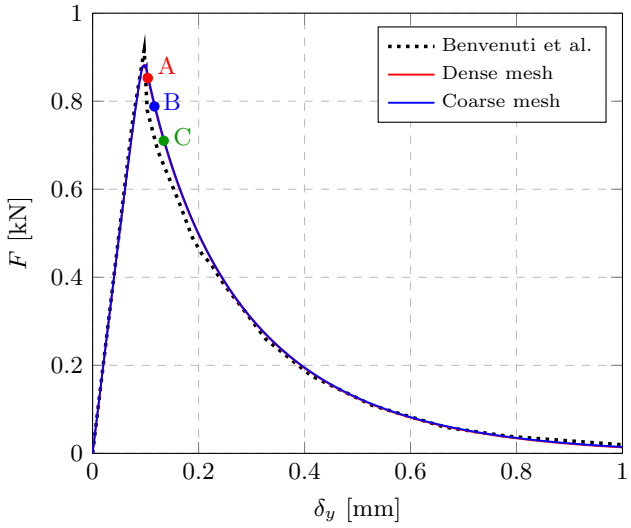

Figure 7.13: Example 4 - Load-displacement curves. Markers A, B, C indicate three states for which the deformed shapes are plotted in Figure 7.14.

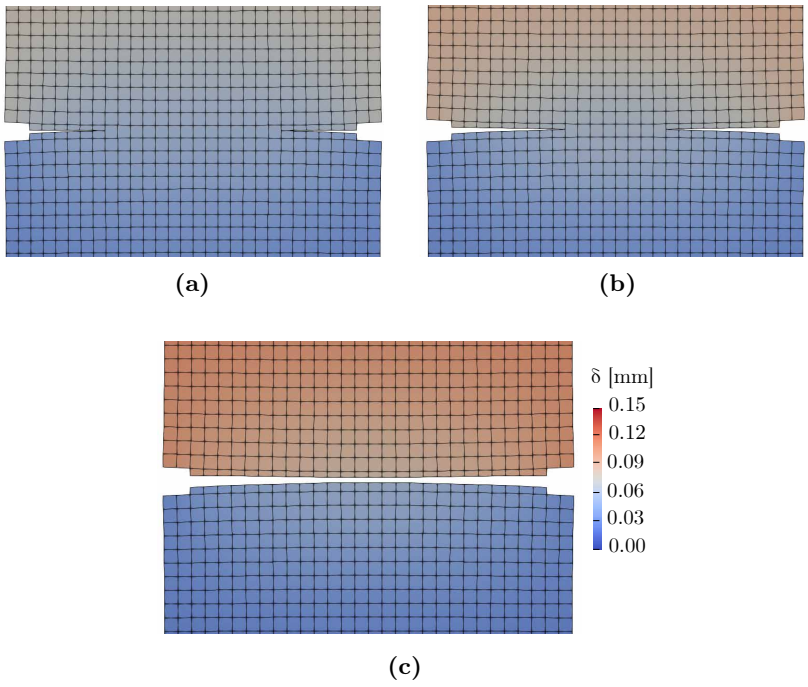

Figure 7.14: Example 4 - Crack evolution on deformed shapes at steps (a) A, (b) B, (c) C of Figure 7.13.

7.5 Example 5: double edge notched specimen under mixed mode

Table 7.8: Example 5 - Material parameters.

$E\ [MPa]$	ν	ε_0	$\frac{\varepsilon_f}{\varepsilon_0}$	$w_b\ [mm]$	D_{crit}
20000	0.2	$1.38E-4$	140	1	0.1

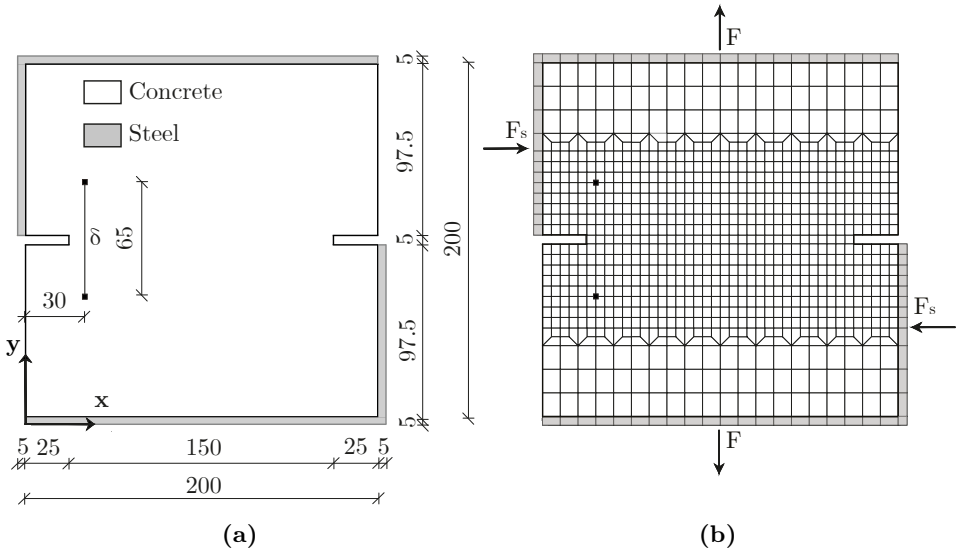

Figure 7.15: Example 5 - (a) Geometry and boundary conditions; (b) Numerical mesh. Dimensions are given in mm.

The aim of this example is to compare numerical results with experimental data. Experimental reference is the double edge notched concrete specimen tested by Nooru-Mohamed in 1993 [89], which was subjected to a mixed-mode loading machine. The experimental apparatus consisted of two independent rigid plates capable of causing a combination of shear and tensile (or compressive) stress on the specimen. Among the different experimental tests conducted in [89], the so-called loading paths '4*a*' and '4*b*' have been simulated, based on a 200 *mm* square specimen with two symmetrical notches, as depicted in Figure 7.15-a. The two rigid loading frames were fully anchored to the specimen

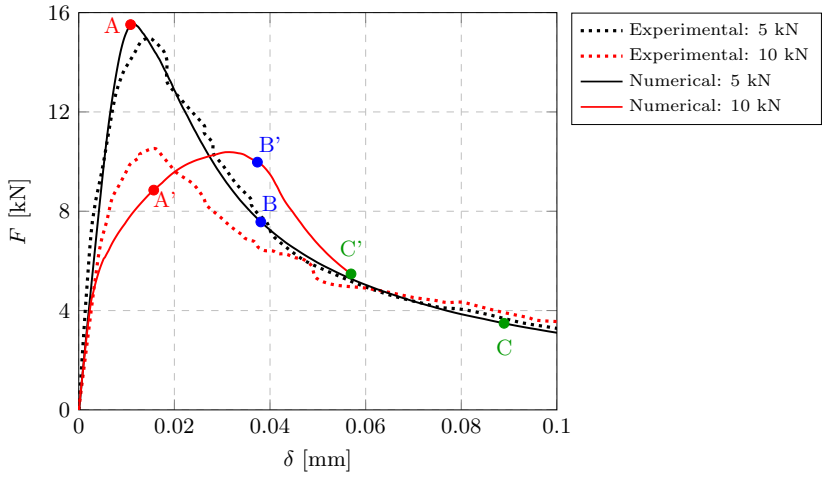

Figure 7.16: Example 5 - Load-displacement curves. Markers A, B, C indicate three states for which the deformed shapes are plotted in Figure 7.17. Markers A', B', C' indicate three states for which the deformed shapes are plotted in Figure 7.18.

throughout its entire thickness of 50 mm. The experimental load was applied in two stages. In the first stage, the specimen was laterally pushed in displacement control until the resultant force F_s reached the values of 5 kN for paths 4a and 10 kN for paths 4b. In the second stage, the horizontal force F_s achieved was held constant, while the test continued by imposing incremental vertical displacements on the lower and upper edges.

In [89] the experimental load-displacement curves were reported in terms of vertical resultant force F versus the relative vertical displacement δ between the two control points highlighted in Figure 7.15-a. The resulting experimental curves are plotted as dotted lines in Figure 7.16. The observed crack pattern consisted of two curved fractures that originated at the notches with a greater slope the higher the F_s lateral force, and propagated symmetrically in parallel. Nooru-Mohamed stated that, although the experimental machine was precise and sophisticated, undesirable eccentricities associated with the skew-symmetry of the test were observed. These effects could be the cause of imperfectly symmetrical experimental cracks and could influence the load-displacement curves.

Numerical tests have been simulated considering the mesh shown in Figure 7.15-b. This is composed of 910 initially quadrilateral linear elements, with a denser mesh in the crack propagation zone. In order to accurately reproduce the loading phases, elements representing the steel frames, modelled with

structural steel constitutive parameters, have been firstly pushed horizontally under displacement control. The imposed displacements have been calibrated in order to obtain F_s exactly equal to 5 kN or 10 kN. Once F_s has reached its prescribed value, horizontal constraints on the lateral loaded edges have been converted into externally applied forces which have been maintained constant throughout the rest of the test. Then, the specimen has been vertically stretched under displacement control. The vertical displacement δ reported in Figure 7.16 is the relative one between the two control points marked in Figure 7.15-b. Material parameters are those provided by [93] and given in Table 7.8.

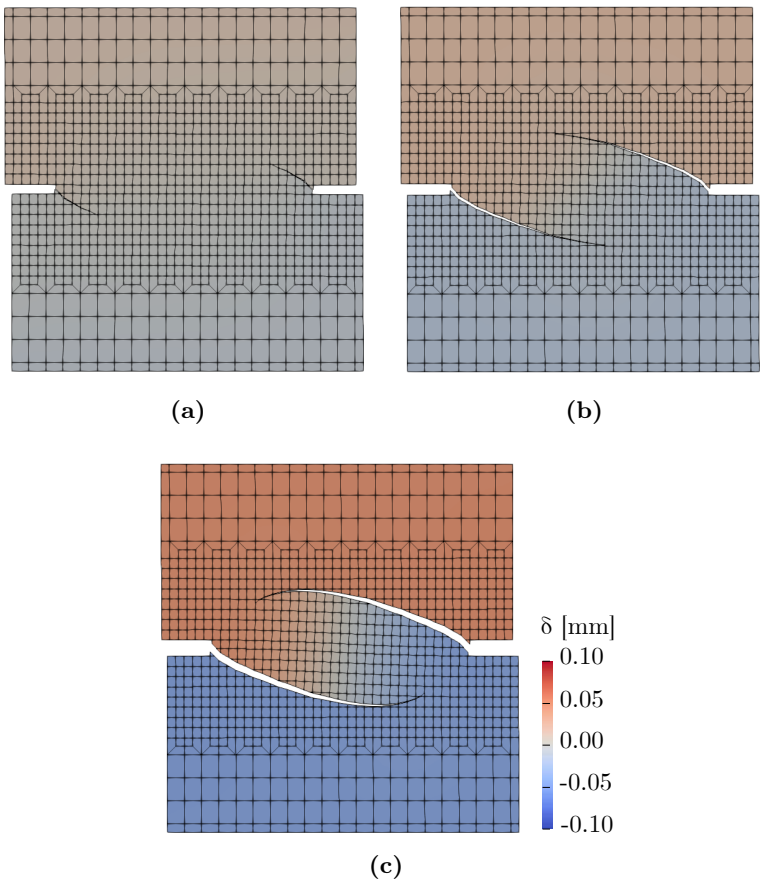

Figure 7.17: Example 5 - Crack evolution at steps (a) A, (b) B, (c) C of Figure 7.16, when $F_s = 5$ kN.

In Figure 7.16 is evident a good match between numerical and experimental curves in the 5 kN case, for which the numerical parameters are calibrated. The numerical response associated with the 10 kN case, moreover, shows a peak equal to the experimental one, the same initial stiffness and a similar nonlinear trend. However, after crack initiation, the nonlinear behaviour results more deformable and, consequently, for the same force there is a higher δ value in the numerical curve with respect to the experimental curve. From the numerical point of view, this discrepancy could be possibly associated with the value of interphase thickness adopted for both cases; on the other hand, from an experimental point of view, it could be related to the undesirable eccentricities mentioned above.

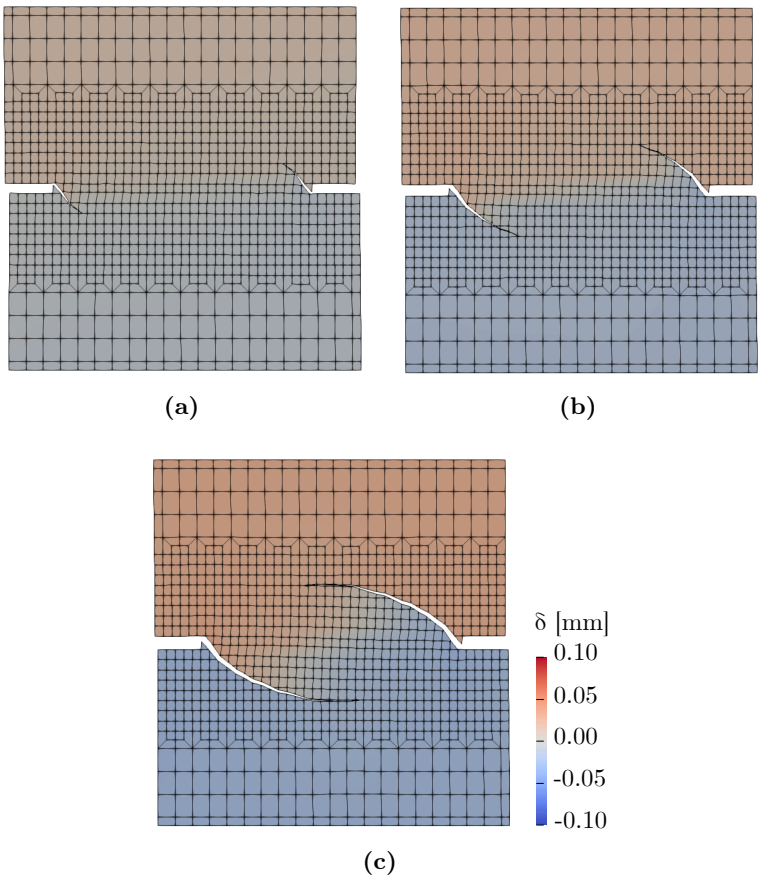

Figure 7.18: Example 5 - Crack evolution at steps (a) A', (b) B', (c) C' of Figure 7.16, when $F_s = 10\ kN$.

The crack evolution at points A, B, and C marked in Figure 7.16 is shown in Figure 7.17 for the $F_s = 5\ kN$ case. Similarly, Figure 7.18 shows the crack evolution at the points A', B', and C' marked in Figure 7.16. Cracks nucleate and propagate symmetrically, as expected. Cracks propagating in the 5 kN case are more flattened with respect to the 10 kN case, as happened experimentally. Overall, it can be concluded that the comparison between the numerical and experimental results is generally good.

In order to show the influence of internal stresses and strains in the overall mechanical response of the FE model, the $F_s = 5\ kN$ case is run considering an interface element, that is obtained by neglecting the internal components in the stiffness matrix of the interphase element. The mechanical response in terms of load-displacement curves is shown in Figure 7.19-a and the associated crack patterns in Figure 7.19-b. Almost overlapping cracks appear, both modelling the discontinuity as an interphase or an interface element. Given the same boundary and constitutive conditions, although the fracture process is governed by tensile tractions, the load-displacement response in the post-peak stage is lower respect to the interphase one. Not taking into account the internal components implies that the interface element underestimates the stresses developed in the discontinuity and, therefore, the associated forces.

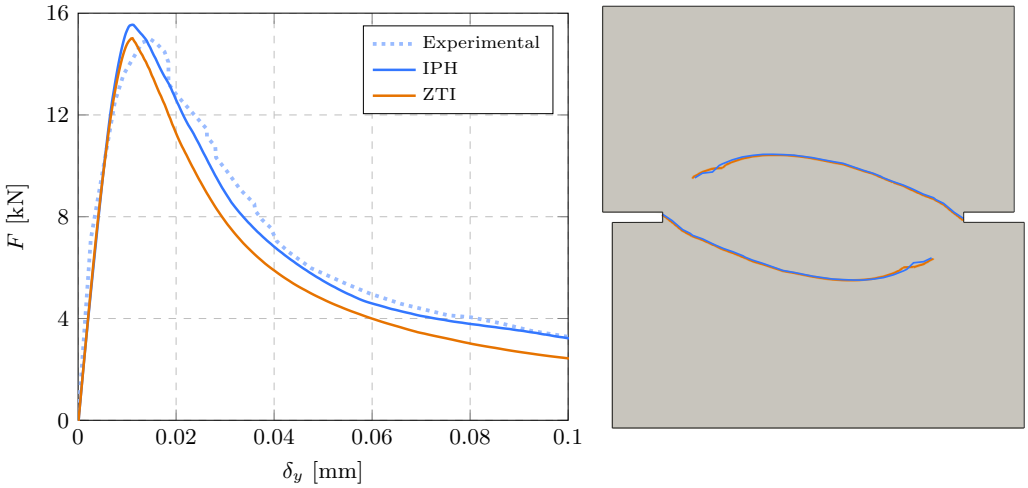

Figure 7.19: Example 5 - IPH/ZTI comparison: (a) Load-displacement curves; (b) crack patterns.

7.6 Example 6: L-shaped concrete specimen

Table 7.9: Example 6 - Material parameters.

$E\ [MPa]$	ν	ε_0	$\frac{\varepsilon_f}{\varepsilon_0}$	$w_b\ [mm]$	D_{crit}
18000	0.18	$1.5E-4$	30	10	0.1

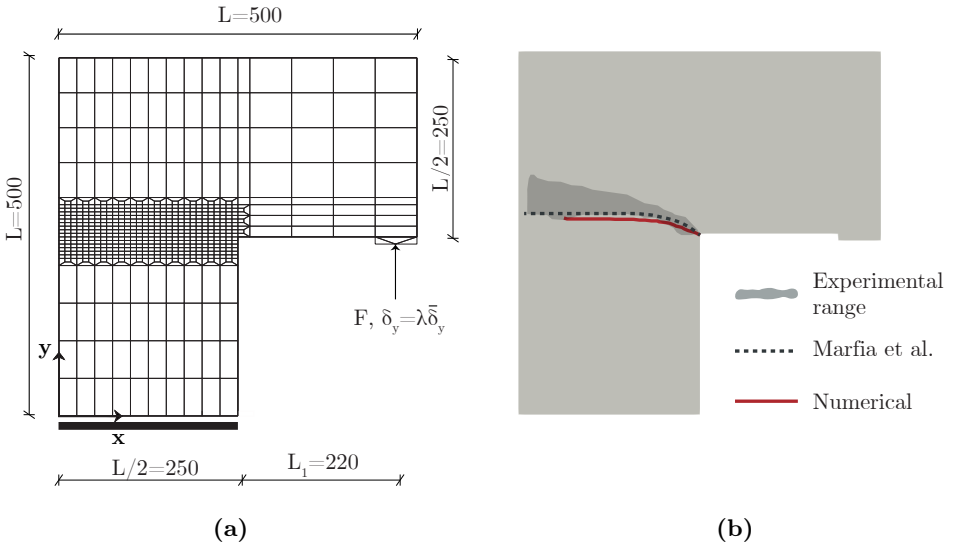

Figure 7.20: Example 6 - (a) Geometry and boundary conditions, with dimensions given in mm. (b) Comparison between experimental and numerical crack patterns.

A concrete L-shaped specimen experimentally investigated in [127], is addressed in this section. Numerical simulations have been carried out using the constitutive and geometrical parameters reported in Table 7.9, which are the same of those used by Marfia et al. in [77, 85]. The specimen is constrained on the bottom side, while a single point at $(L_1 + \frac{L}{2}, \frac{L}{2})$ is subjected to a vertical incremental displacement $\lambda\bar{\delta}_y$. The thickness of the specimen is 100 mm. Figure 7.20-a shows the geometry of the specimen and the simulated mesh. The final value of the vertical maximum applied displacement is $\bar{\delta}_y = 1\ mm$.

Fracture originates at the inner L-node at $\lambda = 0.05$, which corresponds to the point of greatest strain concentration, and then propagates almost hori-

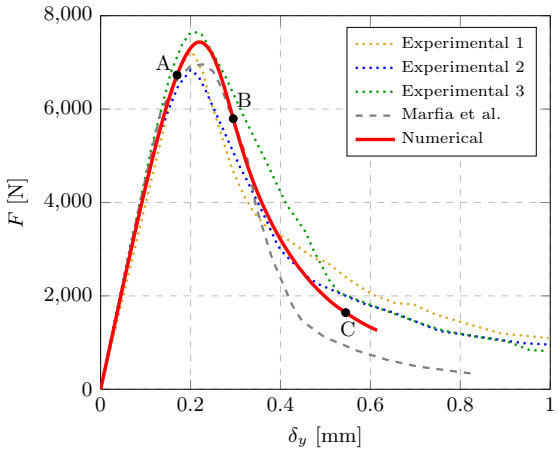

Figure 7.21: Example 6 - Load-displacement curves. Markers A, B, C indicate three states for which the deformed shapes are plotted in Figure 7.22.

zontally. Figure 7.20-b shows the area of propagation of experimental cracks, together with the numerical patterns obtained in this study and in [77]. These two appear to be mostly overlapping.

The load-displacement curves, both for the experimental tests and the numerical ones, are reported in Figure 7.21. Curves are in good agreement: during the softening branch the evolution of the fracture separates the specimen in two parts.

In Figure 7.22 the deformed shapes and crack patterns are reported at the three marked points of Figure 7.21, corresponding to a multiplier λ equal to 0.175 (point A), 0.3 (point B), 0.550 (point C), respectively.

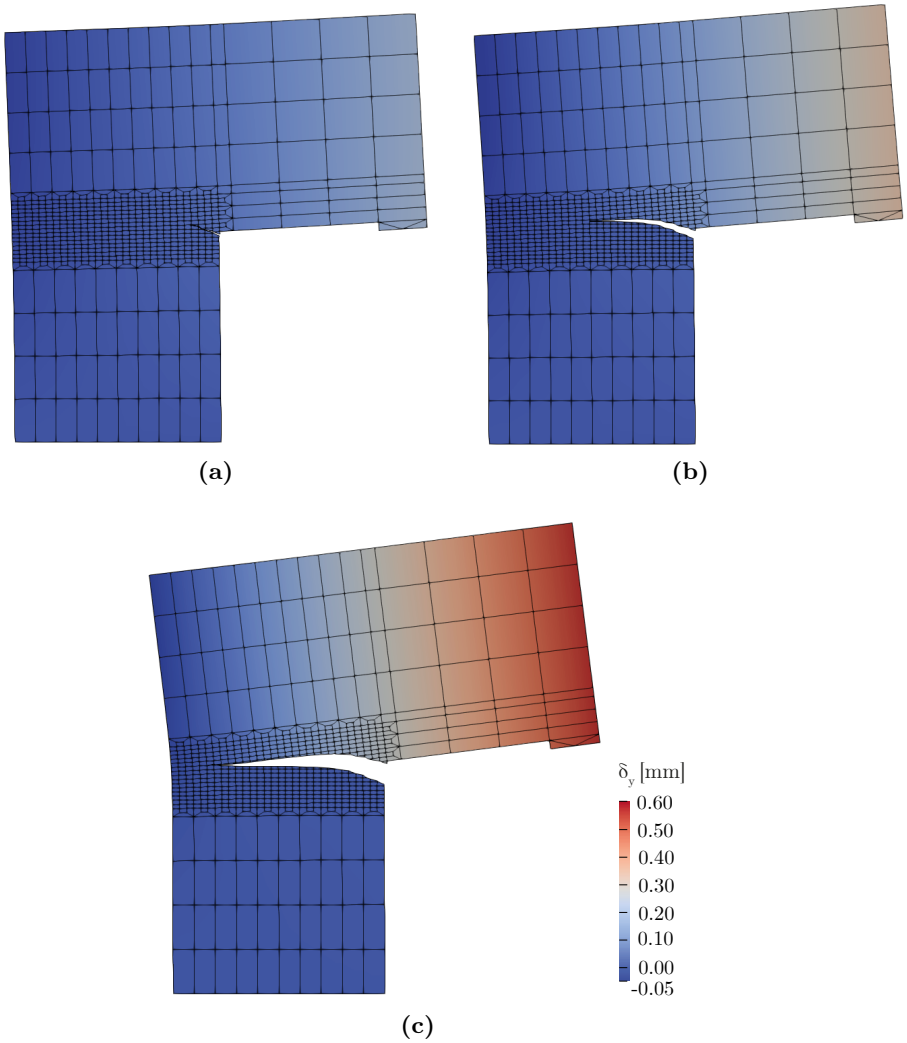

Figure 7.22: Example 6 - Deformed shapes and crack patterns at points (a) A, (b) B, and (c) C indicated in Figure 7.21.

7.7 Example 7: pull-out test on a concrete specimen

Table 7.10: Example 7 - Material parameters.

$E\ [MPa]$	ν	ε_0	$\frac{\varepsilon_f}{\varepsilon_0}$	$w_b\ [mm]$	D_{crit}
30000	0.2	$1.27E-4$	300	3	0.1

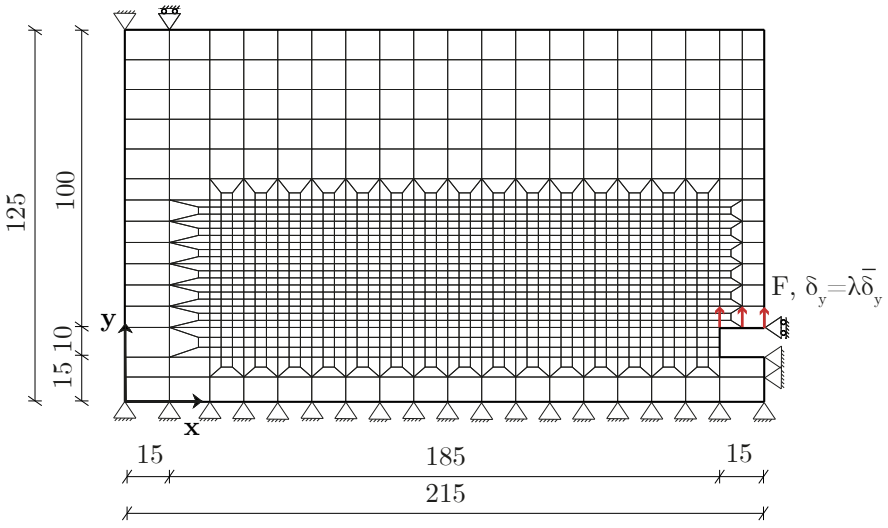

Figure 7.23: Example 7 - Geometry and boundary conditions, with dimensions given in mm.

This example simulates the pull-out test of an anchor bolt embedded in concrete, presented by RILEM Technical Committee 90-FMA [37]. In this test crack evolves primarly in mode-II. A concrete specimen with a thickness of 100 mm was investigated.

The constitutive and geometrical parameters reported in Table 7.10 and referred to [116], are used. The specimen is constrained on the bottom side and in the vertical edge of the lower right-hand corner; the effect of the anchor bolt, instead, is reproduced by imposing an incremental vertical displacement $\lambda\bar{\delta}_y$ on the upper edge of the notch until a final value of $\bar{\delta}_y = 0.4\ mm$. Figure 7.23 reports the geometry, the mesh and the boundary conditions adopted.

Crack begins to propagate from the notch, proceeding in a roughly recti-

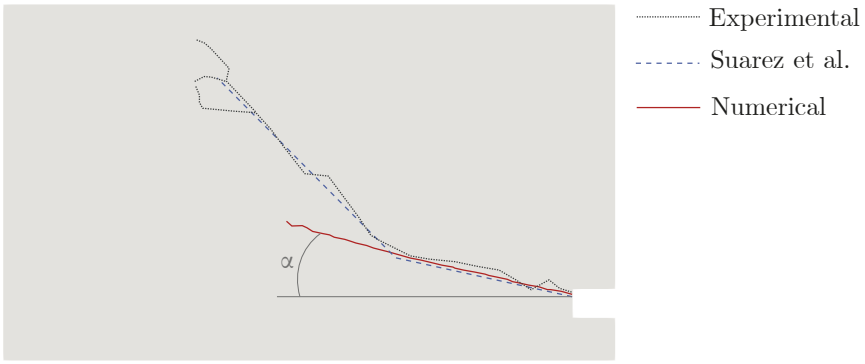

Figure 7.24: Example 7 - Comparison between experimental and numerical crack patterns.

linear way, with a slope $\alpha \simeq 13°$ toward the top edge. Figure 7.24 shows a comparison between the crack patterns obtained experimentally, in reference [116] and in the implemented code.

Load-displacement curves are reported in Figure 7.25: the numerical curve was obtained activating the possibility to localize bands in elements, using an interphase thickness equal to $w_b = 3\ mm$. The numerical result is in good agreement with the experimental one.

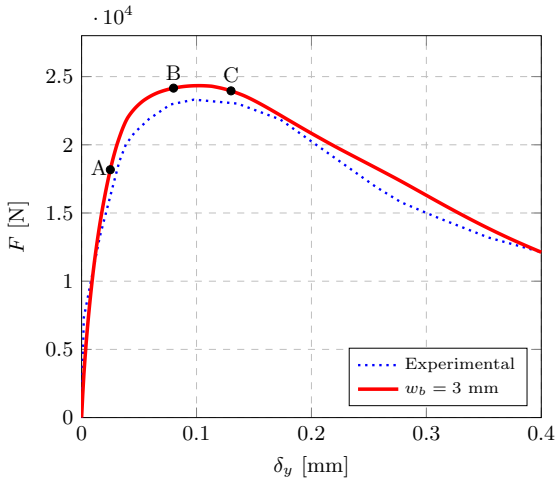

Figure 7.25: Example 7 - Load-displacement curves. Markers A, B, C indicate three states for which the deformed shapes are plotted in Figure 7.26.

Figure 7.26 shows the deformed shapes at the three marked points A-B-C of Figure 7.25, corresponding to a multiplier λ equal to 0.0625 (point A), 0.2 (point B) and 0.325 (point C), respectively.

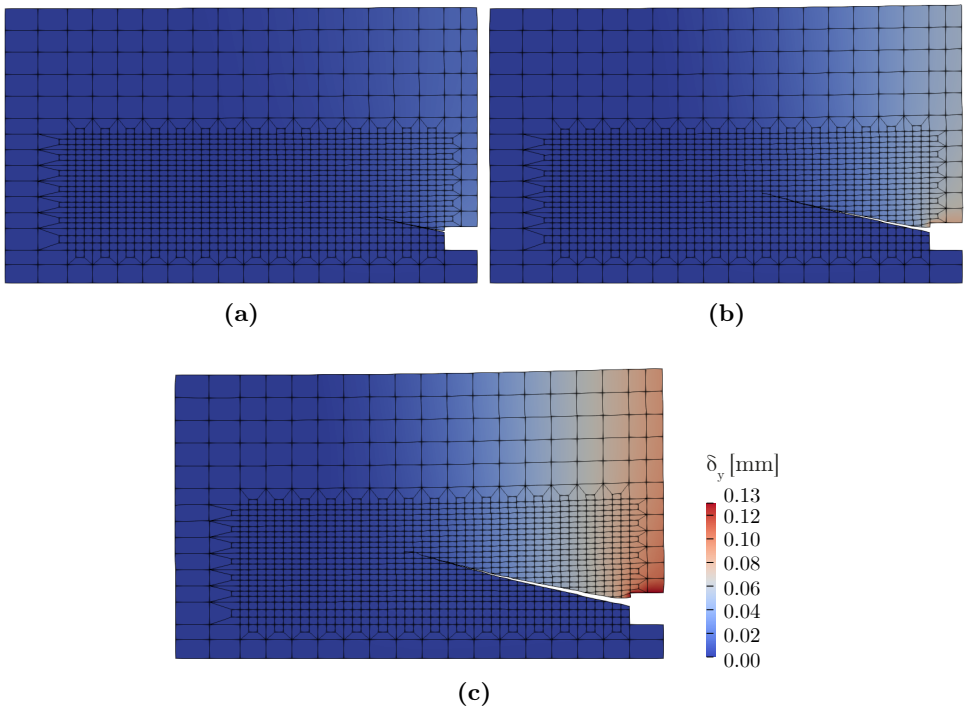

Figure 7.26: Example 7 - Deformed shapes at points (a) A, (b) B, and (c) C indicated in Figure 7.25.

Chapter 8

Conclusions and remarks

The present thesis concerns strain localization and fracture modeling in the framework of isotropic damage mechanics. This phenomenon has been analyzed from both static and dynamic points of view, making a comparison between the various approaches usually adopted, in order to highlight the purely physical significance of this phenomenon. An extensive overview of the computational strategies used to model strain localization has been presented and the A-FEM has been selected as the reference approach.

An alternative numerical strategy has been proposed in this work, based on the continuous-discontinuous approach in which the localization band within the finite element is modelled by an interphase element instead of a zero-thickness interface (ZTI) or a cohesive zone model (CZM). Since the interphase is a continuous thin material layer with the same constitutive behaviour as the bulk material, the proposed approach does not need a new traction-discontinuous displacement constitutive law for the localization band. Therefore, the proposed approach overcomes the problems related to what constitutive model and what related mechanical parameters should be attributed to these devices because the material maintains the same constitutive model, before and after strain localization. In addition, the interphase element permits to introduce a discontinuity as an element with a real volume and not a vanishing one.

The main difference of the proposed approach with respect to the classical A-FEM and X-FEM regards the possibility to follow the material failure from the strain localization in a thin layer band to the crack opening by using the IPH concept instead of the quite common ZTI one.

It has been proposed a general procedure so any constitutive model could

be implemented. The IDM has been here adopted, based on the formulation of Jirásek and Mazars.

Thus, taking inspiration by the A-FEM technique, an operating procedure for modeling a finite element with an embedded interphase at the local level has been implemented. The best strategy for simulating fracture propagation at the global structure level has been also analyzed. Therefore, special attention must be paid to the criterion used to identify when the band has to be inserted, defining its position and correct inclination. An appropriate crack tracking algorithm has been implemented, founded on the procedure of clustering among different elements, the concept of substructuring and some heuristic criteria for crack propagation.

The numerical examples on specimens subjected to mode-I and mixed-modes stress states show the advantages and the effectiveness of the proposed strategy with respect to the smeared damage models. The mechanical responses in terms of load-displacement curves and crack patterns are not dependent on the mesh size or mesh bias.

The numerical procedure and the implemented crack tracking algorithm show a quite good convergence behaviour and accuracy of the results. Therefore, the numerical code can be considered an efficient tool for those applications where the structural collapse depends on localized strains or crack propagation.

Several future developments are related to the scope of this thesis. First of all, the implementation of a different damage model, as well as the possibility of reproducing numerical simulations considering the case of elastoplastic constitutive models. The analysis of the conditions for giving rise to flutter instability (in Section 4.3), in fact, showed that it cannot be achieved in any way by adopting an isotropic damage model. A chance to identify cases in which flutter instability occurs could arise by the introduction of anisotropic damage models. Anisotropy can be either induced by damage or initially present due to the material microstructure. The model proposed by Desmorat et al. [33]-[61], for example, presents a damage anisotropy that is loading induced and can be represented by a tensorial damage variable.

Another possible development regards the improvement of the crack tracking algorithm for the case of fracture branching and inter-element localization bands. An in-depth analysis of the physical significance of the critical damage variable, a fundamental parameter within our numerical analyses, is being pursued. It might be also useful to identify some iso-lines associated with the same damage value $\hat{D}$ and to evaluate the direction of localization not only with the local data of the individual element but rather to those associated

with all elements within a certain iso-line region.

The extension of the numerical procedure to mesh constituted by 3D elements or elements with more than 4 nodes is also straightforward.

Finally, it can be concluded that the analysis of strain localization remains a field in continuous growth and evolution. This thesis sought to present a detailed overview of what has already been done in the literature by providing a new computational approach to complement those recently developed.

Bibliography

[1] J. Achenbach. *Wave propagation in elastic solids*. Elsevier, 2012.

[2] E. C. Aifantis. Update on a class of gradient theories. *Mech. Mater.*, 35(3-6):259–280, 2003.

[3] E. Artioli, S. Marfia, and E. Sacco. VEM-based tracking algorithm for cohesive/frictional 2D fracture. *Comput. Methods Appl. Mech. Eng.*, 365:112956, 2020.

[4] I. Babuška, G. Caloz, and J. Osborn. Special finite element methods in a class of second order elliptic problems with rough coefficients. *SIAM J. Numer. Anal.*, 31:945–981, 1994.

[5] G. I. Barenblatt. The formation of equilibrium cracks during brittle fracture. General ideas and hypotheses. Axially-symmetric cracks. *J. Appl. Math. Mech.*, 23(3):622–636, 1959.

[6] Z. P. Bažant and P. G. Gambarova. Crack shear in concrete: Crack band microflane model. *J. Struct. Eng.*, 110(9):2015–2035, 1984.

[7] Z. P. Bažant and M. Jirásek. Nonlocal integral formulations of plasticity and damage: survey of progress. *J. Eng. Mech.*, 128(11):1119–1149, 2002.

[8] Z. P. Bazănt and G. Pijaudier-Cabot. Nonlocal continuum damage, localization instability and convergence. *J. Appl. Mech.*, 1988.

[9] F. Beer, E. Johnston, J. DeWolf, and D. Mazurek. Mechanics of Materials. 7th edition. *New York. MeGraw-Hill Education Ltd*, 2015.

[10] L. Beirão da Veiga, F. Brezzi, A. Cangiani, G. Manzini, L. D. Marini, and A. Russo. Basic principles of virtual element methods. *Math. Models Methods Appl. Sci.*, 23(01):199–214, 2013.

[11] T. Belytschko, J. Fish, and B. E. Engelmann. A finite element with embedded localization zones. *Comput. Methods Appl. Mech. Eng.*, 70(1):59–89, 1988.

[12] E. Benvenuti and N. Orlando. A mesh-independent framework for crack tracking in elastodamaging materials through the regularized extended finite element method. *Comput. Mech.*, pages 1–25, 2021.

[13] D. Bigoni. *Nonlinear solid mechanics: bifurcation theory and material instability*. Cambridge University Press, 2012.

[14] D. Bigoni and T. Hueckel. Uniqueness and localization: associative and non-associative elastoplasticity. *Int. J. Solids Struct.*, 28(2):197–213, 1991.

[15] D. Bigoni and D. Zaccaria. On strain localization analysis of elastoplastic materials at finite strains. *Int. J. Plast.*, 9(1):21–33, 1993.

[16] D. Bigoni and D. Zaccaria. On the eigenvalues of the acoustic tensor in elastoplasticity. *Eur. J. Mech. A/Solids*, 13(5):621–638, 1994.

[17] G. Borré and G. Maier. On linear versus nonlinear flow rules in strain localization analysis. *Meccanica*, 24(1):36–41, 1989.

[18] R. d. Borst, J. J. Remmers, A. Needleman, and M.-A. Abellan. Discrete vs smeared crack models for concrete fracture: bridging the gap. *Int. J. Numer. Anal. Methods Geomech.*, 28(7-8):583–607, 2004.

[19] F. Brezzi and L. D. Marini. Finite elements and virtual elements on classical meshes. *Vietnam J. Math.*, 49(3):871–899, 2021.

[20] G. T. Camacho and M. Ortiz. Computational modelling of impact damage in brittle materials. *Int. J. Solids Struct.*, 33:2899–2938, 1996.

[21] L. Cedolin et al. *Stability of structures: elastic, inelastic, fracture and damage theories*. World Scientific, 2010.

[22] M. Cervera, G. Barbat, M. Chiumenti, and J. Wu. A comparative review of XFEM, mixed FEM and phase-field models for quasi-brittle cracking. *Archives of Computational Methods in Engineering*, 29:1009–1083, 2022.

[23] M. Cervera and M. Chiumenti. Mesh objective tensile cracking via a local continuum damage model and a crack tracking technique. *Comput. Methods Appl. Mech. Eng.*, 196(1-3):304–320, 2006.

[24] M. Cervera and J.-Y. Wu. On the conformity of strong, regularized, embedded and smeared discontinuity approaches for the modeling of localized failure in solids. *Int. J. Solids Struct.*, 71:19–38, 2015.

[25] J.-L. Chaboche. Continuum damage mechanics: Part 1- General concepts. *J. Appl. Mech.*, 1988.

[26] J.-L. Chaboche. Continuum damage mechanics: Part 2- Damage growth, crack initiation, and crack growth. *J. Appl. Mech.*, 1988.

[27] C. Comi, S. Mariani, and U. Perego. An extended FE strategy for transition from continuum damage to mode I cohesive crack propagation. *Int. J. Numer. Anal. Meth. Geomech.*, 31:213–238, 2007.

[28] P. A. Cundall and R. D. Hart. Numerical modeling of discontinua. In *Analysis and design methods*, pages 231–243. Elsevier, 1993.

[29] R. De Borst. Bifurcations in finite element models with a non-associated flow law. *Int. J. Numer. Anal. Methods Geomech.*, 12(1):99–116, 1988.

[30] R. De Borst, L. J. Sluys, H.-B. Muhlhaus, and J. Pamin. Fundamental issues in finite element analyses of localization of deformation. *Eng. Comput.*, 1993.

[31] J. De Vree, W. Brekelmans, and M. van Gils. Comparison of nonlocal approaches in continuum damage mechanics. *Comput. Struct.*, 55(4):581–588, 1995.

[32] A. Deb, B. Loret, and J. H. Prevost. Automated band identification procedure for dynamic strain localization. *Comput. Methods Appl. Mech. Eng.*, 137(3-4):307–330, 1996.

[33] R. Desmorat. Anisotropic damage modeling of concrete materials. *Int. J. Damage Mech.*, 25(6):818–852, 2016.

[34] R. Desmorat and S. Cantournet. Modeling microdefects closure effect with isotropic/anisotropic damage. *Int. J. Damage Mech.*, 17(1):65–96, 2008.

[35] D. Dias-da Costa, J. Alfaiate, L. Sluys, and E. Júlio. A comparative study on the modelling of discontinuous fracture by means of enriched nodal and element techniques and interface elements. *Int. J. Frac.*, 161(1):97–119, 2010.

[36] D. S. Dugdale. Yielding of steel sheets containing slits. *J. Mech. Phys. Solids*, 8(2):100–104, 1960.

[37] L. Elfgren, R. Eligehausen, and J. G. Rots. Anchor bolts in concrete structures: summary of round robin tests and analysis arranged by RILEM TC 90-FMA 'Fracture Mechanics of Concrete-Applications'. *Mater. Struct.*, 34(8):451–457, 2001.

[38] S. Essongue, G. Couégnat, and E. Martin. Performance assessment of the augmented finite element method for the modeling of weak discontinuities. *Int. J. Numer. Methods Eng.*, 122:172–189, 2021.

[39] T.-P. Fries and T. Belytschko. The extended/generalized finite element method: an overview of the method and its applications. *Int. J. Numer. Methods Eng.*, 84(3):253–304, 2010.

[40] G. Giambanco and E. La Malfa Ribolla. A phase-field model for strain localization analysis in softening elastoplastic materials. *Int. J. Solids Struct.*, 172-173:84–96, 2019.

[41] G. Giambanco and Z. Mroz. The interphase model for the analysis of joints in rock masses and masonry structures. *Meccanica*, 36(1):111–130, 2001.

[42] G. Giambanco, S. Rizzo, and R. Spallino. Numerical analysis of masonry structures via interface models. *Comput. Methods Appl. Mech. Eng.*, 190(49-50):6493–6511, 2001.

[43] G. Giambanco, G. F. Scimemi, and A. Spada. The interphase finite element. *Comput. Mech.*, 50(3):353–366, 2012.

[44] R. E. Goodman, R. L. Taylor, and T. L. Brekke. A model for the mechanics of jointed rock. *J. Soil Mech. Found. Div.*, 1968.

[45] A. A. Griffith. The phenomena of rupture and flow in solids. *Philosophical transactions of the royal society of London. Series A, containing papers of a mathematical or physical character*, 221(582-593):163–198, 1921.

[46] M. E. Gurtin. The linear theory of elasticity. In *Linear theories of elasticity and thermoelasticity*, pages 1–295. Springer, 1973.

[47] J. Hadamard. *Leçons sur la propagation des ondes et les équations de l'hydrodynamique*. A. Hermann, 1903.

[48] A. Hansbo and P. Hansbo. A finite element method for the simulation of strong and weak discontinuities in solid mechanics. *Comput. Methods Appl. Mech. Eng.*, 193:3523–3540, 2004.

[49] L. R. Herrmann. Finite element analysis of contact problems. *Journal of the engineering mechanics division*, 104(5):1043–1057, 1978.

[50] R. Hill. A general theory of uniqueness and stability in elastic-plastic solids. *J. Mech. Phys. Solids*, 6(3):236–249, 1958.

[51] A. Hillerborg, M. Modéer, and P.-E. Petersson. Analysis of crack formation and crack growth in concrete by means of fracture mechanics and finite elements. *Cem. Concr. Res.*, 6(6):773–781, 1976.

[52] F. Jacob and T. Belytschko. *A first course in finite elements*. Wiley Edition, 2007.

[53] M. Jirásek. Comparative study on finite elements with embedded discontinuities. *Comput. Methods Appl. Mech. Eng.*, 188(1-3):307–330, 2000.

[54] M. Jirásek. Modeling of localized damage and fracture in quasibrittle materials. In *Continuous and discontinuous modelling of cohesive-frictional materials*, pages 17–29. Springer, 2001.

[55] M. Jirásek. Objective modeling of strain localization. *Revue française de génie civil*, 6(6):1119–1132, 2002.

[56] M. Jirásek. Nonlocal theories in continuum mechanics. *Acta Polytechnica*, 44(5-6), 2004.

[57] M. Jirásek. Mathematical analysis of strain localization. *Revue européenne de génie civil*, 11(7-8):977–991, 2007.

[58] M. Jirásek. Damage and smeared crack models. In *Numerical modeling of concrete cracking*, pages 1–49. Springer, 2011.

[59] M. Jirásek and T. Belytschko. Computational resolution of strong discontinuities. In *Proceedings of fifth world congress on computational mechanics, WCCM V, Vienna University of Technology, Austria*. Citeseer, 2002.

[60] M. Jirásek and B. Patzák. Consistent tangent stiffness for nonlocal damage models. *Comput. Struct.*, 80(14-15):1279–1293, 2002.

[61] M. Jirásek and F. Suárez. Localization properties of Desmorat's anisotropic damage model. *Comput. Struct.*, 174:139–153, 2016.

[62] M. Jirásek and T. Zimmermann. Rotating crack model with transition to scalar damage. *J. Eng. Mech.*, 124(3):277–284, 1998.

[63] M. Jirásek and T. Zimmermann. Embedded crack model: I. Basic formulation. *Int. J. Numer. Methods Eng.*, 50(6):1269–1290, 2001.

[64] L. M. Kachanov. Time of the rupture process under creep conditions. *Akad. Nauk SSR*, 8:26–31, 1958.

[65] V. Kaliakin and J. Li. Insight into deficiencies associated with commonly used zero-thickness interface elements. *Comput. Geotech.*, 17(2):225–252, 1995.

[66] J. Lagrange. Mécanique analytique (2 vols.), Edition Albert Blanchard, 1788.

[67] J. Lemaitre. A continuous damage mechanics model for ductile fracture. *J. Eng. Mater. Technol.*, 1985.

[68] J. Lemaitre and J.-L. Chaboche. Aspect phénoménologique de la rupture par endommagement. *J. Méc. Appl.*, 2(3), 1978.

[69] D. Ling, Q. Yang, and B. Cox. An augmented finite element method for modeling arbitrary discontinuities in composite materials. *Int. J. Fract.*, 156:53–73, 2009.

[70] A. Lisjak and G. Grasselli. A review of discrete modeling techniques for fracturing processes in discontinuous rock masses. *J. Rock Mech. Geotech. Eng.*, 6(4):301–314, 2014.

[71] W. Liu, Q. Yang, S. Mohammadizadeh, and X. Su. An efficient augmented finite element method for arbitrary cracking and crack interactions in solids. *Int. J. Numer. Methods Eng.*, 80(4), 2013.

[72] W. Luders. On the manifestation of plasticity in steel-like iron bars and in steel bars; on the observation of molecular movement when bending such bars. *Polytechnisches Jnl.*, 155(1):18–22, 1860.

[73] A. Lyapunov. On the general problem of stability of motion. Master's thesis, Kharkov Mathematical Society, Soviet Union, 1892.

[74] Z. Ma, Q. Yang, and X. Su. A conforming augmented finite element method for modeling arbitrary cracking in solids. *J. Appl. Mech.*, 86:071002, 2019.

[75] J. Maire and J. Chaboche. A new formulation of continuum damage mechanics (CDM) for composite materials. *Aerosp. Sci. Technol.*, 1(4):247–257, 1997.

[76] A. Marchand and J. Duffy. An experimental study of the formation process of adiabatic shear bands in a structural steel. *J. Mech. Phys. Solids*, 36(3):251–283, 1988.

[77] S. Marfia, E. Monaldo, and E. Sacco. Cohesive fracture evolution within virtual element method. *Eng. Fract. Mech.*, page 108464, 2022.

[78] T. J. Massart. *Multi-scale modeling of damage in masonry structures.* PhD thesis, Technische Universiteit Eindhoven (The Netherlands), 2004.

[79] J. Mazars. A description of micro-and macroscale damage of concrete structures. *Eng. Fract. Mech.*, 25(5-6):729–737, 1986.

[80] J. M. Melenk and I. Babuška. The partition of unity finite element method: basic theory and applications. *Comput. Methods Appl. Mech. Eng.*, 139(1-4):289–314, 1996.

[81] C. Miehe, M. Hofacker, and F. Welschinger. A phase field model for rate-independent crack propagation: Robust algorithmic implementation based on operator splits. *Comput. Methods Appl. Mech. Eng.*, 199(45-48):2765–2778, 2010.

[82] N. Moës and T. Belytschko. Extended finite element method for cohesive crack growth. *Eng. Fract. Mech.*, 69(7):813–833, 2002.

[83] N. Moës, J. Dolbow, and T. Belytschko. A finite element method for crack growth without remeshing. *Int. J. Numer. Methods Eng.*, 46(1):131–150, 1999.

[84] S. Mohammadizadeh. *A novel augmented finite element method for modeling arbitrary cracking in solids.* PhD thesis, University of Miami, 2013.

[85] T. Most and C. Bucher. Energy-based simulation of concrete cracking using an improved mixed-mode cohesive crack model within a meshless discretization. *Int. J. Numer. Anal. Methods Geomech.*, 31(2):285–305, 2007.

[86] H.-B. Mühlhaus and E. Alfantis. A variational principle for gradient plasticity. *Int. J. Solids Struct.*, 28(7):845–857, 1991.

[87] A. Munjiza and K. Andrews. NBS contact detection algorithm for bodies of similar size. *Int. J. Numer. Methods Eng.*, 43(1):131–149, 1998.

[88] A. Needleman and M. Ortiz. Effect of boundaries and interfaces on shear-band localization. *Int. J. Solids Struct.*, 28(7):859–877, 1991.

[89] M. B. Nooru-Mohamed. *Mixed-mode fracture of concrete: An experimental approach.* PhD thesis, Technische Universiteit Delft (The Netherlands), 1993.

[90] J. Oliver. Modelling strong discontinuities in solid mechanics via strain softening constitutive equations. Part 1: Fundamentals. Part 2: Numerical Simulation. *Int. J. Numer. Methods Eng.*, 39:3575–3624, 1996.

[91] M. Ortiz and J. Quigley Iv. Adaptive mesh refinement in strain localization problems. *Comput. Methods Appl. Mech. Eng.*, 90(1-3):781–804, 1991.

[92] N. S. Ottosen and K. Runesson. Properties of discontinuous bifurcation solutions in elasto-plasticity. *Int. J. Solids Struct.*, 27(4):401–421, 1991.

[93] B. Patzák and M. Jirásek. Adaptive resolution of localized damage in quasi-brittle materials. *J. Eng. Mech.*, 130(6):720–732, 2004.

[94] R. d. Peerlings, R. d. Borst, W. d. Brekelmans, J. d. Vree, and I. Spee. Some observations on localization in non-local and gradient damage models. *Eur. J. Mech. A Solids*, 15(6):937–953, 1996.

[95] M. Petrangeli and J. Ožbolt. Smeared crack approaches - material modeling. *J. Eng. Mech.*, 122(6):545–554, 1996.

[96] D. Pham and A. Afify. Clustering techniques and their applications in engineering. *Proceedings of the Institution of Mechanical Engineers, Part C: Journal of Mechanical Engineering Science*, 221(11):1445–1459, 2007.

[97] C. Polizzotto. Unified thermodynamic framework for nonlocal/gradient continuum theories. *Eur. J. Mech. A Solids*, 22(5):651–668, 2003.

[98] M. Puccia, A. Spada, and G. Giambanco. Finite elements with embedded interphases for strain localization in quasi-brittle materials. *Eng. Frac. Mech.*, page 108956, 2022.

[99] T. Rabczuk, G. Zi, A. Gerstenberger, and W. A. Wall. A new crack tip element for the phantom-node method with arbitrary cohesive cracks. *Int. J. Numer. Methods Eng.*, 75(5):577–599, 2008.

[100] Y. R. Rashid. Ultimate strength analysis of prestressed concrete pressure vessels. *Nucl. Eng. Des.*, 7(4):334–344, 1968.

[101] E. Rizzi. Localization analysis of damaged materials. Master's thesis, University of Colorado, 1993.

[102] E. Rizzi, I. Carol, and K. Willam. Localization analysis of elastic degradation with application to scalar damage. *J. Eng. Mech.*, 121(4):541–554, 1995.

[103] J. W. Rudnicki and J. Rice. Conditions for the localization of deformation in pressure-sensitive dilatant materials. *J. Mech. Phys. Solids*, 23(6):371–394, 1975.

[104] E. Sacco and F. Lebon. A damage-friction interface model derived from micromechanical approach. *Int. J. Solids Struct.*, 49 (26):3666–3680, 2012.

[105] S. Saloustros, M. Cervera, and L. Pelà. Challenges, tools and applications of tracking algorithms in the numerical modelling of cracks in concrete and masonry structures. *Arch. Comput. Methods Eng.*, 26(4):961–1005, 2019.

[106] S. Saloustros, L. Pelà, M. Cervera, and P. Roca. Finite element modelling of internal and multiple localized cracks. *Comput. Mech.*, 59(2):299–316, 2017.

[107] J. Schellekens and R. De Borst. On the numerical integration of interface elements. *Int. J. Numer. Methods Eng.*, 36(1):43–66, 1993.

[108] G.-H. Shi and R. E. Goodman. Two dimensional discontinuous deformation analysis. *Int. J. Numer. Anal. Methods Geomech.*, 9(6):541–556, 1985.

[109] D. Shuttle and I. Smith. Numerical simulation of shear band formation in soils. *Int. J. Numer. Anal. Methods Geomech.*, 12(6):611–626, 1988.

[110] J. C. Simo and J. Ju. Strain- and stress-based continuum damage models-I: Formulation. *Int. J. Solids Struct.*, 23(7):821–840, 1987.

[111] J. C. Simo, J. Oliver, and F. Armero. An analysis of strong discontinuity induced by strain-softening in rate-independent inelastic solids. *Comput. Mech.*, 12:277–296, 1993.

[112] L. J. Sluys and A. H. Berends. Discontinuous failure analysis for mode-I and mode-II localization problems. *Int. J. Solids Struct.*, 35(31-32):4257–4274, 1998.

[113] G.-H. Song, P. Areias, and T. Belytschko. A method for dynamic crack and shear band propagation with phantom nodes. *Int. J. Numer. Methods Eng.*, 67:868–893, 2006.

[114] M. Stolarska, D. L. Chopp, N. Moës, and T. Belytschko. Modelling crack growth by level sets in the extended finite element method. *Int. J. Numer. Methods Eng.*, 51(8):943–960, 2001.

[115] T. Strouboulis, K. Copps, and I. Babuška. The generalized finite element method. *Comput. Methods Appl. Mech. Eng.*, 190(32-33):4081–4193, 2001.

[116] F. Suárez, J. Gálvez, and D. Cendón. A material model to reproduce mixed-mode fracture in concrete. *Fatigue Fract. Eng. Mater. Struct.*, 42(1):223–238, 2019.

[117] J. Sulem. Bifurcation theory and localization phenomena. *Eur. J. Environ. Civ. Eng.*, 14(8-9):989–1009, 2010.

[118] E. B. Tadmor, R. E. Miller, and R. S. Elliott. *Continuum mechanics and thermodynamics: from fundamental concepts to governing equations.* Cambridge University Press, 2012.

[119] M. T. Takemori. Competition between crazing and shear flow during fatigue. In *Crazing in Polymers Vol. 2*, pages 263–300. Springer, 1990.

[120] E. Tamayo-Mas, J. Feliu-Fabà, M. Casado-Antolin, and A. Rodríguez-Ferran. A continuous-discontinuous model for crack branching. *Int. J. Numer. Methods Eng.*, 120(1):86–104, 2019.

[121] E. Tamayo-Mas and A. Rodríguez-Ferran. A medial-axis-based model for propagating cracks in a regularised bulk. *Int. J. Numer. Methods Eng.*, 101:489–520, 2015.

[122] T. Y. Thomas. *Plastic flow and fracture in solids.* Elsevier, 1961.

[123] A. Vermeltfoort, D. Martens, and G. Van Zijl. Brick-mortar interface effects on masonry under compression. *Can. J. Civ. Eng.*, 34(11):1475–1485, 2007.

[124] K. Y. Volokh. Comparison between cohesive zone models. *Commun. Numer. Methods Eng.*, 20(11):845–856, 2004.

[125] Y. Wang and H. Waisman. From diffuse damage to sharp cohesive cracks: a coupled XFEM framework for failure analysis of quasi-brittle materials. *Comput. Methods Appl. Mech. Eng.*, 299:57–89, 2016.

[126] G. N. Wells. *Discontinuous modelling of strain localisation and failure.* Delft University of Technology, 2001.

[127] B. J. Winkler. *Traglastuntersuchungen von unbewehrten und bewehrten Betonstrukturen auf der Grundlage eines objektiven Werkstoffgesetzes für Beton.* Innsbruck University Press, 2001.

[128] J. Wolf, P. Longère, J.-M. Cadou, and J.-P. Crété. Numerical modeling of strain localization in engineering ductile materials combining cohesive models and X-FEM. *Int. J. Mech. Mater. Des.*, 14(2):177–193, 2018.

[129] X. P. Xu and A. Needleman. Numerical simulations of fast crack growth in brittle solids. *J. Mech. Phys. Solids*, 42(9):1397–1434, 1994.

Appendix A

Rotation from global to principal reference system

The objective of this Appendix is to obtain the principal strains in the $x_1 - x_2$ reference system from the displacement field expressed in the $x - y$ reference system. Let us consider a displacement vector $\mathbf{u} = [u_x \quad u_y]^T$ and its projection $\mathbf{u}_p = [u_1 \quad u_2]^T$ into a second reference system $x_1 - x_2$, forming a θ angle between axes $x - x_1$ (Figure A.1).

Considering that $\mathbf{u}_1 = \bar{AB} + \bar{BC}$ and $\mathbf{u}_2 = \bar{PC} - \bar{DC}$, it can be written that

$$\begin{bmatrix} u_1 \\ u_2 \\ u_3 \end{bmatrix} = \begin{bmatrix} \cos\theta & \sin\theta & 0 \\ -\sin\theta & \cos\theta & 0 \\ 0 & 0 & 1 \end{bmatrix} \begin{bmatrix} u_x \\ u_y \\ u_3 \end{bmatrix} = \begin{bmatrix} u_x \cos\theta + u_y \sin\theta \\ u_y \cos\theta - u_x \sin\theta \\ u_3 \end{bmatrix}. \tag{A.1}$$

As better explained in Appendix B, the strain field is derived from the associated displacement vector through a compatibility matrix, so it can be written

$$\boldsymbol{\varepsilon}_p = \boldsymbol{B}'\mathbf{u}_p \qquad \boldsymbol{\varepsilon} = \boldsymbol{B}\mathbf{u}. \tag{A.2}$$

A plane stress condition is considered, so the component ε_3 is not independent as explained in (4.48). It is considered $\boldsymbol{\varepsilon}_p = \begin{bmatrix} \varepsilon_{x_1} & \varepsilon_{x_2} & \gamma_{x_1 x_2} \end{bmatrix}^T$ and $\boldsymbol{\varepsilon} = \begin{bmatrix} \varepsilon_x & \varepsilon_y & \gamma_{xy} \end{bmatrix}^T$. Considering that x_3 is already a principal direction, previous relationships in extended form become

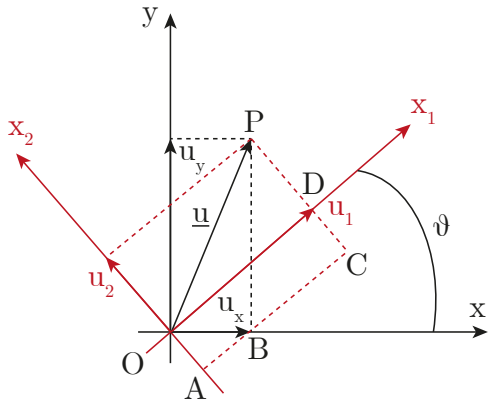

Figure A.1: Displacement field in $x-y$ and x_1-x_2 reference systems.

$$\boldsymbol{\varepsilon}_p = \begin{bmatrix} \frac{\partial}{\partial x_1} & 0 \\ 0 & \frac{\partial}{\partial x_2} \\ \frac{\partial}{\partial x_2} & \frac{\partial}{\partial x_1} \end{bmatrix} \begin{bmatrix} u_1 \\ u_2 \end{bmatrix} \qquad \boldsymbol{\varepsilon} = \begin{bmatrix} \frac{\partial}{\partial x} & 0 \\ 0 & \frac{\partial}{\partial y} \\ \frac{\partial}{\partial y} & \frac{\partial}{\partial x} \end{bmatrix} \begin{bmatrix} u_x \\ u_y \end{bmatrix}. \tag{A.3}$$

By substituting expressions (A.1) in (A.3), strains in x_1-x_2 can be expressed as follows

$$\boldsymbol{\varepsilon}_p = \begin{bmatrix} \frac{\partial}{\partial x_1}(u_x\cos\theta + u_y\sin\theta) \\ \frac{\partial}{\partial x_2}(u_y\cos\theta - u_x\sin\theta) \\ \frac{\partial}{\partial x_2}(u_x\cos\theta + u_y\sin\theta) + \frac{\partial}{\partial x_1}(u_y\cos\theta - u_x\sin\theta) \end{bmatrix}. \tag{A.4}$$

Considering the following chain rule to differentiate composite functions

$$\frac{\partial}{\partial x_i} f(x,y,z) = \frac{\partial f}{\partial x}\frac{\partial x}{\partial x_i} + \frac{\partial f}{\partial y}\frac{\partial y}{\partial x_i} + \frac{\partial f}{\partial z}\frac{\partial z}{\partial x_i} \tag{A.5}$$

expressions in (A.4) become

$$\boldsymbol{\varepsilon}_p = \begin{bmatrix} \frac{\partial x}{\partial x_1}(\frac{\partial u_x}{\partial x}\cos\theta + \frac{\partial u_y}{\partial x}\sin\theta) + \frac{\partial y}{\partial x_1}(\frac{\partial u_x}{\partial y}\cos\theta + \frac{\partial u_y}{\partial y}\sin\theta) + \frac{\partial z}{\partial x_1}(\frac{\partial u_x}{\partial z}\cos\theta + \frac{\partial u_y}{\partial z}\sin\theta) \\ \frac{\partial x}{\partial x_2}(\frac{\partial u_y}{\partial x}\cos\theta - \frac{\partial u_x}{\partial x}\sin\theta) + \frac{\partial y}{\partial x_2}(\frac{\partial u_y}{\partial y}\cos\theta - \frac{\partial u_x}{\partial y}\sin\theta) + \frac{\partial z}{\partial x_2}(\frac{\partial u_y}{\partial z}\cos\theta - \frac{\partial u_x}{\partial z}\sin\theta) \\ \left[\begin{array}{l} \frac{\partial x}{\partial x_2}(\frac{\partial u_x}{\partial x}\cos\theta + \frac{\partial u_y}{\partial x}\sin\theta) + \frac{\partial y}{\partial x_2}(\frac{\partial u_x}{\partial y}\cos\theta + \frac{\partial u_y}{\partial y}\sin\theta) + \frac{\partial z}{\partial x_2}(\frac{\partial u_x}{\partial z}\cos\theta + \frac{\partial u_y}{\partial z}\sin\theta) + \\ + \frac{\partial x}{\partial x_1}(\frac{\partial u_y}{\partial x}\cos\theta - \frac{\partial u_x}{\partial x}\sin\theta) + \frac{\partial y}{\partial x_1}(\frac{\partial u_y}{\partial y}\cos\theta - \frac{\partial u_x}{\partial y}\sin\theta) + \frac{\partial z}{\partial x_1}(\frac{\partial u_y}{\partial z}\cos\theta - \frac{\partial u_x}{\partial z}\sin\theta) \end{array}\right] \end{bmatrix}. \tag{A.6}$$

The following transformation relations also hold:

$$\frac{\partial x}{\partial x_1} = \cos x\hat{x}_1 = \cos\theta; \quad \frac{\partial y}{\partial x_1} = \cos(90^\circ - \theta) = \sin\theta; \quad \frac{\partial z}{\partial x_1} = \cos(90^\circ) = 0;$$
$$\frac{\partial x}{\partial x_2} = (90^\circ + \theta) = -\sin\theta; \quad \frac{\partial y}{\partial x_2} = \cos\theta; \quad \frac{\partial z}{\partial x_2} = \cos(90^\circ) = 0.$$

Substituting them into (A.6), it is obtained

$$\boldsymbol{\varepsilon}_p = \begin{bmatrix} \frac{\partial u_x}{\partial x}\cos^2\theta + \frac{\partial u_y}{\partial y}\sin^2\theta + (\frac{\partial u_x}{\partial y} + \frac{\partial u_y}{\partial x})\sin\theta\cos\theta \\ \frac{\partial u_x}{\partial x}\sin^2\theta + \frac{\partial u_y}{\partial y}\cos^2\theta - (\frac{\partial u_x}{\partial y} + \frac{\partial u_y}{\partial x})\sin\theta\cos\theta \\ (\frac{\partial u_x}{\partial y} + \frac{\partial u_y}{\partial x})(\cos^2\theta - \sin^2\theta) + (-2\frac{\partial u_x}{\partial x} + 2\frac{\partial u_y}{\partial y})\sin\theta\cos\theta \end{bmatrix}. \tag{A.7}$$

Remembering expressions in (A.2)-(A.3) and considering $c = \cos\theta$ and $s = \sin\theta$ for abbreviations, previous relationships become

$$\boldsymbol{\varepsilon}_p = \begin{bmatrix} c^2 & s^2 & sc \\ s^2 & c^2 & -sc \\ -2sc & 2sc & c^2 - s^2 \end{bmatrix} \begin{bmatrix} \frac{\partial u_x}{\partial x} \\ \frac{\partial u_y}{\partial y} \\ \frac{\partial u_x}{\partial y} + \frac{\partial u_y}{\partial x} \end{bmatrix} = \boldsymbol{A}_p\boldsymbol{\varepsilon} = \boldsymbol{A}_p\boldsymbol{B}\mathbf{u}. \tag{A.8}$$

It can be concluded that the principal strain vector can be calculated from the nodal displacement one. The associated value of the equivalent strain is calculated with the relation (4.37) and the related damage value is obtained from equation (4.28). In summary, choosing any point of coordinates $\xi \in [-1, 1]$ and $\eta \in [-1, 1]$ in the parent element, the compatibility matrix can be calculated as later explained in (B.8) in order to obtain the strain field in this point.

Appendix B

Four-node isoparametric elements formulation

Let us consider a 4-node *physical element* referred to the $x-y$ physical system and the *parent element* referred to the natural coordinate system $\xi-\eta$ (Figure B.1). These two coordinates systems are mutually related, so physical coordinates (x, y) are obtained by mapping the natural ones (ξ, η) through a set of 4-node shape functions $\boldsymbol{N}(\xi, \eta)$ [52]. It can be written that

$$x(\xi,\eta) = \sum_{i=1}^{4} N_i(\xi,\eta) x_i^e = \mathbf{N}\cdot\mathbf{x}^e \qquad y(\xi,\eta) = \sum_{i=1}^{4} N_i(\xi,\eta) y_i^e = \mathbf{N}\cdot\mathbf{y}^e \quad \text{(B.1)}$$

being $\mathbf{x}^e$ and $\mathbf{y}^e$ the nodal coordinates vectors and $\mathbf{N}$ the shape functions vector, defined as follows

$$\mathbf{x}^e = \begin{bmatrix} x_1 & x_2 & x_3 & x_4 \end{bmatrix}^T \quad \mathbf{y}^e = \begin{bmatrix} y_1 & y_2 & y_3 & y_4 \end{bmatrix}^T \quad \mathbf{N} = \begin{bmatrix} N_1 & N_2 & N_3 & N_4 \end{bmatrix}. \quad \text{(B.2)}$$

The shape functions contain a constant term, terms linear in ξ and η and the term $\xi\eta$, that is the bilinear monomial; for this reason they are called bilinear shape functions. By writing monomials in terms of arbitrary parameters, the following expression is obtained:

$$x(\xi,\eta) = \alpha_0 + \alpha_1\xi + \alpha_2\eta + \alpha_3\xi\eta \quad \text{(B.3)}$$

where $\alpha_0, \alpha_1, \alpha_2, \alpha_3$ are constants to be determined by imposing that the function interpolates the four nodal values, whose coordinates are expressed in table, as follows

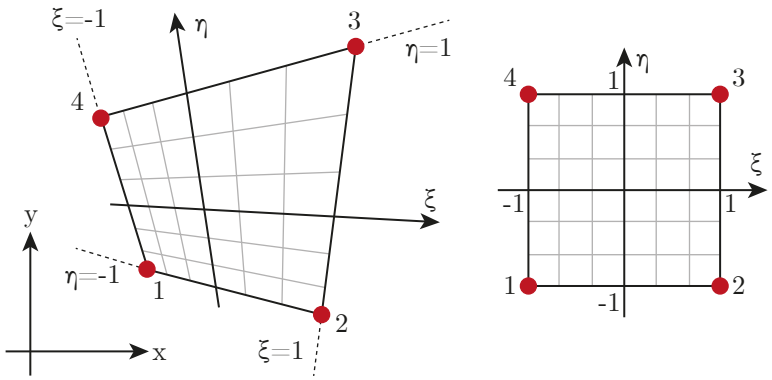

Figure B.1: Relation between the physical element in $x-y$ and the parent one in $\xi-\eta$.

$$x(\xi_i,\eta_i)=x_i \quad \text{where} \quad \begin{array}{ccc} i & \xi_i & \eta_i \\ 1 & -1 & -1 \\ 2 & 1 & -1 \\ 3 & 1 & 1 \\ 4 & -1 & 1 \end{array} . \tag{B.4}$$

By solving equations (B.4) it is obtained that

$$N_i(\xi,\eta)=\frac{1}{4}(1+\xi_i\xi)(1+\eta_i\eta) \tag{B.5}$$

$$\begin{aligned} N_1(\xi,\eta)&=\frac{1}{4}(1-\xi)(1-\eta) \\ N_2(\xi,\eta)&=\frac{1}{4}(1+\xi)(1-\eta) \\ N_3(\xi,\eta)&=\frac{1}{4}(1+\xi)(1+\eta) \\ N_4(\xi,\eta)&=\frac{1}{4}(1-\xi)(1+\eta). \end{aligned}$$

Same passages could be done by considering y instead of x in (B.3)-(B.4) and same shape functions will be obtained. These shape functions have to respect some conditions:

- they are *regular functions* (at least class $\mathbf{C}^1$) within the element, that means they are analytic and single-valued throughout this region;

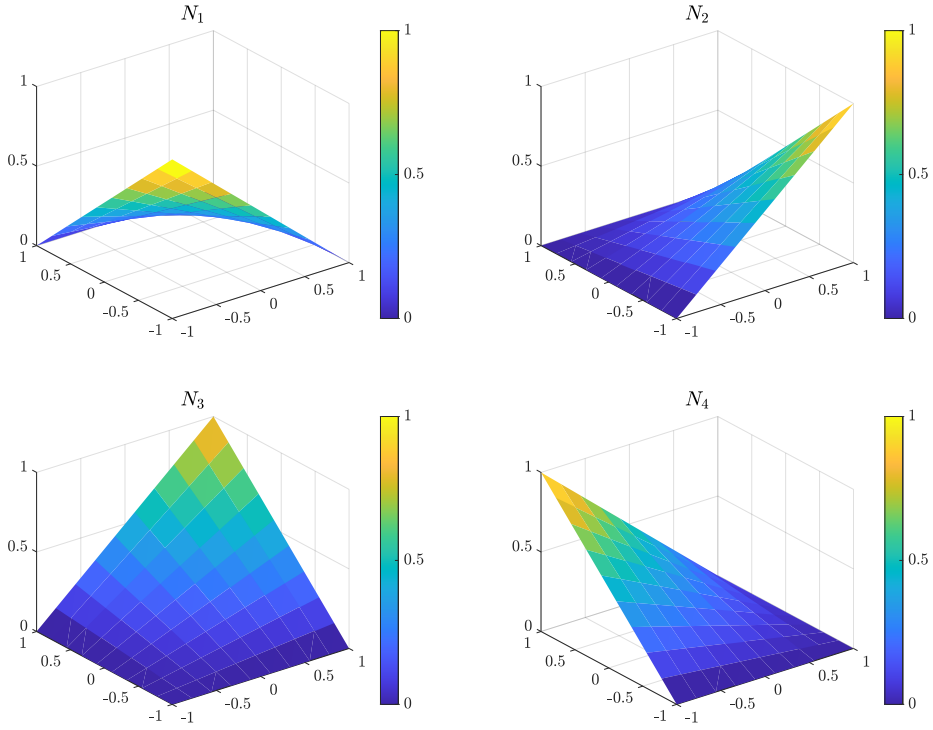

Figure B.2: Shape functions of 4-node isoparametric element.

- they are *continuous* along the boundaries of the element. Along each element edge they changes in a linear way since depending only on the extremes values. It can be concluded that they assume a typical hyperbolic paraboloid shape inside the element, as represented in Figure B.2.

The essential feature of the isoparametric elements is that the physical coordinates are mapped by the same shape functions as those used for the approximation (of displacements, for example). So, similarly to relations (B.1), the displacement field $\mathbf{u}$ on the element can be obtained by mapping the nodal displacement vector $\mathbf{d}^e$ as follows

$$\mathbf{u}(\xi, \eta) = \mathbf{N}\mathbf{d}^e. \tag{B.6}$$

The strain field ε in the element could also be calculated from the nodal displacements

$$\boldsymbol{\varepsilon} = \boldsymbol{B}\mathbf{d}^e \tag{B.7}$$

where

$$\boldsymbol{B} = \nabla \boldsymbol{N} = \begin{bmatrix} \frac{\partial N_1}{\partial x} & 0 & \frac{\partial N_2}{\partial x} & 0 & \frac{\partial N_3}{\partial x} & 0 & \frac{\partial N_4}{\partial x} & 0 \\ 0 & \frac{\partial N_1}{\partial y} & 0 & \frac{\partial N_2}{\partial y} & 0 & \frac{\partial N_3}{\partial y} & 0 & \frac{\partial N_4}{\partial y} \\ \frac{\partial N_1}{\partial y} & \frac{\partial N_1}{\partial x} & \frac{\partial N_2}{\partial y} & \frac{\partial N_2}{\partial x} & \frac{\partial N_3}{\partial y} & \frac{\partial N_3}{\partial x} & \frac{\partial N_4}{\partial y} & \frac{\partial N_4}{\partial x} \end{bmatrix}. \tag{B.8}$$

To obtain the derivatives of shape functions expressed in the parent element coordinates (ξ, η) with respect to the physical coordinates (x, y), the following transformation formulas have to be applied:

$$\begin{aligned} \frac{\partial N_i}{\partial \xi} &= \frac{\partial N_i}{\partial x}\frac{\partial x}{\partial \xi} + \frac{\partial N_i}{\partial y}\frac{\partial y}{\partial \xi} \\ \frac{\partial N_i}{\partial \eta} &= \frac{\partial N_i}{\partial x}\frac{\partial x}{\partial \eta} + \frac{\partial N_i}{\partial y}\frac{\partial y}{\partial \eta} \end{aligned} \quad or \quad \begin{bmatrix} \frac{\partial N_i}{\partial \xi} \\ \\ \frac{\partial N_i}{\partial \eta} \end{bmatrix} = \underbrace{\begin{bmatrix} \frac{\partial x}{\partial \xi} & \frac{\partial y}{\partial \xi} \\ \\ \frac{\partial x}{\partial \eta} & \frac{\partial y}{\partial \eta} \end{bmatrix}}_{\boldsymbol{J}} \begin{bmatrix} \frac{\partial N_i}{\partial x} \\ \\ \frac{\partial N_i}{\partial y} \end{bmatrix}$$

where $\boldsymbol{J}$ is the *Jacobian matrix* and it relates the derivatives of the physical coordinates with respect to the parent element ones. From the previous expression it follows

$$\begin{bmatrix} \frac{\partial N_i}{\partial x} \\ \\ \frac{\partial N_i}{\partial y} \end{bmatrix} = \boldsymbol{J}^{-1} \begin{bmatrix} \frac{\partial N_i}{\partial \xi} \\ \\ \frac{\partial N_i}{\partial \eta} \end{bmatrix} \tag{B.9}$$

that can be substituted in (B.8) in order to obtain the compatibility matrix $\boldsymbol{B}$ and derive the associated strain field $\boldsymbol{\varepsilon}$ and the related stress field $\boldsymbol{\sigma}$.

Appendix C

Newton-Raphson iterative procedure

The first two blocks of the Algorithm 1 on page 157 are related to the classical way of solving a nonlinear problem; this Appendix will only point out the iterative procedure used in the implemented code.
Generally, if a structure behaves elastically the *Elastic prediction* block of Algorithm 1 has to be applied. If instead the elastic conditions are not verified, the solving system of equations will be nonlinear. It is possible to distinguish three different cases: a *material nonlinearity*, when an external load increment doesn't correspond to a proportional strain increment; a *geometry nonlinearity*, in which the small displacements hypothesis could no longer be respected; a *constraints nonlinearity*, in which constraints conditions vary during the load applications.
A nonlinear problem implies finding the equilibrium between external and internal forces at every step n

$$F_n^{ext} = F_n^{int} \tag{C.1}$$

This kind of equilibrium has been here solved by implementing a displacement-control *incremental procedure* coupled with the classic Newton-Raphson *iterative method* and the residual norm *convergence criterion*. This procedure performs satisfactorily when handling snap-through problems, but it fails at a snap-back point and has the disadvantage that every iteration is relatively time-consuming since it is based on the progressive modification of the consistent tangent stiffness matrix for each iteration. It is an explicit integration scheme, since the time interval of each step is maintained fixed. It is calibrated and set

with not excessively large load increment sizes, in order to avoid convergence problems. A quadratic convergence has been obtained in the implemented code.

The *Nonlinear correction* block in Algorithm 1 summarizes an incremental procedure that starts from the assumption that the solution at a given step (U_{n-1}, F_{n-1}) is known and a linearization around this equilibrium point to calculate the next solution at the step (n) is operated. So, starting from the equilibrium equation at step $(n-1)$

$$\boldsymbol{K}_{n-1}\mathbf{U}_{n-1} = \mathbf{F}_{n-1}, \tag{C.2}$$

a new solution at the step (n) is been looking for

$$\boldsymbol{K}_n\mathbf{U}_n = \mathbf{F}_n \rightarrow \boldsymbol{K}_n(\mathbf{U}_{n-1} + \Delta\mathbf{U}) = \mathbf{F}_{n-1} + \Delta\mathbf{F}_n \Rightarrow \boldsymbol{K}_n\Delta\mathbf{U} = \Delta\mathbf{F}_n. \tag{C.3}$$

Considering the first iteration, it results $\boldsymbol{K}_n^{(1)} = \boldsymbol{K}_{n-1}$ so it can be written

$$\boldsymbol{K}_n^{(1)}\Delta\mathbf{U} = \Delta\mathbf{F}_n^{(1)} \tag{C.4}$$

From the displacement increment $\Delta\mathbf{U}$ the stiffness matrix $\boldsymbol{K}_n^{(2)}$ is updated, so the residual force vector is evaluated as follows

$$\boldsymbol{K}_n^{(2)}\Delta\mathbf{U} - \Delta\mathbf{F}_n^{(1)} = Err^{(1)}. \tag{C.5}$$

If the convergence check is not verified we proceed with a second iteration by solving the equilibrium system obtained by applying the error vector as the external forces vector:

$$\boldsymbol{K}_n^{(2)}\Delta\mathbf{U}_n^{(2)} = Err_n^{(1)}. \tag{C.6}$$

By evaluating the displacements increment $\Delta\mathbf{U}_n^{(2)}$ the stiffness matrix $\boldsymbol{K}_n^{(3)}$ is updated and a new error is calculated

$$\boldsymbol{K}_n^{(3)}\Delta\mathbf{U}_n^{(2)} - Err_n^{(1)} = Err^{(2)}. \tag{C.7}$$

The general procedure can be summarized for an iteration j as follows:

$$\boldsymbol{K}_n^{(j)}\Delta\mathbf{U}_n^{(j)} = Err_n^{(j-1)} \tag{C.8}$$

$$\text{Stiffness matrix updating} \Rightarrow \boldsymbol{K}_n^{(j+1)} \tag{C.9}$$

$$\text{Residual vector evaluation} \Rightarrow \boldsymbol{K}_n^{(j+1)}\Delta\mathbf{U}_n^{(j)} - Err_n^{(j-1)} = Err^{(j)}. \tag{C.10}$$

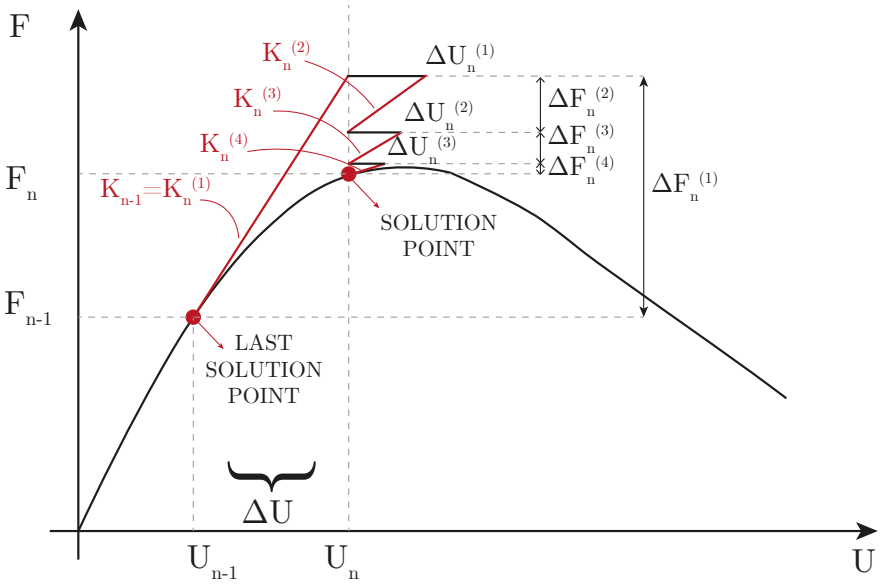

Figure C.1: Newton-Raphson iterative method with a displacement control procedure.

Acknowledgements

Il presente lavoro di tesi è frutto di un lavoro di ricerca condotto nel Dipartimento di Ingegneria dell'Università degli studi di Palermo.
Risulta doveroso fare un ringraziamento a chi ha positivamente contribuito durante lo svolgimento del mio Dottorato di Ricerca:
il Professore Giuseppe Giambanco, che primo fra tutti mi ha immesso in questo percorso, trasmettendomi la sua curiosità ed audacia nell'esplorare campi a me finora sconosciuti, fornendomi consigli utili e sempre stimolanti;
il Professore Antonino Spada, con cui ho condiviso la scrittura del codice implementato nella presente tesi e di cui ammiro l'umiltà e l'instacabile voglia di apprendere;
la ricercatrice Emma La Malfa Ribolla, per la sua disponibilità e cura verso ogni minimo dettaglio;
il Professore Milan Jirásek e l'Ing. Martin Horák per avermi accolto durante il mio periodo di soggiorno estero a Praga, fornendo un ampio contributo sull'analisi della `flutter instability` discussa nella presente tesi;
i colleghi e amici che hanno condiviso con me le giornate lavorative, Chiara, Santo ed Erika, per la serenità da loro trasmessami;
i miei amici, quelli intramontabilmente presenti nella vita, sempre pronti a credere nei miei obiettivi;
Domenico, per aver condiviso ogni mia gioia e dolore;
i miei compagni di palestra e di vita, per riuscire ad alleggerire le mie giornate;
la mia famiglia, il mio supporto costante e onnipresente, a cui dedico questo traguardo.

Palermo, September 2022.